Research & Technology Transfer

Alaska Department of Transportation & Public Facilities

Testing and Analysis of the Effects of Infiltrated Water and Ice on Friction Pendulum Bearings

Prepared by:
Rolando Grijalva Alvarado
Keri L. Ryan
University of Nevada Reno/MS 0258
1664 N. Virginia St.
Reno, NV 89557

Date
Feb. 17, 2023

Prepared for:
Alaska Department of Transportation & Public Facilities
Statewide Research Office
3132 Channel Drive
Juneau, AK 99801-7898

REPORT DOCUMENTATION PAGE

Form approved OMB No.

1. AGENCY USE ONLY (LEAVE BLANK)	2. REPORT DATE	3. REPORT TYPE AND DATES COVERED
FHWA-AK-RD-4000(197)	02-17-2023	Research Report, 01-01-2019 to 12-31-2022

4. TITLE AND SUBTITLE
Testing and Analysis of the Effects of Contamination of Friction Pendulum Bearings

5. FUNDING NUMBERS
HFHWY00181
FHWA 4000(197)

6. AUTHOR(S)
Rolando Grijalva Alvarado
Keri L. Ryan

7. PERFORMING ORGANIZATION NAME(S) AND ADDRESS(ES)
Department of Civil and Environmental Engineering
University of Nevada, Reno MS 0258
1664 N. Virginia Street
Reno, NV 89557

8. PERFORMING ORGANIZATION REPORT NUMBER

9. SPONSORING/MONITORING AGENCY NAME(S) AND ADDRESS(ES)
State of Alaska, Alaska Dept. of Transportation and Public Facilities
Research and Technology Transfer
3132 Channel Drive
Juneau, AK 99801-7898

10. SPONSORING/MONITORING AGENCY REPORT NUMBER
FHWA-AK-RD-4000(197)
HFHWY00181

11. SUPPLENMENTARY NOTES
Performed in cooperation with Earthquake Protection Systems

12a. DISTRIBUTION / AVAILABILITY STATEMENT
No restrictions

12b. DISTRIBUTION CODE

13. ABSTRACT (Maximum 200 words)

Field contamination of friction pendulum system (FPS) isolation bearings (water, ice, dirt and other debris) has been observed in several Alaskan bridges during routine bridge inspections. Characterization testing was performed on four FPS bearings in clean/dry conditions as well as wet, frozen and soil-filled. Three of the four were double pendulum bearings (DPBs); two of these formerly in-service abutment bearings from the Susitna River Bridge and one new matching Susitna DPB. The fourth was a new single pendulum bearing (SPB) representing the Robertson River Bridge abutment bearing. The experimental configuration utilized could not constrain the bearing top plate against rotation, so dynamic behavior was influenced by bearing rotation. Evidence was presented to support the hypothesis that water/ice and bearing top plate rotation cause dynamic variation of the bearing friction, which can manifest as a change in the bearing post-yield stiffness. In addition, these same effects can constrain multi-pendulum bearings to slide unevenly on top and bottom surfaces, or constrain the bearing from sliding on one surface altogether, which effectively doubles the post-yield stiffness. Analysis of the Susitna River Bridge under several different contamination scenarios showed that peak bearing displacement and forces can be substantially affected by contamination, but the pier column forces to a lesser extent. Changes are proposed to some of the property modification factors used in bounding analysis procedures as part of the bearing design process.

14- KEYWORDS :
Friction pendulum bearings, contamination, water, ice, friction coefficient, pendulum length, single pendulum bearings, double pendulum bearings, bridge bearings, seismically isolated bridges

15. NUMBER OF PAGES

16. PRICE CODE
N/A

17. SECURITY CLASSIFICATION OF REPORT	18. SECURITY CLASSIFICATION OF THIS PAGE	19. SECURITY CLASSIFICATION OF ABSTRACT	20. LIMITATION OF ABSTRACT
Unclassified	Unclassified	Unclassified	N/A

METRIC (SI*) CONVERSION FACTORS

APPROXIMATE CONVERSIONS TO SI UNITS

Symbol	When You Know	Multiply By	To Find	Symbol
		LENGTH		
in	inches	25.4		mm
ft	feet	0.3048		m
yd	yards	0.914		m
mi	Miles (statute)	1.61		km
		AREA		
in^2	square inches	645.2	millimeters squared	cm^2
ft^2	square feet	0.0929	meters squared	m^2
yd^2	square yards	0.836	meters squared	m^2
mi^2	square miles	2.59	kilometers squared	km^2
ac	acres	0.4046	hectares	ha
		MASS (weight)		
oz	Ounces (avdp)	28.35	grams	g
lb	Pounds (avdp)	0.454	kilograms	kg
T	Short tons (2000 lb)	0.907	megagrams	mg
		VOLUME		
fl oz	fluid ounces (US)	29.57	milliliters	mL
gal	Gallons (liq)	3.785	liters	liters
ft^3	cubic feet	0.0283	meters cubed	m^3
yd^3	cubic yards	0.765	meters cubed	m^3

Note: Volumes greater than 1000 L shall be shown in m^3

		TEMPERATURE (exact)		
ºF	Fahrenheit temperature	5/9 (ºF-32)	Celsius temperature	ºC
		ILLUMINATION		
fc	Foot-candles	10.76	lux	lx
fl	foot-lamberts	3.426	candela/m^2	cd/cm^2
		FORCE and PRESSURE or STRESS		
lbf	pound-force	4.45	newtons	N
psi	pound-force per square inch	6.89	kilopascals	kPa

These factors conform to the requirement of FHWA Order 5190.1A *SI is the symbol for the International System of Measurements

APPROXIMATE CONVERSIONS FROM SI UNITS

Symbol	When You Know	Multiply By	To Find	Symbol
		LENGTH		
mm	millimeters	0.039	inches	in
m	meters	3.28	feet	ft
m	meters	1.09	yards	yd
km	kilometers	0.621	Miles (statute)	mi
		AREA		
mm^2	millimeters squared	0.0016	square inches	in^2
m^2	meters squared	10.764	square feet	ft^2
km^2	kilometers squared	0.39	square miles	mi^2
ha	hectares (10,000 m^2)	2.471	acres	ac
		MASS (weight)		
g	grams	0.0353	Ounces (avdp)	oz
kg	kilograms	2.205	Pounds (avdp)	lb
mg	megagrams (1000 kg)	1.103	short tons	T
		VOLUME		
mL	milliliters	0.034	fluid ounces (US)	fl oz
liters	liters	0.264	Gallons (liq)	gal
m^3	meters cubed	35.315	cubic feet	ft^3
m^3	meters cubed	1.308	cubic yards	yd^3

		TEMPERATURE (exact)		
ºC	Celsius temperature	9/5 ºC+32	Fahrenheit temperature	ºF
		ILLUMINATION		
lx	lux	0.0929	foot-candles	fc
cd/cm^2	candela/m^2	0.2919	foot-lamberts	fl
		FORCE and PRESSURE or STRESS		
N	newtons	0.225	pound-force	lbf
kPa	kilopascals	0.145	pound-force per square inch	psi

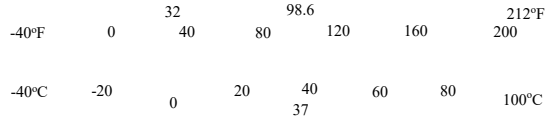

TABLE OF CONTENTS

LIST OF FIGURES

LIST OF TABLES

ACKNOWLEDGEMENTS

The research herein was performed under Contract FHWA-AK-RD-4000(197) by the Department of Civil and Environmental Engineering at University of Nevada, Reno (UNR). Keri L. Ryan, Professor at UNR, was the principal investigator. Rolando Grijalva Alvarado, PhD Student at UNR, performed the majority of the work. Grijalva Alvarado and Ryan are the authors of this report. Dynamic testing of isolation bearings was performed at UNR's Earthquake Engineering Laboratory (EEL). EEL Laboratory Manager Patrick Laplace, and EEL Technicians Chad Lyttle and Todd Lyttle provided invaluable assistance in designing an experimental configuration and instrumentation plan to meet the project goals. Furthermore, the Lyttles helped daily throughout the test program by assembling the configuration; installing, swapping, cleaning and preparing bearings for testing; and troubleshooting. UNR undergraduates Lili Pakko and Otto Kellner also assisted during laboratory testing, especially with late night dry ice refills.

The authors also acknowledge the contributions of the following individuals/corporations. Earthquake Protection Systems (EPS) supplied four bearings for this project, including two bearings to replace those removed from the Susitna River Bridge, and two new bearings supplied directly to UNR. Victor Zayas, President of EPS, offered feedback at various stages that assisted with test planning and interpretation of the data. Mustafa Hadj-Nacer, ME Research Assistant Professor at UNR, who provided guidance when designing and implementing the freezing protocol. Lili Pakko generated the figures in Appendix C. Finally, Muzaffer Borekci, Assistant Professor at Yildiz Technical University of Turkey, was responsible for development and testing of the Susitna River Bridge superstructure and substructure model. The authors are grateful for all this assistance.

EXECUTIVE SUMMARY

This project was motivated by evidence of field contamination of FPS isolation bearings in several bridges in Alaska during routine bridge inspections. Contaminants include water, dirt, and other debris, and freezing temperatures are experienced in these regions throughout much of the year. The current knowledge on property variation, bounding analysis concepts, and property modification factors was developed based on an extensive body of research. However, these particular contamination effects, especially water and ice, don't appear to have been robustly considered, if at all.

In this project, characterization tests were performed on four FPS bearings in a clean/dry state and infiltrated with water, ice and soil. Three of the four were double pendulum bearings (DPBs); two of these formerly in-service abutment bearings from the Susitna River Bridge and one new matching Susitna DPB. The fourth was a new single pendulum bearing (SPB) representing the Robertson River Bridge abutment bearing. A specialized experimental assembly was built at UNR's Earthquake Engineering Laboratory. The assembly utilized a bidirectional shake table as an actuator to impose a displacement history on the bearing, while the top of the bearing was constrained with a reactionary frame over the top. An axial load was applied with a hydraulic ram, but the assembly could not hold axial load perfectly constant or constrain the bearing top plate against rotation. Water contamination was examined by lifting the top frame and filling the bearing inner cavity with water, and ice contamination was examined by freezing the bearing overnight after surrounding it with an insulation box filled with dry ice. Loading protocols included constant sine waves, increasing amplitude (ramping) sine waves, and limited displacement histories computed from analysis of a single degree-of-freedom isolated structure subjected to ground motions.

The key findings from the testing are as follows. For the SPBs, the characterized/observed stiffness and hence pendulum length was different for movement in the positive and negative directions, and in general did not match well with theoretical. This is believed to reflect a time varying friction effect caused primarily by the bearing top plate rotation that manifests as a change in stiffness; however, the rotation data was insufficient to verify the cause. In DPBs, uneven sliding on the two surfaces and even single surface sliding (i.e. sliding limited to one surface) was observed throughout the test program. This uneven sliding phenomenon had several potential causes. First, unequal friction coefficients due to water or other contaminants, or rusted surfaces in the aged bearings could induce the uneven sliding or even prevent sliding on one surface entirely if the discrepancy was large enough. Second, ice or caked on soil were both observed to prevent the bottom surface from moving entirely until the displacement capacity of the top surface was reached. Finally, the single surface sliding was observed occasionally even in a clean, dry bearing. This also could be caused by rotation of the bearing top plate, which induces a dynamic variation in effective friction and thus unequal friction on the two surfaces, but again could not be verified. The observed pendulum length in the DPB varied from about 37" (single surface sliding limit) to more than 74" (double surface sliding limit). The pendulum length from characterization was shown to be correlated to observations of the nature of sliding, characterized by % one surface to total sliding (%OST), measured in individual cycles.

The average friction coefficients during testing were quantified from the characterization process, although the procedure cannot control for the influence of the dynamic variations. The characterized friction coefficient generally exceeded the target friction coefficient by noteworthy margins. The average friction coefficient was largest in the new bearings, and not as large in the formerly in-service aged Susitna bearings. The wet friction coefficient was found to be lower than the dry friction coefficient in all bearings except the new Robertson bearing. The friction coefficient during ice contaminated bearing tests, after ice breakaway and during the free sliding phase, was about the same on average as the dry friction coefficient. Overall, no evidence was found to support substantial increases in friction due to aging, contamination, and low

temperatures, as is often assumed in design. The ice breakaway strength was measured in the range of 10 to 18 kips in these bearings. While this resistance is significant for a lightly loaded bearing, it would be unimportant for a typical bridge bearing supporting several hundred kips. An SPB must overcome ice breakaway strength immediately to slide, whereas a DPB slides initially on one surface and thus experiences only a moderate ice breakaway effect when the single surface displacement capacity is reached, forcing the ice to break on the second surface. The ice breakaway strength is hypothesized to be independent of axial load, but vary with the size of the bearing cavity.

Next, the influence of contamination on the seismic response of the isolated Susitna River Bridge was examined through computational simulation. A spine model of the bridge structure was developed in OpenSees, and validated by comparison with a high-fidelity model developed in CSI Bridge. A combination of bearing models (representing different forms of contamination) and contamination scenarios (number of contaminated bearings) were considered. The bridge models were subjected to a suite of motions that were scaled to the target design spectrum for the bridge based on seismicity. Water contamination was modeled as a 20% decrease in the friction coefficient, interpreted as a property modification factor $\lambda_{Qd,min} = 0.8$. The water contamination was found to increase the bearing displacement demand by 5% to 17% on average over the ground motion suite depending on the scenario. The isolator forces in general decreased due to the reduced friction, and the pier forces decreased marginally (inconsequentially). The biggest risk of water contamination is that the isolators are more likely to reach their displacement capacity; however, with typical reserve capacities allotted in design, this risk is not significant.

Single surface sliding was modeled generally as an increase in the bearing stiffness K_d (reflecting the decreased pendulum length) using a standard bearing model. This represents a bounding analysis approach; in reality the bearing will transition from single surface to conventional sliding response after the displacement capacity of the one surface is reached. For comparison, a transition model approach was developed that uses an additional hysteretic material with a min-max wrapper in parallel with the bearing model. With the wrapper, the additional resistance terminates when a threshold displacement is reached. The consequences of single surface sliding, determined by bounding analysis, were as follows: contamination of isolators at any abutment or pier substantially increased the force demands of the corresponding isolators, by an average of 25-30% in the affected abutments or piers. Sometimes – but not always – this induced an accompanying increase in force demands of the corresponding piers. The consequences for the pier forces were unpredictable; in some motions the forces in affected piers increased substantially (10% or more), while in others they were unchanged or decreased. However, the consequences of increasing isolator forces due to contamination may vary for other bridge configurations with different dynamic properties. The bounding analysis is a reasonable representation of the response when the bearing displacement is not far past the point where transition occurs; however, for bearing displacements well beyond transition, the bounding analysis may underestimate displacements and response should be more carefully considered.

Finally, the effect of ice contamination in an SPB was modeled by an additional hysteretic material representing the backbone curve of ice breakaway with a max-min wrapper in each direction. Like the transition model described above, the ice breakaway backbone curve was in parallel with the conventional bearing model. The termination of ice backbone curve should be determined by load reversal, which is unknown at the start of the simulation. Thus, iteration is required to set displacement bounds on the max-min wrapper, and proceeds until the simulated bounds match the observed ones. The proposed approach is not suitable for general ice resistance simulations, but allowed the effect of ice resistance to be explored. Because the ice resistance was small relative to the axial loads on the bearings, the effects of ice resistance on the response of the bearing was less significant than the cases described above. However, these

conclusions are sensitive to the magnitude of the ice breakaway force to the bearing shear force, and could vary significantly for other bridges.

Based on observations, the authors believe no actions are needed for existing bridges. Bridge owners should feel confident that with the usual bounding analysis and other procedures to account for uncertainties, the FPS bearings on isolated bridges will have sufficient capacity/robustness to perform their function even under field conditions that cause the bearings to collect and retain water, dirt, ice, or other unwanted contaminants. If contamination is occurring, bearings should be inspected regularly for excessive corrosion or other structural damage that may necessitate their replacement.

For design of new isolated bridges or bridge retrofits, bridge engineers should consider reasonable contamination scenarios as part of the usual bounding analysis process, to the extent that such analysis can be performed with existing bearing models and design software. The transition model (single surface to double surface sliding) and ice contamination models developed for this project are insufficiently validated. They are in a developmental phase – suitable for exploratory research on potential contamination effects, but not yet robust for routine design implementation. However, some contamination scenarios can be considered as part of the typical bounding analysis process using property modification factors as prescribed in the AASHTO Guide Specifications for Seismic Isolation (AASHTO, 2014). In general, $\lambda_{min,Qd}$, $\lambda_{max,Qd}$, $\lambda_{min,Kd}$ and $\lambda_{max,Kd}$ correspond to upper and lower bound property modification factors for bearing strength (friction coefficient) and post-yield stiffness (pendulum length).

Recommended contamination scenarios to be considered for bridges in all climates are (1): reduced friction coefficient for wet friction, and (2) single surface sliding for DPBs or TPBs. More data is needed to develop a final recommended value for property modification due to wet friction. In the interim, a reduction of 80% of target is recommended based on the data from this report, interpreted as $\lambda_{min,Qd} = 0.8$. AASHTO explicitly states that $\lambda_{min,Qd}$ can be taken as 1 for sliding bearings, so this suggested property modification is not already considered under current interpretations of the design code. For single surface sliding, the effective stiffness is twice the nominal stiffness, which equates to a property modification factor $\lambda_{max,Kd} = 2$. AASHTO currently permits that for sliding bearings $\lambda_{min,Kd}$ and $\lambda_{max,Kd}$ can both be taken as 1, since the sliding radius that determines the stiffness is theoretically known. Thus, this suggested property modification also is not accounted for under current interpretations of the design code. Forces predicted by this single surface sliding bounding analysis should be evaluated for over conservatism using engineering judgment if the bearing displacement is well beyond the single surface sliding limit. Potential displacement capacity issues should be identified by combination of analyses with nominal properties and the single surface sliding bounding analyses.

Under normal bounding analysis procedures, the property modification factors are applied to all bearings. While such an approach could certainly be utilized, considering all bearings to be contaminated is probably unnecessarily conservative. Assumed contamination on the order of 25-50% of the bearings, selected strategically based on knowledge of bridge conditions or randomly in the absence of better information, is considered sufficient. However, localized peak forces are likely to be similar regardless of the scenario specifics, except in the case where total contamination fundamentally alters the dynamic characteristics while partial contamination does not.

Worth noting, Appendix A of the AASHTO provisions do provide recommended upper bound property modification factors for friction ($\lambda_{max,Qd}$) that vary depending on whether the bearing is lubricated or unlubricated, sealed or unsealed, and in a normal or extreme climate. The recommended factor combines effects of aging ($\lambda_{max,a}$), contamination ($\lambda_{max,c}$), and temperature ($\lambda_{max,t}$). Standard design likely assumes the bearings are sealed, whereas the conditions that led to this research would seem better interpreted as

unsealed, for which the recommended increase in friction is substantial (or $\lambda_{max,Qd} \geq 3$ with combined effects). However, there was no evidence of increased friction due to any combination of aging, contamination or low temperatures in the bearings tested in this project (all three conditions were represented). Data on the aging effect in particular is inconclusive since EPS acknowledges that the technologies used to achieve target friction coefficient have evolved since the aged bearings were manufactured.

CHAPTER 1: INTRODUCTION

1.1.PROBLEM STATEMENT

Seismic isolation is a passive earthquake protection concept that has been widely used to improve the performance of buildings and bridges subjected to seismic loads. In bridges, seismic isolation devices between the bridge piers and the superstructure lengthen the natural period of the structure, thus reducing the spectral acceleration demands.

One type of seismic isolation device is a spherical sliding bearing, which is composed of a top plate, a bottom plate, and one or more spherical sliding surface(s). When the device is subjected to lateral force demands, sliding occurs and energy is dissipated through friction between an articulated slider and the spherical sliding surface(s); hence, the effectiveness of these devices depends directly on their friction properties. This study will focus on Friction Pendulum System (FPS) bearings, which are spherical sliding bearings manufactured by Earthquake Protection Systems (EPS).

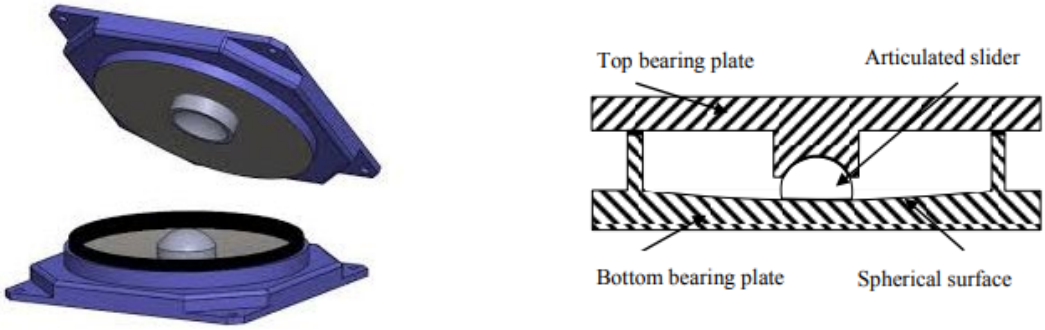

(a) (b)

Figure 1.1. Single pendulum bearing (a) 3D view and (b) Section view (Gillich et al, 2018)

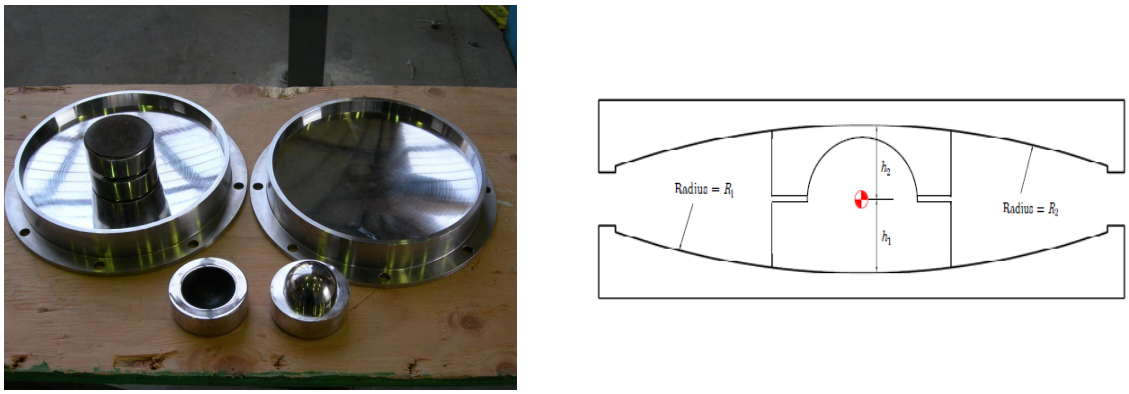

(a) (b)

Figure 1.2. Double pendulum bearing (a) Disassembled and (b) Section view (Morgan and Mahin, 2011).

There are several types of FPS bearings. Single pendulum bearings (SPBs) and double pendulum bearings (DPBs) are the focus of this study. SPBs have only one sliding surface. As shown in Figure 1.1, the bearing slides between the bottom spherical surface and the slider. The top plate is fixed to the slider, and so moves along with it. The DPBs have two independent sliding surfaces (Figure 1.2): one on top of the slider and another below the slider. The slider moves along the bottom spherical surface and the top spherical sliding plate moves relative to the slider. To achieve a comparable displacement capacity, DPBs are more compact than SPBs as displacements occur on two sliding surfaces.

Several factors influence the friction characteristics of FPS bearings, such as lubrication, slide velocity, pressure, temperature, surface roughness, contamination, corrosion, load dwell, and cumulative travel. One factor that has not been addressed adequately in the literature is water contamination. Water inside the bearing can freeze in cold climates. Entrapped ice may obstruct the movement of the bearing, and the resulting shear demand may increase to a point that could be damaging for the structure. Bridge engineers are increasingly concerned about how friction characteristics and the overall response of FPS bearings will be affected by such water or ice contamination. The Alaska Department of Transportation and Public Facilities (DOT&PF) has reported water contamination in several SPB and DPB bearings from Susitna River Bridge, Kodiak Near Island Bridge, and Robertson River Bridge. Figure 1.3 shows water contamination in the Robertson River Bridge.

Figure 1.3. Water contamination in Robertson River Bridge (Alaska DOT&PF, 2019).

The consequences of water and ice contamination in bearings should be studied to determine their effects on the seismic performance of devices. Depending on the findings, revised design procedures can be developed to account for these effects in the design process.

1.2. OBJECTIVES AND SCOPE

Numerous studies have been conducted on how variables such as velocity, temperature, lubrication, corrosion, load dwell, and others affect the frictional properties of spherical sliding bearings. A good summary is given by Constantinou et al. (2007) and summarized in Appendix A. McVitty et al. (2015) presents a thorough review and assessment of the latest guidance for using property modification factors in design to account for expected variation in response over the life of the structure. However, no documented studies on how water contamination affects the response of FPS bearings were found in the literature. Mens & Gee (2001), Wang et al. (2009), and Jia et al. (2005) studied the effect of water on the frictional properties

of steel-polymer friction interfaces in general, and these studies found some evidence that water may reduce the coefficient of friction.

Entrapped ice in an FPS bearing is a problem specific to very cold climates, and again, no public studies have been reported. The authors were supplied with an internal report of ice contamination tests conducted on FPS bearings at the EPS facility for the Tappan Zee bridge project (Tappan Zee Constructors 2017). This report noted no major effects of ice contamination on the bearing's responses, but the report stated that application of axial load might have cracked the ice before the test began. In addition, liquid nitrogen was used to freeze water in the bearing, which led to a very rapid freezing process that might have weakened the ice due to differential thermal stresses that arise under rapid freezing (Petrenko & Whitworth, 1999). A detailed literature review of available information on the effects of the effect of water on the friction coefficient, and the mechanics of ice adhesion and cohesion to related surfaces can be found in Appendix A.

To date, almost no experimental work has been conducted to examine the effects of ice and water contamination in FPS or generally in spherical sliding bearings. In this project, the seismic response of one new SPB and three DPBs (one new and two removed from service) are evaluated under clean conditions as well as contaminated with water, ice, and soil.

The objectives of this research are: (1) to characterize how water and ice contamination affects the performance of FPS bearings, (2) to evaluate the performance of aged bearings relative to new bearings, and (3) to predict the influence of water and ice contamination on the response of representative bridges through computational simulation of various contamination scenarios. The authors will provide recommendations for DOTs to consider to account for contamination in the design process.

One bearing at a time was placed within a test assembly that used the shake table as an actuator and constrained movement at the top with a load frame. Various cyclic sinusoidal and earthquake loadings were applied. For all tests, a controlled axial load was applied to the bearing using a hydraulic ram and transmitted through the load frame. Further, analytical models were developed to account for the effects of water and ice contamination on the bearings' frictional properties, and bridge models were built to investigate the effects of contamination on the overall response of the bridge.

CHAPTER 2: EXPERIMENTAL METHODOLOGY

2.1 EXPERIMENTAL SETUP

One SPB and three DPBs were tested at UNR Earthquake Engineering Lab. The SPB was a new bearing with the same characteristics as the abutment bearings from Robertson River Bridge (Robertson). Two of the DPBs were formerly in-service bearings removed from the abutments on Susitna River Bridge (Aged Susitna 1 and Aged Susitna 2) while the third DPB was a new bearing (New Susitna) with the same characteristics as Aged Susitna 1 and 2. Figure 2.1 shows the experimental assembly used to test the bearing. The shake table was used as an actuator to impose displacements on the bearing bottom plate. Reference X- and Y-directions used to load the bearings are shown in Figure 2.1(a). A steel frame (A-frame) was designed, constructed, and assembled on top of the bearing to restrain the bearing top plate from movement in both horizontal directions, as shown in Figure 2.1(a). Furthermore, the A-frame was connected on one end to two rigid steel columns using a swivel pin connection, thus allowing for rotation in the connection. Vertical load was applied on the end opposite the steel columns using a hydraulic ram, then the vertical load was transmitted by the A-frame to the top of the bearing vertical arrangement. The design of the steel frame is presented in detail in Grijalva (2021).

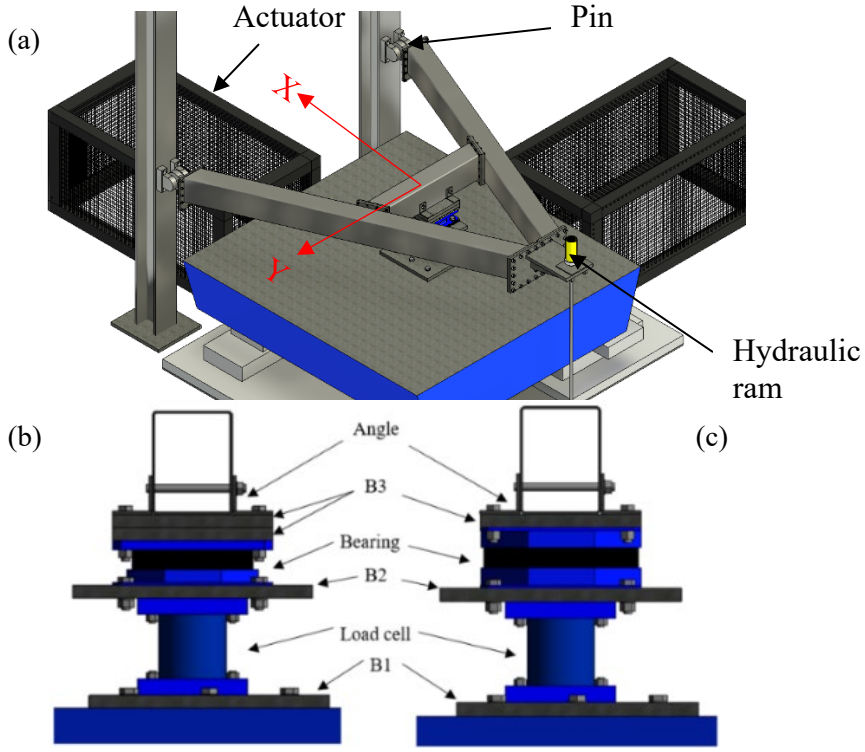

Figure 2.1. Experimental setup (a) 3D rendering (b) SPB setup elevation (c) DPB setup elevation.

As shown in Figure 2.1(b) and (c), the bearing was connected to the A-frame using two steel adapter plates with angles on top. Bolts were placed through the angle and top adapter plate and secured beneath the bearing top plate. Two or three ½" fiber reinforced polymer (FRP) insulation plates, depending on the bearing, were placed between the steel adapter plates and the bearing top plate. A load cell, which was connected to the bearing using a steel adapter plate, was placed below the bearing to measure shear force in both horizontal directions and axial load. Three ½" FRP insulation plates were placed between the bearing bottom plate and the adapter plate.

Bearing bottom plate and slider displacements were measured using string pots in both horizontal directions. To measure relative displacement between the A-frame and the bearing bottom plate, the string pot housings were attached to the A-frame and the strings were attached to the bearing bottom plate. To measure relative displacement between the A-frame and the inner articulated slider (DPB only), the string pot housings were attached to the A-frame and the strings were wrapped around the slider.

For wet tests, the bearing seals were cut and pulled back, allowing for a hose to be inserted to fill the inner cavity with water. Three water levels were tested: a thin layer of water lubrication, water to the top of the bottom ring (water height ~ 2.52”), and water halfway to the top of the bottom ring (water height ~ 1.26”). An insulation box was developed to freeze water in the bearing. The insulation was made of four pieces of 2” polyurethane insulation panels held together using steel sheets fastened to the connecting panels by Tek screws, as shown in Figure 2.2(b). Two pieces were sandwiched together to form the bottom of the box, while the remaining two pieces formed the lid. The insulation box was designed to wrap around the bearing and to rest on top of the adapter plate between the bearing and the load cell (Figure 2.2(a)).

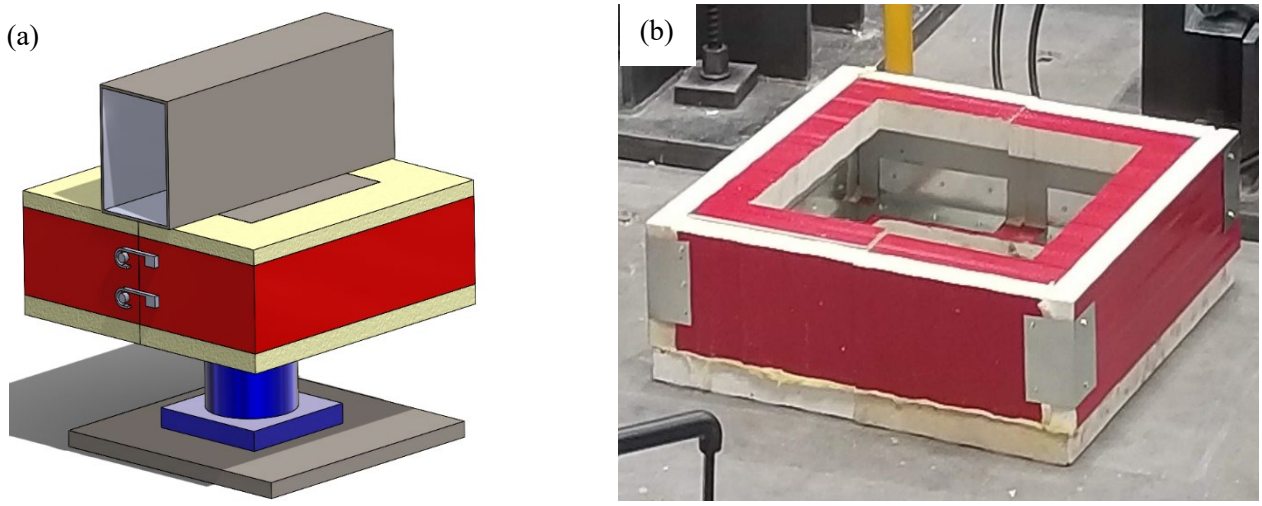

Figure 2.2. Insulation box (a) 3D rendering (b) Physical box.

To freeze water inside a bearing prior to frozen tests, the bearing was filled with water using the process described above and the bottom portion of the insulation box was wrapped around the bearing. The insulation box was then filled with dry ice and the lid pieces were put in place. Based on preliminary thermal element analysis and off-table experimental freezing tests to validate the effectiveness of the insulation box, it was expected that the ice would reach a temperature of -40°F after approximately 14 hours of freezing with dry ice (Grijalva, 2021). After some trial and error, freezing the bearing overnight for about 15 hours and refilling the dry ice after 5-6 hours was found to be effective to reach the lowest temperature at the time of testing. The temperature was monitored using thermocouples around and inside the bearings. Similar to the wet tests, two ice layer heights were considered: 2.52” and 1.26”.

Most of the testing – including tests on Robertson, Aged Susitna 1, and New Susitna bearings – was conducted in a first phase (Phase 1). Toward the end of Phase 1, visible rotation of the top plate about the Y-axis and overall movement/slip was observed in some of the bearing components. Testing was concluded in Phase 2 with tests on Aged Susitna 2 and additional tests on the other bearings. The following changes were implemented for Phase 2:

- The A-frame was secured to the bearing top plate with through rods from the top of the frame to prevent the bearing from slipping with respect to the frame.

- Extra care was taken to straighten the bearing in the setup as much as possible by making use of all steel adapter and insulation plates.
- Frozen tests (and corresponding control tests) were conducted in the Y-direction instead of the X-direction to minimize rotation-based asymmetries.
- Rotation history in the X-direction was recorded by two string pots attached from a fixed point above to either side of the A-frame cross piece. Unfortunately, the initial reference rotation as each bearing was placed could not be observed.

These key differences in setup between the two phases are illustrated in Figure 2.3.

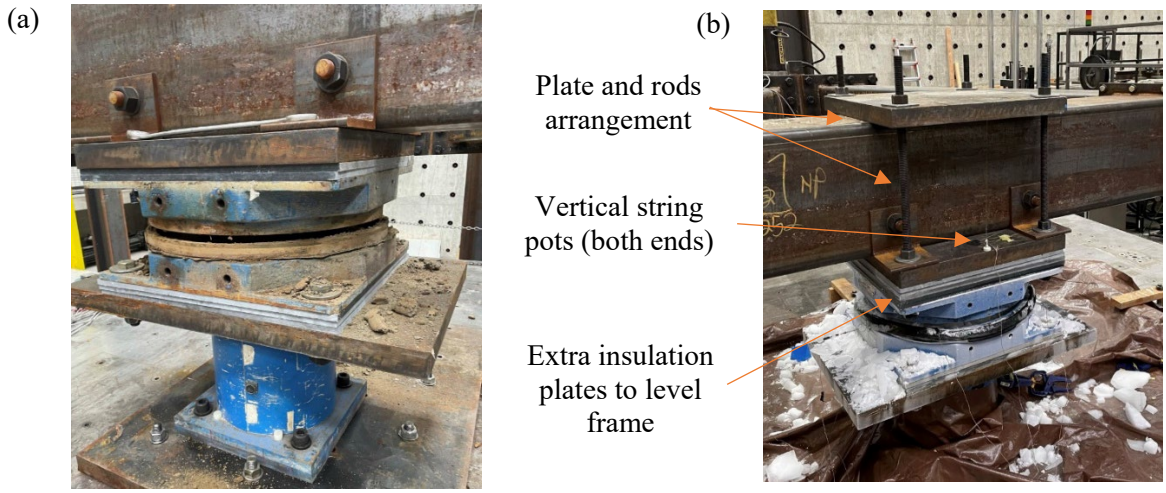

Figure 2.3. Bearing set up and connection to A-frame (a) Phase 1 (b) Phase 2.

2.2 TEST SPECIMENS

The test bearings for this study were supplied by Earthquake Protection Systems (EPS). Figure 2.4 shows the bearings tested and cross section drawings. The Robertson bearing is shown in Figure 2.4(a) and (b), while the Susitna bearings are shown in Figure 2.4(c) and (d).

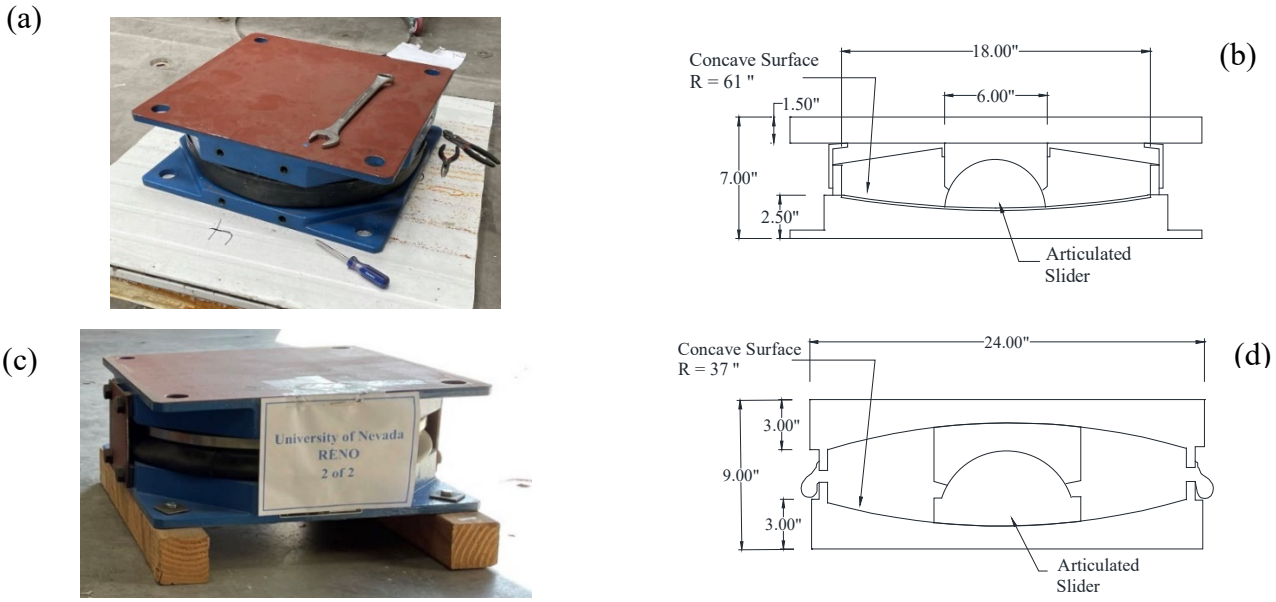

Figure 2.4. SPB (a) Photo (b) Cross section, and DPB (c) Photo (d) Cross section.

The target friction coefficient and bearing pendulum length for Robertson and Susitna, respectively, were used to estimate the design parameters of each bearing, following AASTHO Guide Specifications for Seismic Isolation (AASHTO, 2014). The following equations were used to calculate design displacement *D* and effective period T_{eff}, respectively:

$$D = \left(\frac{g}{4\pi^2}\right)\frac{S_{D1}T_{eff}}{B_L} \qquad \textbf{(Eq. 2.1)}$$

$$T_{eff} = 2\pi\sqrt{\frac{m}{K_{eff}}} \qquad \textbf{(Eq. 2.2)}$$

where S_{D1} is the 1 sec spectral acceleration, B_L is an adjustment factor for damping, K_{eff} is the secant stiffness to the design displacement, and *m* is the mass supported by the bearing or system. The bearing design parameters are summarized in Table 2.1. These design parameters were estimated based on current seismic hazard using (63.4971N, -143.836W) and (62.1747N, -150.1737W) geographic coordinates for Robertson and Susitna River Bridges, respectively. Although the actual design of the in-service bridges was based on earlier versions of the code, current design procedures were used to estimate design parameters shown in Table 2.1.

Table 2.1. Bearing design parameters

Spectral Parameters	**Robertson**	**Susitna**
S_s (g)	0.4164	1.025
S_1 (g)	0.2302	0.371
Soil type	D	B
PGA (g)	0.175	0.486
S_{DS} (g)	0.612	1.025
S_{D1} (g)	0.447	0.362
Bearing Response	**Robertson**	**Susitna**
Target friction μ	0.10	0.075
Pendulum length *L* (in)	61	74
Pendulum period *T* (s)	2.50	2.75
Axial force/Weight *W* (kip)	18	100
Effective stiffness K_{eff} (kip/in)	0.737	3.363
Effective period T_{eff} (s)	1.578	1.743
Design displacement *D* (in)	4.05	3.72

2.3 LOADING PROTOCOL

As mentioned previously, the shake table was used as an actuator to impose displacement protocols onto the bearings. Imposed loading included constant amplitude sine waves, increasing amplitude sine waves (ramping sine), and ground motions. Sinusoidal displacement histories are preferred for smooth hysteresis loops that can be systematically characterized. In ramping sine waves, the maximum displacement was

increased after each cycle. Furthermore, with ramping sines, the maximum displacement capacity of a single sliding surface was not reached until the fifth cycle, hence providing information about the effects of ice contamination before and after the ice broke.

In contrast to a theoretical sine wave, the shake table actuators need to start the motion at velocity 0. Hence a Tukey window ($w(x)$) was used to taper the signal at the start and end of the sine wave signal (Bloomfield, 2000):

$$w(x) = \begin{cases} \frac{1}{2}\left(1 + \cos\left(\frac{2\pi}{r}\left[x - {}^{r}/_{2}\right]\right)\right) & 0 \le x \le \frac{r}{2} \\ 1 & \frac{r}{2} \le x \le 1 - \frac{r}{2} \\ \frac{1}{2}\left(1 + \cos\left(\frac{2\pi}{r}\left[x - 1 + {}^{r}/_{2}\right]\right)\right) & 1 - \frac{r}{2} \le x \end{cases} \qquad \textbf{(Eq. 2.3)}$$

where r is the percentage of the signal to be tapered and x is the point in time at which the signal is being tapered as a percentage of the total signal length. Furthermore, the theoretical sine waves were multiplied by $w(x)$ to get the tapered signal, using r as 0.1. Figure 2.5 shows a comparison between the original sine wave and the tapered one for a test conducted on the Robertson bearing at 4.05" maximum displacement.

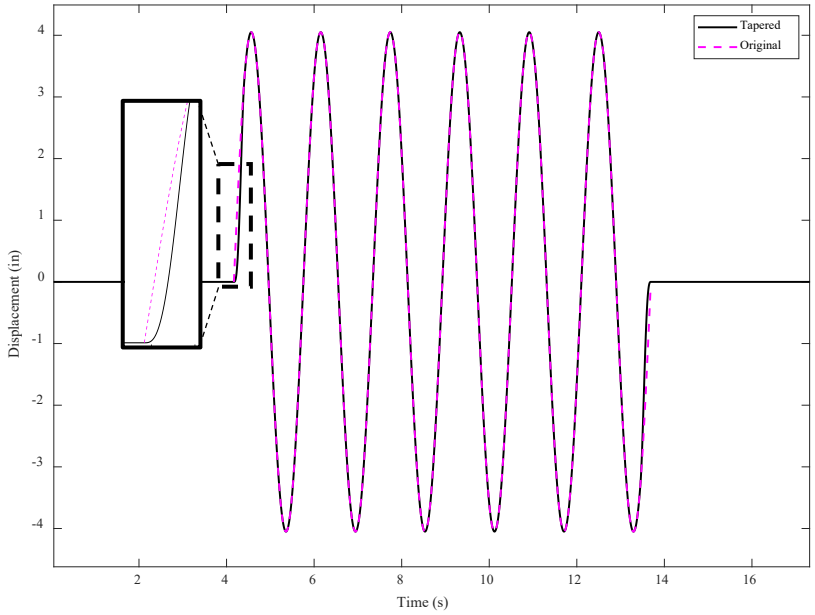

Figure 2.5. Tapered constant amplitude sine wave with maximum amplitude of 4.05".

The design displacement and effective period in Table 2.1 were used for many of the sine wave trials. In addition, trials at increments of the design displacement with corresponding variation of the frequency were implemented to represent standard qualification testing. Larger amplitude displacements were sometimes imposed on the Susitna bearings to induce sliding on both surfaces. The increasing amplitude sine wave (also referred to as ramping sine wave) was developed to more carefully analyze the behavior of the Susitna bearing where ice initially constrained the movement on one surface.

Constraints on the hydraulic ram required that two target axial loads be selected for each bearing to allow for swapping between the targets easily throughout the test program. One value was intended to be close to the design axial load (Table 2.1), while the other allowed for assessment of axial load variation. Key variations in the sinusoidal loading protocol are summarized in Table 2.2.

Table 2.2. Loading protocol variations

	Robertson	Susitna
Displacement (in)	4.05, 1.02, 2.05, 3.03 and 5.06.	3.72, 0.94, 1.85, 2.80, 4.64, 8.00 (ramping sine) and 10.00.
Frequency (hz)	0.63, 1.06, 0.80, 0.69 and 0.59.	0.57, 0.96, 0.73, 0.63, 0.54, 0.29, 1.14, 0.48 (ramping sine) and 0.45.
Axial load (kips)	25 and 15	100 and 55.

Two recorded ground motions were selected to represent the design level earthquake for each bearing. The bearing response to the ground motions was calculated using OpenSees, and the motions were scaled to match the target displacement. The bearing displacement history response in both horizontal directions was used as an input for the shake table. The motions were chosen by inspection after considering records from several databases; criteria were that the motion was recorded on similar site conditions, produced several cycles of significant displacement in the bearing, and the scale factor was to be limited to 2. The 1940 Imperial Valley – El Centro Array #9 station and the 1994 Northridge – Saticoy station ground motions, scaled by factors of 1.56 and 1.48, respectively, were selected for the Robertson bridge bearing. Two different versions of the 1940 Imperial Valley – El Centro Array #9 ground motion, scaled by factors of 1.43 and 2.02, were selected for the Susitna bridge bearing. The El Centro motion was also scaled up to a maximum displacement of 8.50” for an additional trial in which both sliding surfaces were engaged.

Aged Susitna 1 was received in a soil contaminated state with soil stuck to the bottom sliding surface (Figure 2.6). The bearing was tested in the “as-received” condition up to the design displacement, which induced sliding only on the top surface. However, the condition was not discovered until removing the seals after the test. Aged Susitna 2 was received with modest soil contamination and a 1” water layer on top of the soil layer. The bearing was tested frozen as-received out to a displacement of 10” in the initial trial.

Figure 2.6. Condition of Aged Susitna 1 upon removing the seals following “as received” test.

In an attempt to recreate the initial condition of Aged Susitna 1, Aged Susitna 2 was tested in a baked soil condition. High clay-content soil was selected because clay would cause the soil to stick to the bottom sliding surface, creating conditions similar to those observed on Aged Susitna 1. The soil was procured from a construction site close to the UNR Earthquake Engineering Laboratory. Prior to testing, the soil was

saturated and compacted in layers in the bearing, then heat guns were used to dry the soil for approximately 6 hours. Afterward, the bearing was left to continue drying overnight without using the heat guns.

A total of 227 trials were conducted throughout the test program. A complete test log is included in Appendix B, with trials listed in order and parsed into tables by test date. Included in the test log are: date, bearing tested, loading protocol, maximum displacement, axial load, rate, condition (e.g., frozen, wet, or dry), and any special notes concerning the specific trial. Phase 1 with 14 test days commenced on 09/20/21 and ended 10/07/21 while Phase 2 with 7 test days commenced on 12/07/21 and concluded on 01/05/22.

2.4 IDEALIZED BILINEAR LOOP FIT

A procedure was developed to fit an idealized bilinear hysteresis loop to the experimentally observed hysteresis loop. Given the axial load variation observed during the tests, the bearing shear force was normalized by the axial force. The idealized loop is quantified by the post-yield stiffness, which is correlated to the pendulum length, and the friction coefficient. First, a best fit line was fitted independently to the top and bottom lines of the normalized hysteresis loops, which represent movement in the positive and negative directions, respectively. Then, the slope was averaged to derive the post-yield stiffness of the idealized bilinear loop. Furthermore, the energy dissipated per cycle (EDPC) was calculated as the area of the normalized hysteresis loop, and μ was calculated according to:

$$\mu = \frac{EDPC}{2(D_{max} - D_{min})} \quad \textbf{(Eq. 2.4)}$$

where D_{max} and D_{min} are the maximum and minimum recorded bearing displacement, respectively. The first cycle was omitted because it was affected by the initial static friction, hence the linear curve would not reflect the post-yield stiffness or energy dissipation properly. The last cycle of each trial was also omitted because the force declines at the end of the trial as displacement approaches zero, which creates discontinuity between the positive and negative displacement regions of the hysteresis loop. Figure 2.7 shows an example of the idealization process using the fifth cycle of one of the dry tests on Aged Susitna 2 at 55 kips axial load and 10” maximum displacement in the Y direction. Both direct linear fits of the top and bottom lines and an average – labeled Bilinear fit – are shown in Figure 2.7.

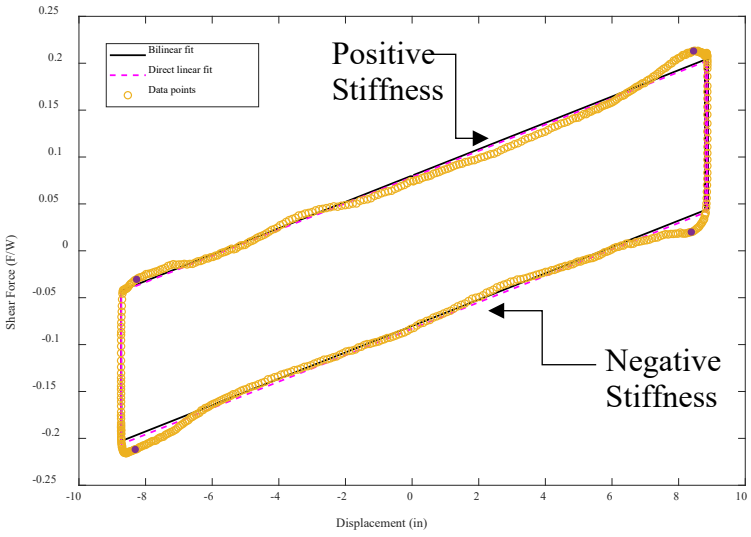

Figure 2.7. Idealized bilinear loop fit

CHAPTER 3: EXPERIMENTAL RESULTS

This chapter presents and interprets key findings of the experimental program. First, general properties of the observed hysteresis loops are discussed, including discussion of some irregularities and potential causes of those irregularities (Section 3.1). Next, trends for pendulum length (Sections 3.2 and 3.3.4) and friction coefficient (Section 3.4) of SPBs and DPBs are presented. The irregularities induced uneven sliding on DPBs, which affected the characterization results. This phenomenon and its implications are presented in detail. Finally, the nature of sliding in an ice-filled bearing is presented and ice breakaway strength is computed (Section 3.5).

3.1 OBSERVED ASYMMETRIES

Figure 3.1 shows an example set of axial load history, hysteresis loop, and normalized hysteresis loop for a dry test conducted on Robertson at 15 kips target axial load and 4.05" of maximum displacement in the X-direction. Figure 3.1(a) shows that the axial load varied throughout the test in correspondence with the cyclic displacement. Such variation was observed throughout the test program and indicates that the hydraulic ram was not able to hold the load exactly constant. Greater variation was observed in the X-direction trials (along the length of the frame). Variations in axial load were likely due to changes in pressure in the hydraulic ram as the slider moves upward along the spherical surface. Furthermore, in the X-direction tests, the moment arm changes as the bearing moves toward and away from the hydraulic ram.

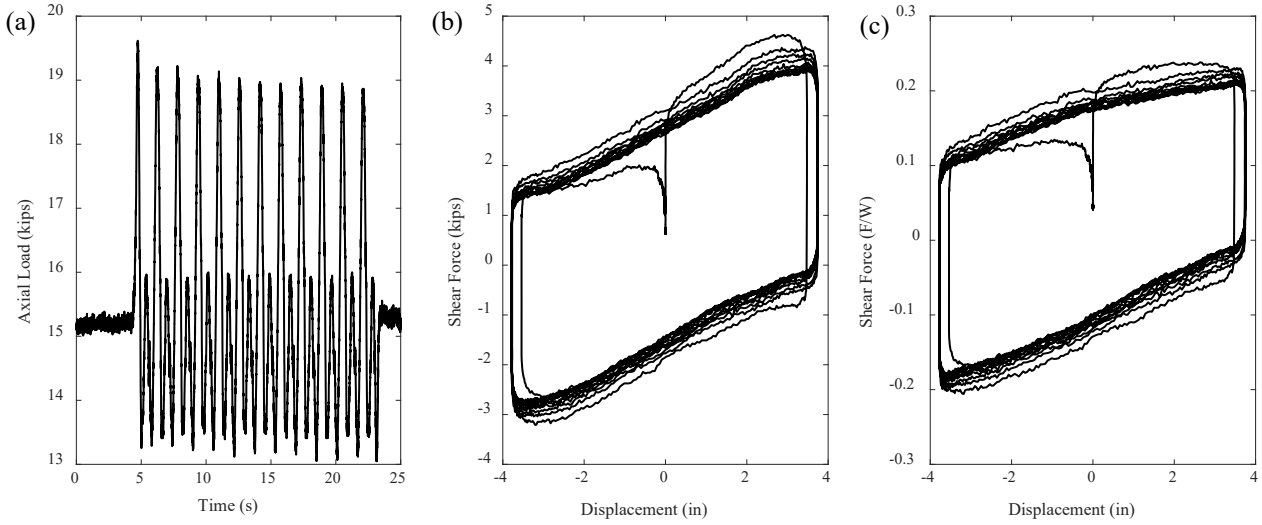

Figure 3.1. SPB at 15 kips target axial load and 4.05" displacement (a) Axial load history (b) Hysteresis loop (c) Normalized hysteresis loop.

Variation in axial force affects the hysteresis loops. When axial force is constant, the absolute (shear force versus displacement) and normalized (shear force normalized by axial force versus displacement) hysteresis loops are identical. Overturning-induced variation in axial force can cause proportional variation in shear force due to the proportional (friction) relation. In Figure 3.1(b), the absolute hysteresis loop does not appear to be affected by variations in axial force, although it is a little wider near the ends (peak displacements). If the asymmetry is due to axial force alone, it would disappear in the normalized hysteresis loop. However, asymmetry can still be observed and in fact is amplified in the normalized hysteresis loop in Figure 3.1(c), which suggests that axial force variation is not the only source of the observed asymmetries.

Asymmetries in the hysteresis loops were observed in many of the sinusoidal characterization tests. shows an example idealized bilinear loop for two tests on Robertson at 15 kips target axial load and 4.05" maximum displacement, one in the X-direction (Figure 3.2(a)) and the other in the Y- direction (Figure 3.2(b)). In general, differences between the bilinear fit (solid black line) and the direct linear fit (magenta dashed line) are more evident in X-direction than in Y-direction tests. Positive post-yield stiffnesses for this example are 0.0149 1/in in the X-direction and 0.0188 1/in in the Y-direction, while negative post-yield stiffnesses are 0.0257 1/in and 0.0132 1/in, respectively. On average, characterized loops from Y-direction tests are closer to the theoretical value of 0.016 1/in (equivalent to a pendulum length of 61" or 1/0.016), and positive and negative stiffnesses tend to be closer to each other.

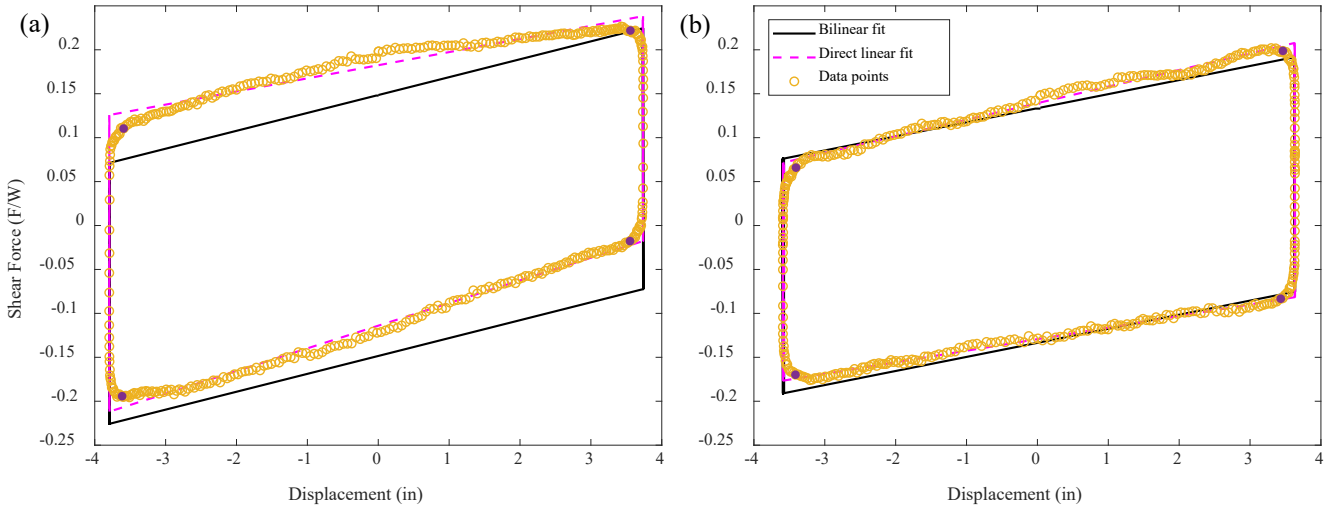

Figure 3.2. Idealized bilinear loop Robertson at 15 kips target axial load and 4.05" displacement (a) X direction (b) Y direction.

Differences between the X- and Y-directions are attributed to the experimental configuration. A hypothesis is that the asymmetry in the hysteresis loops, especially in the X-direction, was caused by rotation of the frame imposed on the bearing top plate. Figure 3.3 illustrates how the bearing movement is accompanied by rotation. Dashed black lines show the initial bearing position while red lines show the bearing in the deformed configuration for different directions of movement. (Note that the rotations are exaggerated in these images for clarity.) There was initial rotation on the bearing top plate due to fabrication tolerances of the frame, plates, and bearing even after adding extra insulation plates in Phase 2. As shown in Figure 3.3(a), when the bearing moves away from the hydraulic ram (shown on the left end), the frame experiences a counterclockwise rotation and the slider moves "with gravity". On the other hand, when the bearing moves toward the hydraulic ram (Figure 3.3(b)), the frame experiences a clockwise rotation and the slider moves "against gravity". Under this hypothesis, the stiffness increases for movement in the negative direction and decreases for movement in the positive direction, which is consistent with observation (Figure 3.2(a)).

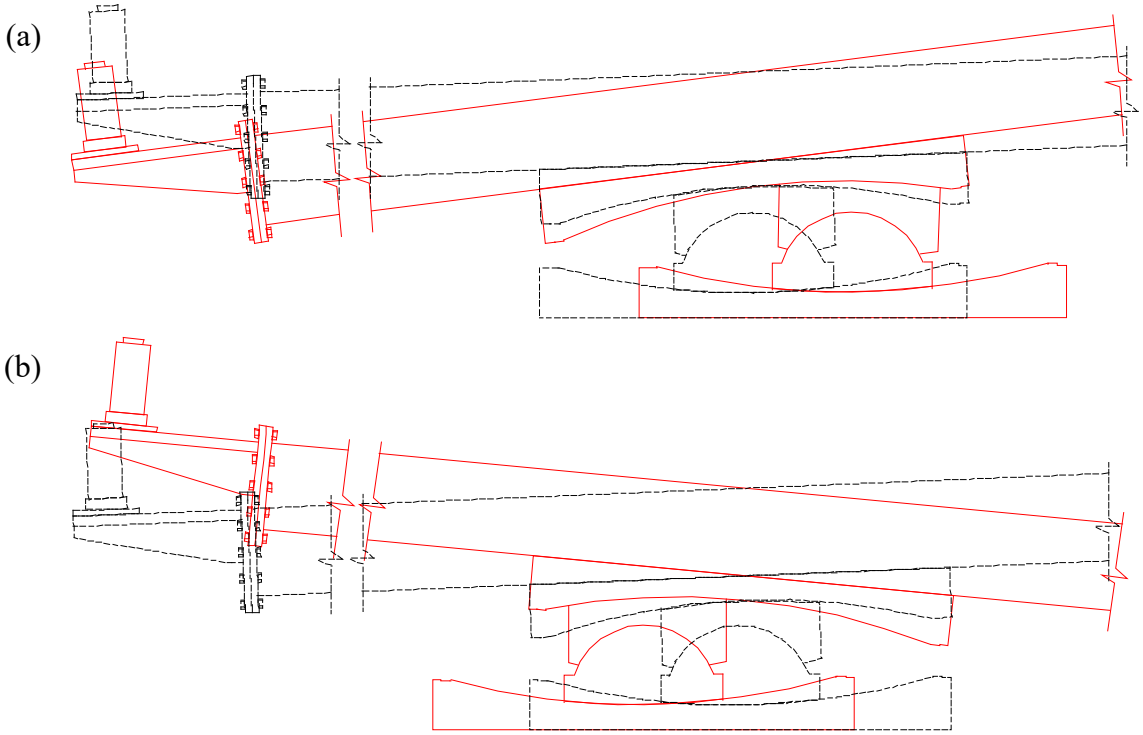

Figure 3.3. Bearing movement and frame rotation (a) Counter clockwise rotation (b) Clockwise rotation.

Theoretical formulations of the effect of bearing top or bottom plate rotation on overall hysteresis response of FPS bearings were developed by Mosqueda et al. (2004) and Fenz & Constantinou (2008). In summary, a constant rotation is predicted to shift the hysteresis loop up or down so that it is no longer centered on the X-axis (displacement axis). A rotation that varies linearly through the cycle is expected to manifest itself as an apparent change in the stiffness or pendulum length over the duration of that movement. The effects of rotation on FPS bearings is discussed in more detail in Section 3.3.3.

3.2 PENDULUM LENGTH IN SINGLE PENDULUM BEARINGS

Figure 3.4 summarizes observed pendulum lengths for all dry tests with the sine wave protocol on the Robertson bearing. Pendulum lengths were calculated as the inverse of the experimental post-yield stiffness (1/k). The dashed line represents the theoretical pendulum length. Fitted pendulum lengths are shown for positive direction movement, negative direction movement, and the average of both. Each data marker represents an individual cycle, and connected lines represent multiple cycles in a single test. Furthermore, Y-direction tests have been plotted underneath their reciprocal X-direction tests. The varied parameters for each trial shown in Figure 3.4 are summarized in Table 3.1.

Differences in negative and positive pendulum length were observed in all tests for both directions. However, average pendulum length is closer to the theoretical values in the Y-direction. Furthermore, the last two tests on the Y-direction were conducted during Phase 2, hence the modifications to the test setup might have reduced the differences between positive and negative pendulum length. On the other hand, average pendulum length in the X-direction tests seemed to consistently differ from the theoretical value by about 20% and modifications in Phase 2 did not seem to have an important effect on the experimental pendulum length. As stated in Section 3.1, the observed differences between the X- and Y-direction tests might have been caused by the experimental setup.

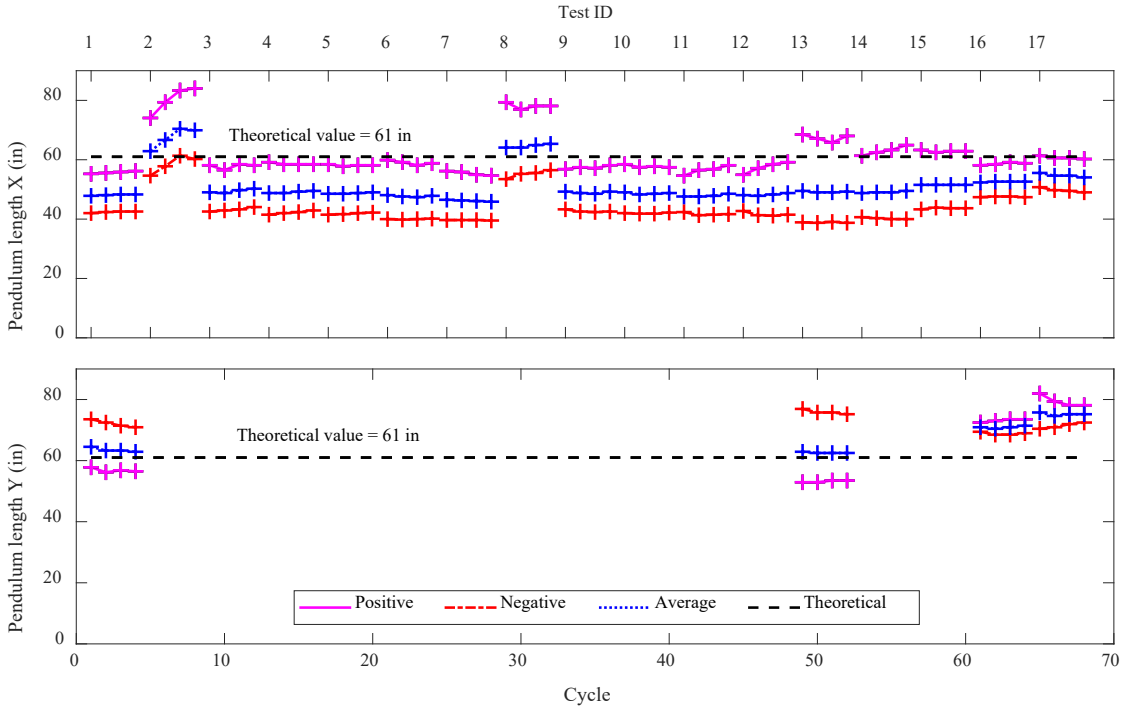

Figure 3.4. Robertson dry tests pendulum length.

Table 3.1. Robertson dry tests summary

Test ID	Maximum displacement (in)	Axial load (kips)	Testing Phase
1	4.05	25.00	Phase 1
2	1.02	25.00	Phase 1
3	2.05	25.00	Phase 1
4	3.03	25.00	Phase 1
5	4.05	25.00	Phase 1
6	5.08	25.00	Phase 1
7-12	4.05	25.00	Phase 1
13-15	4.05	15.00	Phase 1
16	4.05	25.00	Phase 2
17	4.05	15.00	Phase 2

3.3 SLIDING PHENOMENON IN DOUBLE PENDULUM BEARINGS

Theoretical formulation of a symmetric DPB (equal radii on top and bottom surfaces) generally assumes that the displacement is evenly distributed over both sliding surfaces, as long as shear demands are higher than the characteristic strength (μW) of both sliding surfaces (Morgan & Mahin, 2011). However, several displacement regimes were observed throughout the test program, as illustrated in the sample

displacement histories in Figure 3.5. These plots show independent movement on the top and bottom surfaces, as well as total movement. Response behavior ranged from sliding only on one surface (Figure 3.5(a)) to sliding evenly distributed on both sliding surfaces (Figure 3.5(c)). Sliding on one surface will be referred to as *single surface sliding* while sliding evenly distributed on both sliding surfaces will be referred to as *double surface sliding*.

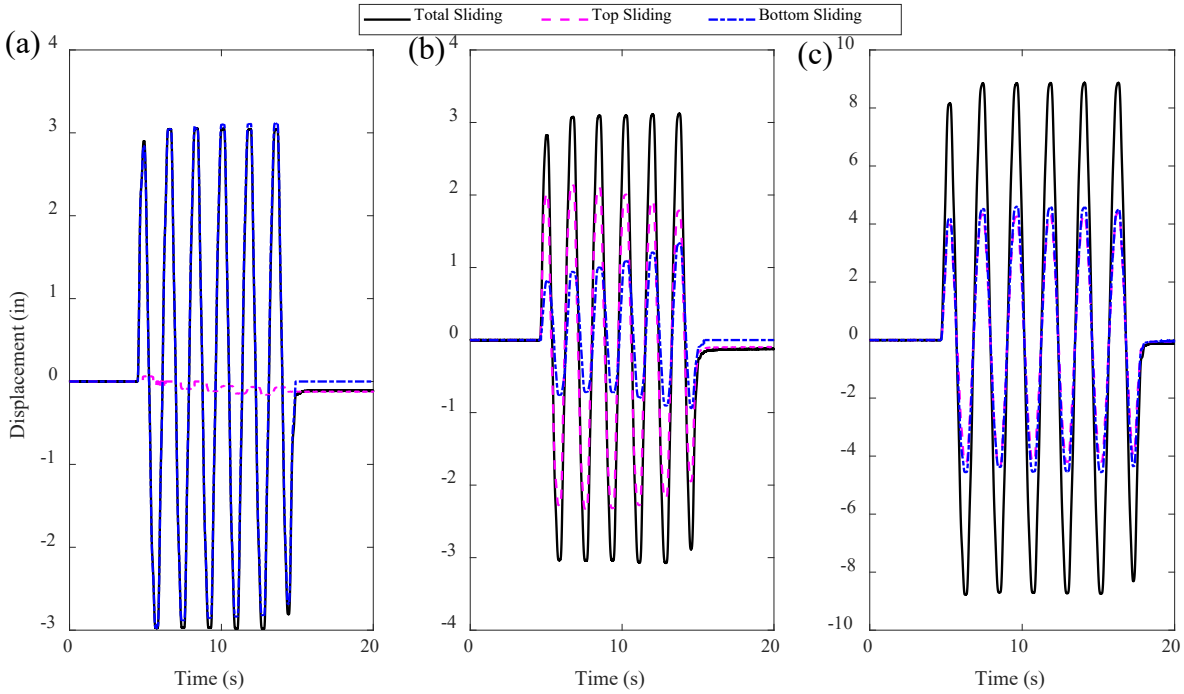

Figure 3.5. Displacement history Aged Susitna 2 (a) 3.74" maximum displacement and 55 kips axial load wet (b) 3.72" maximum displacement and 55 kips axial load dry (c) 10" maximum displacement and 55 kips axial load dry.

3.3.1. EFFECTS OF CONTAMINATION ON SLIDING BEHAVIOR

DPBs were tested under water, soil, and ice contaminated conditions, which all seemed to cause uneven sliding or single surface sliding. In Phase 1, water tests were conducted at three different water levels, as stated in Section 2.1. Figure 3.6 shows the different sliding regimes observed on wet tests at 100 kips target axial load and 3.72" maximum displacement, which is lower than the displacement capacity of one sliding surface or 5.5". Variations in these trials include water height and displacement loading direction. Double surface sliding is reached after a few cycles for the trials with 2.52" of water, and the response is similar in the X-direction (Figure 3.6(a)) and the Y-direction (Figure 3.6(b)). Based on literature review, the static friction coefficient for wet sliding may be greater than for dry sliding. Thus, these plots suggest that sliding initiated on the top (non-immersed) surface but balanced out quickly once sliding was triggered on the bottom surface, likely due to higher force demands associated with single surface sliding. Figure 3.6 (c) shows single surface sliding on the top (non-contaminated) sliding surface for the X-direction trial with 1.26" of water, and Figure 3.6(e) shows that even though both sliding surfaces were engaged in the X-direction test with a thin lubrication layer, the top sliding surface dominated the movement. Comparing Figure 3.6(a), (c), and (e) shows that even though water induces uneven sliding, the amount of water does not systematically affect the bearing response. Also, some differences were observed between the X- and Y-direction tests, which are more obvious in some cases (Figure 3.6(e) and (f)) than others (Figure 3.6 (a) - (d)). These differences could have been caused by the experimental setup.

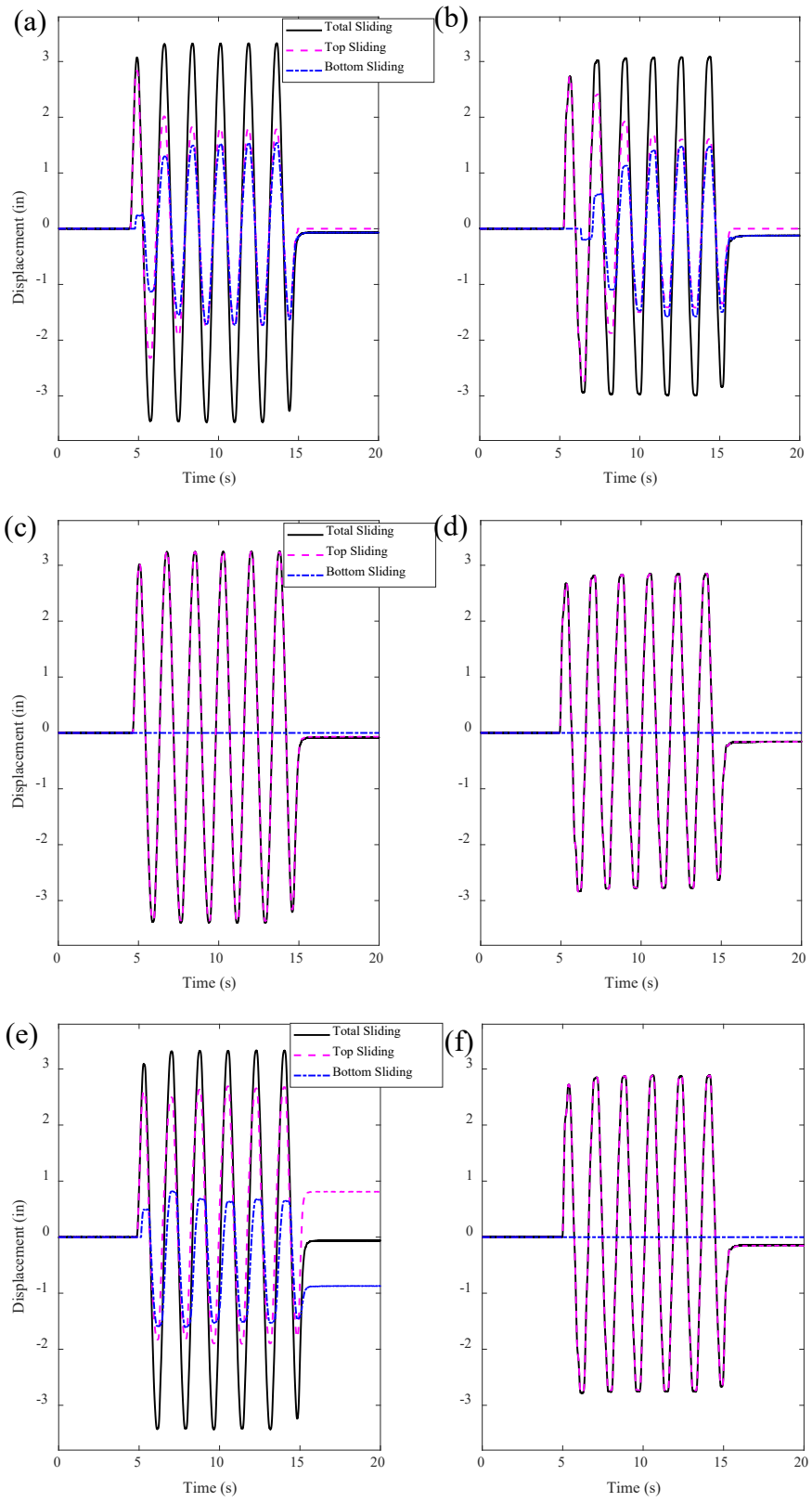

Figure 3.6. Displacement history for wet tests in Aged Susitna 1 at 3.72" maximum displacement and 100 kips axial load: (a) 2.52" water height in X (b) 2.52" water height in Y (c) 1.26" water height in X (d) 1.26" water height in Y (e) Thin lubrication layer in X (f) Thin lubrication layer in Y.

Normalized hysteresis loops for tests shown in Figure 3.6(e) and (f) are compared to their corresponding dry tests, as shown in Figure 3.7. First, note a significant decrease in the friction coefficient for wet tests compared to dry tests, which can be deduced by a direct comparison of the y-axis (normalized shear force) intercept. The overall trends in friction coefficient are discussed in Section 3.4. Friction coefficient aside, for the case where water caused the top sliding surface to dominate the movement (Figure 3.7(a)), a slight increase in post-yield stiffness is observed in the wet test hysteresis loop compared to the later cycles of the dry tests where sliding is well established. Furthermore, in the dry test shown in Figure 3.7(a) (black solid line), the top sliding surface was not engaged until the second half of the second cycle, hence the difference in stiffness on the first two cycles in comparison with the rest of the trial. When water caused single surface sliding (Figure 3.7(b)), an important increase in post-yield stiffness was observed in the wet test (magenta dashed lines) compared to the dry test (solid black line).

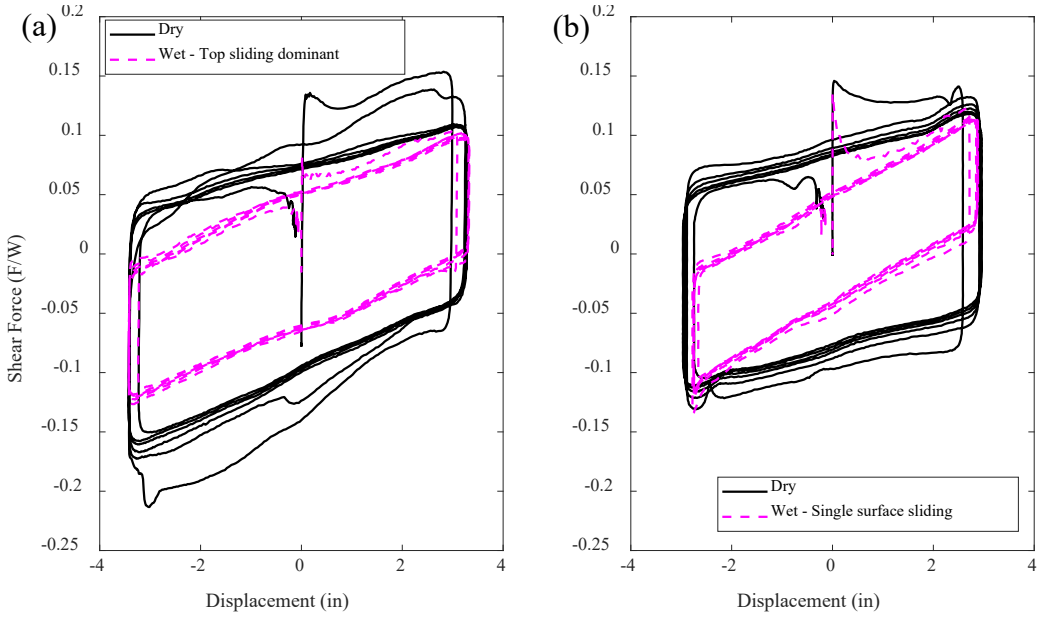

Figure 3.7. Dry and wet test normalized hysteresis loops for Aged Susitna 1 at 100 kips and 3.72" maximum displacement (a) X direction (b) Y direction.

The average post-yield stiffness in the wet test shown in Figure 3.7(a) is 0.0174 1/in, while the average post-yield stiffness in the wet test shown in Figure 3.7(b) is 0.0238 1/in (theoretical value is 0.0135 1/in). This suggests that the closer the displacement regime is to single surface sliding, the higher the post-yield stiffness. As pendulum length is inversely proportional to post-yield stiffness, suggests that the closer the displacement regime is to single surface sliding, the lower the pendulum length.

As mentioned above, soil contaminated tests were conducted on Aged Susitna 1 (as received) and Aged Susitna 2 (baked soil). Figure 3.8 shows hysteresis loops and displacement histories for X-direction soil contaminated tests conducted on Aged Susitna 1 and 2. A similar phenomenon was observed on soil contaminated tests. When the maximum imposed displacement was lower than the displacement capacity of one sliding surface, the soil restrained the slider from moving and hence only engaged the top sliding surface. As shown in Figure 3.8(a) and (b), observed post-yield stiffness was higher for soil contaminated tests (0.0249 and 0.0235 1/in) than for dry tests (0.0164 and 0.0139 1/in). Furthermore, displacement histories in Figure 3.8(c) and (d) show that only one sliding surface was engaged, similar to the phenomenon described above for some of the water contamination tests. Thus, the bearing responded similar to an SPB, causing the post-yield stiffness to be much higher than that for double surface sliding.

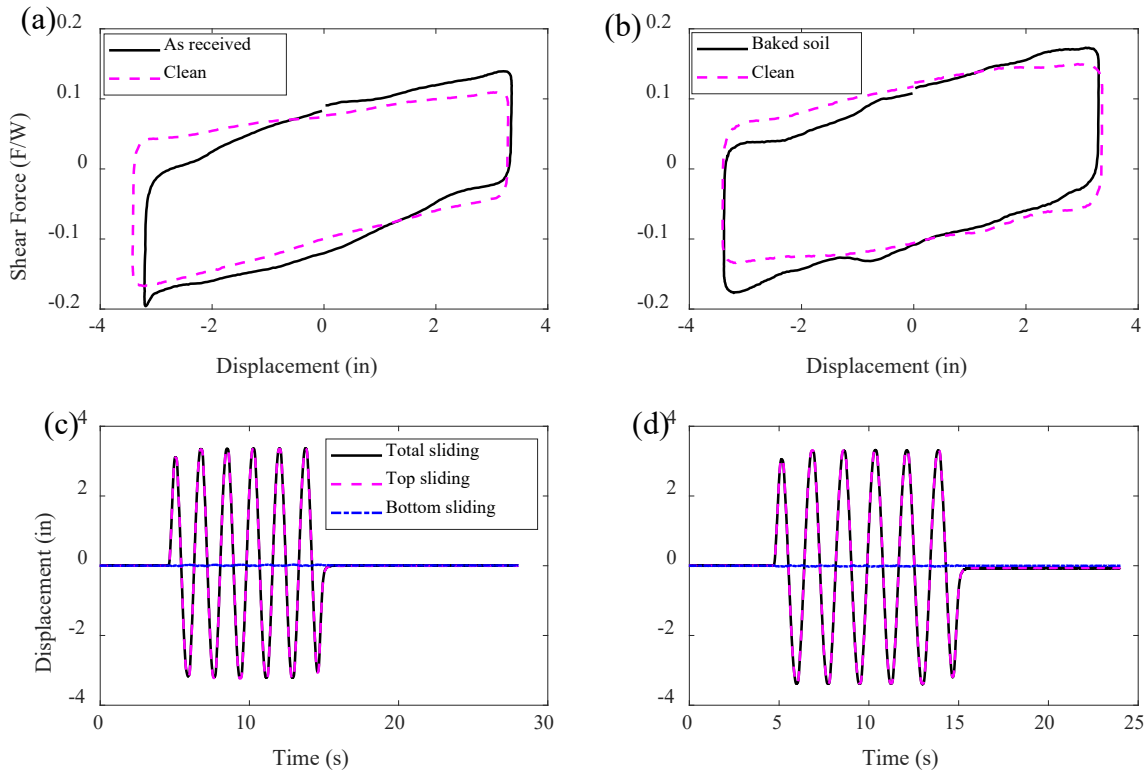

Figure 3.8. Soil contaminated tests at 3.74" maximum displacement (a) Aged Susitna 1 at 100 kips axial load (b) Aged Susitna 2 at 55 kips axial load (c) Aged Susitna 1 at 100 kips displacement history (d) Aged Susitna 2 at 55 kips displacement history.

A similar effect was observed in ice-contaminated tests. Ramping sine waves were used to assess how ice contamination affects the bearing response at different displacement amplitudes. Figure 3.9 shows the displacement history and hysteresis loop for a frozen test conducted on Aged Susitna 1 at 55 kips target axial load and 8" maximum displacement. As shown in Figure 3.9(a), the displacement capacity of the bottom sliding surface (5.5") was not reached until the fifth cycle and from that point both sliding surfaces were engaged with a transition around the sixth cycle. Furthermore, a sharp change in post yield stiffness can be observed in Figure 3.9(b) after the fifth cycle, or when both sliding surfaces were engaged. This behavior is similar to that of the soil contaminated bearing; the bearing responds similar to an SPB when only one sliding surface is engaged, hence causing the post-yield stiffness to be about twice that of double surface sliding. Figure 3.10 illustrates a constant amplitude sine wave frozen test with maximum displacement of 3.72", which was not sufficient to trigger sliding on the lower sliding surface. The post-yield stiffness for the frozen test (magenta dashed lines) in Figure 3.10 is about 50% higher than that of the dry test (black solid lines): 0.024 vs. 0.0164 1/in.

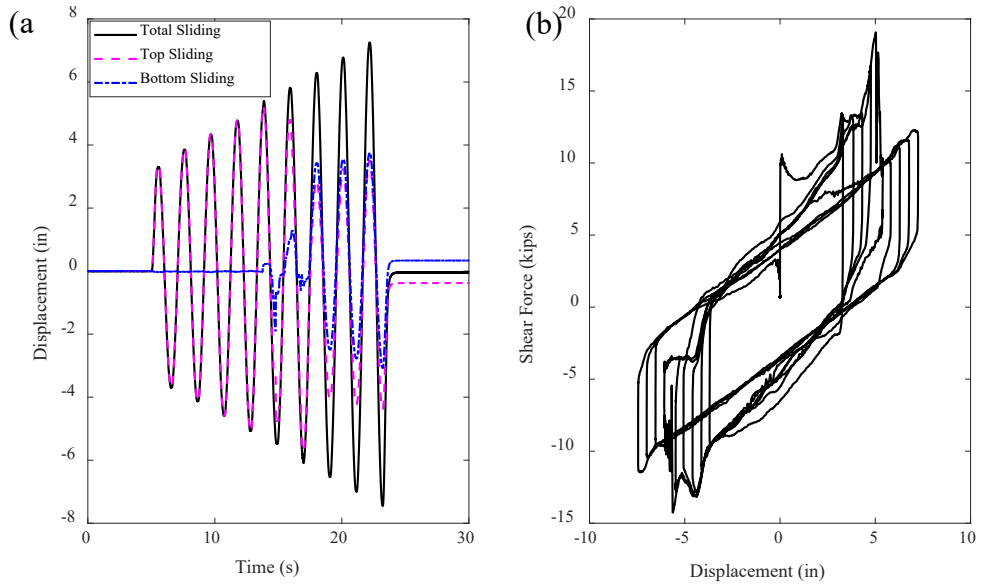

Figure 3.9. Frozen test on Aged Susitna 1 at 55 kips axial load and 8" maximum displacement (a) Displacement history (b) Hysteresis loop.

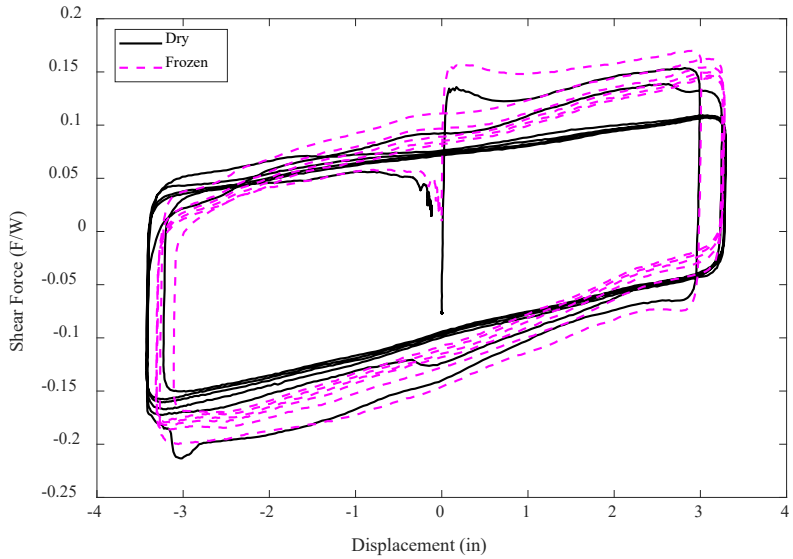

Figure 3.10. Hysteresis loops for Aged Susitna 1 at 100 kips axial load and 3.72" maximum displacement; dry versus frozen tests.

All types of contamination tested caused single surface sliding at some point during the test program. Single surface sliding was even observed during some tests on a dry clean bearing, either throughout the whole trial or during the first cycles. The trends with regard to pendulum length and single surface sliding are discussed next.

3.3.2. DOUBLE PENDULUM BEARING FORMULATION

To better understand single surface sliding phenomena, it is necessary to consider the DPB formulation. Fenz and Constatinou (2006) described the behavior of DPBs as two separate sliding surfaces;

the equations for each surface are then combined based on compatibility and equilibrium. The shear force for each sliding surface (i^{th} surface) is calculated by the following equation:

$$F_i = \frac{W}{L_i} u_i + W\mu_i \quad \textbf{(Eq. 3.1)}$$

where W is the axial load, L_i is the pendulum length defined as $R_i - h_i$, h_i is the distance between the center of articulation of the slider and the concave surface, u_i is the displacement on the concave surface and μ_i is the coefficient of friction of the sliding interface considered. Since W is the same for both sliding surfaces, no subscript i is needed.

Furthermore, Morgan and Mahin (2011) described the behavior of the DPB as two SPB acting in series, both of which follow (Eq. 3.1). In general terms, n SPBs acting in series leads to the following system of uncoupled equations in matrix form:

$$\begin{bmatrix} F_1 \\ \vdots \\ F_n \end{bmatrix} = \begin{bmatrix} \mu_1 W & \cdots & 0 \\ \vdots & \ddots & \vdots \\ 0 & \cdots & \mu_n W \end{bmatrix} + W \begin{bmatrix} L_1 & \cdots & 0 \\ \vdots & \ddots & \vdots \\ 0 & \cdots & L_n \end{bmatrix}^{-1} \begin{bmatrix} u_1 \\ \vdots \\ u_n \end{bmatrix} \quad \textbf{(Eq. 3.2)}$$

from which displacement vector can be written as:

$$\begin{bmatrix} u_1 \\ \vdots \\ u_n \end{bmatrix} = \frac{1}{W} \begin{bmatrix} L_1 & \cdots & 0 \\ \vdots & \ddots & \vdots \\ 0 & \cdots & L_n \end{bmatrix} \left[\begin{bmatrix} F_1 \\ \vdots \\ F_n \end{bmatrix} - \begin{bmatrix} \mu_1 W & \cdots & 0 \\ \vdots & \ddots & \vdots \\ 0 & \cdots & \mu_n W \end{bmatrix} \right] \quad \textbf{(Eq. 3.3)}$$

The assumption is that the system presented in (Eq. 3.2) and (Eq. 3.3) is in series, thus $F_1 = F_2 = \ldots = F_n = F$ and $u_b = \sum_{i=1}^{n} u_i$. It is implicit in the formulation that all elements in the system are sliding because for all forces to be equal, $F_i - \mu_i W \geq 0$ must be true for all i. If the friction coefficients vary on independent surfaces, uneven sliding or different displacements on the independent surfaces can be induced (i.e. displacement u_i decreases relative to others to balance an increase in μ_i while keeping F_i constant in (Eq. 3.2)). If all elements are sliding, then u_b can be written as:

$$u_b = F\left(\frac{\sum_{i=1}^{n} L_i}{W}\right) - \sum_{i=1}^{n} L_i \mu_i \quad \textbf{(Eq. 3.4)}$$

(Eq. 3.4) can be rearranged to obtain an expression for F:

$$F = \frac{W}{\sum_{i=1}^{n} L_i} u_b + \frac{W \sum_{i=1}^{n} L_i \mu_i}{\sum_{i=1}^{n} L_i} \quad \textbf{(Eq. 3.5)}$$

As stated earlier, the formulation presented in this section implies that all sliding surfaces are engaged. Hence for a DPB, with both sliding surfaces engaged (n = 2), shear force can be calculated by:

$$F = \left(\frac{W}{L_1 + L_2}\right) u_b + \frac{W\mu_1 L_1 + W\mu_2 L_2}{L_1 + L_2} \quad \textbf{(Eq. 3.6)}$$

which, if the pendulum length (L_i) is equal for both sliding surfaces, can be simplified to:

$$F = \left(\frac{W}{2L}\right) u_b + \frac{W(\mu_1 + \mu_2)}{2} \quad \textbf{(Eq. 3.7)}$$

However, if only one sliding surface is engaged, then $n = 1$ and (Eq. 3.5) becomes:

$$F = \frac{W}{L_1} u_b + W\mu_1 \quad \textbf{(Eq. 3.8)}$$

(Eq. 3.8) is the same equation of that of a SPB, which suggests that when one sliding surface is restrained from movement, DPB behaves essentially as a SPB. Furthermore, the theory suggests that post-yield stiffness when single surface sliding occurs is twice that of double surface sliding, which can be deduced by comparing (Eq. 3.7) with (Eq. 3.8).

The cause of single surface sliding in an ice contaminated bearing is rather obvious, as the ice constrains the bottom surface from moving. Single surface sliding could occur in a wet or otherwise contaminated bearing test if the contaminant were to cause a substantial increase in friction on one surface relative to the other that prevents sliding from initiating on that surface. However, single surface sliding was even observed in some trials on clean, dry bearings. The influence of rotation on the bearing mechanics is discussed next.

3.3.3. CONCAVE PLATE ROTATION THEORY

As mentioned earlier, the experimental set up caused rotation of the top concave plate on all trials conducted. X-direction rotation was measured in Phase 2 tests only, and initial rotation could not be quantified. Figure 3.11 shows a sample displacement and corresponding rotation history for a trial on Aged Susitna 2 at 100 kips axial load and 10" maximum displacement, conducted both in the X-direction (Figure 3.11(a) and (c)) and the Y-direction (Figure 3.11(b) and (d)). Due to the test set up, observed rotation in X-direction was higher than the observed rotation in Y-direction, as shown in Figure 3.11.

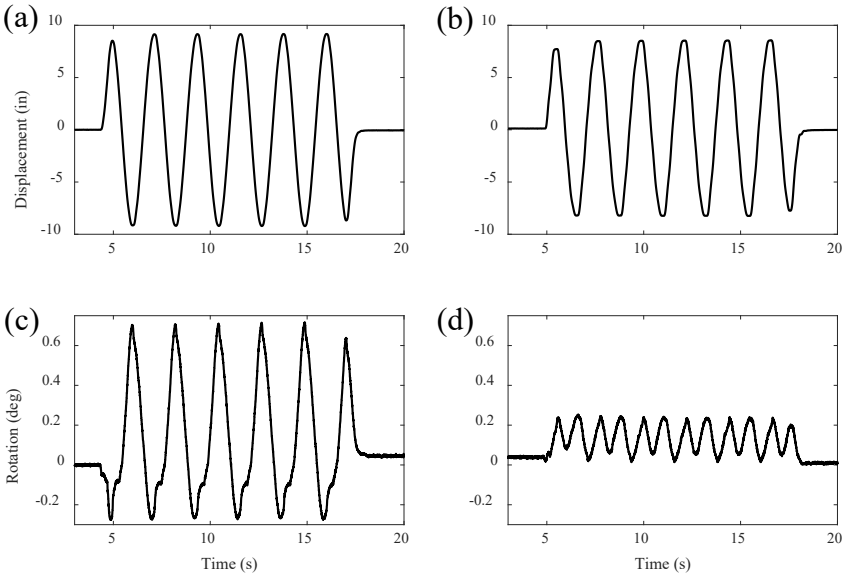

Figure 3.11. Dry test on Aged Susitna 2 at 100 kips axial load and 10" maximum displacement (a) Displacement history X-direction (b) Displacement history Y-direction (c) Rotation history X-direction (d) Rotation history Y-direction.

The observed rotation could have induced single surface sliding in some of the trials. Mosqueda et al. (2004) studied the effects of rotation on the hysteresis response of FPS bearings. In essence, rotation of the concave plate shifts the static equilibrium position from P_0 to P_r, a distance u_r as shown in Figure 3.12. Furthermore, u is the relative displacement between the slider and the original position of static equilibrium P_0. Given the additional displacement u_r, the resisting force F of the FPS bearing becomes:

$$F = \frac{W}{L}(u - u_r) + W\mu \qquad \textbf{(Eq. 3.9)}$$

where u_r is defined as $u_r = L\sin(\alpha)$ and it is positive when rotation is clockwise and negative when rotation is counterclockwise.

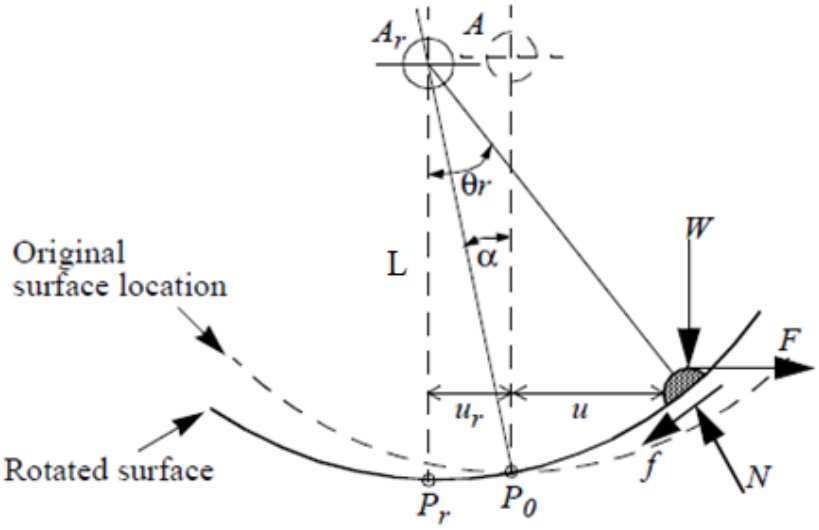

Figure 3.12. Counterclockwise rotated concave surface of FPS bearing free body diagram (Mosqueda et al., 2004).

Fenz and Constantinou (2008) also studied the effects of rotation with reference to the work by Mosqueda et al. (2004). Fenz and Constantinou (2008) recast (Eq. 3.9) by presenting the additional displacement term u_r, which is constant, as an adjustment to the friction term as follows:

$$F = \frac{W}{L}u + W(\mu \pm \alpha) \qquad \textbf{(Eq. 3.10)}$$

where the additional term α is the angle of rotation and it is positive when rotation is counterclockwise and negative when rotation is clockwise. For constant rotation, α either adds or subtracts a constant value of αW to the shear force, hence causing the hysteresis loop to shift up or down depending on the sign of α, as shown in Figure 3.13. For rotation varying proportional to displacement, as seen in Figure 3.11, the friction would vary approximately linearly over the cycle, which could manifest as an effective change in stiffness over the hysteresis loops that could explain both asymmetries (e.g. Figure 3.2) and changes to pendulum length (Figure 3.4) in SPBs.

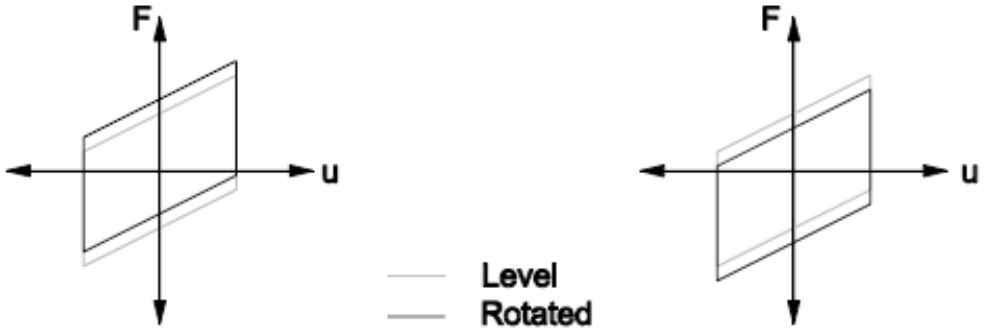

Figure 3.13. Hysteresis loop shift due to concave plate rotation (a) Counterclockwise rotation (b) Clockwise rotation (Fenz and Constantinou, 2008).

As described in Section 3.3.2, the model for a DPB is formulated as two SPBs connected in series and each sliding surface has its pendulum length and friction coefficient. Susitna DPBs have the same pendulum length and target friction coefficient for both sliding surfaces. Furthermore, the experimental set up caused the top sliding surface to continuously rotate as the slider moved. These rotations might have caused the coefficient of friction of the top sliding surface to change by $\pm\alpha W$, hence causing the friction coefficient of both sliding surfaces to differ from each other. Single surface sliding could be triggered if the coefficient of friction of one surface is larger than the other surface, if displacements are not large enough for F to overcome the static characteristic strength (μW) of the sliding surface with the higher coefficient of friction.

At the time of this writing, the authors plan to further investigate the rotation data recorded in Phase 2 to look for correlation between rotation and effective friction in SPBs and DPBs, and evidence that rotation may have triggered single surface sliding in DPBs. Such an approach, if successful, could change the conclusions regarding observed pendulum length. However, for this report, the techniques described in Section 2.4 are used throughout.

3.3.4. PENDULUM LENGTH IN DOUBLE PENDULUM BEARINGS

As mentioned in Section 3.3.1, single surface sliding was observed even on dry tests. Figure 3.14 plots observed pendulum length vs. cycle (similar format to Figure 3.4) for tests on dry DPBs in the X- and Y-directions, with distinct plots for each bearing. Two theoretical pendulum lengths are shown in Figure 3.14 the upper theoretical pendulum length (74") corresponds to double surface sliding (expected response of a symmetric DPB) while the lower theoretical pendulum length (37") corresponds to single surface sliding (movement on one of the two surfaces is entirely constrained). Test parameters are summarized in Table 3.2. Aged Susitna 2 was tested during Phase 2 only. In the X-direction, for tests with bearing movement on both surfaces, average pendulum length was about 20% lower than the theoretical value. The reduction in apparent pendulum length might have been caused by the test setup and bearing top plate initial rotation, as observed for SPBs. Furthermore, observed pendulum length seems to be lower for New Susitna (Figure 3.14 (a)) than for the formerly in-service bearings Aged Susitna 1 and 2 (Figure 3.14(b) and (c)). As for SPBs, asymmetric loops were observed with differences in positive and negative stiffness. In general, negative and positive pendulum length tend to be closer to each other in Phase 2 tests.

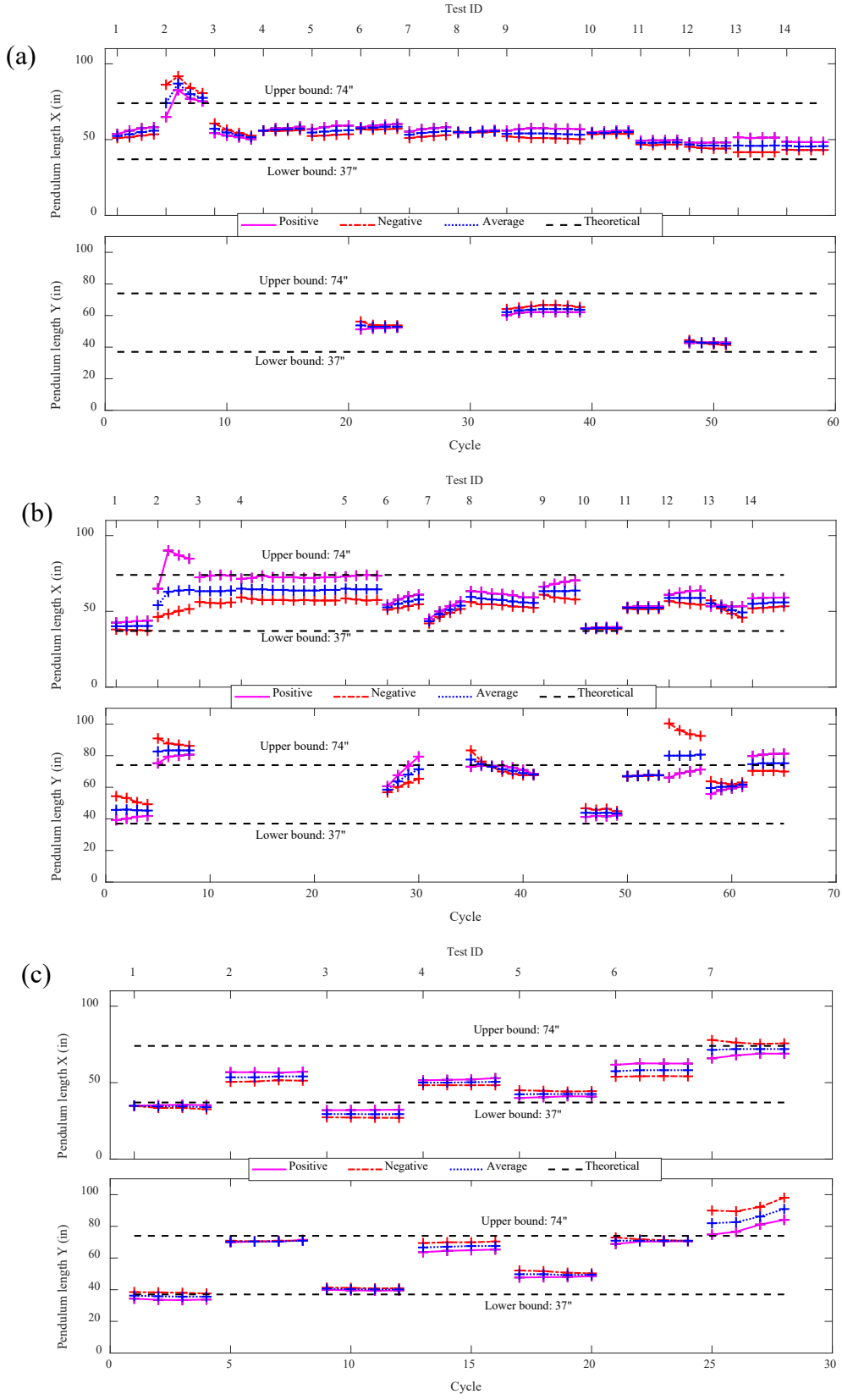

Figure 3.14. DPBs dry tests pendulum length (a) New Susitna (b) Aged Susitna 1 (c) Aged Susitna 2.

Table 3.2. DPB bearing dry tests summary

New Susitna				Aged Susitna 1				Aged Susitna 2			
Test	**Maximum displacement (in)**	**Axial load (kips)**	**Testing Phase**	**Test**	**Maximum displacement (in)**	**Axial load (kN)**	**Testing Phase**	**Test**	**Maximum displacement (in)**	**Axial load (kips)**	**Testing Phase**
1	3.74	100	Phase 1	1	3.74	100	Phase 1	1	3.74	55	Phase 2
2	0.94	100	Phase 1	2	3.74	100	Phase 1	2	10.00	55	Phase 2
3	1.85	100	Phase 1	3	3.74	100	Phase 1	3	3.74	100	Phase 2
4	2.80	100	Phase 1	4	3.74	100	Phase 1	4	10.00	100	Phase 2
5	4.65	100	Phase 1	5	3.74	100	Phase 1	5	3.74	55	Phase 2
6	3.74	100	Phase 1	6	3.74	55	Phase 1	6	10.00	55	Phase 2
7	3.74	100	Phase 1	7	3.74	55	Phase 1	7	3.74	55	Phase 2
8	3.74	100	Phase 1	8	3.50	100	Phase 1				
9	3.50	100	Phase 1	9	3.74	100	Phase 1				
10	3.74	100	Phase 1	10	3.74	55	Phase 2				
11	3.74	100	Phase 1	11	10.00	55	Phase 2				
12	3.74	55	Phase 1	12	3.74	55	Phase 2				
13	3.74	55	Phase 1	13	3.74	55	Phase 2				
14	3.74	55	Phase 1	14	10.00	55	Phase 2				

3.3.5. DOUBLE AND SINGLE SURFACE SLIDING ASSESSMENT

Single surface sliding might cause the post-yield stiffness to double, which would lead to increased shear force demand on bridge piers. Unexpectedly large shear force demand could potentially damage the substructure, so the significance of single surface sliding throughout the test program was evaluated by numerically quantifying its extent for individual cycles of all tests on DPBs where the independent sliding of the two surfaces was measured. The percentage of one surface sliding with respect to total sliding (*%OST*) is defined as:

$$\%OST = \frac{d_s}{t_s} \times 100 \qquad \textbf{(Eq. 3.11)}$$

where d_s is the peak displacement on the dominant sliding surface and t_s is the total peak displacement (sum of both surfaces). By definition, *%OST* varies from 50 to 100%, where 50% corresponds to equal sliding on both sliding surfaces and 100% corresponds to single surface sliding on either of the sliding surfaces. The values of d_s and t_s were computed by averaging the peak positive and peak negative amplitudes for the half cycles.

Figure 3.15 shows scatter plots of pendulum length against *%OST* for all DPBs. All points represent individual cycles on each test, excluding the first and last cycle. Markers distinguish between dry, wet, and frozen tests. Two theoretical values are shown in all plots in Figure 3.15, where the upper bound (74") corresponds to double surface sliding (expected behavior of a symmetric DPB) while the lower bound (37") corresponds to single surface sliding. Furthermore, cycles from X-direction tests are shown in the left subfigures of Figure 3.15 while cycles from Y-direction tests are shown in the right subfigures. Movement of the slider was not recorded for New Susitna in the dry condition, so dry data points are not presented for this bearing. The overall trend supports the hypothesis that when sliding occurs evenly on both surfaces (%*OST*~50), the observed pendulum length approaches that of theoretical double surface sliding. When sliding occurs on a single surface (%*OST* ~100), the observed pendulum length matches or approaches that

of theoretical single surface sliding, consistent with the response of an SPB. A continuum is observed between the two bounds.

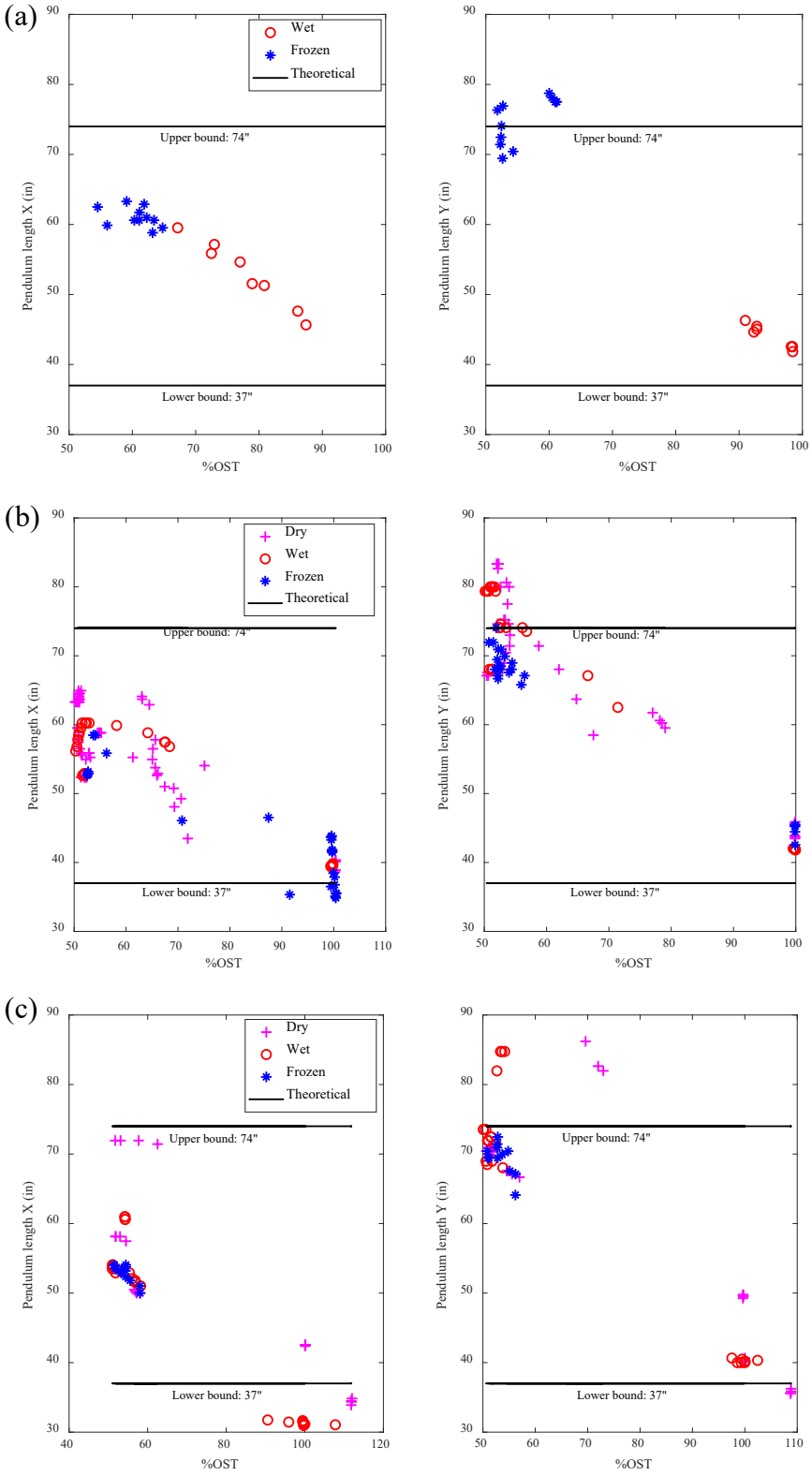

Figure 3.15. Sliding percentage relative to total displacement (a) New Susitna (b) Aged Susitna 1 (c) Aged Susitna 2

In addition to the types of contamination mentioned previously, bearing configuration or imperfections might cause single surface sliding as well. Some imperfections were observed on the top sliding surface, which might have caused uneven sliding on Aged Susitna 2 regardless of whether the bearing was contaminated or not. Furthermore, Aged Susitna 2 was tested in an inverted slider configuration compared to Aged Susitna 1 and New Susitna, as shown in Figure 3.16. The difference in configuration might have caused Aged Susitna 2 to behave differently.

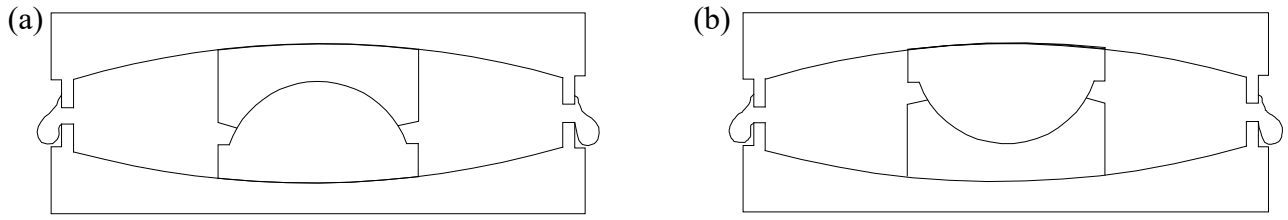

Figure 3.16. DPB configuration (a) Aged Susitna 1 (b) Aged Susitna 2.

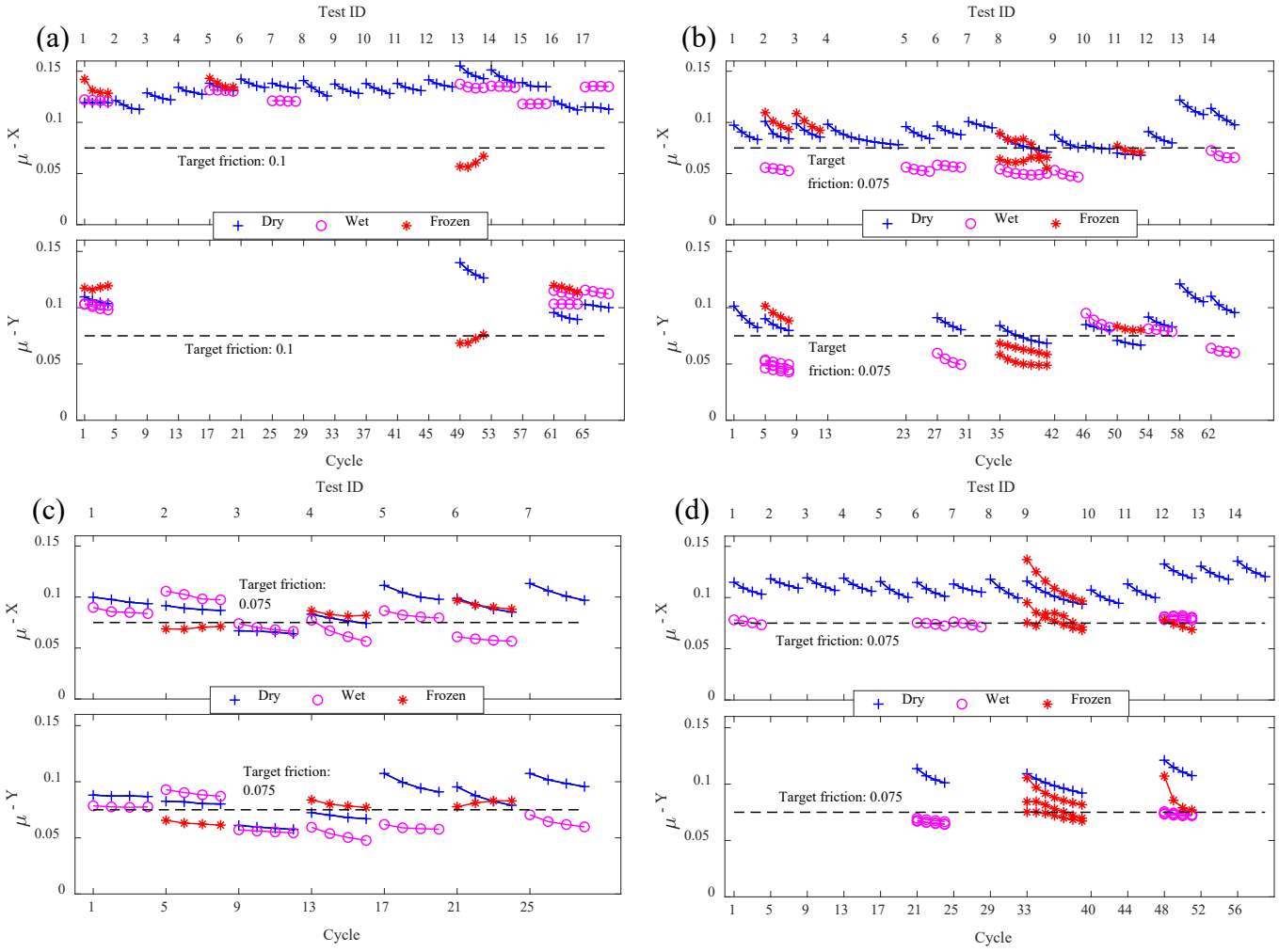

Figure 3.17. μ per cycle (a) Robertson (b) Aged Susitna 1 (c) Aged Susitna 2 (d) New Susitna.

3.4 COEFFICIENT OF FRICTION

FPS bearings dissipate energy through friction between the articulated slider and the sliding surfaces, hence friction coefficient is an essential part of the bearing characterization. The characterized friction coefficient μ vs. cycle over all tests is shown in Figure 3.17, with each bearing represented on different subplots. Each point represents a cycle and all points connected with lines represent the cycles from the same test. Y-direction tests have been aligned with corresponding X-direction tests, and dry, wet, and frozen tests with the same loading protocol are aligned. Data for frozen tests represents the free sliding phase on one surface of a DPB or after ice breakaway has occurred. In general, the observed μ in dry tests was higher than the theoretical value for all bearings. Furthermore, in wet tests, a decrease in μ with respect to dry tests was observed on all DPBs, as shown in Figure 3.17(b), (c), and (d). However, no consistent trend for wet friction compared to dry friction can be discerned for Robertson SPB (Figure 3.17(a)). Data is also inconclusive as to how ice contamination affects μ. In contrast to the literature (McVitty & Constantinou, 2015; Constantinou et al., 2007), the observed μ was higher on New Susitna DPB (Figure 3.17(d)) than the aged DPBs (Figure 3.17(b) and (c)). However, manufacturing processes have changed since the formerly in-service bearings were installed (Zayas, 2021), so no conclusions can be made about the effect of aging. The friction coefficients on aged DPBs are relatively close to the target, so the authors have no concerns about the sliding response of aged bearings.

The possible reduction in friction coefficient in DPBs during wet tests is further explored next. Recall that water contamination tests with different water levels, axial loads, and displacement protocols were conducted. Figure 3.18 compares hysteresis loops for three tests on Aged Susitna 1 with three different water levels at 100 kips of axial load and to 3.74" maximum displacement. "Thin layer" refers to a small lubrication layer of water on the bottom sliding surface. Only the third cycle of each test, which was selected randomly, is shown for visual ease. Visually, the Y-axis intercept can be directly interpreted as the friction coefficient when the hysteresis lines are linear. Water level does not seem to affect μ, as the Y-axis intercept is essentially the same for all water contaminated loops shown in Figure 3.18. The Y-axis intercept is smaller for the three wet tests compared to the reference dry test (Figure 3.18). This is a visual confirmation that the average μ of the two sliding surfaces is decreased by the water contamination.

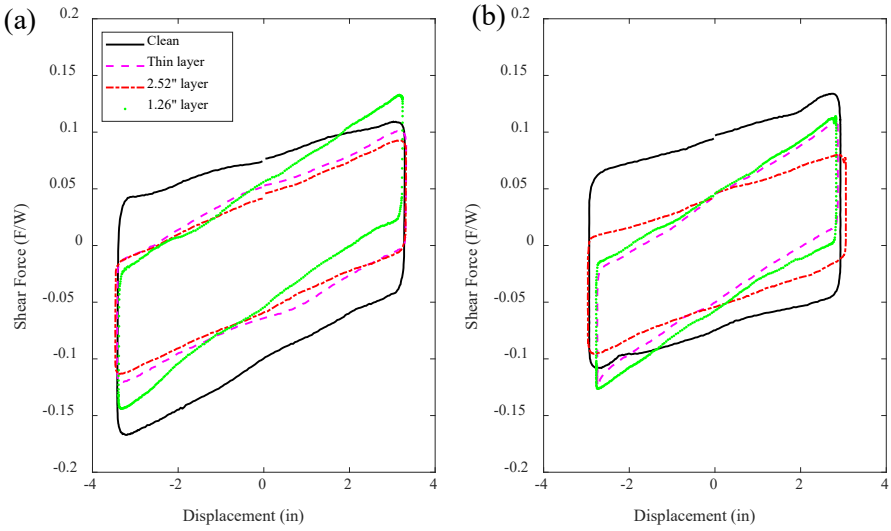

Figure 3.18. Normalized hysteresis loop for third cycle and different water heights at 100 kips and 3.74" maximum displacement, Aged Susitna 1 (a) X direction (b) Y direction.

Interestingly, post-yield stiffness is higher on the 1.26" water layer tests than on the other tests shown in Figure 3.18(a). Likewise, post-yield stiffness is higher on the 2.52" and 1.26" tests than on the other tests shown in Figure 3.18(b). These comparisons serve as further evidence of the occurrence of single surface sliding (Section 3.3.1). The presence of water seems to affect the way displacement is distributed among both sliding surfaces, in some cases causing only one sliding surface to be engaged.

In addition to sine waves, the bearings were subjected to unidirectional and bidirectional ground motions under water contamination conditions. Figure 3.19 compares water contaminated and dry tests on Aged Susitna 1 subjected to bidirectional 1940 Imperial Valley – El Centro Array #9 ground motion with a scale factor of 1.43. Figure 3.19(b) shows that the displacement path of the bearing was essentially identical in the two tests. An overall decrease in shear force was observed on the water contaminated bearing compared to the dry bearing, as shown in Figure 3.19(a), which corresponds to a decrease in the coefficient of friction. This is in agreement with the trends shown in Figure 3.17. However, the dry test exhibits a much stiffer post-yield response than the wet test. Closer inspection of the data revealed that the dry bearing sustained single surface sliding in this test.

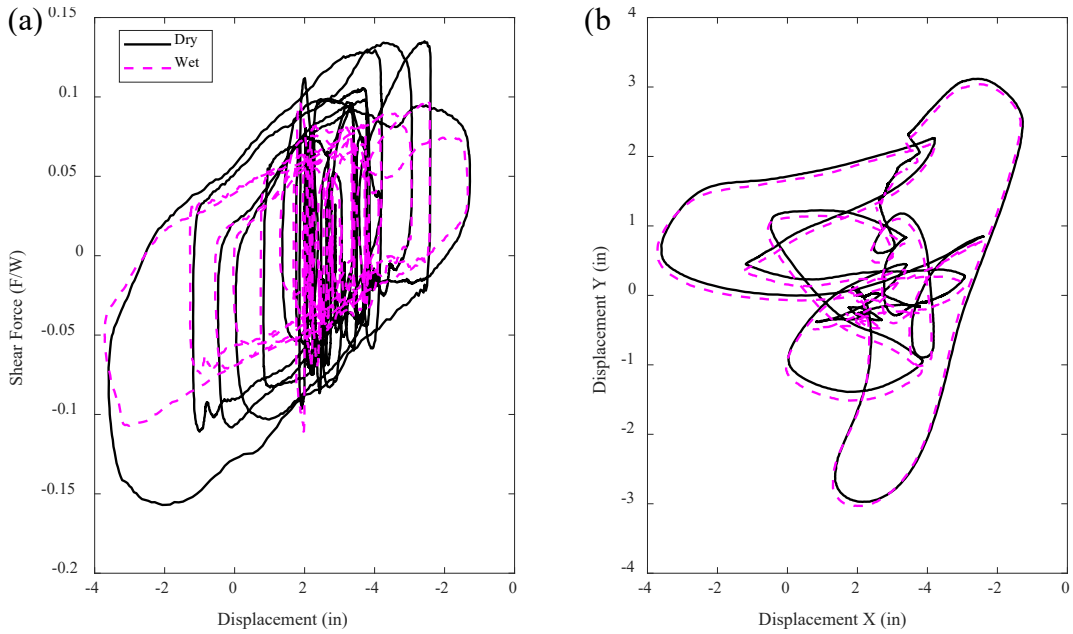

Figure 3.19. Comparison between wet and dry ground motion tests on Aged Susitna 1 (a) Normalized hysteresis loop Y direction (b) Displacement trace.

3.5 ICE BREAKAWAY STRENGTH

Three types of displacement protocols were used to assess the effects of ice contamination on the behavior of FPS bearings: 4.05" constant amplitude sine wave (SPB), 8" maximum amplitude ramping sine wave (DPB), and 10" constant amplitude sine wave (DPB). Examples of hysteresis loops for all three types of sine waves are shown in Figure 3.20. Figure 3.20(a) shows a sample hysteresis loop for a frozen test conducted on the Robertson SPB bearing. Because the bearing only has one sliding surface, the ice breaks immediately to initiate movement in the bearing, causing a high peak in shear force. Then the shear force decreases as the slider moves. However, as the slider crushes the ice on its path, shear force increases slightly. After all the ice on the slider's path is broken, a normal hysteresis loop is observed. Figure 3.20(b) shows a sample hysteresis loop for an 8" ramping sine wave on Aged Susitna 1 DPB. As explained in Section 3.3.1,

during the first five cycles the ice is not broken and sliding occurs only on the top sliding surface. When the capacity of the top surface is reached, the ice breaks and the bearing transitions to double surface sliding on subsequent cycles. Ramping sine wave protocols were not used to characterize ice strength because the bearing reaches the displacement capacity of the top sliding surface at a low velocity, making it hard to distinguish and isolate ice breakaway strength from the hysteresis loop. Finally, a sample hysteresis loop for 10" constant amplitude sine wave on Aged Susitna 1 DPB is shown in Figure 3.20(c). For this case, single surface sliding occurs until the displacement capacity of the top sliding surface is reached. The slider hits the top outer ring of the bearing with considerable impact, breaking the ice free and causing the ringing shown in Figure 3.20(c). Upon motion direction reversal, single surface sliding is again engaged until the slider contacts the ice in the negative direction. After the ice breaks free in both directions, double surface sliding is observed.

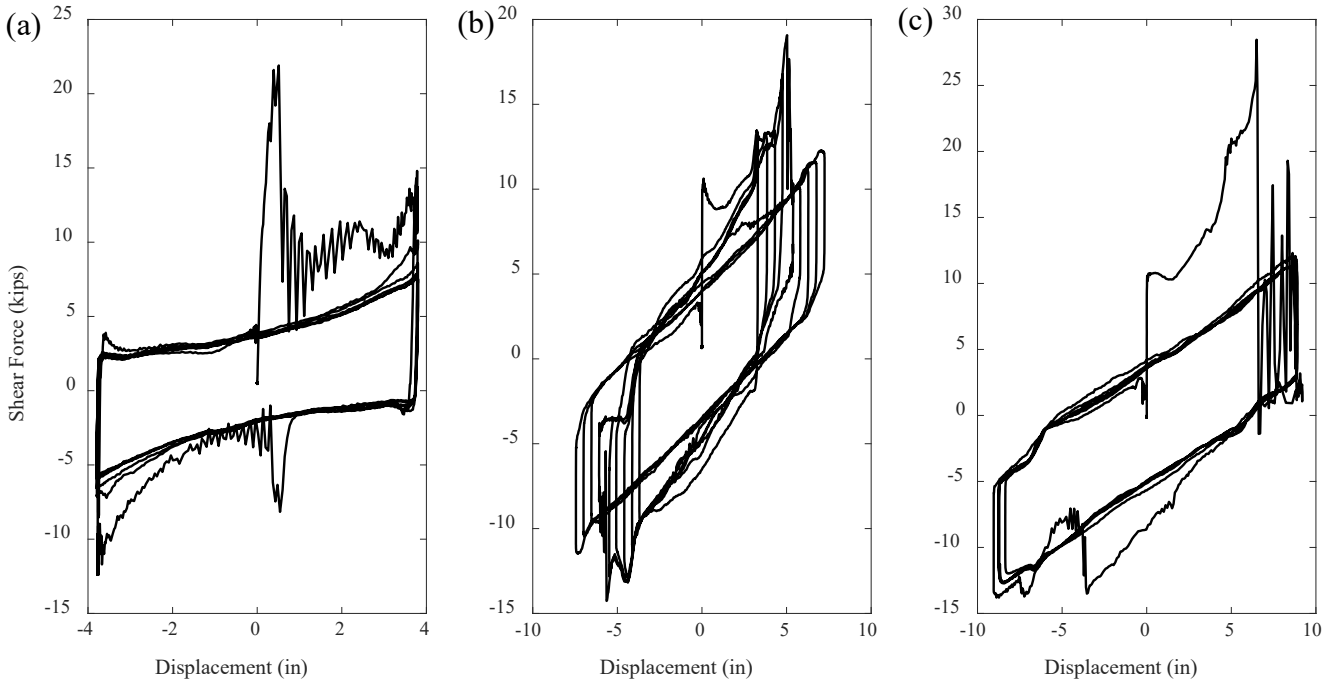

Figure 3.20. Hysteresis loop (a) 4.05" constant amplitude sine on Robertson SPB (b) 8" ramping sine wave on Aged Susitna 1 DPB (c) 10" constant amplitude sine wave on Aged Susitna 1 DPB.

These examples seem to suggest that the ice resistance is significant primarily in the first cycle for an SPB (Figure 3.20(a)) or the first cycle that engages the ice for a DPB (Figure 3.20(b) and (c)). The behavior of the hysteresis loop is pretty typical in subsequent cycles. This seems to suggest that ice detachment is complete after a complete cycle with load reversal and any lingering effects of ice in the bearing (e.g. crushing against the outer rim) have fairly minor contributions to resistance. The question naturally arises whether the response seen in an earthquake would be of the same nature. For ease of characterization, most of the trials were conducted using sinusoidal motions.

A ground motion simulation of an ice-filled bearing was conducted on Robertson SPB. A simple isolated rigid structure model was analyzed to predict the response from 1940 Imperial Valley Earthquake ground acceleration recorded at El Centro Array #9, and the bidirectional displacement history was imposed to the bearing. Figure 3.21 shows the displacement histories and normalized hysteresis loops in X and Y directions. The primary resistance to ice, interpreted here as ice breakaway, appears in the X-direction hysteresis loop (Figure 3.21(c)) for a 1" excursion in the -X direction at about 3 seconds into the history (Figure 3.21(a)). This is followed by a load reversal and 2" excursion in the +X direction, which is noted by

minor additional resistance in the hysteresis loop. Some small additional resistance in the hysteresis loop are also apparent in Y-direction (Figure 3.21(d)) due to the displacement in Y, which starts slightly later than the displacement in X. Overall, consistent with the sinusoidal motions, the effects of ice breakaway seem to be limited to the first major cycle of motion. This observation will be fundamental when devising strategies for modeling the ice breakaway effect.

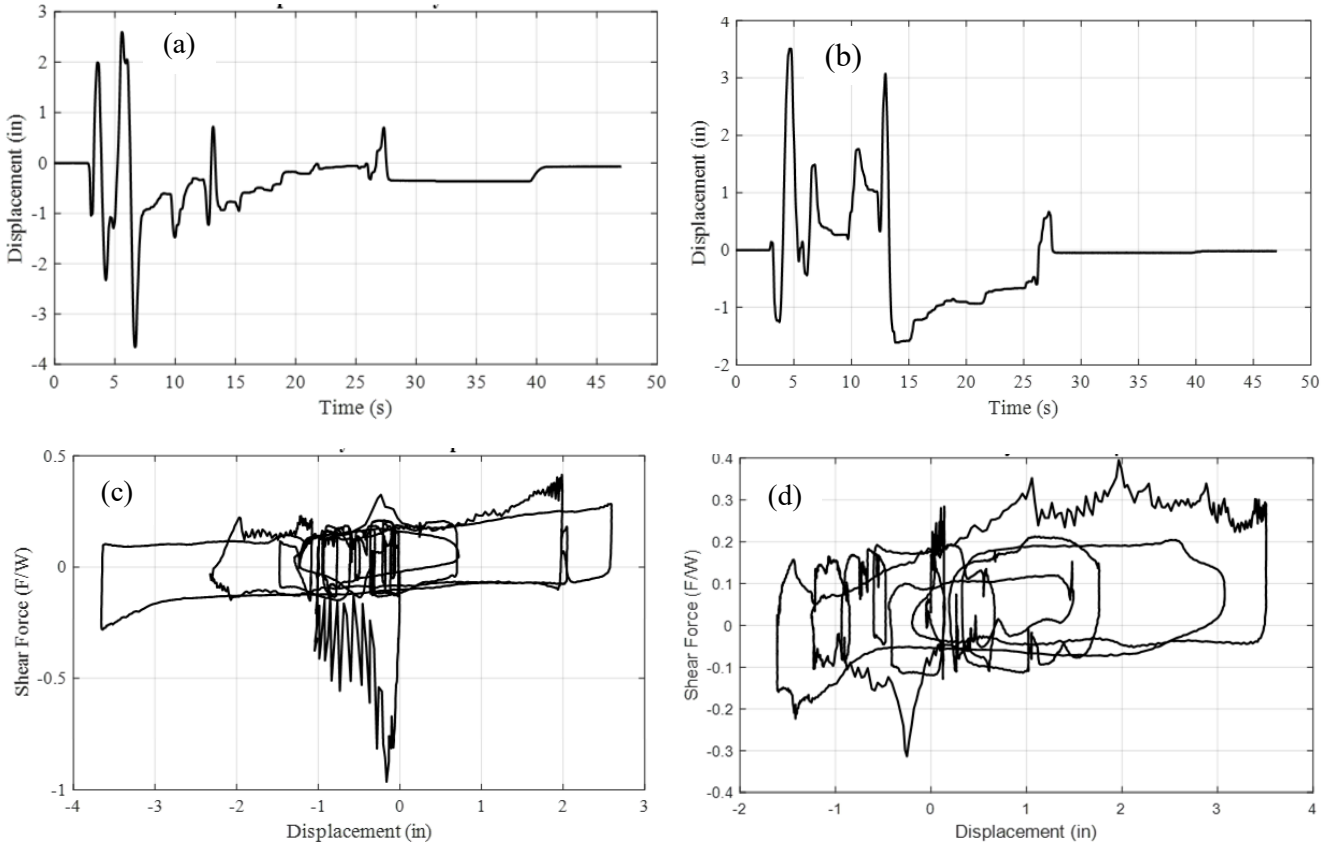

Figure 3.21. Simulation of bidirectional displacement from 1940 Imperial Valley Earthquake at El Centro Array #9 w/ scale factor = 1.56 on Robertson SPB (a) Displacement history X (b) Displacement history Y (c) Normalized hysteresis X (d) Normalized hysteresis Y.

Ice breakaway strength or additional resistance caused by ice adhesion to the slider and sliding surface was quantified. Constant amplitude sine waves were used to characterize ice strength. Due to variation in axial load throughout each trial, normalized hysteresis loops were first used to separate additional ice resistance beyond the typical frictional resistance. First, individual bearing cycles were identified and normalized hysteresis loops were characterized for each cycle as described in Section 2.4. To interpret ice breakaway strength, the average characterized bilinear loop was subtracted from the first cycle and then multiplied by the instantaneous axial load of the first cycle, resulting in an absolute value of ice breakaway strength. Figure 3.22(a) shows the measured ice breakaway strength for several tests conducted on the Robertson bearing. Ice breakaway strength vs. displacement represents an ice resistance backbone curve. The ice strength for the trial with a 1.26” ice layer (blue dotted line) is significantly smaller than the rest of the trials with 2.52” ice layers. Hence, as the ice volume increases, ice breakaway strength is expected to increase. Furthermore, ice breakaway strength does not seem to increase with axial load, as the highest value of ice breakaway strength was achieved at the lowest axial load (red dashed-dot line). However, the data is too limited to make a strong conclusion about the relationship between axial load and breakaway strength.

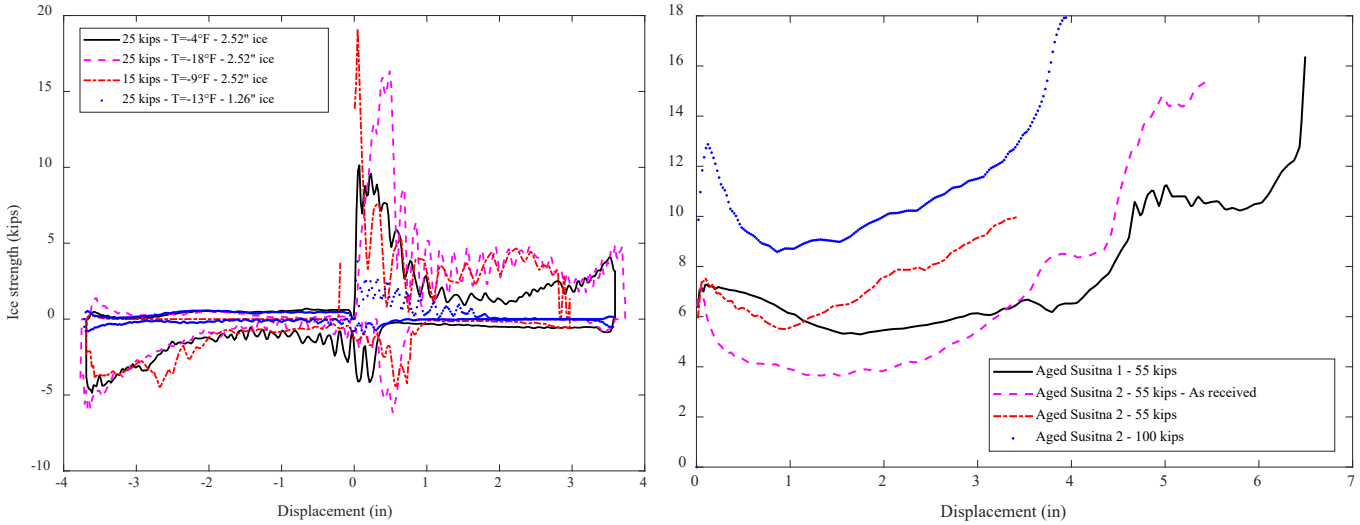

Figure 3.22. Ice breakaway strength (a) SPB (b) DPB.

A similar procedure was used to estimate the ice breakaway strength on frozen tests conducted on Aged Susitna 1 and 2. To avoid any possible confusion caused by the ringing shown in Figure 3.20(c), only the portion of the hysteresis loop before the ice breaks up to the peak in shear force was considered (approximately 0 to 6.50" displacement). The rest of the process was the same as the one used to calculate ice strength on the Robertson bearing.

Figure 3.22(b) shows different ice breakaway strength backbone curves for all 10" amplitude sine wave frozen tests conducted in Phase 2 on Aged Susitna 1 and 2. All the tests were conducted with an ice layer of 2.65" except for the test labeled "as received" (magenta dashed line in Figure 3.22(b)). Aged Susitna 2 was received with soil contamination and a 1" layer of water on top of the soil; the water in the bearing was subsequently frozen and the bearing was tested under mixed soil and ice contamination. Several attempts at a meaningful frozen test were applied to the New Susitna bearing; however, a significant ice resistance was never observed. Furthermore, inspection of the New Susitna bearing following frozen tests suggested that ice did not adhere to the surface in the same manner as the Aged Susitna bearings. In other words, ice broke cleanly in New Susitna suggesting that adhesion of ice to the surface was the weak mode, whereas ice did not break cleanly in the Aged Susitna bearings suggesting a mix of adhesion and cohesion behavior. One hypothesis is that the new virgin (possibly freshly lubricated) surface of New Susitna impeded ice adhesion to the surface. A similar response was not observed in the New Robertson SPB; however, the ice breakaway phenomenon is fundamentally different in an SPB as ice must break free for any movement to occur.

Considering data for both SPBs (Figure 3.22(a)) and DPBs (Figure 3.22(b)), ice strength values range from approximately 10 to 18 kips and do not seem to depend on axial load. However, the amount of data is limited. Furthermore, despite a thinner ice layer, mixed soil and ice contamination (magenta dashed line in Figure 3.22(b)) exhibits similar breakaway strength to pure ice contamination (all other lines in Figure 3.22(b)).

CHAPTER 4: NUMERICAL INVESTIGATION OF EFFECTS OF CONTAMINATION ON BRIDGE SEISMIC RESPONSE

Building on observations presented in Chapter 3, the effects of contamination on the overall response of a bridge isolated with FPS bearings is explored in this chapter. A numerical model of the Susitna River Bridge before the retrofit (non-isolated) has been developed in CSI Bridge and OpenSees. The CSI Bridge model is used a baseline to determine the superstructure cross-sectional properties and overall dynamic properties. The OpenSees model is a spine model, simplified for nonlinear dynamic analysis but intended to capture the principal dynamic properties of the bridge. The OpenSees model has been validated by comparing its dynamic properties with those calculated using the CSI Bridge model, and then extended to consider isolation with both SPBs and DPBs and analyzed under a suite of ground motions developed to represent the design earthquake at the Susitna River Bridge site. Contaminated bearing models are implemented using existing OpenSees materials and elements, and applied to contamination cases that vary from limited contamination of some bearings to full contamination of all bridge bearings. The analysis results are synthesized to draw conclusions about the general response trends of the bridge under contamination, with focus on peak isolator displacements and peak shear forces in the bridge piers.

4.1. BRIDGE MODELING AND VALIDATION

Susitna River Bridge is located in Mile 104.2 of Parks Hwy, Alaska. It was built in 1965 and retrofitted in 2006 using DPBs. The bridge has two 150 ft spans and three 250 ft spans for a total length of 1050 ft. Figure 4.1 shows an elevation view of Susitna River Bridge along with typical pier sections before and after the 2006 retrofit. The structural system consists of steel I-girders and stringers to support the bridge concrete deck, as shown in Figure 4.1. Furthermore, the stringers are supported by steel trusses that transfer the load to the I-girders. All piers are single column bents with an ellipsoidal column cross-section and different column height at each pier. The main differences between the original bridge and the 2006 retrofitted bridge is the replacement of rocker bearings by DPBs and the replacement of pier trusses to accommodate for the DPBs. In general, the structure is very stiff with several elements contributing to the overall stiffness of the structure, such as:

- Transverse trusses (stiffeners) approximately every 25 ft.
- Rocker bearings that allow for translation in the longitudinal direction but restrain movement in the transverse direction at all piers, with the exception of the bearings at Pier 4, which are fixed in both horizontal directions.
- Large column piers, with ellipsoidal cross-section dimensions of 20’ (transverse) by 5’ (longitudinal).

Due to the high structural system stiffness, the isolated bridge response was expected to be dominated by the DPB properties. Furthermore, the main objective of building a numerical model in CSI Bridge was to determine the superstructure cross-sectional properties and the system dynamic properties as a reference and validation for the spine model. An additional objective was to check that the dynamic properties (fundamental frequencies and modes) represent the expected behavior of the bridge in the non-isolated condition prior to modeling the isolators. Thus, the typical pier section (Figure 4.1(c)) was considered for the model but with rocker bearings instead of the DPBs shown in Figure 4.1(c).

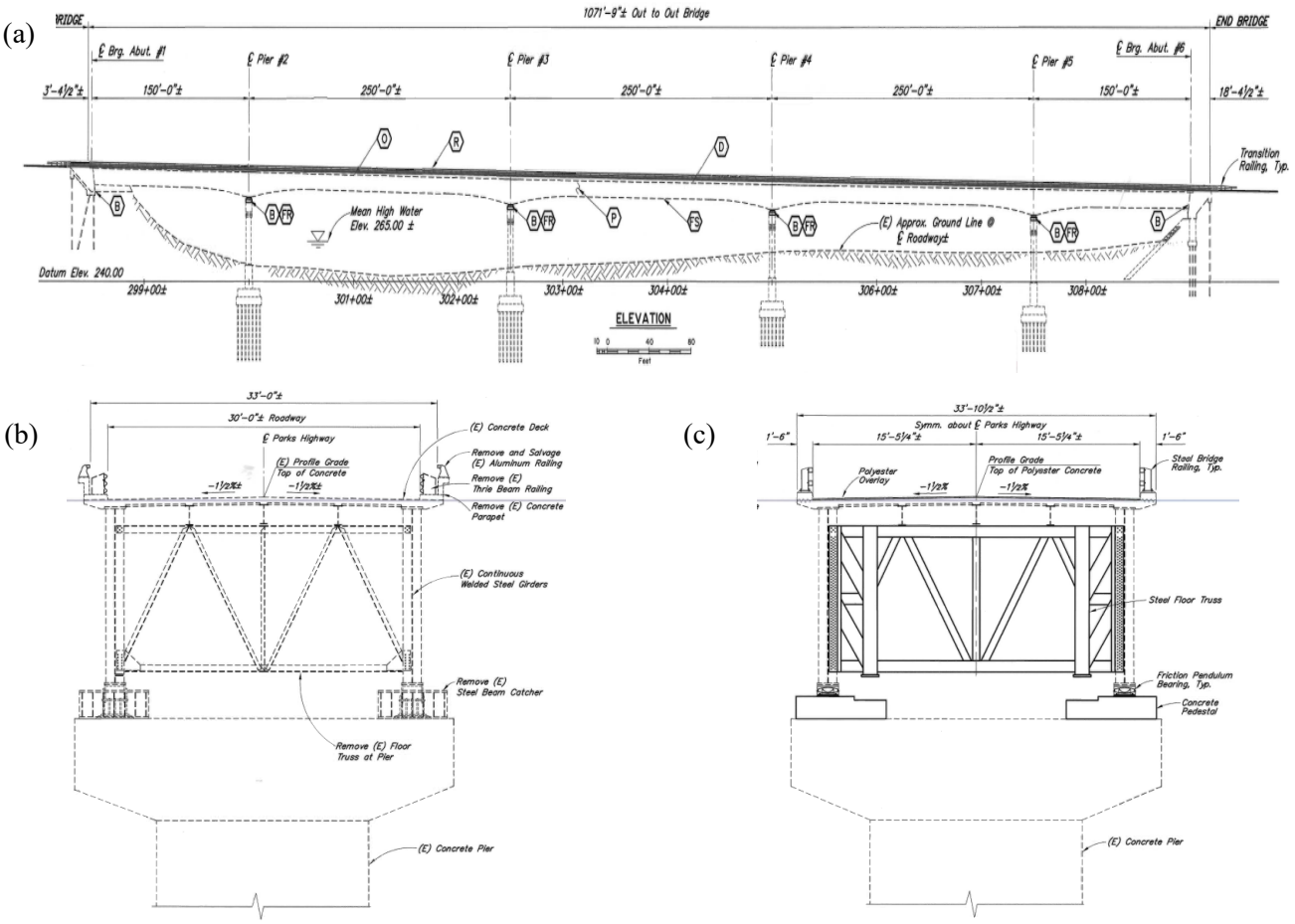

Figure 4.1. Susitna River Bridge structural system (a) Longitudinal view (b) Typical pier section before retrofit (c) Typical section after retrofit (Alaska DOT&PF, 2021).

Figure 4.2 shows a 3D view of the CSI Bridge model. The substructure was modeled using frame elements for the columns and the cap beams on all piers. All columns were considered as fixed at the base and the foundation was not modeled. The superstructure was modeled using frame elements for the girder flanges, stringers, trusses, and lateral bracing at the bottom of the girders. Shell elements were used to model the bridge deck and the webs of the girders. As previously stated, rocker bearings were considered for all supports. Thus, all bearings except at Pier 4 were restrained from translation but free to rotate in both directions, while Pier 4 bearings were restrained from any translation or rotation.

All concrete members were assigned a modulus of elasticity (E) = 3625.5 ksi (corresponding to f'_c = 3000 psi, per drawing specifications) and structural steel was assigned E = 29000 ksi. Figure 4.3 shows the cross-section geometry used to calculate the section properties, where the contribution of the stringers to the section properties was considered negligible. Furthermore, concrete was used as the base material to calculate section properties (effective EI and EA for the spine model).

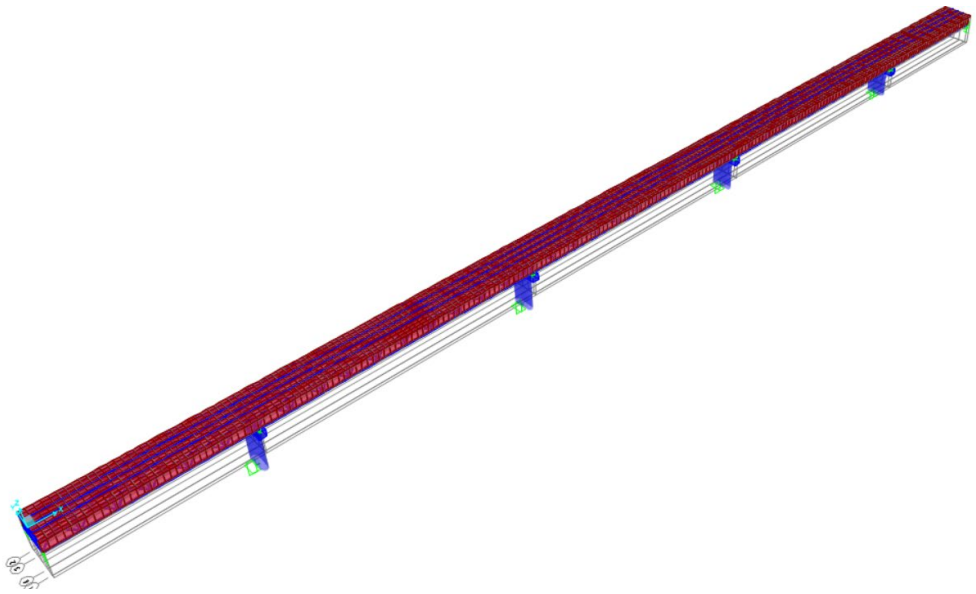

Figure 4.2. CSI Bridge model 3D view.

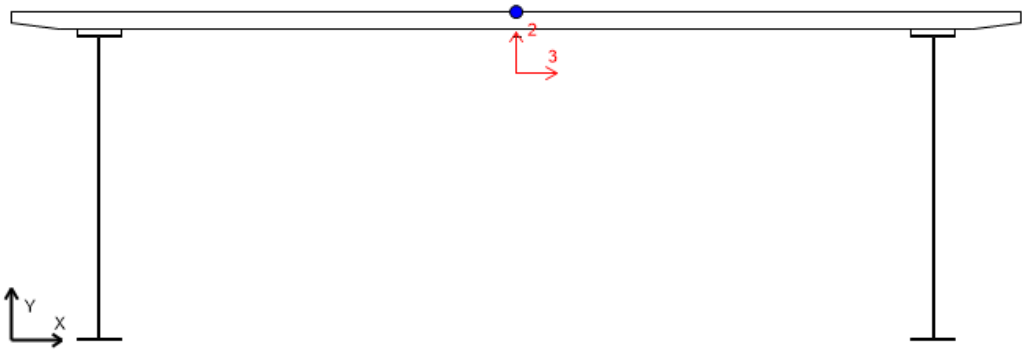

Figure 4.3. Superstructure cross-section.

The Susitna River Bridge has different girder sections with considerably different section properties. Figure 4.4 shows the location of the different I girder sections along the length of the bridge, while Table 4.1 shows the properties for each girder section with reference to the local axis shown in Figure 4.3. The section properties in Table 4.1 refer to the dimensions of the built-up steel I-girders. Table 4.1 also includes the section properties of the cap beam and pier columns. Given the analysis objectives, only dead loads were added to the model, which included self-weight, future wearing surface, utilities and rails. The total superstructure dead load was 5265 kips while the total substructure dead load was 2682 kips.

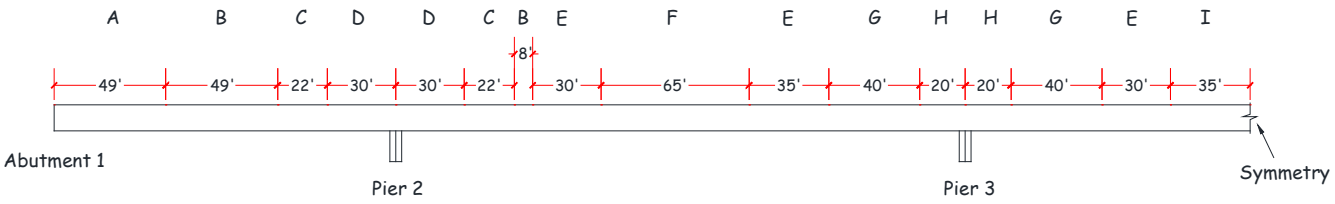

Figure 4.4. Girder sections along Susitna River Bridge length.

Table 4.1. Susitna River Bridge component section properties

Label	Section (in)		A (ft^2)	I_{33} (ft^4)	I_{22} (ft^4)
	Flanges	Web			
A	18x3/4	120x7/16	28.44	311.89	3587.16
B	20x1	120x7/16	29.89	368.97	3870.73
C	24x1 1/4	120x1/2	32.98	469.87	4478.97
D	24x1 5/8	120x5/8	36.53	571.51	5173.66
E	24x1 1/4	120x7/16	32.15	453.62	4315.65
F	24x1 3/4	120x7/16	34.65	551.19	4806.42
G	24x2	120x1/2	36.73	612.96	5215.11
H	24x2 1/4	120x5/8	39.65	685.84	5787.11
I	24x1 1/2	120x7/16	33.4	502.87	4561.04
Cap Beam	-		36	108	108
Column	-		94.5	2843.4	186.54

As mentioned before, the bridge was modeled for nonlinear dynamic analysis using the spine model approach in OpenSees using modeling techniques described in Mojidra and Ryan (2019). The model is graphically depicted in Figure 4.5. The bridge superstructure was modeled using 3D elastic beam–column elements with section properties as developed from CSI Bridge (Table 4.1). The torsional constant J computed by CSI Bridge could not be utilized, since the steel cross frames represent the majority contribution to the torsional stiffness, and they are not accounted for in the CSI Bridge section properties. The torsional stiffness was estimated by preparing (again in CSI Bridge) an independent cantilever beam model of the bridge superstructure with appropriately placed stiffeners (Figure 4.1(c)). A torque was applied to the center of gravity of the deck model and the rotation was computed. An equivalent J of 360 ft^4 was estimated from the torque versus rotation formula.

The superstructure was divided into multiple elements per span, with sections assigned according to Figure 4.4 and the tributary mass lumped at the nodes, which were located at the center-of-gravity of the section. The element length was variable to accommodate the section geometry; each span had an average of 26 elements. Translational mass and rotational inertia were lumped at nodes based on the tributary length L_{trib} of the adjacent elements. An average unit weight w and unit mass m were computed by dividing the total superstructure weight by the bridge length, leading to w = 5.012 kip/ft and m = 0.156 kip-s^2/ft^2. The translational nodal mass was then computed as:

$$M_{\text{node}} = mL_{\text{trib}} \qquad \textbf{(Eq. 4.1)}$$

The rotational inertia assignment is also important to capture fundamental mode shapes of the bridge, especially in the transverse direction. The rotational inertia of the superstructure about the transverse (I_{trans}), longitudinal (I_{long}), and vertical (I_z) axes were computed based on tributary length and deck width d_w:

$$I_{long} = \frac{mL_{trib}d_w^2}{12} \qquad I_{trans} = \frac{mL_{trib}^3}{12} \qquad I_z = \frac{mL_{trib}\left(L_{trib}^2 + d_w^2\right)}{12} \qquad \textbf{(Eq. 4.2)}$$

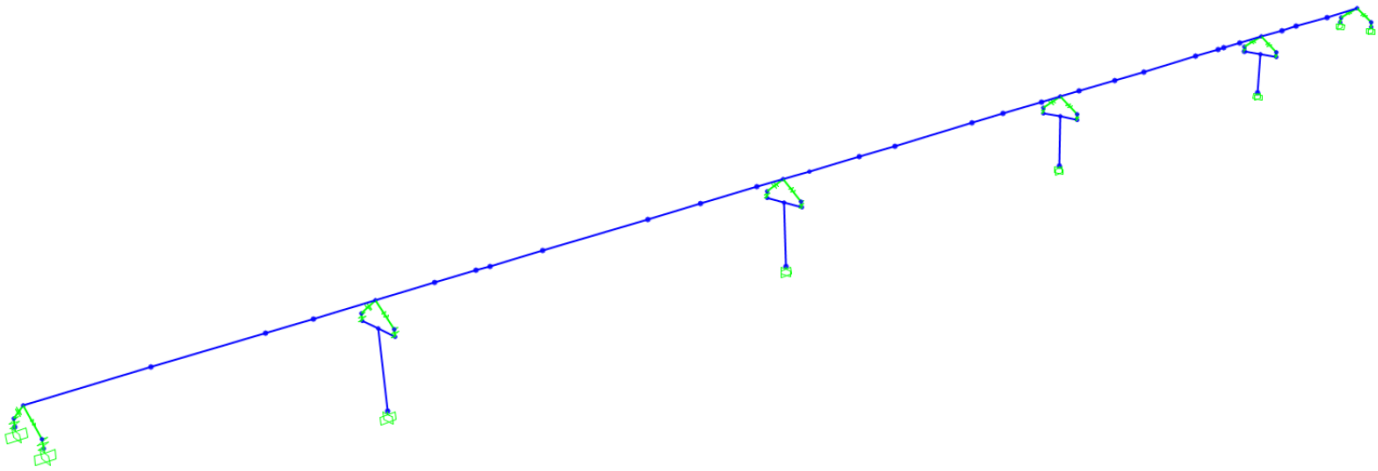

Figure 4.5. OpenSees spine model of the Susitna River Bridge.

For equivalence with the CSI Bridge model, bearings were modeled as multi-point constraints with rotations released as needed. Superstructure nodes were connected to the bearings with rigid links. Cap–beam elements were also connected to the base of the bearings via rigid links. Columns and cap beams were modeled as elastic frame elements with section properties from Table 4.1; however, the cap beam section properties were stiffened by a factor of 1200 after observing flapping at its ends, due to the fact that a spine model represents the cap beam with a considerable clear length from the column that does not represent reality. The column and abutment bearings were fixed at the base. Substructure masses were distributed appropriate to the cap beam and top of column nodes; substructure mass collected at the fixed column base node need not be considered.

With these considerations, modal analysis was conducted in both CSI Bridge and in OpenSees and the fundamental vibration modes in each direction were identified. Periods for dominant longitudinal, vertical and transverse modes are shown in Table 4.2. The periods of these primary modes are approximately equal for the two models, confirming that the OpenSees spine model is a reasonable representation of the higher fidelity CSI Bridge model. Given the system's high stiffness in the transverse direction, the first transverse mode had a shorter period than many local modes in other directions; it was identified as Mode 49 in CSI Bridge based on the mode shape. However, many of these local modes are not represented in a spine model, so the first transverse mode equates to Mode 9 in OpenSees. Additionally, the period of Mode 1 (longitudinal) was estimated from stiffness calculations with the assumption that only Pier 4 is engaged and only the superstructure mass participates. The estimated period was 1.109 s, while the period computed by CSI bridge was 1.179 s, which was considered sufficient for validation.

Table 4.2. Susitna River Bridge modal properties with CSI Bridge and OpenSees

CSI Bridge Model		OpenSees Model		Direction
Mode	Period (s)	Mode	Period (s)	
1	1.179	1	1.170	Longitudinal
2	0.824	2	0.826	Vertical
49	0.347	9	0.298	Transverse

Following verification of the bridge model based on modal analysis, the constraints used to represent the fixed and rocker bearings were replaced with isolation bearings. For dynamic analysis, Rayleigh damping

was assigned. The nominal bearing properties were represented with OpenSees *singleFPBearing* element, which can represent the response characteristics of both SPBs and DPBs with consistent single surface sliding and double surface sliding behavior. The element represents bidirectionally coupled bilinear force-deformation behavior, with shear force computed based on the instantaneous axial force on the bearing. Required input properties include selection of a friction model, friction coefficient μ, pendulum length L, and an initial stiffness. For all analyses, the Coulomb friction model representing constant friction was selected, and the initial stiffness was computed assuming a yield displacement of 0.01". The vertical stiffness (linear and uncoupled from the horizontal directions) was computed based on a vertical period of 0.03 sec and average static weight on the bearings.

For dynamic analysis, Rayleigh damping was applied with 3% damping anchored at T = 2.5 sec (close to the effective period of the isolated bridge) and 0.75 sec. The intent was to limit damping in the isolated mode, while damping out all but the lowest superstructure modes. (Effective periods of superstructure modes increase with isolation.) Analysis was applied with the NewtonLineSearch algorithm and a Newmark average acceleration integrator; a time step of 0.005 sec was applied for all analyses regardless of the time step of the input motion. Contamination scenarios and corresponding modeling variations are described in Section 4.2, and the selection and scaling of the ground motion suite is described in Section 4.3.

4.2. CONTAMINATION MODELS AND ANALYSIS CASE MATRIX

To represent the variety of behaviors seen in the experimental program, models representing both the Susitna DPBs and Robertson SPBs were applied to this bridge model even though it was built with DPBs. The parameters of the Robertson SPBs were considered acceptable for this bridge given its seismicity.

The isolator contamination models in Table 4.3 have been considered. Several of them require only straightforward parameter modifications to the *singleFPBearing* element. The Trans and IC models both utilize additional material models in parallel with the bearing element; the additional material is applied with a *MinMax* wrapper that triggers the material to breakaway when a threshold displacement is reached. These models required additional validation, as presented in Sections 4.2.1 and 4.2.2. The models in Table 4.3 represent the variety of behaviors seen in the experimental program. Reduced friction due to water contamination in SPBs is plausible, but was not seen in the experimental data and thus not represented here. As described in Chapter 3, single-surface sliding of DPBs was seen extensively and could arise due to water, ice or dirt contamination, or initial rotation of the bearings. Because the additional resistance of a DPB at the instance of ice breakaway is only moderately larger than the single surface sliding slope (Figure 3.20), it was not included in any isolator contamination model.

In addition, three different contamination scenarios have been considered. In Scenario 1, all bearings on Abutments 1 and 6 are contaminated, while all pier bearings are uncontaminated. This scenario reflects observations that abutment bearings beneath the finger joints tend to be more frequently contaminated than other bearings. In Scenario 2, all bearings on Piers 2 and 3 are contaminated, while all remaining bearings are uncontaminated. This scenario reflects perhaps a limit for consequences of random contamination that tends to be localized in one area of the bridge. In Scenario 3, all bearings are contaminated. This scenario reflects the upper bound consequences of contamination, but is unlikely to be seen over the life of the bridge. In reality, bearing contamination may be more randomly distributed, while the scenarios considered here are likely to be conservative, unless torsional responses are induced, which seem unlikely given the stiffness of the bridge and the capacity of the bearings to absorb any differential displacements.

Table 4.3. Isolator contamination models

Name	Type	L (in)	μ	Description
Nominal DPB	DPB	74	0.075	Nominal properties of DPB
Water contaminated (WC)	DPB	74	0.06	Friction coefficient reduced to 80% of its nominal value. Normal sliding on both surfaces was assumed.
Single-surface sliding bounding analysis (SSSB)	DPB	37	0.075	Pendulum radius reduced by half to represent single-surface sliding. Intended for bounding analysis as bearing model does not transition to normal behavior when single surface displacement limit is reached.
Single-surface sliding with transition (Trans)	DPB	74	0.075	Implemented with an additional material in parallel to the bearing that fails when the displacement limit is reached.
Nominal SPB	SPB	61	0.1	Nominal properties of SPB
Ice-contaminated (IC)	SPB	61	0.1	Additional materials in parallel to the bearing to represent the ice breakaway force

Table 4.4. Contamination scenario matrix

Name	Baseline No contamination	Scenario 1 (S1) Abutment bearings contaminated	Scenario 2 (S2) Pier 2 and 3 bearings contaminated	Scenario 3 (S3) All bearings contaminated
Nominal DPB (NDPB)	X			
Water contaminated (WC)		X	X	X
SSSB		X	X	
Trans			Select	Select
Nominal SPB (NSPB)	X			
Ice-contaminated (IC)		Select	Select	Select

Table 4.4 provides an analysis matrix of isolator contamination models applied to bridge contamination scenarios. In the cases marked with X, the entire ground motion suite is applied to obtain response statistics. In the cases marked Select, a limited subset of the ground motions are applied. The Trans model is applied to ground motions that exhaust the single surface sliding capacity, and in some cases the intensity scale is increased by a factor of 1.5 to induce a larger displacement demands. For the IC bearing model, iterations must be applied for each ground motion to correctly represent the ice breakaway response (see Section 4.2.2 for details). Due to the overhead in performing these iterations, only limited simulations with a couple ground motions per scenario could be applied.

4.2.1. SINGLE-SURFACE SLIDING WITH TRANSITION (TRANS) MODEL

As described in Chapter 3, several sliding regimes were observed during the test program. This material model represents the scenario of single surface sliding transitioning to double surface sliding once the displacement capacity of the initial single sliding surface is reached. An Opensees *singleFPBearing* with $\mu = 0.075$ and pendulum length $L = 74$" was used to model the standard response of the DPB sliding on both surfaces. A *Hysteretic* material applied in parallel modeled the additional resistance (increased stiffness) of the bearing during single surface sliding. The *Hysteretic* material allows the user to define a multi-linear custom backbone curve as a series of force-deformation points, in this case to represent the additional stiffness of the bearing. However, a limitation of this approach is that the friction-based variation in force with variable axial load cannot be represented. A constant axial load (representative of the average static axial load on abutment and pier bearings, respectively) was assumed to calculate the force-displacement points. A *MinMax* wrapper – used generally to simulate collapse of a material – was used to terminate the hysteretic material after the threshold displacement was reached. Additionally, a *CoupledZeroLength* element was applied to the *Hysteretic* material to represent the bidirectional interaction; i.e. the *Hysteretic* backbone curve is replicated in any radial direction.

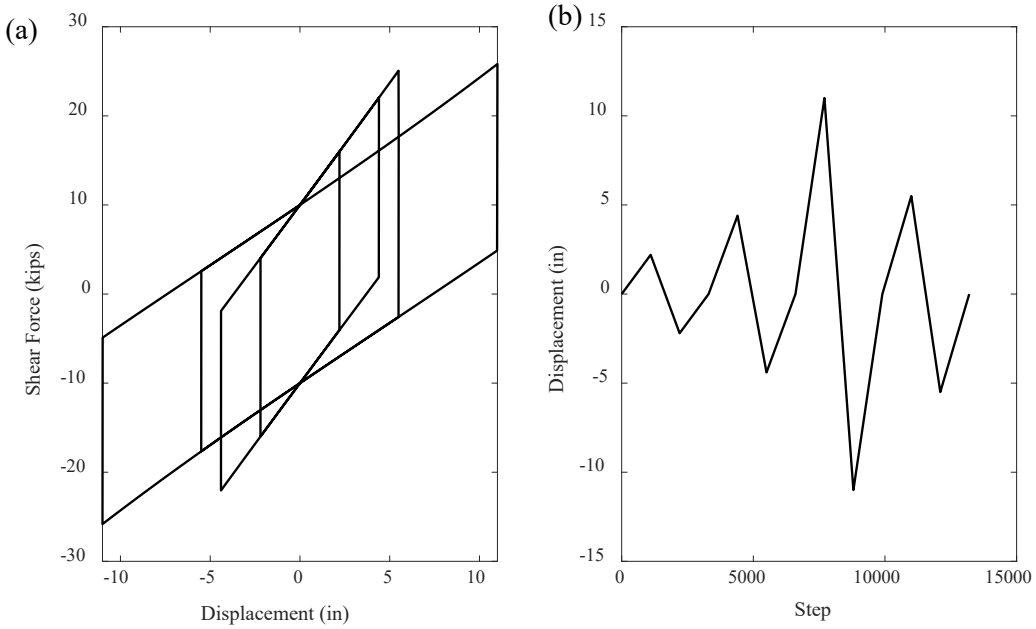

Figure 4.6. Transition material validation (a) Hysteresis loop (b) Imposed displacement.

Displacement controlled protocols were used to validate the transition material on a simple SDOF system. Figure 4.6 shows the resulting hysteresis loop and imposed displacements in one of the validation runs. The maximum displacements of the first two cycles (Figure 4.6(b)) are smaller than the displacement capacity of one sliding surface, engaging both elements such that the stiffness is approximately twice that of the Susitna bridge bearing. The maximum displacement on the third cycle exceeded the displacement capacity of a single sliding surface, causing the stiffness to drop at the instant the displacement capacity was reached (Figure 4.6(a)). The last cycle confirmed that the *Hysteretic* material was not engaged anymore in subsequent cycles, even after returning to lower intensity displacement cycles.

4.2.2. ICE-CONTAMINATED (IC) BEARING MODEL

As shown in Section 3.5, ice contamination in SPBs induces additional shear resistance manifested in the first cycle of motion until ice breakaway. For modeling purposes, the observed ice contaminated SPB hysteresis loop was represented as a smoothed backbone curve, divided into three zones on each side of the hysteresis loop, shown with green, red and blue lines in Figure 4.7(a). Solid lines represent the combined effect of the bearing response and ice strength in the first direction of movement – positive in Figure 4.7(a) – while dashed lines represent the combined effect of bearing response and ice strength after the first load reversal – negative in Figure 4.7(a). The residual effects upon load reversal represent the condition that the slider is not attached to the ice but it is still crushing it (e.g movement in a direction with ice attached to the sliding surface but not to the slider).

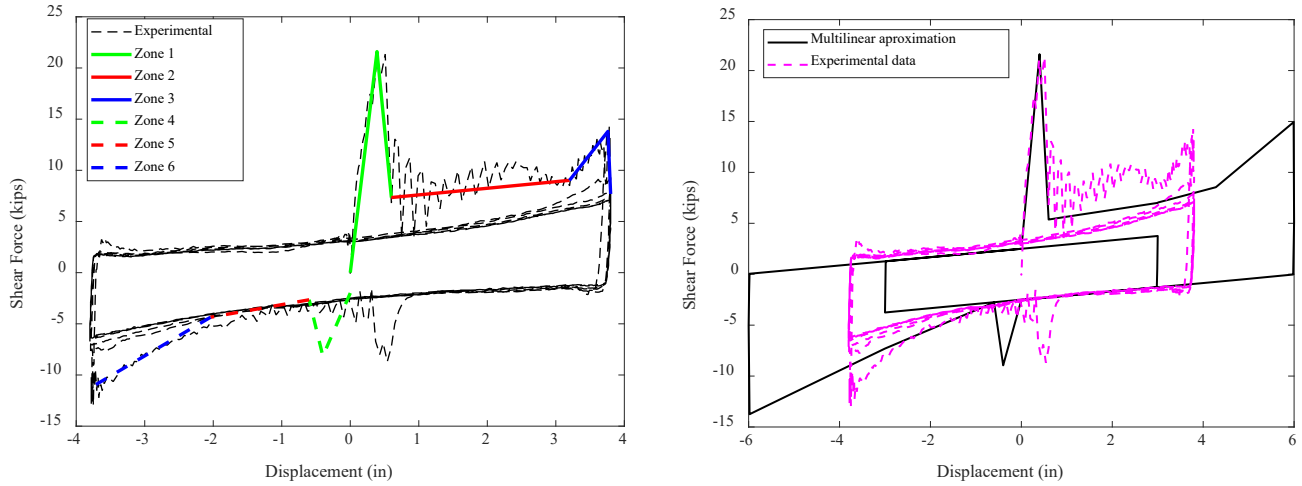

Figure 4.7. Multilinear approximation of observed ice strength (a) Conceptual (b) Implemented.

Similar to the Trans element model, the ice-contaminated IC bearing was modeled with a *singleFPBearing* element in parallel with Hysteretic materials with *MaxMin* wrappers to model the additional ice resistance at first excursion and load reversal. Essentially, the *Hysteretic* material defined the backbone curve consistent with the multilinear approximation in Figure 4.7(a). The *MinMax* material was used to simulate ice breakaway (termination of the *Hysteretic* material), and the behavior was embedded in a *CoupledZeroLength* element to represent bidirectional interaction.

Figure 4.7(b) compares the multilinear curve obtained using the parallel elements and the recorded hysteresis loop from an ice contaminated test on the Robertson bearing at an axial load of 25 kips and target maximum displacement of 4.05". (Note that the measured displacement during the experiment was slightly smaller than the target displacement.) The ice-contaminated bearing model was tested by subjecting a 1-DOF system to a displacement-controlled loading protocol. Two cycles are shown in Figure 4.7(b) for the multilinear approximation. A maximum displacement of 6" (Robertson bearing displacement capacity) was imposed on the first cycle and the *MinMax* material was set to simulate termination of the hysteretic material on the positive (initial excursion) and negative (load reversal) directions, independently, at an absolute displacement of 6". Note that this extension is a projection of the expected resistance beyond 4" – induced by ice crushing at the outer rim of the bearing – since the peak displacement in the experiment was 4.05". The maximum absolute displacement imposed on the second cycle was 3", which represents only the *singleFPBearing* element after the effect of the ice resistance was terminated.

The implementation of the bidirectionally coupled ice-contaminated bearing model described in this section requires the user to define the input values for the *MinMax* wrapper to correspond to the maximum displacements for the first and second directions of movement. The first direction is characterized as initial movement in an outward radial direction and the second direction is characterized as outward radial movement in the opposite hemisphere (corresponding to the algorithm of the *CoupleZeroLength* element). Thus, iteration was required, as the contaminated bearings maximum displacements during the first and second directions of movement, when subjected to ground motions, was unknown. The iterative process was implemented as follows:

1. Maximum displacements in the first and second directions of movement were determined by inspecting the uncontaminated bearings response.
2. The observed displacements were used to define the displacement at which the ice materials collapse (i.e. minimum and maximum values for the *MinMax* material).
3. Simulation was repeated with the *Hysteretic* material with *MinMax* and *CoupledZeroLength* wrappers to account for the ice contamination.
4. Displacements at ice breakaway (input values for *MinMax* materials) were updated iteratively by inspecting displacement histories until the assumed breakaway displacement matched the bearings' response.

In summary, the ice-contaminated bearing model accounts for ice resistance in the first two directions of movement and causes termination of the ice material in each direction as the absolute maximum displacements in each direction are reached. After ice material has collapsed, the behavior is that of a nominal SPB bearing. Furthermore, the first two directions of movement can be in any radial direction and need not be parallel to each other.

4.3. GROUND MOTION SUITE

Eleven horizontal ground motion pairs were selected and scaled to match the target spectrum for the Susitna River Bridge, as derived from the bearing design parameters in Table 2.1. The 5% damped target spectrum is shown in Figure 4.8. Motions were selected from a general search of the PEER NGA ground motion database (Ancheta et al., 2013). The search criteria input to the database is as follows: shear wave velocity ranging from 2,500 to 5,000 ft/s (Site class B) and scale factor ranging from 0.33 to 3 (roughly consistent with ASCE 7-22 as discussed further below).

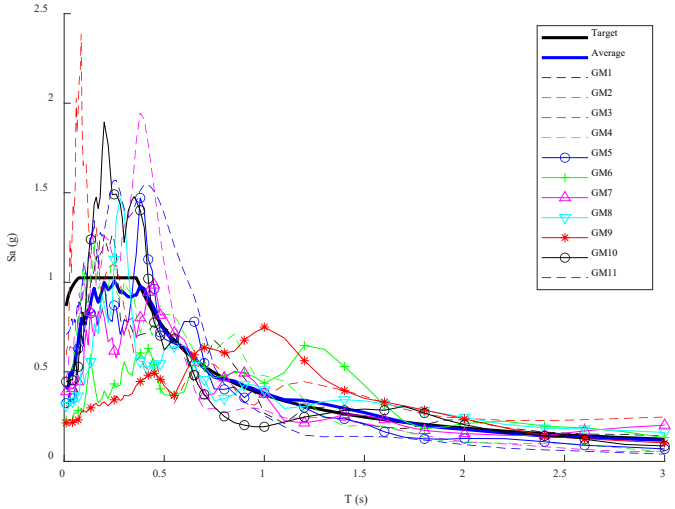

Figure 4.8. 5% damped target spectrum and acceleration response spectra for individual motions along with suite average.

The ground motions were scaled following procedures in current design codes. The AASHTO Guide Specification (AASHTO, 2014) provides only limited guidance; therefore, the more specific language in ASCE 7-22 (2022) was consulted. While ASCE 7-22 allows both amplitude scaling and spectrum matching, amplitude scaling procedures were utilized to preserve the natural frequency content and variation of the motions to meet the intent of this analysis case study. The motions were scaled to "best fit" the 5% damped target spectrum in a minimum least squares sense over the period range 0.30 sec to 2.50 sec, which was selected to include the range of participating modes in the isolated structure. Per ASCE 7-22, the scaling is based on the maximum direction spectrum, or maximum (vector) acceleration response for the ground motion pair, sometimes referred to as the ROTD100 spectrum. After the initial scaling, minor adjustments were made to some scale factors to meet the criteria that the average maximum direction spectrum of the scaled ground motion suite does not fall below 90% of the target spectrum over the scaling period range.

Software integrated with the PEER NGA database allowed the ground motion search, selection and scaling to seamlessly be integrated in a single step. Individual motions were accepted or rejected according to how well they matched the target spectrum. The selected ground motions and their scale factors are listed in Table 4.5. Furthermore, transverse and longitudinal acceleration component files for each ground motion are listed on Table 4.6. Maximum direction spectra for individual scaled motions and the average maximum direction spectrum are plotted against the target spectrum in Figure 4.8.

Table 4.5. Ground motion suite characteristics

Tag	Earthquake	Year	Station Name	Magnitude	R_{jb} (Km)	Scale Factor	Scaled PGA (g)
GM1	Tabas, Iran	1978	Tabas	7.35	1.79	0.345	0.303
GM2	Loma Prieta, CA	1989	Gilroy Array #1	6.93	8.84	0.915	0.456
GM3	Landers, CA	1992	Lucerne	7.28	2.19	0.738	0.593
GM4	Northridge-01, CA	1994	LA - Wonderland Ave	6.69	15.11	2.759	0.459
GM5	Northridge-01, CA	1994	Vasquez Rocks Park	6.69	23.1	1.882	0.325
GM6	Kobe, Japan	1995	Kobe University	6.9	0.9	0.700	0.231
GM7	Kocaeli, Turkey	1999	Gebze	7.51	7.57	1.424	0.389
GM8	Kocaeli, Turkey	1999	Izmit	7.51	3.62	1.260	0.312
GM9	Loma Prieta, CA	1989	Los Gatos - Lexington Dam	6.93	3.22	0.464	0.215
GM10	Tottori, Japan	2000	SMNH10	6.61	15.58	1.845	0.445
GM11	Parkfield-02, CA	2004	Parkfield – Turkey Flat #1 0M	6	4.66	2.765	0.709

Table 4.6. Ground motion suite longitudinal and transverse components

Tag	Record Number	Transverse Acceleration	Longitudinal Acceleration
GM1	RSN143	TAB_L1	TAB_T1
GM2	RSN765	G01000	G01090
GM3	RSN879	LCN260	LCN345
GM4	RSN1011	WON095	WON185
GM5	RSN1091	VAS000	VAS090
GM6	RSN1108	KBU000	KBU090
GM7	RSN1161	GBZ000	GBZ270
GM8	RSN1165	IZT180	IZT090
GM9	RSN3548	LEX000	LEX090
GM10	RSN3954	SMNH10NS	SMNH10EW
GM11	RSN4083	36529270	36529360

4.4. ANALYSIS RESULTS

The general response trends of the bridge under the contamination scenarios are discussed next. First, the response characteristics of the uncontaminated bridge with DPBs (NDPB) is presented. Figure 4.9 presents time histories of various responses when subjected to Tabas (GM 1). The dynamic behavior varies somewhat in the transverse (X) direction compared to the longitudinal Y-direction. Displacements at the deck level – sampled at the top of each abutment (A1, A6) and pier (P2-P5) vary slightly in the transverse direction (Figure 4.9(a)) but are identical in the longitudinal direction (Figure 4.9(b)), confirming that the superstructure is rigid axially but can bend slightly about its vertical axis. Mid-span displacements, not shown here, were also similar to those at the top of the piers. The bridge piers are very rigid in the transverse direction, displacing a maximum of about 0.05” (Figure 4.9(c)), and more flexible in the longitudinal direction, displacing a maximum of about 0.5” (Figure 4.9(d)), as expected given their elliptic cylinder shapes. Individual pier displacements vary significantly, with the largest displacements observed in Piers 2 and 3, and significantly smaller displacements in Pier 5, in proportion to their relative heights. Differences in observed frequencies and phases in the pier responses are noted. Most differences in relative displacements of the superstructure or piers are absorbed by the isolators. As such, displacement histories of individual isolators vary somewhat (Figure 4.9(e) and (f)), although the differences appear minor relative to the much more substantial movement across the isolators. For a compatibility check, the displacement at the top of the isolator is compared to the corresponding deck displacement at three locations in Figure 4.9(g) and (h). The corresponding displacements are essentially identical in the transverse direction, but vary slightly in the longitudinal direction, where the discrepancies are attributed to rotations at the tops of the piers and bending of the superstructure about its transverse axis.

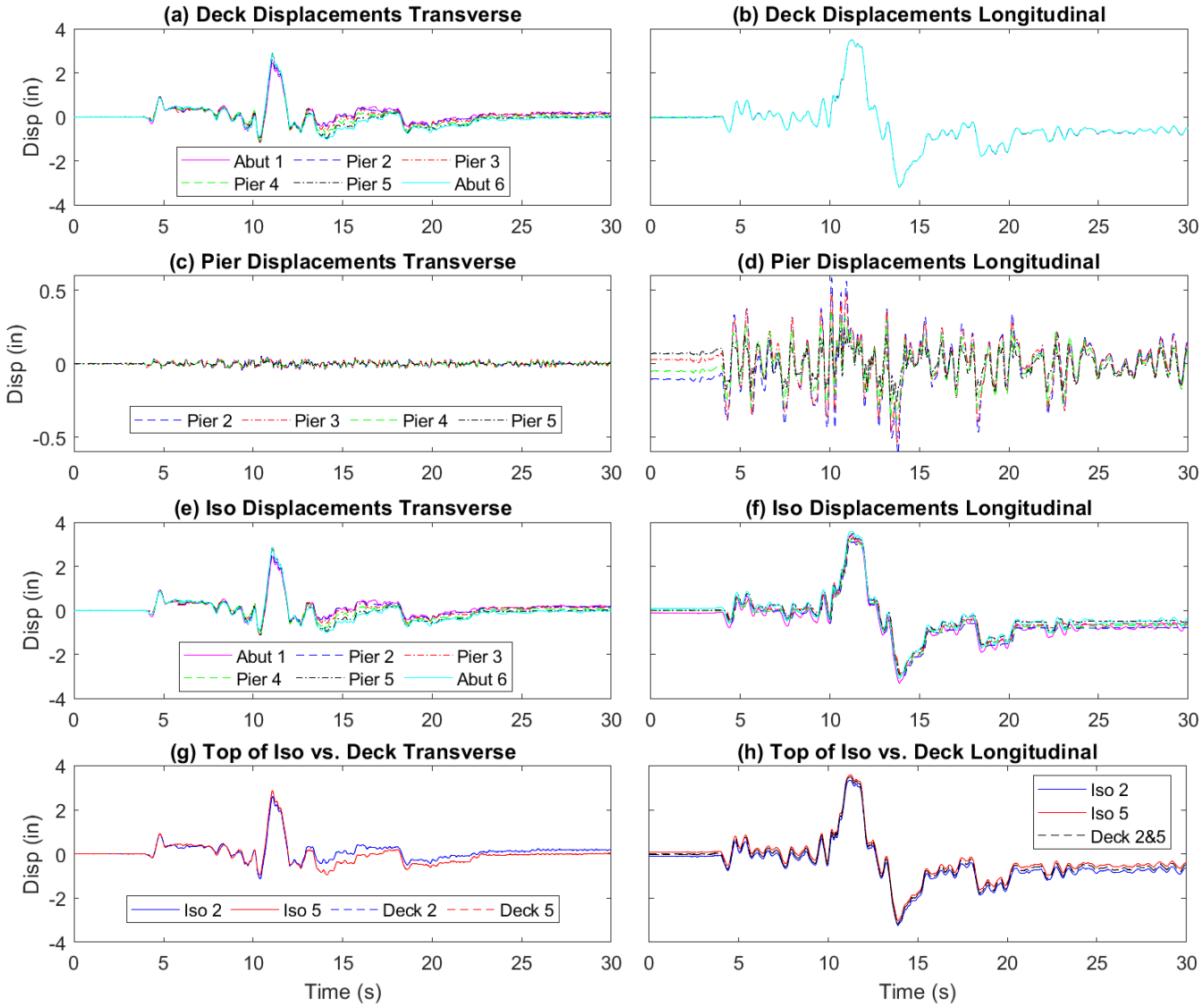

Figure 4.9. Select response versus time for GM 1 Tabas with nominal DPB properties (a)-(b) Deck displacements transverse and longitudinal (c)-(d) Pier displacements transverse and longitudinal (e)-(f) Iso displacements transverse and longitudinal (g)-(h) Top of iso vs. deck transverse and longitudinal, respectively.

The average peak isolator displacement over the ground motion suite was 4.17” (very close to the target) and ranged from 2.21” to 9.0”. Peak displacements can vary by as much as 20% over individual isolators in the bridge, with larger variation during lower intensity ground motions. Figure 4.10 compares the peak force summed over the isolators at each pier with the peak shear force of the corresponding pier (color coded by pier), for each ground motion in the suite. The isolator shear force and pier shear force differ due to the inertial force of the pier and bent cap. This image shows that although they are related, larger isolator forces do not necessarily lead to larger pier shear forces. For instance, pier shear forces in motions 2, 4, 5, 10, and 11 seem disproportionately large relative to the isolator forces. The peak shear force may be influenced by its own vibration and phasing relative to the isolation system. This observation may help explain why, as seen shortly, changes in individual isolator responses due to contamination often have little influence on the peak pier forces.

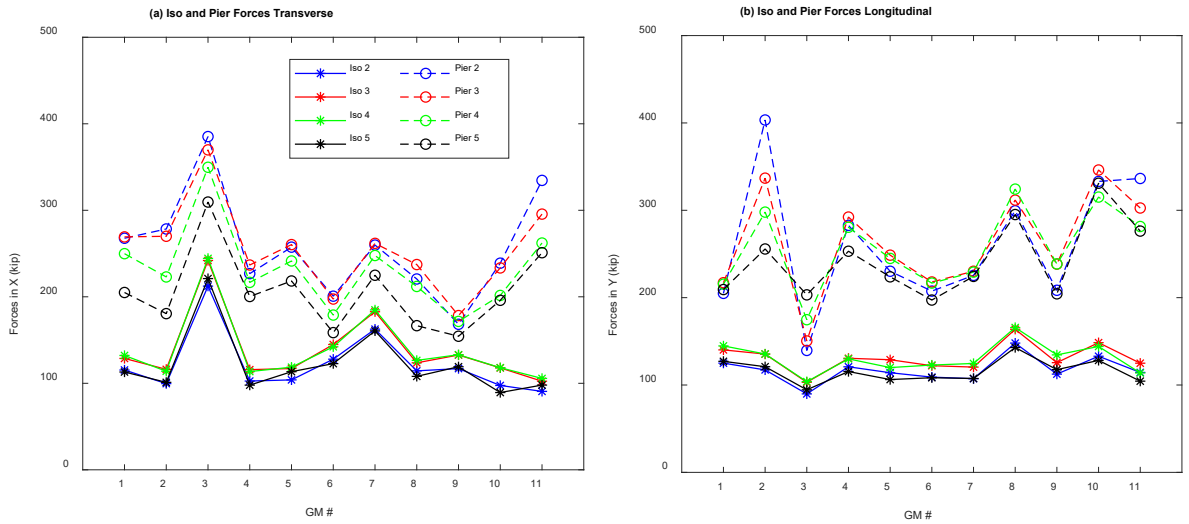

Figure 4.10. Peak isolator and pier column by pier versus ground motion (a) Transverse (b) Longitudinal direction.

Figure 4.11-Figure 4.13 summarize responses of interest in the various contamination scenarios for DPBs. Responses include peak displacement in any isolator (Figure 4.11), isolator shear coefficient in transverse and longitudinal directions (Figure 4.12), and peak shear force in each pier in each direction (Figure 4.13). These responses are presented as scatter plots with colored markers for individual motions in the suite, and black line/circle marker as the average over the suite. The responses are aligned with their scenarios on the x-axis, as labeled in Table 4.4, and the trend with respect to the nominal properties (NDPB) can easily be evaluated for each scenario. These results are supplemented by detailed spreadsheets in Appendix D that tabulate, for each response, the response ratio of the contaminated to uncontaminated case. In these appendix spreadsheets, ratios of 1.05-1.10 (approximately 5-10% increase) are highlighted in light pink and ratios above 1.10 are highlighted in magenta. Similarly, ratios from 0.9-0.95 (approximately 5-10% decrease) are highlighted in tan and ratios below 0.9 are highlighted in copper. Some of the synthesis reported here was informed by these tables.

The water contamination scenarios are identified as WC S1, WC S2 and WC S3 (abutments, Pier 2-3, and total water contamination, respectively). In general, water contamination causes the peak displacement demand in any isolator to increase relative to the bearing nominal properties. On average, the peak displacement increases by about 5%, 10% and 17% for WC S1, WC S2 and WC S3, respectively. The bearing displacement capacities are 8" for pier bearings and 11" for abutment bearings. According to Figure 4.11, the displacement capacity is reached in one simulation (GM 3) for nominal properties, and the demand is further increased with water contamination. Note that the ultimate behavior – pounding of the isolator against its outer rim and the consequences - is not simulated here, but must be avoided in design. Notably, increased displacement due to water contamination does not cause the displacement capacity to be reached in any other ground motion for any of the scenarios. The nature of the displacement increase is different in the various scenarios. In WC S1 (abutment contamination only), displacement increases tend to be limited to abutment bearings and are primarily in the transverse direction, where the differential displacements are absorbed by the deck rotation or bending about its vertical axis. The isolator force coefficient decreases only slightly (Figure 4.12) and the pier forces are unaffected (Figure 4.13). In WC S2 (contamination of Piers 2 and 3), displacements in the transverse direction increase primarily at the left end of the bridge, and again the deck bends or rotates about its vertical axis to accommodate this. Increases in the isolator displacement in the longitudinal direction tend to be more uniform across the bridge, as the isolators move with the longitudinally stiff deck. The isolator force coefficient decreases further; while pier forces decrease slightly

in the contaminated piers (Piers 2 and 3) only. Contamination of all bearings has the most pronounced effect; displacement increases tend to be uniform across all isolators as the fundamental dynamic properties of the isolation system are altered. The isolator shear coefficient decreases substantially, and the pier forces generally decrease. Thus, the biggest risk of water contamination is that the isolators are more likely to reach their displacement capacity; however, with typical reserve capacities allotted in design, this risk is not significant.

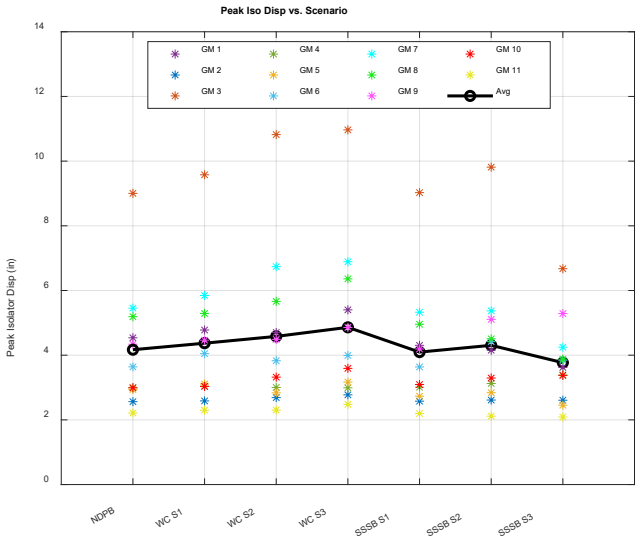

Figure 4.11. Peak isolator displacement vs contamination scenario.

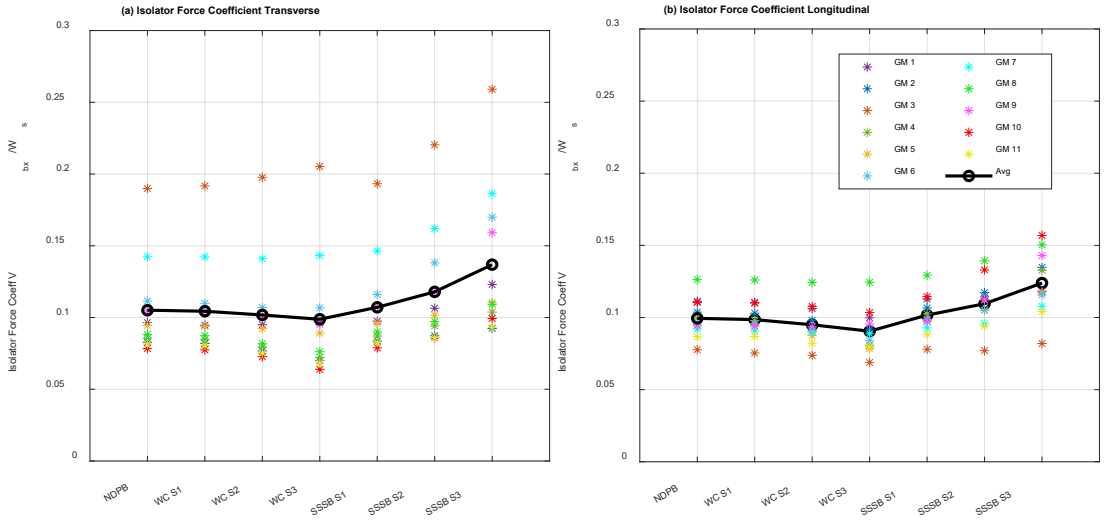

Figure 4.12. Peak isolator force coefficient vs contamination scenario (a) Transverse (b) Longitudinal direction.

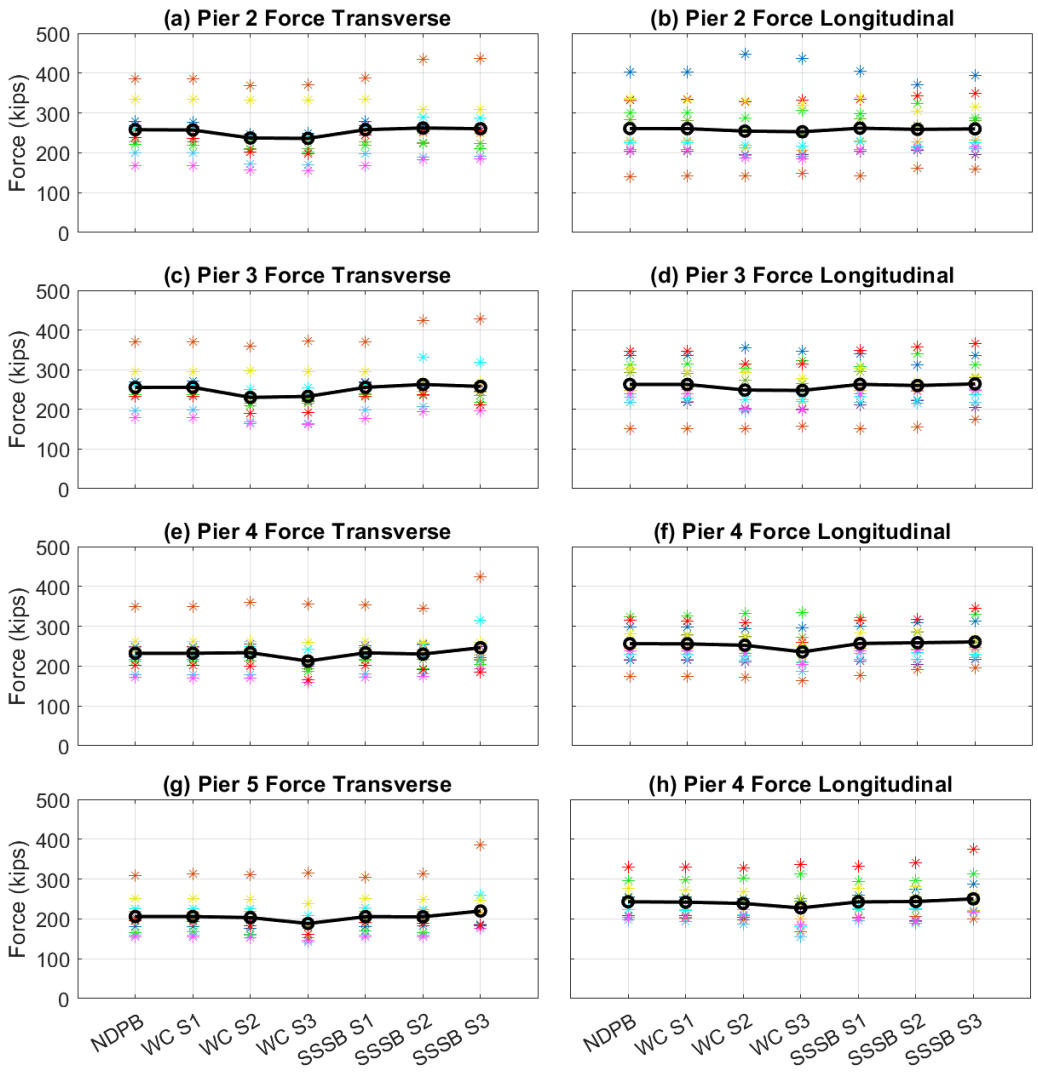

Figure 4.13. Peak pier force vs contamination scenario (a)-(b) Pier 2 (c)-(d) Pier 3 (e)-(f) Pier 4 (g)-(h) Pier 5, in transverse and longitudinal direction, respectively.

The single-surface sliding scenarios (bounding analysis) are identified as SSSB S1, SSSB S2 and SSSB S3. These analyses are denoted as bounding analyses because the isolator model does not transition to nominal hysteresis properties after the single surface displacement limit (4" for pier bearings and 5.5" for abutment bearings) is reached, and thus represents an upper bound of the force demands that might be induced. For instance, the single-surface sliding displacement limit will be reached in about 4 of the 11 ground motions. The benefit is that these analyses can be performed with standard isolator models. On average, the peak isolator displacement is reduced (Figure 4.11), but the reduction is generally accompanied by an increase in forces in the affected bearings and the overall isolator force coefficient (Figure 4.13). The nature of the isolator response and its consequences for these scenarios is similar to water contamination. For the abutment contamination scenario SSSB S1, isolator forces in the abutments increase substantially (average of 25-30% in each direction). However, this effect is localized, the force increase is absorbed at the abutment supports and the rest of the bridge is unaffected. For the pier contamination scenario SSSB S2, the forces increase in the isolators at Piers 2 and 3 (again by about 25% on average), but the effect is localized. The consequences for the pier forces are unpredictable; in some motions the forces in Piers 2 and 3 increase substantially (10% or more), while in others they are unchanged or decrease. This is likely an indication of the higher mode effects that determine the vibration of the pier subassemblies. Note that the ground motions

inducing larger displacements and forces appear to be more likely to induce substantial increases in Pier 2 and 3 shear forces (compare NDPB and SSSB S2 in Figure 4.13(a)-(d)). Finally, the complete contamination scenario SSSB S3 induces increases in isolator forces ranging from 25-30% on average over all the bridge isolators, with similar unpredictable consequences to the shear forces in the bridge piers. In summary, the consequences are: contamination of isolators at any pier substantially increases the force demands of the corresponding isolators and could induce – but does not always induce – an accompanying increase in force demands of the corresponding piers. In the bridge analyzed, increases in pier shear forces, when they occur, are less than half the increases (by percentage) in the isolators. However, the consequences of the increase in isolator forces due to contamination may vary for other bridge configurations with different dynamic properties.

Next, the importance of accounting for the transition from single surface sliding to sliding on both surfaces is examined. It is hypothesized that bounding analysis using properties associated with single surface sliding will be a reasonable (not overly conservative) upper bound to bearing shear force and associated design parameters. The single surface sliding bounding analysis could underestimate displacement demands, so a more accurate analysis may be necessary when the demands approach the displacement capacity of the bearing. In summary, transition behavior is expected to make a difference when the bearing displacement demand is driven well beyond the single surface limit. To test the hypothesis, Trans S2 and S3 scenarios are analyzed for select ground motions and the results compared to the corresponding motions for SSSB S2 and S3. For the ground motion scaling described in Section 4.3, only 3 of 11 ground motions (GM 3, 7 and 9) have displacement demands that reach the single surface sliding limit, given that the target displacement is around 4”. To consider additional cases, the remaining motions were scaled by 150% and several from this set (GM 1, 6, 8 and 10) have been considered for further investigation.

The nature of the response of the Trans model relative to SSSB is illustrated for one of the Pier 3 bearings for Scenario 3, GM 8 applied at a 150% scale factor in Figure 4.14. The response in the remaining bearings is similar. This particular motion has been selected because the resultant displacement demand is large, and the effect of the transition behavior is notable. The bearing displacement histories (Figure 4.14(a)) indicate that a single large pulse relatively early in the history, primarily in the negative longitudinal direction, exhausts the single surface sliding limit (4” for the pier bearing). The instant that transition initiates is indicated by a red marker in all the subplots. After this instant, the displacement histories of the two models diverge significantly and the Trans model reaches a substantially larger peak displacement (shown also in the displacement trace in Figure 4.14(b)). The instant of transition in the hysteresis loops is most evident in the longitudinal direction (Figure 4.14(d)), where the shear force of the transition element sees a sudden drop and continuation at lower slope, ultimately tracing out a loop with much lower stiffness than the SSSB model. As a result, the peak force in the bearing with the Trans model is much lower than the SSSB model. The effect of transition is not as evident in the transverse direction (Figure 4.14(c)), which is typical for the weaker direction of motion where the bidirectional interaction effects tend to introduce waviness into the hysteresis loop. Note that the hysteresis loops of the two models should be identical prior to transition, but are not since the effect of axial load variation is not fully accounted for in the Trans model.

Table 4.7 and Table 4.8 summarize effects of SSSB relative to the Trans model (considered to be more accurate) for Scenario 2 and 3 considered motions, respectively. In these tables, the GM columns are ordered from greatest to least displacement demand, with the expectation that larger displacement demands will equate to larger deviations in peak responses in SSSB relative to Trans. Responses shown in these tables include: (1) absolute peak displacement demand in any bearing in the transverse, longitudinal, and overall (vector sum) for both SSSB and Trans models, and (2) ratios of peak SSSB relative to Trans model response for isolator displacement, isolator force in transverse and longitudinal directions, and pier force in transverse and longitudinal directions. The Min/Max column lists the relevant (minimum or maximum) peak response

ratio over all the isolators or all the piers, while the Avg column lists the average peak response ratio over all the isolators or all the piers.

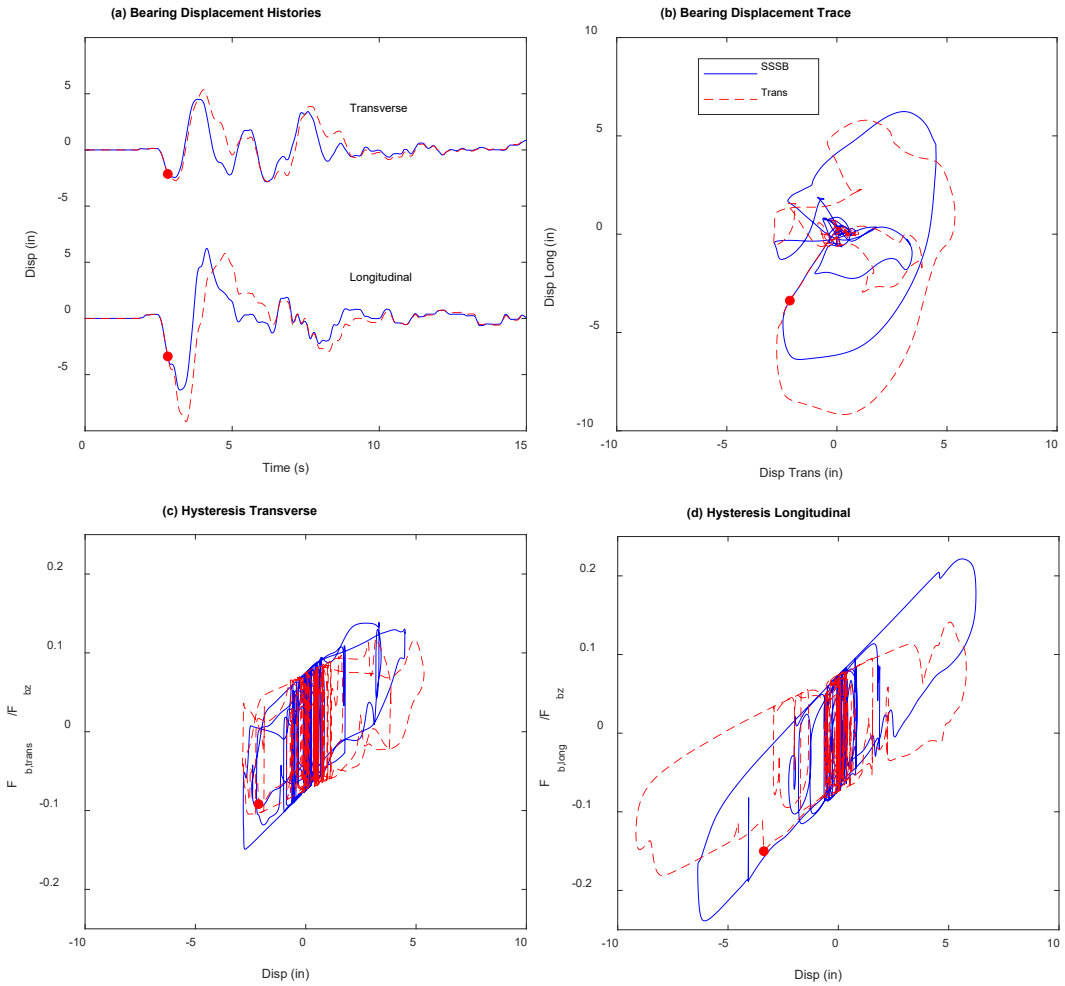

Figure 4.14. SSSB versus Trans-S3 model in Pier 3 bearing for GM 8 applied at 150% scale factor (a) Bearing displacement histories (b) Bearing displacement trace (c) Hysteresis transverse (d) Hysteresis longitudinal.

Observing the numbers in the tables, there is not a big difference in the peak bearing displacements for the two models for Scenario 2 (Table 4.7). The peak displacement is generally larger for the Trans model, but not always (consider GM 6). However, the ratios of SSSB to Trans isolator displacements are considerably lower for the first few GMs, indicating that peak displacement for the SSSB model is much lower than the Trans model in one or some of the bearings. These numbers seem to conflict with the peak displacements, but is explained by the fact that the ratio is computed independently for each bearing. Not apparent from the table data, displacement demands in individual bearings can differ substantially in Scenario 2 because some isolators are contaminated while others are not, and the bridge flexes as it is able to accommodate the differential movements. As a result of the bounding behavior, peak isolator force demands are greatly overestimated in SSSB relative to Trans model in some bearings. The first five GMs in the table have a max force ratio exceeding 1.4 (i.e. SSSB overestimates the isolator forces at a given pier or abutment by more than 40%). In many simulations, the increased force is somewhat offset by the reduced displacement; however, the force ratio is particularly large in GM 6 where the displacement due to SSSB is substantially larger than Trans. The difference in these isolator force ratios are minor for GM 7 and 9, which are not driven much beyond their single surface sliding capacity. Finally, pier forces, consistent with earlier

results, are persistently unaffected or only marginally affected by changes in peak bearing forces. Where bearing force ratios are on the order of 1.4 to 1.7 (overestimated by 40 to 70%), pier force ratios are on the order of 1.05 to 1.15 (overestimated by 5 to 15%). It seems evident, though not statistically proven, that discrepancies in the isolator displacements, isolator forces, and pier forces between the two models diminish as the displacement demand decreases (across the table from GM 8 to GM 9).

Table 4.7. Isolator displacements and ratios SSSB/Trans responses, Scenario 2

Response	**GM 8 150%**		**GM 3**		**GM 1 150%**		**GM 10 150%**		**GM 6 150%**		**GM 7**		**GM 9**	
	SSSB	*Trans*	*SSSB*	*Trans*	*SSSB*	*Trans*	*SSSB*	*Trans*	*SSSB*	*Trans*	*SSSB*	*Trans*	*SSSB*	*Trans*
u_{bxo} **(in)**	6.31	5.79	9.81	9.25	6.19	6.16	2.29	2.38	9.31	6.56	5.28	5.14	3.77	3.76
u_{byo} **(in)**	8.99	10.36	1.26	1.26	5.66	6.26	6.46	6.89	4.00	4.01	2.04	2.12	3.46	3.48
u_{bo} **(in)**	9.19	**10.38**	9.81	**9.25**	8.24	**8.47**	6.46	**6.89**	9.91	**6.79**	5.37	**5.26**	5.11	**5.11**
	Ratio SSSB/Trans.													
	Min/ Max	*Avg*	*Min/ Max*	*Avg*	*Min/ Max*	*Avg*	*Min/ Max*	*Avg*	*Min/ Max*	*Avg*	*Min/ Max*	*Avg*	*Min/ Max*	*Avg*
Disp any iso.	0.805	0.860	0.785	0.914	0.885	0.941	0.932	0.956	0.970	1.137	0.905	0.969	0.954	0.986
Iso force any pier														
Transverse	1.378	1.097	1.451	1.138	1.444	1.127	1.269	1.096	1.717	1.223	1.077	1.006	1.074	1.020
Longitudinal	1.471	1.105	1.124	1.027	1.527	1.074	1.507	1.149	1.140	1.029	1.011	0.994	1.208	1.010
Force any pier														
Transverse	1.151	1.053	1.022	1.004	1.013	1.004	1.090	1.016	1.104	1.044	1.228	1.076	1.011	1.002
Longitudinal	1.175	1.045	1.099	1.043	1.073	1.025	1.094	1.046	1.002	1.000	1.004	1.000	1.002	0.988

In Scenario 3 simulations (Table 4.8), discrepancies between peak isolator displacements in SSSB and Trans models are more significant across all ground motions. With contamination across all bearings rather than just a few, the overall dynamics of the isolation system changes and all bearings are affected comparably by the transition behavior. As a result, the average isolator displacement ratios are considerably lower than Scenario 2 (e.g. 0.775 vs. 0.860, 0.810 vs. 0.914, 0.887 vs. 0.941 for GM 8, GM 3, and GM 1, respectively). Likewise, the average isolator force ratios – SSSB/Trans – are considerably higher than Scenario 2 (e.g. 1.317 vs. 1.097, 1.347 vs. 1.138, 1.348 vs. 1.127 in the transverse direction for GM 8, GM 3 and GM 1, respectively). However, pier force ratios do not seem any more affected on average.

Table 4.8. Isolator displacements and ratios SSSB/Trans responses, Scenario 3

Response	**GM 8 150%**		**GM 3**		**GM 1 150%**		**GM 10 150%**		**GM 6 150%**		**GM 9**		**GM 7**	
	SSSB	*Trans*	*SSSB*	*Trans*	*SSSB*	*Trans*	*SSSB*	*Trans*	*SSSB*	*Trans*	*SSSB*	*Trans*	*SSSB*	*Trans*
u_{bxo} **(in)**	4.71	5.60	6.66	8.23	5.06	5.78	2.28	2.36	7.47	6.75	3.62	3.70	4.21	4.51
u_{byo} **(in)**	7.36	9.86	1.26	1.26	4.54	5.44	6.51	7.10	3.99	4.66	3.98	4.12	1.85	2.08
u_{bo} **(in)**	7.89	**9.97**	6.67	**8.23**	6.71	**7.47**	6.51	**7.10**	8.11	**6.95**	5.29	**5.41**	4.25	**4.55**
	Ratio SSSB/Trans.													
	Min/ Max	*Avg*	*Min/ Max*	*Avg*	*Min/ Max*	*Avg*	*Min/ Max*	*Avg*	*Min/ Max*	*Avg*	*Min/ Max*	*Avg*	*Min/ Max*	*Avg*
Disp any iso.	0.743	0.775	0.781	0.810	0.874	0.887	0.916	0.945	1.144	1.208	0.924	0.947	0.933	0.973
Iso force any pier														
Transverse	1.422	1.317	1.431	1.347	1.462	1.348	1.531	1.389	1.730	1.579	1.358	1.189	1.067	1.031
Longitudinal	1.371	1.324	1.167	1.076	1.378	1.249	1.485	1.369	1.116	1.054	1.150	1.055	1.105	1.024
Force any pier														
Transverse	1.088	1.015	1.114	1.052	1.020	1.012	1.181	1.044	1.281	1.226	1.010	1.004	1.190	1.110
Longitudinal	1.088	1.060	1.100	1.048	1.018	1.008	1.011	1.003	1.000	0.996	1.002	0.999	1.004	0.999

Next, simulations with the IC model are compared to the nominal SPB model (Table 4.4). As described in Section 4.2.2, simulation using the ice contamination model is an iterative process that involves updating the limits for the *MinMax* wrapper after each simulation until the displacements converge to the same limit. This time intensive process limited the number of ground motions that could be considered. Three ground motions have been selected for these simulations: GM 1 (Tabas - Tabas), GM 2 (Loma Prieta - Gilroy Array #1) and GM 4 (Northridge – LA Wonderland). All IC scenarios shown in Table 4.4 are simulated with all three ground motions.

Figure 4.15 compares ice contamination only in Piers 2 and 3 (S2) and the nominal properties (NSPB) for GM 1. The red circle markers in Figure 4.15 show the displacements at which the *Hysteretic* material is set to terminate – representing ice breakage – during the first two directions of movement. There is a small displacement peak 5 sec into the motion, which triggers breakage of the "positive" side of the backbone curve simulating the ice strength (Figure 4.7). After that point, for displacement in the positive hemisphere (right half of Figure 4.15(b)), only the bearing element (*singleFPBearing*) is engaged. Then, as the resultant displacement becomes negative (left half of Figure 4.15(b)), the negative portion of the backbone curve (Figure 4.7) is engaged. The second red dot in Figure 4.15(a) shows the termination of the ice model for the second direction of movement, at about -0.76" in the transverse direction, 1.06" in the longitudinal direction, and a resultant displacement of 1.30". As shown in Figure 4.15(a) and (b), displacement in pier bearings seems almost unaffected by ice contamination. A slight increase in shear force before ice breakaway can be observed in Figure 4.15(c) and (d). However, this increase in shear force is smaller than the peak shear force recorded for NSPB case. The contribution is insignificant because each Pier 2 and Pier 3 bearing carries about 500 kips and 625 kips, respectively, while the ice strength during the experiments was between 15 and 20 kips, which is only about 3% of the axial load on Pier 3 bearings. Furthermore, the ice resistance is engaged at the beginning of the motion, at relatively small displacements, where the shear force of the uncontaminated bearing has not reached its peak.

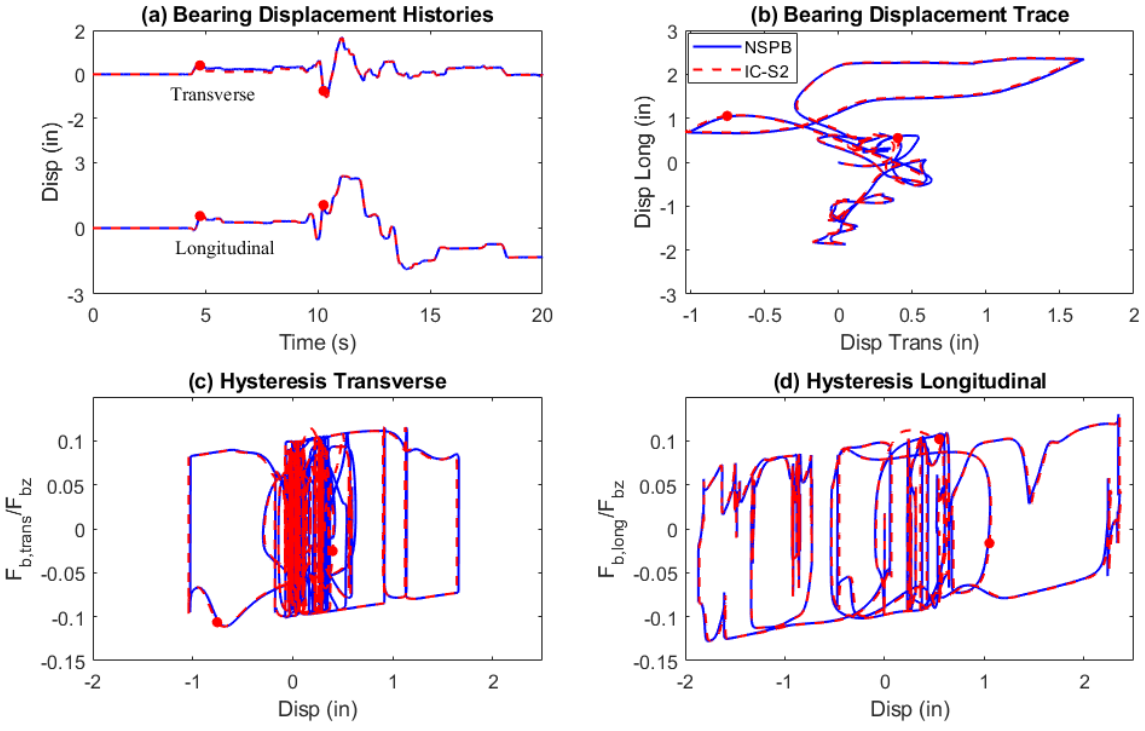

Figure 4.15. NSPB vs IC-S2 in Pier 3 bearing for GM 1 (a) Displacement history (b) Displacement trace (c) Transverse hysteresis loop (d) Longitudinal hysteresis loop.

Axial load is much smaller in the abutment bearings (average of 116 kips); thus the effect of ice contamination on bearing shear force is more noticeable. Figure 4.16 compares the response of one of the Abutment 1 bearings for scenario S1 (contaminated abutments) and NSPB, subjected to ground motion GM 1. Although the displacements are almost the same for both cases (Figure 4.16(a) and (b)), an increase in shear force on the bearing, at the beginning of the motion, can be observed in Figure 4.16(d) as a consequence of ice contamination. Furthermore, since the movement is dominated by the longitudinal direction, most of the increase in shear force is observed in the longitudinal direction while the increase in shear force in the transverse direction is negligible, as shown in Figure 4.16(c) and (d).

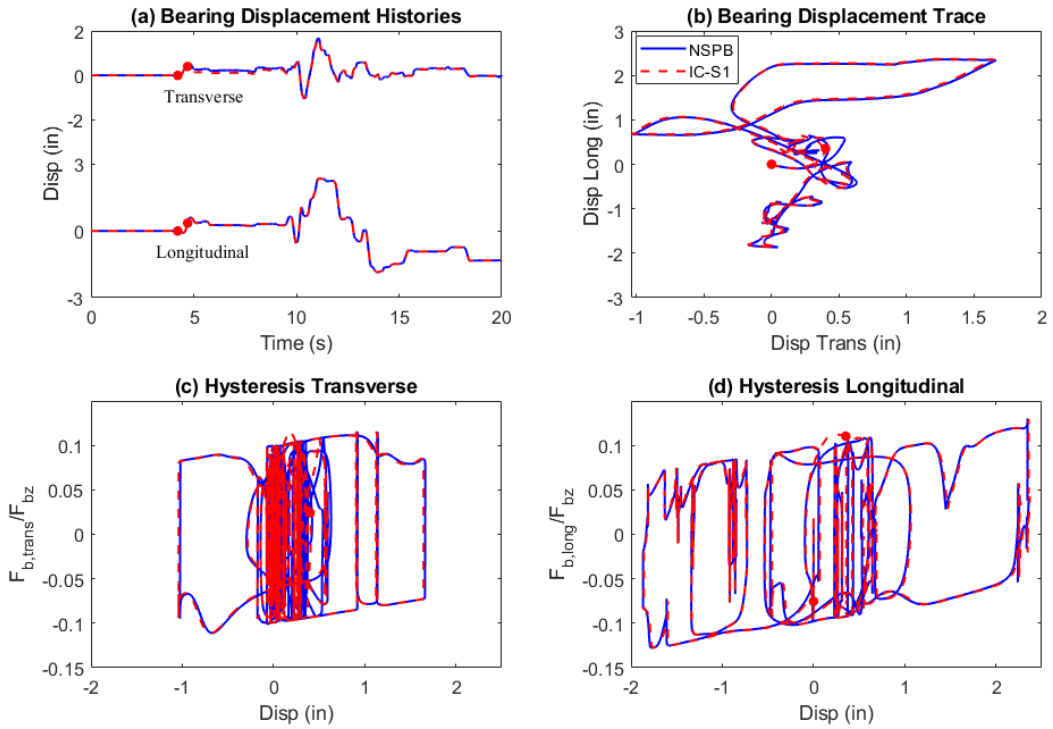

Figure 4.16. NSPB vs IC-S1 in Abutment 1 bearing for GM 1 (a) Displacement history (b) Displacement trace (c) Transverse hysteresis loop (d) Longitudinal hysteresis loop.

Peak displacements and forces have been computed for bearings and piers for all simulations. Figure 4.17 and Figure 4.18 show scatter plots of the absolute peak isolator displacement and peak normalized shear force, respectively, for all the ice contaminated (IC) simulations and NSPB. Scattered markers represent the peak response for all ground motions and all contamination cases, while the black solid lines represent the average peak response of the three ground motions for each contamination scenario. Peak isolator displacement does not seem to be affected by ice contamination, regardless of the contamination scenario or ground motion (Figure 4.17), which is in agreement with Figure 4.15 and Figure 4.16. Isolator shear force also does not seem to be affected by ice contamination (Figure 4.18). In light of the trends for other contamination scenarios discussed earlier, since the pier bearings shear forces are unaffected by ice contamination, peak pier shear forces will also be unaffected (and thus they are not shown).

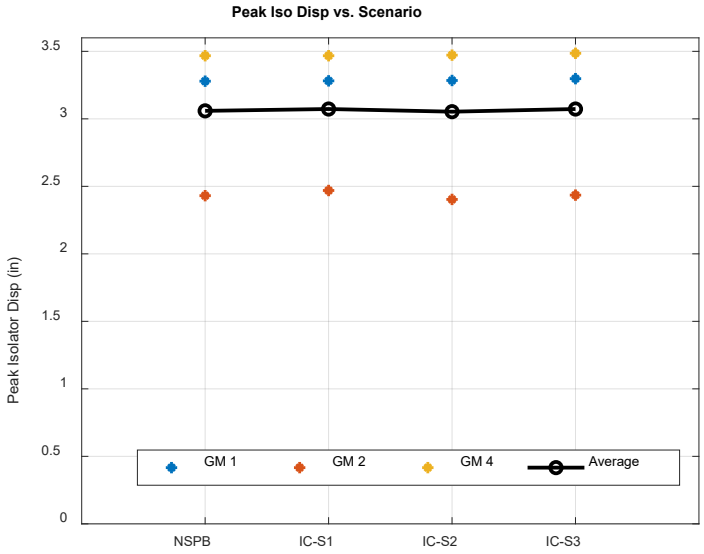

Figure 4.17. Peak isolator displacement vs ice contamination scenario.

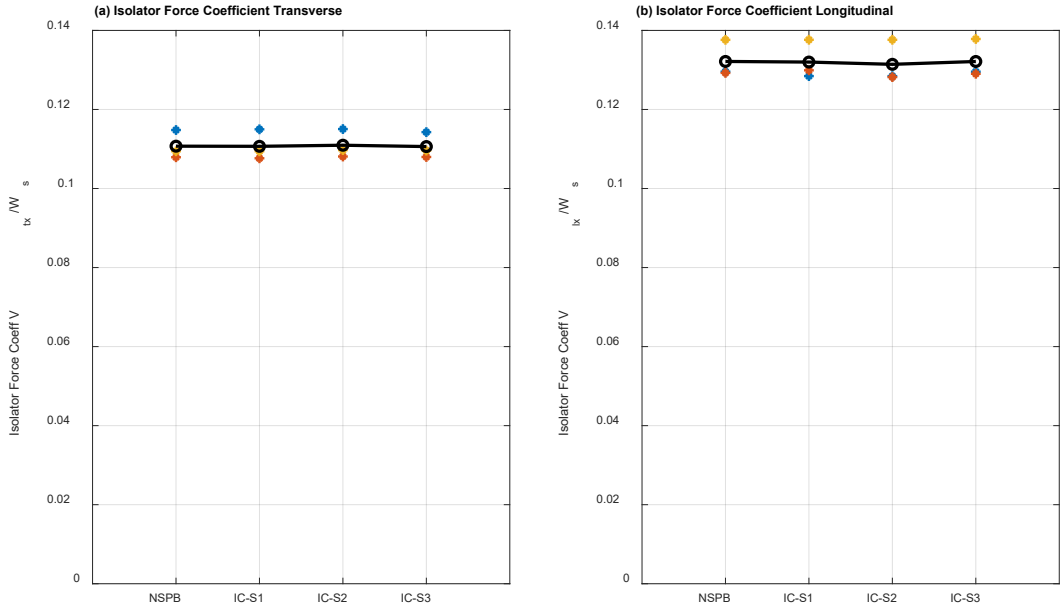

Figure 4.18. Peak isolator force coefficient vs ice contamination scenario (a) Transverse (b) Longitudinal.

Revisiting Figure 4.16 (abutment bearings), there was a noticeable increase in bearing shear force compared to the pier bearings in Figure 4.15, likely because of the lower relative axial load. Recall that this modeling scenario utilized the Robertson bearing ice contamination model on the Susitna River Bridge, whereas the bearings in the Robertson River Bridge had relatively much lower axial loads. In lieu of modeling the Robertson River Bridge directly, the effect of ice contamination on a bridge with lower bearing axial load is estimated. The axial loads on abutment and pier bearings in the Robertson River Bridge are estimated to be 18 and 185 kips, respectively, which are about 10% and 29% of the simulated axial loads on the Susitna River Bridge abutment and pier (3 and 4) bearings, respectively. To estimate the effects of ice contamination on Robertson River Bridge, a ratio of the bearing axial loads on both bridges was calculated:

$$f_{inc} = \frac{W_{Si}}{W_{Ri}} \qquad \textbf{(Eq. 4.3)}$$

where W_{Si} is the average axial load observed on Susitna River Bridge i^{th} bearing and W_{Ri} is the design seismic axial load on Robertson River Bridge i^{th} bearing. Then the backbone curves of the *Hysteretic* ice contamination elements were amplified by f_{inc}. For this simulation S3 to GM 1, Figure 4.19 shows normalized hysteresis loops for Abutment 1 and Pier 3 Susitna River Bridge bearings that reflect the increment in shear force due to the factor f_{inc}. An important increase in shear force in both directions is observed for the Abutment 1 bearings. Given that the movement is dominated by the longitudinal direction, the increase in shear force is greater in the longitudinal direction than the transverse direction. Furthermore, the effect is less noticeable in the pier isolators (Figure 4.19(c) and (d)). The shear force on pier isolators increases by less than 10% at the interface and thus does not affect the overall peak (0.14 for NSPB versus 0.13 for IC-S3 when applying f_{inc} increase, in longitudinal direction). This suggests that the effect of ice contamination is negligible for bearings with an axial load larger than 180 kips (equivalent to the axial load in Robertson Bridge pier bearings). However, more simulations and experimental data are required to validate this.

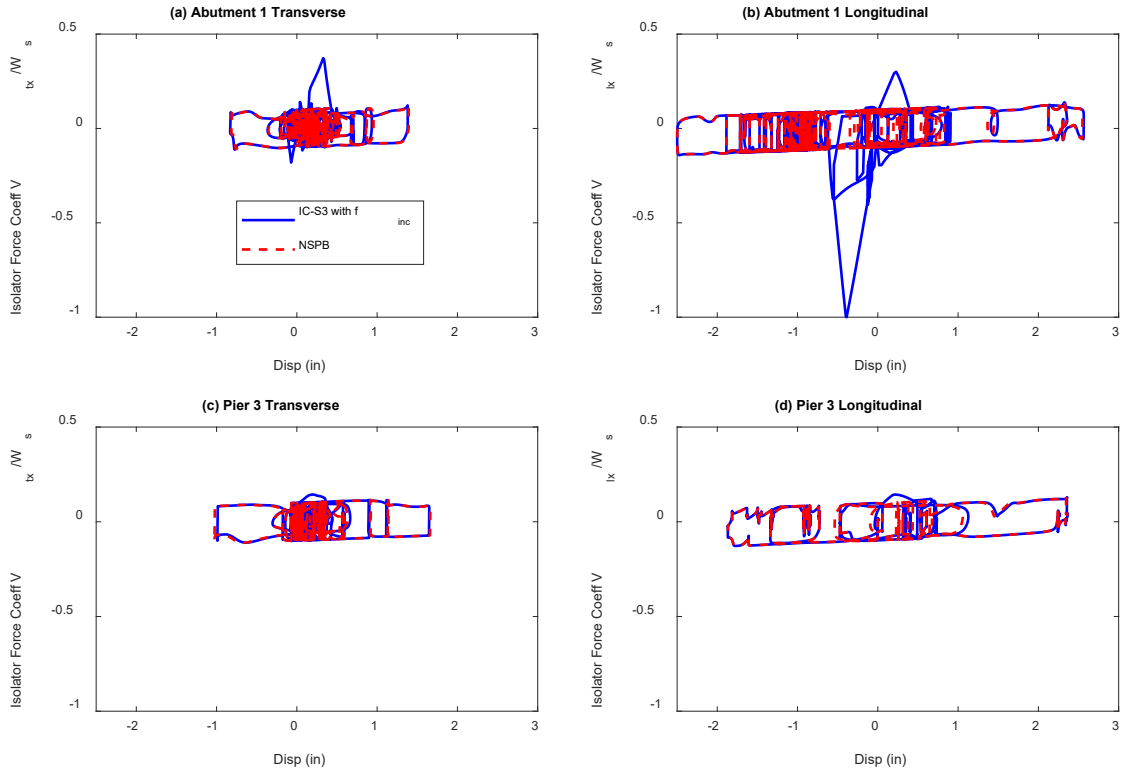

Figure 4.19. Normalized hysteresis loops for IC-S3 (a)-(b) Abutment 1 (c)-(d) Pier 3.

In summary, contamination scenarios are important to consider in design, in that they might substantially affect the peak isolator displacements and forces in individual bearings. For the Susitna bridge model considered here, increases/decreases in the simulated forces in the isolation bearings generally did not translate to comparable increases/decreases in the pier forces (discrepancies in pier forces were generally small relative to isolator forces and somewhat insignificant). However, this particular bridge has a large mass associated with the cap beam and the column pier that may serve to separate it dynamically from the isolators. The governing dynamics may be different in a bridge with a lighter, more flexible pier.

CHAPTER 5: CONCLUSIONS AND RECOMMENDATIONS FOR PRACTICE

5.1. SUMMARY AND CONCLUSIONS

This project included characterization testing of SPBs and DPBs subjected to water, ice and soil contamination, and computational simulation to predict the influence of the contamination on the bridge response for various contamination scenarios. The key findings from the testing are as follows. For the SPBs, the characterized/observed stiffness and hence pendulum length was different for movement in the positive and negative directions, and in general did not match well with theoretical. This is believed to reflect a time varying friction effect caused primarily by the bearing top plate rotation that manifests as a change in stiffness; however, the rotation data was insufficient to verify the cause. In DPBs, uneven sliding on the two surfaces and even single surface sliding (i.e. sliding limited to one surface) was observed throughout the test program. This uneven sliding phenomenon had several potential causes. First, unequal friction coefficients due to water or other contaminants, or rusted surfaces in the aged bearings could induce the uneven sliding or even prevent sliding on one surface entirely if the discrepancy was large enough. Second, ice or caked on soil were both observed to prevent the bottom surface from moving entirely until the displacement capacity of the top surface was reached. Finally, the single surface sliding was observed occasionally even in a clean, dry bearing. This also could be caused by rotation of the bearing top plate, which induces a dynamic variation in effective friction and thus unequal friction on the two surfaces, but again could not be verified. The observed pendulum length in the DPB varied from about 37" (single surface sliding limit) to more than 74" (double surface sliding limit). The pendulum length from characterization was shown to be correlated to observations of the nature of sliding, characterized by % one surface to total sliding (%OST), measured in individual cycles.

The average friction coefficients during testing were quantified from the characterization process, although the procedure cannot control for the influence of the dynamic variations. The characterized friction coefficient generally exceeded the target friction coefficient by noteworthy margins. The average friction coefficient was largest in the new bearings, and not as large in the formerly in-service aged Susitna bearings. The wet friction coefficient was found to be lower than the dry friction coefficient in all bearings except the new Robertson bearing. The friction coefficient during ice contaminated bearing tests, after ice breakaway and during the free sliding phase, was about the same on average as the dry friction coefficient. Overall, no evidence was found to support substantial increases in friction due to aging, contamination, and low temperatures, as is often assumed in design. The ice breakaway strength was measured in the range of 10 to 18 kips in these bearings. While this resistance is significant for a lightly loaded bearing, it would be unimportant for a typical bridge bearing supporting several hundred kips. An SPB must overcome ice breakaway strength immediately to slide, whereas a DPB slides initially on one surface and thus experiences only a moderate ice breakaway effect when the single surface displacement capacity is reached, forcing the ice to break on the second surface. The ice breakaway strength is hypothesized to be independent of axial load, but vary with the size of the bearing cavity.

Next, the influence of contamination on the seismic response of the isolated Susitna River Bridge was examined through computational simulation. A spine model of the bridge structure was developed in OpenSees, and validated by comparison with a high-fidelity model developed in CSI Bridge. A combination of bearing models (representing different forms of contamination) and contamination scenarios (number of contaminated bearings) were considered. The bridge models were subjected to a suite of motions that were

scaled to the target design spectrum for the bridge based on seismicity. Water contamination was modeled as a 20% decrease in the friction coefficient, interpreted as a property modification factor $\lambda_{Qd,min} = 0.8$. The water contamination was found to increase the bearing displacement demand by 5% to 17% on average over the ground motion suite depending on the scenario. The isolator forces in general decreased due to the reduced friction, and the pier forces decreased marginally (inconsequentially). The biggest risk of water contamination is that the isolators are more likely to reach their displacement capacity; however, with typical reserve capacities allotted in design, this risk is not significant.

Single surface sliding was modeled generally as an increase in the bearing stiffness K_d (reflecting the decreased pendulum length) using a standard bearing model. This represents a bounding analysis approach; in reality the bearing will transition from single surface to conventional sliding response after the displacement capacity of the one surface is reached. For comparison, a transition model approach was developed that uses an additional hysteretic material with a min-max wrapper in parallel with the bearing model. With the wrapper, the additional resistance terminates when a threshold displacement is reached. The consequences of single surface sliding, determined by bounding analysis, were as follows: contamination of isolators at any abutment or pier substantially increased the force demands of the corresponding isolators, by an average of 25-30% in the affected abutments or piers. Sometimes – but not always – this induced an accompanying increase in force demands of the corresponding piers. The consequences for the pier forces were unpredictable; in some motions the forces in affected piers increased substantially (10% or more), while in others they were unchanged or decreased. However, the consequences of increasing isolator forces due to contamination may vary for other bridge configurations with different dynamic properties. The bounding analysis is a reasonable representation of the response when the bearing displacement is not far past the point where transition occurs; however, for bearing displacements well beyond transition, the bounding analysis may underestimate displacements and response should be more carefully considered.

Finally, the effect of ice contamination in an SPB was modeled by an additional hysteretic material representing the backbone curve of ice breakaway with a max-min wrapper in each direction. Like the transition model described above, the ice breakaway backbone curve was in parallel with the conventional bearing model. The termination of ice backbone curve should be determined by load reversal, which is unknown at the start of the simulation. Thus, iteration is required to set displacement bounds on the max-min wrapper, and proceeds until the simulated bounds match the observed ones. The proposed approach is not suitable for general ice resistance simulations, but allowed the effect of ice resistance to be explored. Because the ice resistance was small relative to the axial loads on the bearings, the effects of ice resistance on the response of the bearing was less significant than the cases described above. However, these conclusions are sensitive to the magnitude of the ice breakaway force to the bearing shear force, and could vary significantly for other bridges.

5.2. RECOMMENDATIONS FOR PRACTICE

Based on observations, the authors believe no actions are needed for existing bridges. Bridge owners should feel confident that with the usual bounding analysis and other procedures to account for uncertainties, the FPS bearings on isolated bridges will have sufficient capacity/robustness to perform their function even under field conditions that cause the bearings to collect and retain water, dirt, ice, or other unwanted contaminants. If contamination is occurring, bearings should be inspected regularly for excessive corrosion or other structural damage that may necessitate their replacement.

For design of new isolated bridges or bridge retrofits, bridge engineers should consider reasonable contamination scenarios as part of the usual bounding analysis process, to the extent that such analysis can

be performed with existing bearing models and design software. The transition model (single surface to double surface sliding) and ice contamination models developed for this project are insufficiently validated. They are in a developmental phase – suitable for exploratory research on potential contamination effects, but not yet robust for routine design implementation. However, some contamination scenarios can be considered as part of the typical bounding analysis process using property modification factors as prescribed in the AASHTO Guide Specifications for Seismic Isolation (AASHTO, 2014). In general, $\lambda_{min,Qd}$, $\lambda_{max,Qd}$, $\lambda_{min,Kd}$ and $\lambda_{max,Kd}$ correspond to upper and lower bound property modification factors for bearing strength (friction coefficient) and post-yield stiffness (pendulum length).

Recommended contamination scenarios to be considered for bridges in all climates are (1): reduced friction coefficient for wet friction, and (2) single surface sliding for DPBs or TPBs. More data is needed to develop a final recommended value for property modification due to wet friction. In the interim, a reduction of 80% of target is recommended based on the data from this report, interpreted as $\lambda_{min,Qd} = 0.8$. AASHTO explicitly states that $\lambda_{min,Qd}$ can be taken as 1 for sliding bearings, so this suggested property modification is not already considered under current interpretations of the design code. For single surface sliding, the effective stiffness is twice the nominal stiffness, which equates to a property modification factor $\lambda_{max,Kd} = 2$. AASHTO currently permits that for sliding bearings $\lambda_{min,Kd}$ and $\lambda_{max,Kd}$ can both be taken as 1, since the sliding radius that determines the stiffness is theoretically known. Thus, this suggested property modification also is not accounted for under current interpretations of the design code. Forces predicted by this single surface sliding bounding analysis should be evaluated for over conservatism using engineering judgment if the bearing displacement is well beyond the single surface sliding limit. Potential displacement capacity issues should be identified by combination of analyses with nominal properties and the single surface sliding bounding analyses.

Under normal bounding analysis procedures, the property modification factors are applied to all bearings. While such an approach could certainly be utilized, considering all bearings to be contaminated is probably unnecessarily conservative. Assumed contamination on the order of 25-50% of the bearings, selected strategically based on knowledge of bridge conditions or randomly in the absence of better information, is considered sufficient. However, localized peak forces are likely to be similar regardless of the scenario specifics, except in the case where total contamination fundamentally alters the dynamic characteristics while partial contamination does not.

Worth noting, Appendix A of the AASHTO provisions do provide recommended upper bound property modification factors for friction ($\lambda_{max,Qd}$) that vary depending on whether the bearing is lubricated or unlubricated, sealed or unsealed, and in a normal or extreme climate. The recommended factor combines effects of aging ($\lambda_{max,a}$), contamination ($\lambda_{max,c}$), and temperature ($\lambda_{max,t}$). Standard design likely assumes the bearings are sealed, whereas the conditions that led to this research would seem better interpreted as unsealed, for which the recommended increase in friction is substantial (or $\lambda_{max,Qd} \geq 3$ with combined effects). However, there was no evidence of increased friction due to any combination of aging, contamination or low temperatures in the bearings tested in this project (all three conditions were represented). Data on the aging effect in particular is inconclusive since EPS acknowledges that the technologies used to achieve target friction coefficient have evolved since the aged bearings were manufactured.

5.3. FUTURE RESEARCH

An unresolved question from this project is how rotation affects the response of the bearings, including its potential to induce single surface sliding. Furthermore, the importance of this question is determined by the potential for normal field conditions to induce rotation in the bearings. Permanent or transient relative rotations of the bearing top to bottom plate might be induced due by construction

tolerances, live load effects, accommodation of thermal expansion or other joints, and dynamically-induced rotation from seismic or wind effects. Some of these types of rotations might be predicted through computational simulation. The effect of rotation on the bearing response currently cannot be modeled rigorously, but follow-up research is recommended to develop capacity and answer pertinent questions.

Experimentally, the effect of rotation on the bearing response and sliding mechanisms should be explored using an experimental assembly that can impose controlled rotations (constant and variable) on the bearing as it is cycled through various displacement histories. The data provided could be used to validate the theories proposed in this report and elsewhere: rotation equates to an effective change in friction in the bearing that might manifest as a change in apparent stiffness, and ultimately induce single-surface sliding in multi-pendulum bearings if effective friction is larger on one surface than another.

To advance modeling, a bearing model should be developed that tracks the change of friction through the computed bearing rotation angle. This new model could then be combined in series to create a series spring-based model for DPBs or TPBs that tracks movement on independent surfaces that depends on the independent friction on each surface. These models can then be used in simulations of isolated bridges to understand the potential effects of rotations on the seismic response of the bearings (peak deformations and forces). For instance, rotations are expected at the top of a single column bent, which acts effectively as a cantilever in each direction. Incorporating a proven model into common software would allow such effects to be considered automatically in simulation without special bounding analysis procedures.

Regarding ice contamination, the data developed in this project is considered insufficient to develop a general ice contamination model or an upper bound ice breakaway force to be used in static analysis. Ice resistance should be evaluated in a variety of bearing sizes to develop a better theory for how ice resistance scales with volume. This question is considered to be lower priority than the aforementioned bearing rotation concerns; however, the breakaway resistance of caked on dirt and other filler contaminants may be of more general interest. Development and validation of improved seals (either by bearing manufacturers or interested third parties) that can convincingly prevent infiltration of water, ice and soil in the bearings would eliminate the need for further study of these issues.

Finally, the authors would like to provide context that contamination considerations are secondary and do not compromise the ability of the isolation system to provide effective earthquake protection or move reliably in an earthquake while reducing overall force demands throughout the system. Fine tuning the understanding of these effects facilitates more reliable bounding analysis, to better comply with the intent of current codes.

REFERENCES

American Association of State Highway and Transportation Officials. (1999). *Guide Specifications for Seismic Isolation Design*.

American Association of State Highway and Transportation Officials. (2014). *Guide Specifications for Seismic Isolation Design*.

Ancheta, T. D., Darragh, R. B., Stewart, J. P., Seyhan, E., Silva, W. J., Chious, B. S. J., Wooddell, K. E., Graves, R. W., Kottke, A. R., Boore, D. M., Kishida, T., & Donahue, J. L. (2013). Nga-West2 Site Database. *Pacific Earthquake Engineering Research Center*.

Andrews, E. H., & Stevenson, A. (1978). Fracture energy of epoxy resin under plane strain conditions. *Composites, 10*(1), 49-50. doi:10.1016/0010-4361(79)90408-7.

American Society of Civil Engineers. (2021). *Minimum design loads and associated criteria for buildings and other structures (Asce/Sei 7-22): Provisions*.

Andrews, E. H., & Lockington, N. A. (1983). The cohesive and adhesive strength of ice. *Journal of Materials Science, 18*(5), 1455-1465. doi:10.1007/bf01111965.

Bejan, A. (1993). *Heat Transfer*. John Wiley & Sons, Inc.

Benabdallah, H. S. (2007). Static friction coefficient of some plastics against steel and aluminum under different contact conditions. Tribology International, 40(1), 64-73.

Bloomfield, P. (2000). *Fourier Analysis of Time Series: An Introduction*. New York: Wiley-Interscience.

Campbell, T. I., Pucchio, J. B., Roeder, C. W. and Stanton, J. F. (1991), "Frictional Characteristics of PTFE Used in Slide Surfaces of Bridge Bearings", Proc. 3rd World Congress on Joint Sealing and Bearing Systems for Concrete Structures, Toronto, Ontario, Canada, Vol. 2 of Preprints (published by the National Center for Earthquake Engineering Research, Buffalo, NY), 847-870.

Constantinou, M. C., Mokha, A. S. and Reinhorn, A. M. (1990), "Experimental and Analytical Study of a Combined Sliding Disc Bearing and Helical Steel Spring Isolation System", Report NCEER-90-0019, National Center for Earthquake Engineering Research, Buffalo, NY.

Constantinou, M. C., Tsopelas, P., Kim, Y-S. and Okamoto, S. (1993), "NCEER Taisei Corporation Research Program on Sliding Seismic Isolation Systems for Bridges: Experimental and Analytical Study of a Friction Pendulum System (FPS), 404 Report NCEER-93-0020, National Center for Earthquake Engineering Research, Buffalo, NY.

Constantinou, M.C., Tsopelas, P., Kasalanati, A. and Wolff, E.D. (1999), "Property Modification Factors for Seismic Isolation Bearings", Report No. MCEER-99-0012, Multidisciplinary Center for Earthquake Engineering Research, Buffalo, NY.

Constantinou M. C., Whittaker A.S., Kalpakidis Y., Fenz D.M., Warn G.P. (2007). "Performance of Seismic Isolation Hardware under Service and Seismic Loading." Technical Rep. MCEER-07-0012.

Multidisciplinary Center for Earthqueake Engineering Research, State Univ. of New York at Buffalo, NY.

Dolce, M, Cardone, D. and Croatto, F. (2005), "Frictional Behavior of Steel-PTFE Interfaces for Seismic Isolation," *Bulletin of Earthquake Engineering*, Vol.3, No. 1, 75-99.

Dosch, H., Lied, A., & Bilgram, J. (1995). Glancing-angle X-ray scattering studies of the premelting of ice surfaces. *Surface Science, 327*(1-2), 145-164. doi:10.1016/0039-6028(94)00801-9.

Eggert, H. and Kauschke, W (2002), Structural Bearings, Ernst & Sohn, Berlin, Germany.

Fenz, D. M., & Constantinou, M. C. (2006). Behaviour of the double concave friction pendulum bearing. *Earthquake engineering & structural dynamics*, *35*(11), 1403-1424.

Fenz, D. M., & Constantinou, M. C. (2008). *Mechanical behavior of multi-spherical sliding bearings* (No. 7). Multidisciplinary Center for Earthquake Engineering Research.

Fortin, G., Beisswenger, A., & Perron, J. (2010). Centrifuge Adhesion Test to Evaluate Icephobic Coatings. *AIAA Atmospheric and Space Environments Conference*. doi:10.2514/6.2010-7837.

Fortin, G., & Perron, J. (2012). Ice Adhesion Models to Predict Shear Stress at Shedding. *Journal of Adhesion Science and Technology, 26*(4-5), 523-553. doi:10.1163/016942411x574835.

Furukawa, Y., Yamamoto, M., & Kuroda, T. (1987). Ellipsometric study of the transition layer on the surface of an ice crystal. *Journal of Crystal Growth, 82*(4), 665-677. doi:10.1016/s0022-0248(87)80012-x.

Gillich, G. R., Iancu, V., Gillich, N., Korka, Z. I., Chioncel, C. P., & Hatiegan, C. (2018). Decoupling the structure from the ground motion during earthquakes by employing friction pendulums. *IOP Conference Series: Materials Science and Engineering, 294*, 012025. doi:10.1088/1757-899x/294/1/012025.

Golchin, A., Simmons, G., Glavatskih, S., & Prakash, B. (2013). Tribological behaviour of polymeric materials in water-lubricated contacts. *Proceedings of the Institution of Mechanical Engineers, Part J: Journal of Engineering Tribology, 227*(8), 811-825. doi:10.1177/1350650113476441.

Grijalva, R. (2021). *Thermal Analysis and Experiment Design for Seismic Performance Evaluation of Ice and Water Contaminated Friction Pendulum Bearings*. M.S. Thesis, University of Nevada Reno.

Hwang, J.S., Chang, K.C. and Lee, G.C. (1990) Quasi-static and dynamic characteristics of PTFE-stainless interfaces. Journal of Structural Engineering 116(10), 2747–2762.

Jia, J., Chen, J., Zhou, H., Hu, L., & Chen, L. (2005). Comparative investigation on the wear and transfer behaviors of carbon fiber reinforced polymer composites under dry sliding and water lubrication. *Composites Science and Technology, 65*(7-8), 1139-1147.

Jordan, I. J., & Timco, G. W. (1988). Dynamics of the Ice-Crushing Process. *Journal of Glaciology, 34*(118), 318-326. doi:10.3189/s0022143000007085.

Kauschke, W. and Baigent, M. (1986), "Improvements in the Long Term Durability of Bearings in Bridges, Especially of PTFE Slide Bearings", *Proc. 2nd World Congress on Joint Sealing and Bearing Systems for Concrete Structures*, American Concrete Institute, Detroit, Michigan, Publication SP-94, Vol. 2, 577-612.

Kietzig, A., Hatzikiriakos, S. G., & Englezos, P. (2010). Physics of ice friction. *Journal of Applied Physics, 107*(8), 081101. doi:10.1063/1.3340792.

Long, J. E. (1969), "The Performance of PTFE in Bridge Bearings", Civil Engineering and Public Works Review, UK, May, 459-462.

Long, J. E. (1974), *Bearings in Structural Engineering*, J. Wiley & Sons, New York.

Makkonen, L. (2012). Ice Adhesion —Theory, Measurements and Countermeasures. *Journal of Adhesion Science and Technology, 26*(4-5), 413-445. doi:10.1163/016942411x574583.

Makkonen, L., & Tikanmäki, M. (2014). Modeling the friction of ice. *Cold Regions Science and Technology, 102*, 84-93. doi:10.1016/j.coldregions.2014.03.002.

Marmo, B. A., Blackford, J. R., & Jeffree, C. E. (2005). Ice friction, wear features and their dependence on sliding velocity and temperature. *Journal of Glaciology, 51*(174), 391-398. doi:10.3189/172756505781829304.

Morgan, T. A., & Mahin, S. A. (2011). *The use of base isolation systems to achieve complex seismic performance objectives*. Pacific Earthquake Engineering Research Center.

McVitty, W. J., & Constantinou M. C (2015). "Property modification factors for seismic isolators: Design guidance for buildings" MCEER Report 15-0005.

Mens, J., & Gee, A. D. (1991). Friction and wear behaviour of 18 polymers in contact with steel in environments of air and water. *Wear, 149*(1-2), 255-268.

Mokha, A., Constantinou, M. C. and Reinhorn, A. M. (1988), "Teflon Bearings in Aseismic Base Isolation: Experimental Studies and Mathematical Modeling", Report NCEER-88-0038, National Center for Earthquake Engineering Research, Buffalo, NY.

Mokha, A. S., Constantinou, M. C. and Reinhorn, A. M. (1990), "Experimental Study and Analytical Prediction of Earthquake Response of a Sliding Isolation System with a Spherical Surface", Report NCEER-90-0020, National Center for Earthquake Engineering Research, Buffalo, NY.

Mosqueda, G., Whittaker, A. S., Fenves, G. L., & Mahin, S. A. (2004). Experimental and analytical studies of the friction pendulum system for the seismic protection of simple bridges. *EERC 2004*, *1*.

Petrenko, V. F., & Whitworth, R. W. (1999). Adhesion and Friction. In *Physics of ice* (pp. 314-318). Oxford: Oxford University Press.

Raraty, L. E., & Tabor, D. (1958). The adhesion and strength properties of ice. Proceedings of the Royal Society of London. Series A, Mathematical and Physical Sciences, Vol. 245, No. 1241, pp 184-201. doi:10.1016/0043-1648(59)90092-4.

Sukhorukov, S., & Marchenko, A. (2014). Geometrical stick–slip between ice and steel. *Cold Regions Science and Technology, 100*, 8-19. doi:10.1016/j.coldregions.2013.12.007.

Tappan Zee Constructors (2017). FPT Bearing QC Inspection Report: Proof Testing of Affected Bearings.

Taylor, M. E. (1972), "PTFE in Highway Bridge Bearings", Report LR 491, Transport and Road Research Laboratory, Department of the Environment, UK.

Tsopelas, P., Constantinou, M. C., Kim, Y-S. and Okamoto, S. (1996), “Experimental Study of FPS System in Bridge Seismic Isolation”, *Earthquake Engineering and Structural Dynamics*, Vol. 25, 65-78.

Velkavrh, I., Lungevičs, J., Jansons, E., Klien, S., Voyer, J., & Ausserer, F. (2019). The Influence of Isotropic Surface Roughness of Steel Sliders on Ice Friction Under Different Testing Conditions. *Lubricants, 7*(12), 106. doi:10.3390/lubricants7120106.

Wang, J., Yan, F., & Xue, Q. (2009). Tribological behavior of PTFE sliding against steel in sea water. *Wear, 267*(9-10), 1634-1641.

WSDOT Bridge and Structures (2015). SR522 Seismic Isolation Bearings.

Zayas, V. (2021). Personal Communication.

Zayas, V., Low, S. S., and Mahin, S. A. (1987). "The FPS earthquake resisting system, experimental report." Report No. UCB/EERC-87/01, Earthquake Engineering Research Center, Univ. of California, Berkeley, Calif., June.

Zhao, G., Ma, Y., Li, Y., Su, L., & Zhou, F. (2019). An Experimental Study on the Behavior Deterioration Trend of Friction Pendulum Bearings with Corrosion Time for Offshore Isolated Bridges. *IOP Conference Series: Earth and Environmental Science*, 304, 042025.

APPENDIX A: LITERATURE REVIEW

A-1 Prior Documented Influences on Friction in Spherical Sliding Bearings

A thorough study on variables that affect friction, and how these variables influence the behavior of spherical sliding bearings, was conducted by Constantinou et al (2007). The most relevant findings regarding frictional behavior of spherical sliding bearings are summarized below. Note that the materials used in EPS friction pendulum bearings are proprietary, and the findings of published works may not exactly represent current EPS bearings.

Friction is defined as the resistance to movement of one body relative to another. For a sliding bearing, the friction force is directly proportional to the normal force *N*:

$$F = \mu N \qquad \textbf{(Eq. A.1)}$$

where μ is the friction coefficient. There are four main sources of friction in sliding bearings: adhesion, plowing, third body effects and viscoelastic effects. Adhesion refers to an atomic bond between two solids materials when they come into contact. The regions of contact between the surfaces are referred to as junctions, and friction by adhesion is the product of the real contact area and the shear strength of the junctions. When surfaces come into contact, their asperities are subjected to elastic and plastic deformation. The plowing component of friction is the energy dissipated by plastic deformation. Third body effects are generated when the slider contacts other particles that contribute to the friction in the sliding interface. Third body effects play an important role when the bearing is contaminated with debris and other particles, as will be discussed in more detail later. When a hard material slides over a viscoelastic material (e.g. stainless steel (SS) sliding over polytetrafluoroethylene (PTFE)), energy is dissipated through deformation of the viscoelastic material, contributing another component to friction.

The coefficient of friction depends on the materials of the slider and its sliding surface. The most common interface for spherical sliding bearings is PTFE – polished SS. Some bimetallic interfaces have been used in the past as well, such as SS – bronze, steel – steel and bronze – bronze. This report focuses on PTFE – polished SS interfaces. There are several types of PTFE materials and composites. Unfilled PTFE refers to virgin or pure PTFE, without any other material or component added. Filled PTFE refers to PTFE mixed or filled with some other material (e.g. glass or carbon). Another form of PTFE used in FPS bearings is woven PTFE, which is made from unfilled PTFE threads woven into a fabric in a manner similar to weaving other synthetic materials into fabric.

A-1.1 Lubrication Effects

Lubrication reduces the coefficient of friction. Spherical sliding bearings are generally lubricated by grease stored in dimples under hydrostatic pressure. Lubricated bearings have the same response as nonlubricated bearings at the beginning of movement. After some movement, the coefficient of friction drops due to the spread of the lubricant from the dimples along the sliding surface (Constantinou et al., 2007).

Like unlubricated bearings, the friction in lubricated bearings is velocity dependent. The sliding coefficient of friction for an unfilled and unlubricated PTFE sliding surface is about 1.7 times higher than for a lubricated PTFE sliding surface. Dolce et al. (2005) reported that velocity has little effect on the coefficient of friction for lubricated bearings.

Generally, as temperature decreases, the coefficient of friction increases. This low temperature effect is more notable in lubricated bearings because the friction is lower on lubricated surfaces, leading to less frictional heating. With less frictional heating, the temperature on the sliding surfaces of lubricated bearings will be lower than on unlubricated bearings.

A-1.2 Friction Dependence on Sliding Velocity

Two types of friction are generated in sliding bearings: static or breakaway friction and sliding friction. The breakaway friction is the force that needs to be overcome to start movement, while the sliding friction is the friction generated during motion, which is velocity dependent. After movement starts, the friction coefficient generally drops to a value of f_{min}; then, as velocity increases, friction increases up to a value of f_{max} (Figure A.1).

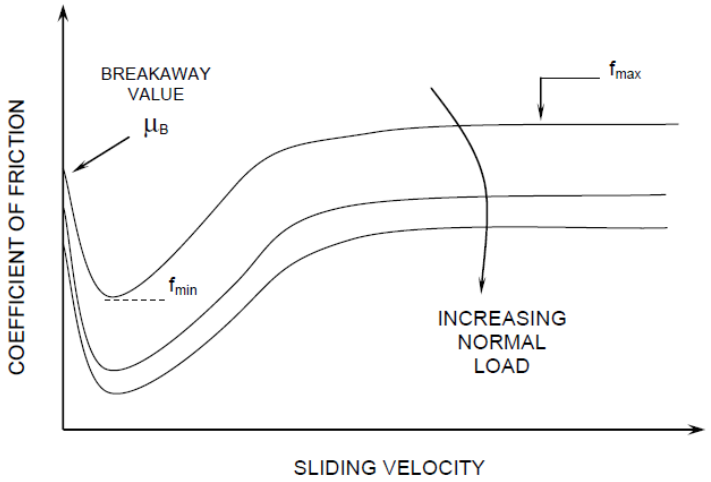

Figure A.1. Coefficient of friction dependence on sliding velocity (Constantinou et al., 2007)

Mokha et al (1988, 1990) and Constantinou et al. (1990) reported the ratio of breakaway friction μ_B to f_{min} in spherical sliding bearings to be in the range of 1.3 to 1.4 for PTFE–polished SS surfaces. Tests from Campbell et al (1991) on PTFE–polished SS surfaces showed μ_B/f_{min} to range from 2.0 to 7.0. Mokha et al. (1990) and Campbell et al. (1991) also reported that for woven PTFE, μ_B/f_{min} ranged from 2.0 and 3.0. In general, μ_B/f_{min} is of the order of 1.20 for the filled PTFE used in FPS bearings with PTFE–polished SS surfaces. According to tests from Constantinou et al. (1993) and Tsopelas et al. (1996), the sliding friction at large velocities f_{max} is higher than the breakaway friction μ_B.

Mokha et al. (1988) and Constantinou et al. (1990) developed the following equation to describe the dependence of the coefficient of friction on sliding velocity V, for a constant value of apparent pressure:

$$\mu = f_{max} - (f_{max} - f_{min})e^{-aV} \qquad \textbf{(Eq. A.2)}$$

where a ranges from 20 to 30 s/m for unfilled PTFE and is about 100 s/m or larger for filled PTFE. According to (Eq. A.2, the friction coefficient μ ranges from f_{min} at zero velocity to f_{max} at peak velocity, which means it does not represent the initial effect of the breakaway friction. The transition between f_{max} and f_{min} is determined by the coefficient a. For a lower value of a, a higher velocity is needed to reach an asymptotic behavior tending to f_{max}. The minimum $a = 20$ s/m implies that the friction coefficient μ tends to its maximum f_{max} for sliding velocities no larger than 150 mm/s (Eq A.2). The increase in sliding friction f_{max} above f_{min} depends on the sliding velocity, but is normally, for seismic applications, about 5 or 6 times f_{min} (Constantinou et al. 2007).

A-1.3 Effect of apparent pressure

From adhesion theory, Constantinou et al. (2007) deduced the following equation relating friction coefficient to pressure, for a PTFE sliding surface:

$$\mu = \frac{s_0}{p_r} + \alpha \qquad \textbf{(Eq. A.3)}$$

where s_0 is the minimum shear strength at the interface, p_r is the pressure in the real area of contact and α is a constant that relates shear strength with pressure. In (Eq. A.**3**, friction is assumed to be proportional to shear strength and inversely proportional to pressure. The real area of contact is assumed to be approximately the same as apparent or gross area (A_o) of contact due to plastic deformation of the surface that is produced by a high normal load, as expected in bridge bearings. Noting that p_r is the ratio between normal load N and A_o, if α is very small compared to $\frac{s_0}{p_r}$ in (Eq. A.**3**, the relationship between $1/\mu$ and N/A_o is linear for a fixed area of contact. Hwang et al. (1990) was the first to observe the linear relationship between $1/\mu$ and N/A_o based on data from Taylor (1972) and Long (1974). Figure A.2 shows the inverse linear relation between sliding coefficient of friction μ and apparent pressure N/A_o as recorded from different authors.

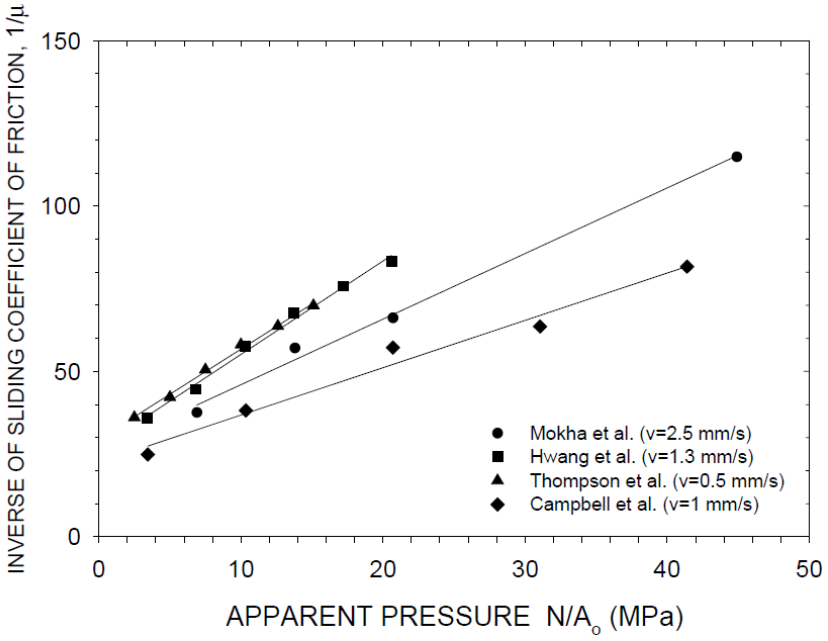

Figure A.2. **Coefficient of friction dependence on apparent pressure (Constantinou et al., 2007)**

A-1.4 Effects of Temperature

Temperature greatly influences breakaway friction and coefficients of friction at very low velocities, but due to frictional heating, has a much smaller effect on sliding friction at high velocities (Campbell et al. 1991). Constantinou et al. (1999) conducted tests on spherical sliding bearings with unfilled and filled PTFE sliding interfaces, at temperatures ranging from -40°C to 50°C. Each specimen was subjected to a continuous normal load of 147 kN for 311 hours before testing. To perform the cold temperature tests, the bearing in its test rig was surrounded by an insulating box. Before testing, the box was filled with dry ice, and chilled for

five hours until the bearing reached a stable temperature of -42°C. To measure temperature, thermocouples were embedded in the stainless steel plate. After the stable temperature was reached, the insulating box was removed and the test was performed. At the end of the test, the temperature was -32°C, so the bearing was chilled down to -39°C and another test was conducted. This procedure was repeated 9 times, with the same temperature and conditions. To test at high temperatures, heating elements were installed around the test rig. For all tests, the bearing was not contaminated and was in dry conditions, with relative humidity of the environment reported to be about 20%. For high velocities, the values of sliding friction coefficient increased by 60% as temperature decreased from 50°C to 40°C. On the other hand, the sliding friction coefficient at low velocities increased by about 400 to 500% with decreasing temperature, within the same temperature bounds. Figure A.3 illustrates the effect of temperature for low and high velocities (Constantinou et al. 1999).

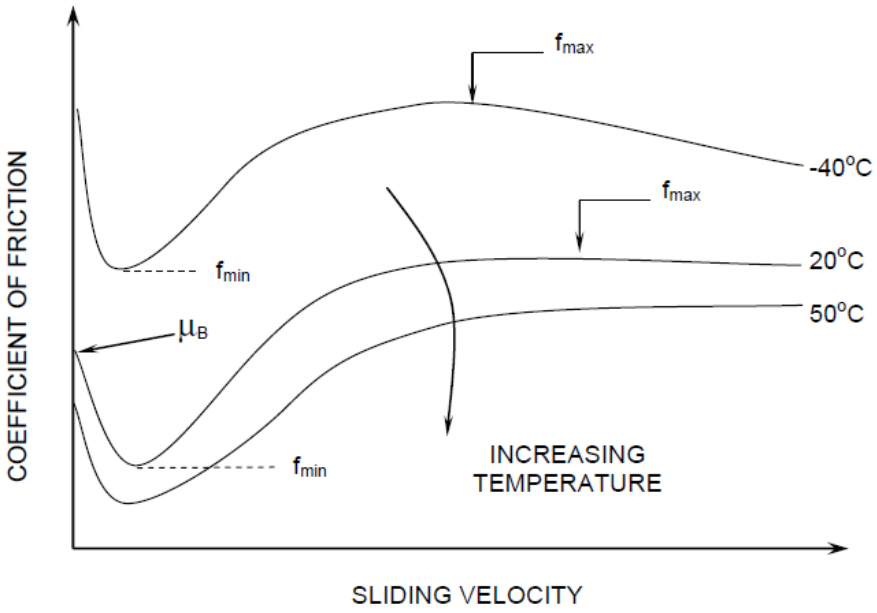

Figure A.3. Effect of temperature on frictional properties of PTFE–polished SS interfaces (Constantinou et al., 2007)

For an unfilled PTFE-SS interface, f_{max} varied from 0.113 to 0.118 at 22°C, and increased to 0.178 to 0.189 at -39°C (Constantinou et al. 1999). The same test was also conducted for a bearing with a filled PTFE - SS interface. The tests on unfilled PTFE were conducted in the months of January and February while tests on filled PTFE were conducted in April and May, with a relative humidity in the lab of 20% and between 25 and 40%, respectively. By comparison, the effect of temperature is even more notable for filled PTFE than unfilled PTFE, because the heat flux in filled PTFE is greater than the heat flux in unfilled PTFE. The heat flux was concluded to be greater in filled PTFE because the temperature measured in the thermocouples was lower, suggesting that most of the heat went to the filled PTFE and not into the steel plate. Constantinou et al. (1999) mentions that the increased heat flux observed in filled PTFE may be due to the minimal thickness of the filled PTFE (0.25 mm).

A-1.5 Debris Contamination

Contamination of the bearing with debris, for example, increases friction due to third body effects and corrosion of the SS surface. Contamination may affect the friction considerably. The effect of contamination is greater in lubricated than unlubricated bearings since contamination interferes with the spread of the lubricant. According to Constantinou et al (2007), contamination is very unlikely when bearings are delivered to the site pre-assembled. However, evidence suggests otherwise, as water contamination of FPS bearings has been reported in several bridges across the country. For instance,

Washington Department of Transportation reported that 14 of 29 bearings from Snohomish River Bridge had significant water contamination; as a result some of these bearings showed corrosion byproducts (WSDOT, 2015). In New York's Tappan Zee Bridge, 64 of the bearings (13%) exhibited some level of water intrusion within the environmental seals after erection and subjected to construction loading (Tappan Zee Constructors, 2017). The likely impacts of contamination, corrosion and surface roughness, are described next.

A-1.6 Corrosion and Surface Roughness

Corrosion of stainless steel in an atmospheric environment is possible, and appears as a form of white stains over the surface. This corrosion can be associated with increased surface roughness, which can increase the resistance to sliding and thus increase the effective friction coefficient. Constantinou et al. (2007) reported an experiment that imposed control of the surface roughness in bearings with PTFE-SS sliding interface, with SS having surface roughness of 0.03, 0.30 and 0.50 μm. A surface roughness of 0.03 μm corresponds to that of a commercially polished to mirror finished SS sheet, while surface roughness of 0.30 μm corresponds to that of an as-rolled SS sheet. For the surface roughness of 0.50 μm, Constantinou et al. (2007) used a wire brush to uniformly roughen an as-rolled SS sheet. The results showed a substantial increase in the coefficient of friction, approximately 100%, due to surface roughness at low velocities of sliding. This friction increase was probably due to plowing of the PTFE by the rough stainless steel and third body effects from wear particles. On the other hand, surface roughness was found to have less effect on the coefficient of friction at high sliding velocities, wherein the friction coefficient increased by approximately 15%. Unfilled PTFE was almost unaffected by surface roughness at high sliding velocities, with an increase in friction coefficient of about 3%.

With regard to the natural development of corrosion in bearings, Constantinou et al. (2007) observed corrosion of the stainless steel in a test bearing that had been tested extensively over 9 years, and was stored indoors disassembled some of the time. The bearing showed rust stains that covered about 15% of the stainless steel surface. The rust surface measured a surface roughness of 0.3 μm and the rest of the surface (clean surface) measured a surface roughness of 0.03 μm. From this data, Constantinou et al. (2007) concluded, conservatively, that surface roughness values of 0.30 and 0.50 μm would develop after 30 years of exposure in industrial/urban and industrial/chemical environment, respectively. Based on the data and assumptions presented in this section, Constantinou et al. (2007) suggest that friction coefficients for high velocity sliding be amplified by factors shown in Table A.1 to account for surface roughness. These factors are proposed to account for the corrosion in the bearing produced by exposure to different environments after 30 years.

Table A.1. Factors of amplification for high velocity sliding coefficient of friction (Constantinou et al, 2007)

	Installation Method of Stainless Steel Plate in Sliding Bearing		
Environment	**Sealed Facing Down**	**Sealed Facing Up**	**Unsealed Facing Down**
Rural	1.10	1.20	1.20
Industrial/Urban	1.20	1.30	1.30
Marine	1.30	1.40	1.40
Industrial/Chemical	1.40	>1.40	>1.40

Reports of corrosion effects due to freshwater contamination have not been identified; however, Zhao et al. (2019) performed tests to identify effects of corrosion for a spherical sliding bearing in a marine environment. Two test arrangements were used; the first test arrangement consisted of bearing specimens

periodically sprayed with salt, while for the second test arrangement, the bearing specimens were submerged in saline water and allowed to dry up. The results for the second test arrangement are shown in Figure A.4. The observed wave-like behavior is a result of the salinity forming a smoother layer on top of the sliding surface that is disrupted by the next wet-drying cycle. The coefficient of friction decreases when the smooth layer is formed and increases as the salt layer is disrupted and the roughness increases (Zhao et al., 2019). Overall, the tendency is that coefficient of friction increases with corrosion associated with saltwater intrusion, due to an increase in surface roughness relative to the initial roughness. Freshwater intrusion is expected to influence the friction less significantly, as a salt layer would not form.

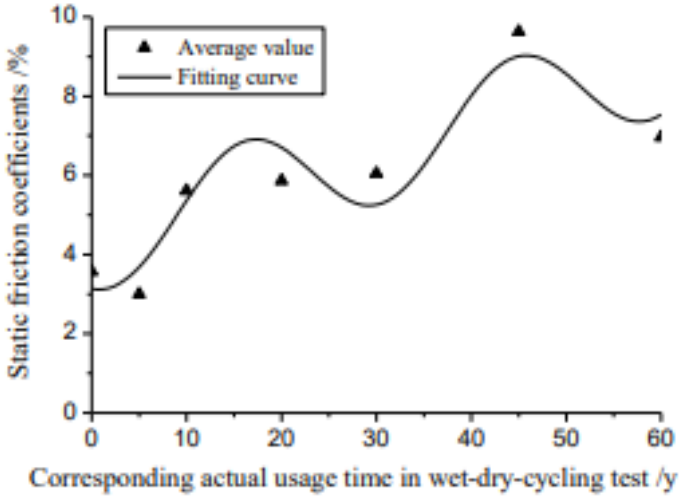

Figure A.4. Effect of temperature on frictional properties of PTFE–polished SS interfaces (Constantinou et al., 2007)

A-1.7 Load Dwell

Load dwell refers to the duration of stationary static loading without any relative movement across the sliding interface. For an interface with bimetallic surfaces (e.g. steel-steel), load dwell or time of loading can cause the static friction to increase. For a PTFE-SS interface, the effect of load dwell is not significant. Experiments on PTFE–polished SS surfaces showed that for load dwell between 0.2 and 118.4 hours the static friction is unaffected (Constantinou et al. 2007).

A-1.8 Effects of Travel

The accumulated distance of relative movement between the bearing slider and sliding surfaces is defined as travel. Constantinou et al. (2007) estimated the cumulative movement of a typical bridge bearing due to traffic loads to be in the order of 5 km, with the following assumptions: steel girder bridge, average speed of traffic of 60 km/h, span length of 100 feet, 30 years of service and 10 crossings per hour.

Kauschke and Baigent (1986) presented travel test results on unlubricated bearings with PTFE-polished SS sliding interface. The results showed that the coefficient of friction increased a little for a travel of 2 km. In contrast, in cumulative movement tests conducted by Long (1969, 1974) on the same sliding interfaces, a small decrease in sliding coefficient of friction was observed for a travel of 5 km. Despite the different trend, the change of the coefficient of friction for travel range of 2 to 5 km was small. According to Eggert and Kauschke (2002), after a travel of about 10 km the coefficient of friction increased due to contamination and loss of lubrication, which led to an increase in the coefficient of friction at low

temperatures. The tests were conducted at a temperature range of -35 to 20°C. Greater temperature sensitivity could be manifested in low temperature testing of bearings removed from service relative to new bearings.

A-2 Influence of Water Contamination on Friction Properties

The response of spherical sliding bearings during a seismic event depends greatly on their frictional properties. In the previous section, the different parameters that affect the friction coefficient of spherical sliding bearings were discussed. However, there is little documented data, if any, that shows how water contamination affects the frictional properties of spherical sliding bearings. The influence of water contamination on the breakaway and sliding friction coefficients between different materials is of great interest, especially PTFE in contact with SS, since this is the most common condition for the sliding interface of FPS bearings.

A-2.1. Effect of Water Lubrication on Sliding Friction

Several authors have performed tests to determine the friction coefficient of water-lubricated polymers in contact with steel (Mens and Gee 1991, Wang et al. 2009 and Jia et al. 2005). These studies examined the friction coefficients of PTFE and other polymers in contact with steel using the test arrangement shown in Figure A.5. In this setup, a specimen with dimensions a x b x c is loaded using pressurized air while the rotating ring rotates at a constant velocity, generating friction between the specimen and the ring. To accommodate for the difference in shape between the ring and the specimen, the ring is rotated until the specimen takes the shape of the ring. Table A.2 summarizes the various test parameters considered by the authors mentioned above.

Table A.2. Test parameters for ring tribometer test

Author(s)	Rotating Ring		Polymer	Test Dimensions (mm)					Axial Load (N)	Velocity (m/s)
	Material	Roughness (µm)	Material	a	b	c	d	e		
Mens and Gee (1991)	N/St	0.10	PA 66 + PTFE	10	10	10	N/S	N/S	500	0.25
Mens and Gee (1991)	N/St	0.10	POM + PTFE	10	10	10	N/S	N/S	500	0.25
Mens and Gee (1991)	N/St	0.10	PETP + PTFE	10	10	10	N/S	N/S	500	0.25
Mens and Gee (1991)	N/St	0.10	PEEK + PTFE	10	10	10	N/S	N/S	500	0.25
Mens and Gee (1991)	N/St	0.10	PPS + PTFE	10	10	10	N/S	N/S	500	0.25
Mens and Gee (1991)	N/St	0.10	PEI + PTFE	10	10	10	N/S	N/S	500	0.25
Wang et al. (2009)	AISI 52100	0.15	PTFE	19	12	12	49.22	43.45	100	0.50
Jia et al. (2005)	SS	0.10	PTFE + CF	30	7	6	40.00	28.00	200	0.43
*N/S = Not specified **N/St = Not specified steel type										

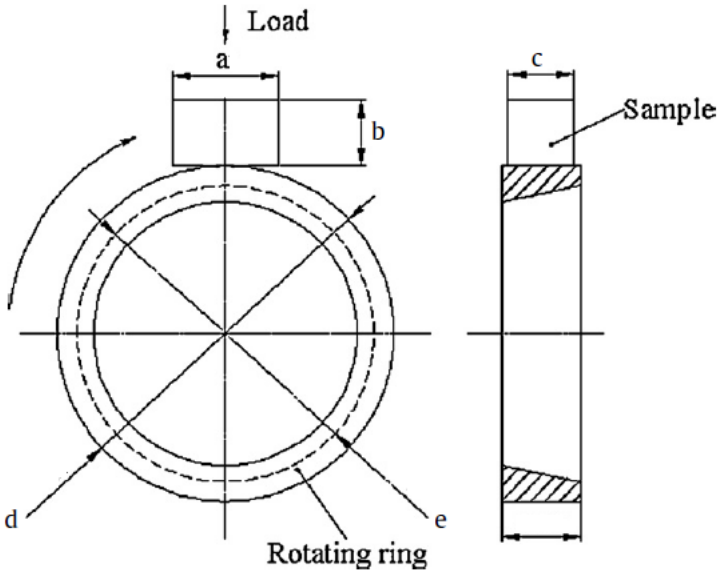

Figure A.5. Rotating ring tribometer (Wang et al., 2009)

Mens and Gee (1991) conducted tests on the following polymers reinforced with PTFE: polyamide 66 (PA 66), polyoxymethylene (POM), polyethyleneterephthalate (PETP), polyetheretherketone (PEEK), polyphenylenesulphide (PPS) and polyetherimide (PEI). Among the polymers tested, POM is frequently used in applications with relative sliding between parts and has properties very similar to PTFE. The tests were performed and sliding friction was measured in dry and wet conditions. Table A.3 tabulates the friction coefficients that were observed when thermal equilibrium was reached, which occurred after 0.5 hours of testing for all the specimens. The coefficient of friction was lower in wet conditions, but more variability was experienced than for dry conditions. For instance, for POM – PTFE composite, sample friction coefficients of 0.21 and 0.22 were observed during dry tests, while corresponding coefficients of 0.15 and 0.20 were observed during wet tests.

Table A.3. Coefficient of friction at thermal equilibrium for dry and wet conditions. **(Mens and Gee, 1991)**

Material	Dry friction coefficient	Wet friction coefficient
PA 66 - PTFE	0.13 0.14	0.19 0.08
POM - PTFE	0.22 0.21	0.15 0.20
PETP - PTFE	0.16 0.13	0.10 0.12
PEEK - PTFE	0.19 0.17	0.10 0.08
PPS - PTFE	0.31 0.29	0.10 0.09
PEI - PTFE	0.22 0.21	0.16 0.15

Wang et al. (2009) explored the variation in water contaminated friction of PTFE on steel imposed by freshwater versus saltwater conditions. The test variations included dry conditions (Air), distilled water lubrication (Distilled), sea water lubrication (Sea), and three additional solutions (S1, S2 and S3) that account for the variation in sea water composition. The Distilled condition is considered of greatest interest for this

study. Tests results showed that coefficient of friction is about 3 times smaller in Distilled (0.05) compared to Air (0.17), and is essentially invariant with time for a sliding time less than 5 minutes (Figure A.6).

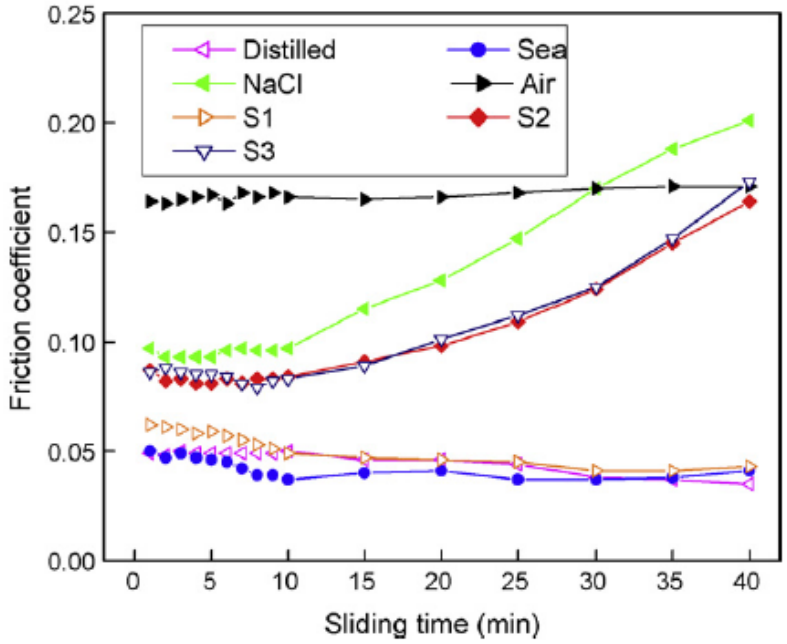

Figure A.6. Variation of friction coefficient with sliding time (Wang et al., 2009)

Jia et al. (2005) conducted tests on 4 different composites sliding on stainless steel, in wet and dry conditions. These composites were: PTFE reinforced by 15% carbon fiber (CF), Polyimide (PI) reinforced by 15% CF and 5% PTFE, PI reinforced by 15% CF and 5% MoS_2, PEEK reinforced by 15% CF and 5% PTFE. Wet friction was observed to be 3 times smaller than dry friction for PTFE, which agrees with Wang et al. (2009). It was also observed that wet friction was about 60% of dry friction comparable to results obtained by Mens et al. (1991). Table A.4 summarizes the results.

Table A.4. Coefficient of friction for dry and wet conditions. (Jia et al., 2005)

Material	Dry friction coefficient	Wet friction coefficient
PTFE + 15% CF	0.20	0.07
PI + 15% CF + 5% PTFE	0.16	0.12
PI + 15% CF + 5% MoS_2	0.18	0.10
PEEK + 15% CF + 5% PTFE	0.15	0.09

A different test arrangement to assess wet friction was used by Golchin et al. (2013). The test setup consisted of a stationary polymer pin in contact with a SS rotating disc submerged in distilled water, as shown in Figure A.7. An axial load was applied to the pin using dead weights. Polymers tested were: ultra high molecular weight polyethylene (UHMWPE), POM, polyethylene therephthalate (PET), polyamide 6 (PA6), PA66, PTFE, polypropylene (PP), polyvinylidene fluoride (PVDF), PEEK, polycarbonate (PC) and polymethyl methacrylate (PMMA). The test parameters are summarized in Table A.5.

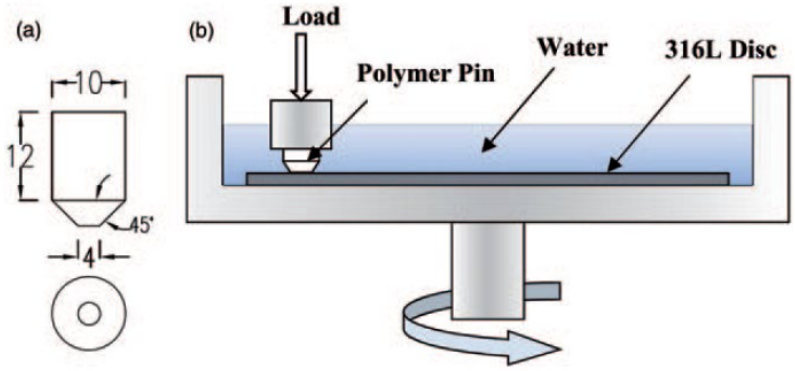

Figure A.7. Schematic diagram of (a) pin and (b) test configuration (Golchin et al., 2013)

Table A.5. Test parameters. (Golchin et al., 2013)

Load	62.8 N
Sliding velocity	0.13 m/s
Test duration	20 h
Steel surface roughness	0.2 μm

The results by Golchin et al. (2013) are shown in Figure A.8. The objective of the research was to compare friction of different polymers with water lubrication, hence only water lubrication or wet friction tests were conducted. The plot in Figure A.8 shows that coefficient of friction for PTFE was about 0.07, constant almost along all the duration of the test, which is in agreement with results by Jia et al. (2005) and is about half the wet friction coefficient obtained by Wang et al. (2009). The difference in friction coefficients produced by different test can be attributed to the different test arrangements, and to the fact that Jia et al. (2005) tested filled PTFE while Golchin et al. (2013) tested unfilled PTFE.

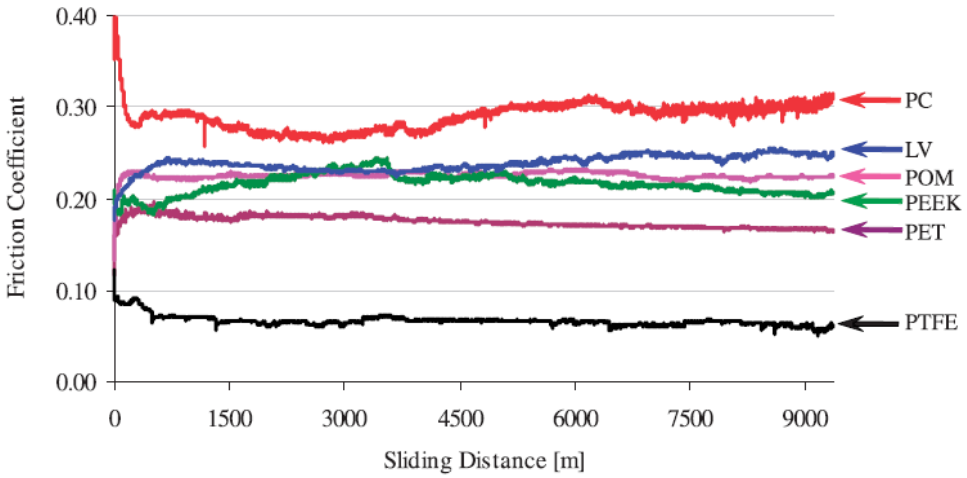

Figure A.8. Coefficient of friction for water lubrication on different polymers (Golchin et al., 2013)

A-2.2. Effect of Water Lubrication on Breakaway Friction

Fewer tests have been conducted to document breakaway friction of water lubricated PTFE in contact with SS in comparison to sliding friction. However, Benabdallah (2007) conducted tests on POM-based polymers designated as DE20076, DE100KM and DE12017; and Nylon-66 designated ZY103HSL, sliding

on a steel platform. As described in Section A-2.1, POM applications and properties are very similar to PTFE. The test setup consisted of a 95 x 12 x 3 mm polymer plate resting on top of a rotating platform, as shown in Figure A.9, with an LED transmitter on top of the plate. Stationary photodiode receivers were placed on top of the arrangement to measure the displacement of the polymer plate. The contact surface of the polymer plate was polished to get a surface roughness of 0.3 μm, and the surface roughness of the ANSI 1045 steel platform was 1.78 μm (much higher than SS in FPS bearings). A weight of 2 N was fixed on top of the polymer plate to apply an axial load.

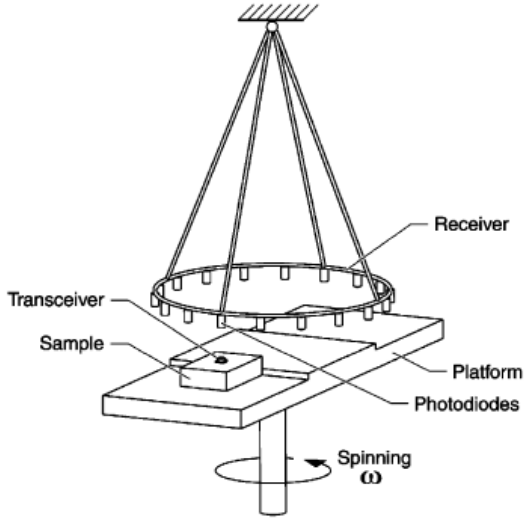

Figure A.9. Break away friction test arrangement (Benabdallah, 2007)

On average, most sliding interfaces experienced about a 60% increase in breakaway friction when lubricated with water (Figure A.10). This increase in friction was attributed to an increase in the adhesion between the polymer and the steel surface due to the formation of meniscus forces, a consequence of the presence of water. No correlation is observed with friction coefficients measured by Golchin et al. (2017) when the distance is 0 (Figure A.8), nor with Wang et al. (2009) when the time is 0 (Figure A.6). However, test set ups used by Golchin et al. (2017) and Wang et al. (2009) were designed to measure sliding friction, which may be the reason for the discrepancy.

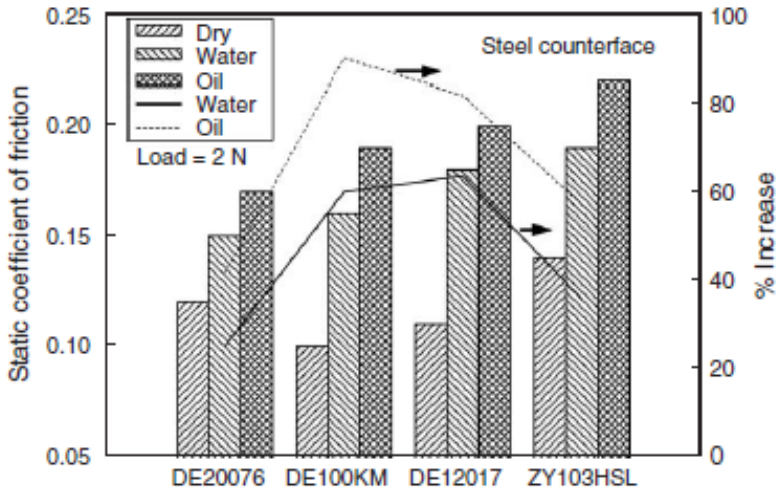

Figure A.10. Effects of lubrication on breakaway friction coefficient (Benabdallah, 2007)

In summary, sliding coefficient of friction decreases with water lubrication. Results shown in Section A-2.1 suggest that there is more variability in wet friction than in dry friction and that the reduction in coefficient of friction depends on the type of PTFE (e.g. unfilled PTFE, PTFE filled with carbon). Only one author studied breakaway friction in a way relatable to this study, and in that study breakaway friction increased with water lubrication.

A-3 Influence of Frozen Water on Frictional Properties

So far, discussion has focused on how water contamination may affect frictional properties of different sliding surfaces. However, at low temperatures, water inside the bearings will freeze, causing a problem of a different nature. For the slider to move or slide along the concave plate of a bearing contaminated with frozen water, the slider will have to either break the bond between the concave plate and the ice or break the ice itself. The first type of failure is denoted adhesive failure while the latter is known as cohesive failure of the ice. From here on, the material of the concave plate or sliding surface will be referred to as "substrate". The ice failure mechanism depends on several variables such as the ice temperature, substrate and freezing process.

A-3.1. Ice Adhesive and Cohesive Strength

Adhesive strength is defined as the maximum force required to mechanically separate ice from any substrate or contact surface. Cohesive strength refers to the shear strength of the ice as a material. When the adhesive strength of the bond is greater than the cohesive strength of the ice, the ice will break before the adhesive bond breaks and a layer of ice will remain bonded to the substrate.

Only one known experiment has documented ice adhesive strength specifically in FPS bearings. In conjunction with EPS, Tappan Zee Constructors (2017) conducted tests on ice contaminated triple pendulum bearings (TPB). In-service bearings that had experienced water contamination were removed from the Tappan Zee Bridge and shipped to EPS. Two of the bearings were tested with different levels of ice, wherein freezing was induced by pumping liquid nitrogen directly into the bearing cavity. Bearing 8833-06 was tested with water levels as received (1/2" layer of ice in the lower concave sliding cavity and ¼" layer of ice in the inner slider cavity) and bearing 8833-08 was tested with water filled to the top of the rim in both the lower concave (3") and inner sliding cavities. Force vs displacement hysteresis loops for both bearings are shown in Figure A.11, and testing conditions are summarized in Table A.6. A small increase of shear force was observed at small displacements just before the ice broke. When compared with a clean bearing, shear force in the ice contaminated bearing increased by about 10%. In both cases, the authors observed that the "initial calibration of the test machine may have broken the ice". Although not ideal, cracking of ice due to the presumably low level forces associated with calibration does not suggest an inherent problem in testing, since the much higher level lateral forces should easily accomplish the same. However, as discussed later, rapid freezing can negatively affect the ice strength. In general, the report lacks sufficient detail to understand the freezing and testing protocol, and freezing by liquid nitrogen may have led to ice conditions that vary substantially from those under the natural environmental conditions in an in-service bridge. The authors also commented that "no movement was observed between the interior slider and the interior bottom concave plate." It is unclear whether this refers to the bottom most concave sliding surface or the inner sliding surface that would be expected to engage at low levels of friction. Inability to engage sliding on the bottom most concave sliding surface would not necessarily significantly impede movement in a DPB or TPB since ice most likely cannot penetrate the top most concave sliding surface. The same would not be true of an SPB.

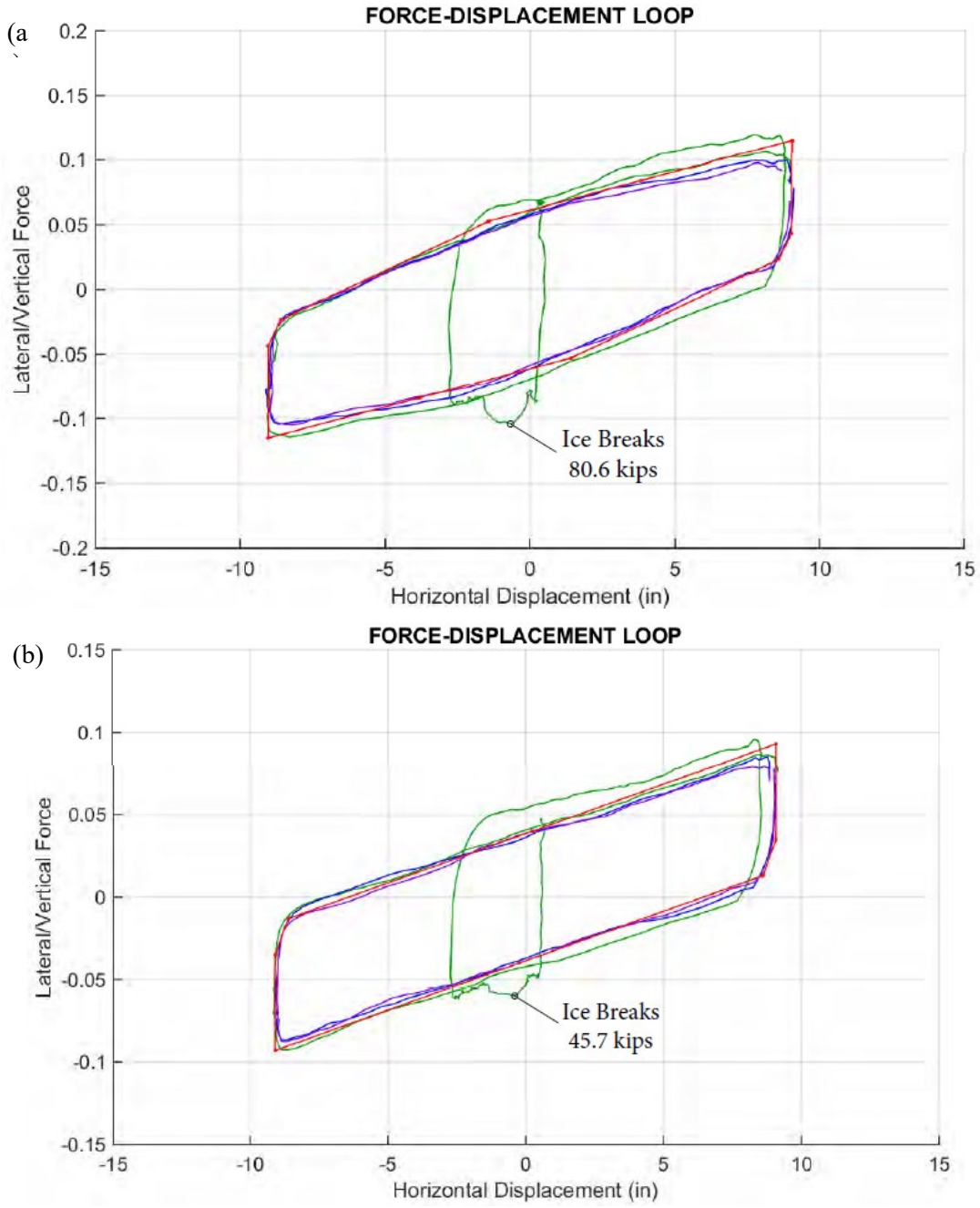

Figure A.11. Ice contaminated bearing hysteresis loop (a) Bearing 8833-08 (b) Bearing 8833-06 (Tappan Zee Constructors., 2017)

Table A.6. Ice contaminated bearings test Conditions (Tapan Zee Constructors, 2017)

Bearing	8833-08	8833-06
Target displacement	8 in	8 in
Target vertical load	700 kips	700 kips
Ice thickness	3 in	0.5 in
Number of cycles	3	3

Besides the specific data pertinent to FPS bearings mentioned above, some authors have experimentally determined ice adhesive strength, cohesive strength, or both. Varying experimental set ups and sampling methods have been applied, and varying environmental conditions and substrates have been considered. The adhesive strength of ice depends greatly on the testing method. Fortin and Perron (2012) compiled the results of tests conducted by different authors regarding ice adhesive strength (Table A.7). Much of the variability in the results of Table A.7 can be associated with the different testing methods and different substrates tested. Other factors affecting ice adhesion are ice purity, nature/texture of the substrate, and temperature. In their own experiments, Fortin and Perron (2012) found that the ice started to fail at a stress of about 0.50 MPa.

Table A.7. Ice adhesive shear strength from different authors (Fortin and Perron, 2012)

Author (s)	Ice	Method	Substrate	Adhesion shear stress (MPa)		
				Minimum	Average	Maximum
Lughborough and Haas	Frozen water	Centrifuge	Aluminum	-	1.52	-
			Copper	-	0.85	-
			Polymers	1.03	-	1.17
Laforte et al.	Rime and glaze		Aluminum	0.067	-	0.4
Itagaki	Artificial ice	Centrifuge	Aluminum	0.002	-	0.11
Jellinek	Ice from snow	Torsion	Stainless Steel	-	0.48	-
Scavuzzo et al.	Artificial ice	Centrifuge	Aluminum	0.05	-	0.30
Raraty and Tabor	Frozen water	Centrifuge	Stainless steel		1.96	
Bascom et al.	Frozen water	Centrifuge	Stainless steel		1.63	
Ford and Nichols	Frozen water	Axial loading	Stainless steel		0.24	
Stallabrass and Price	Artificial Ice	Centrifuge	Aluminum	0.03		0.13
Reich	Frozen water	Axial loading	Aluminum	0.83		0.93

Ice adhesive strength can be experimentally determined through use of a centrifuge. The centrifuge test procedure was described by Fortin et al. (2010). As a first step, samples were generated by freezing water on 340 mm x 31.75 mm x 6.4 mm beams using a Freezing Drizzle Climatic (FDC) chamber. The samples were frozen to a temperature of -8.0 ± 1.0 ºC. Prepared samples were tested on a centrifuge apparatus installed in the FDC chamber. The beam was rotated at a controlled increasing rate correlated to the centrifugal force. When the centrifugal force became sufficiently large, ice detachment was observed, and the adhesive strength was inferred. Figure A.12 shows the centrifuge apparatus.

Figure A.12. Centrifuge apparatus (Fortin et al., 2010)

Raraty and Tabor (1958) also conducted centrifuge type experiments on ice adhesion to SS using an annular interface (Figure A.13). The SS surface was polished, filled with tap water, and frozen slowly. Adhesive strength versus temperature is shown in Figure A.14, wherein the black dots and associated fitted curve represent the experiment described above. For temperatures below -7°C, ice adhesion was independent of the temperature. Raraty and Tabor (1958) concluded that the low temperature failures below -7°C represented cohesive failures.

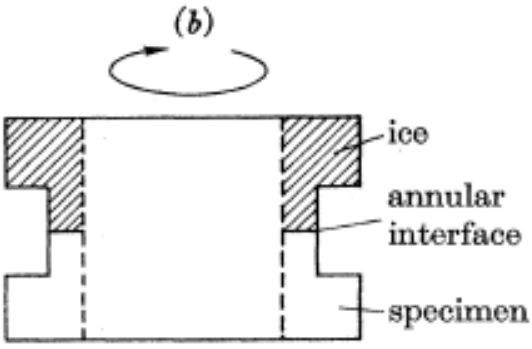

Figure A.13. Test specimen (Raraty and Tabor, 1958)

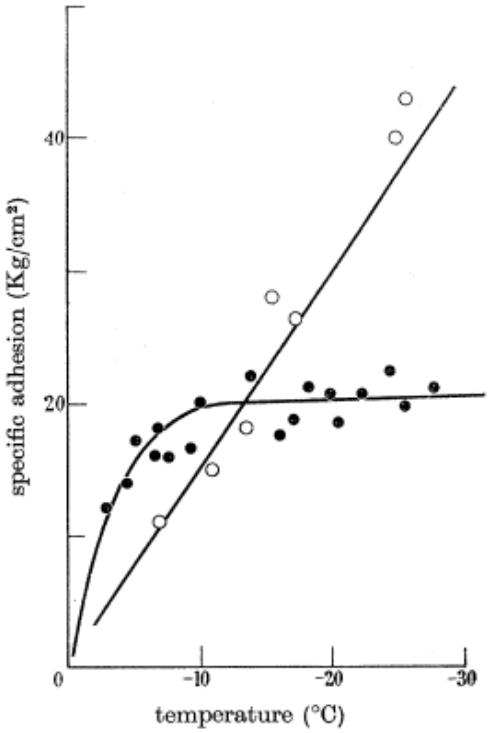

Figure A.14. Adhesive strength of ice to clean stainless steel (Raraty and Tabor, 1958)

Alternatively, Andrews and Lockington (1983) conducted tests using two different axial loading set up arrangements to determine adhesive and cohesive strength, respectively. The layout shown in Figure A.15 was used. For the adhesion tests (Figure A.15(a)), ice was formed over the height F and bonded to the substrate on zone E, and a thin PTFE disk was located on position B to create an initial crack. Axial load was applied to the specimen by pressurizing the orifice D using a pump. The test arrangement for cohesive failure (Figure A.15(b)) was the same as that for adhesive failure, with the PTFE disk located at a height "C" from the ice – SS interface, generating a cohesive type of failure along height "h". For ice on SS substrate, these experiments showed an adhesive failure for temperatures above -5 ºC and a cohesive failure for temperatures below -5 ºC, which was asymptotic and not dependent on temperature (Figure A.16).

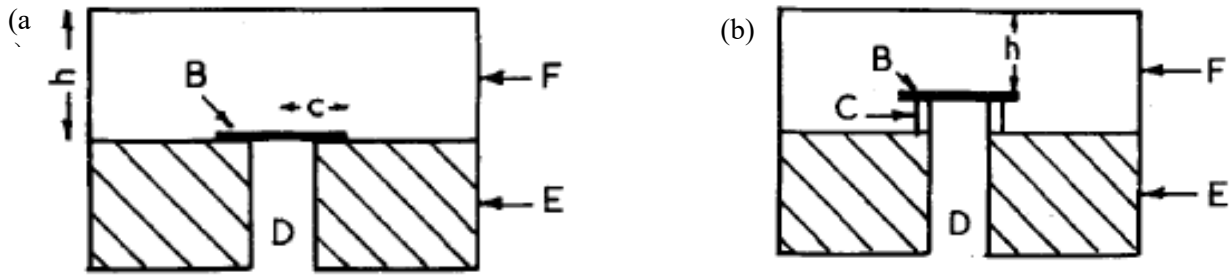

Figure A.15. (a) Adhesive test arrangement, (b) cohesive test arrangement (Andrews and Stevenson, 1978)

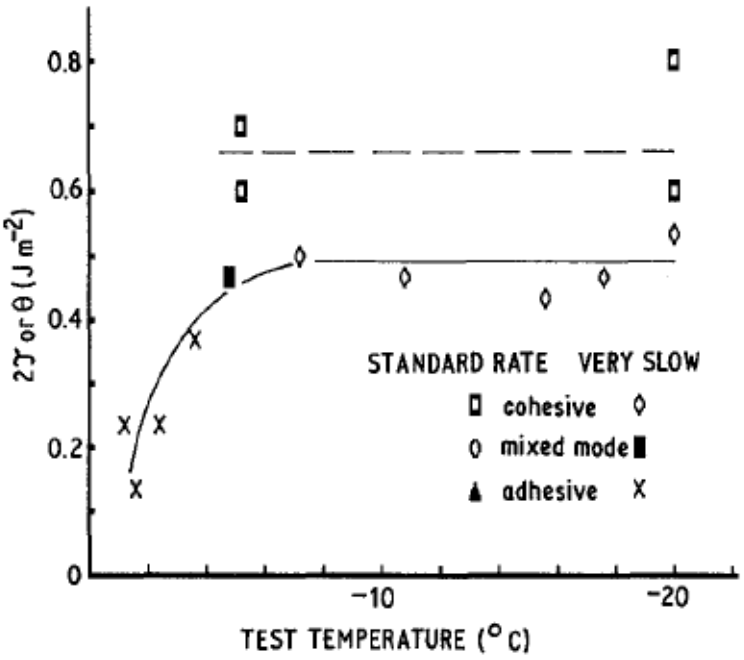

Figure A.16. Variation of failure energy with temperature for stainless steel (Andrews and Lockington, 1983)

Makkonen (2012) reported experiments conducted by VTT Technical Research Centre of Finland on ice adhesive strength using a different procedure. In these experiments, a 30 mm diameter plastic cylinder filled with water was frozen on top of a 100 mm x 100 mm x 10 mm aluminum plate coated with a substrate of interest. Each sample was placed in a freezer for at least 24 hours, and after that a horizontal load was slowly applied to the frozen cylinder. Different substrates were considered and led to different adhesive strengths, as shown in Figure A.17. The substrate considered most relevant is steel, since the sliding surface of an FPS bearing is commonly made of SS. Note that the peak adhesive strength occurs at -15°C and gets lower as temperature drops. The adhesive strength was found to vary from 0 to 1 MPa, wherein the higher values are comparable to cohesive shear strength of the ice. For cohesive type of failures, the axial loading method is expected to better represent the conditions of a bearing slider breaking through ice. However, the methodology presented by Makkonen (2012), which applied a transverse or shear loading between the ice and its substrate, is closer to the conditions of the contaminated sliding bearing in the case of an adhesive failure of ice.

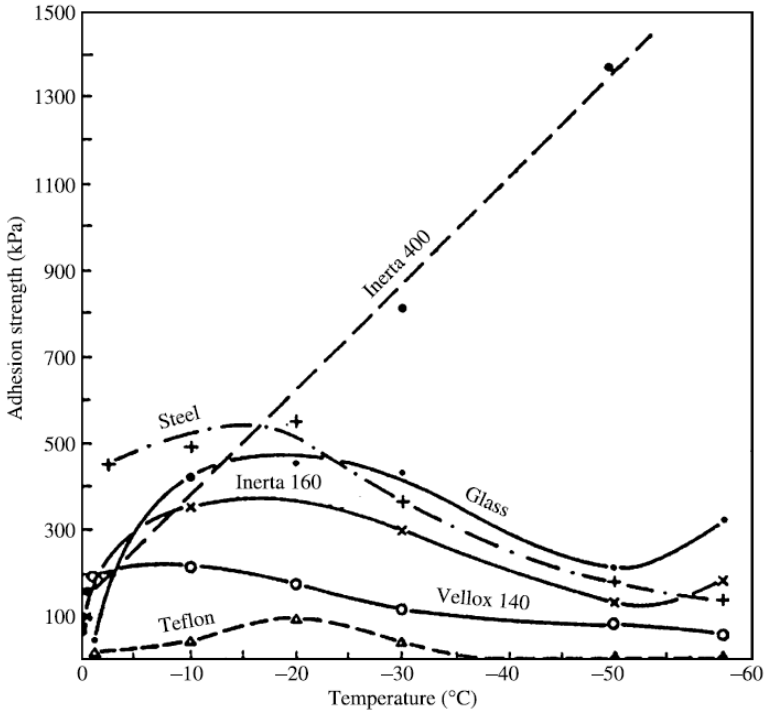

Figure A.17. Effects of temperature in ice adhesion for shear testing (Makkonen, 2012)

Several studies emphasized freezing process and freezing time in their experimental methodology. For example, in Makonnen (2012), slow freezing was applied to avoid cracking of ice due to thermal contraction while freezing and secure the strongest bond possible. Adjacent materials with different specific heat properties experience temperature change at different rates from each other, in this context generating thermal differential stresses between ice and the substrate.

Ice adhesive strength is also affected by the time the sample is kept frozen before testing. Sukhorukov et al. (2013) conducted experiments on ice adhesion using 50 mm inner diameter by 95 mm high cylinder samples. The time needed for the samples to reach thermal equilibrium is given by:

$$t = \frac{d_{cyl}^2}{\frac{k_i}{c_i p_i}} \qquad \textbf{(Eq. A.4)}$$

where d_{cyl} is the diameter of the sample, k_i is the coefficient of thermal conductivity, c_i is the specific heat capacity and p_i is the density of ice. For the specimen with d_{cyl} = 5x10^{-2}m, k_i = 2.1 W/m K, c_i = 2100 J/kg K, and p_i = 916 kg/m^3, the characteristic time was computed to be 40 min.

In the only known freezing tests of FPS bearings, the bearings were frozen rapidly using liquid nitrogen and kept frozen for an unknown length of time. As a consequence, ice may have cracked prematurely; hence, the results may not represent accurately the behavior of FPS bearings in the field (Tappan Zee Constructors, 2017).

A-3.2. Adhesive and Cohesive Strength Model

Fortin and Perron (2012) have developed a set of equations to model combined ice strength τ due to adhesion and cohesion. The equation includes both an adhesive strength term and a cohesive term:

$$\tau_{tot} = \alpha_{ice}\frac{4\gamma_{LV}}{\delta_{0-ice}}\left[f_{RMS} + \frac{\delta_{0-ice}}{k}(1 - f_{RMS})\left(1 - f_{cramp}\right)\right] + (1 - f_{RMS})f_{cramp}\tau_{coh} \quad \textbf{(Eq. A.5)}$$

$$\alpha_{ice} = \frac{\varepsilon_{water}\delta_{0-water}^2}{\varepsilon_{ice}\delta_{0-ice}^2} \quad \textbf{(Eq. A.6)}$$

where:

$\boldsymbol{\delta_{0\text{-}water}}$	=	Molecular distance between water and base substrate
$\boldsymbol{\delta_{0\text{-}ice}}$	=	Molecular distance between ice and base substrate
$\boldsymbol{\varepsilon_{water}}$	=	Relative permittivity of water
$\boldsymbol{\varepsilon_{ice}}$	=	Relative permittivity of ice
$\boldsymbol{\gamma_{LV}}$	=	Surface tension
$\boldsymbol{f_{RMS}}$	=	Fraction of ice in contact with base substrate
$\boldsymbol{k}$	=	Root mean square of roughness height
$\boldsymbol{f_{cramp}}$	=	Fraction of mechanical locking
$\boldsymbol{\tau_{coh}}$	=	Ice cohesive strength

The model idealizes the surface roughness as a regular surface with the geometry shown in Figure A.18. Since every surface has some roughness, water will fill the cavities and after freezing a fraction of ice is locked in these cavities. The model assumes that adhesive failure occurs on top of the substrate asperities (first term of (Eq. A.**5**), and cohesive strength governs the ice locked in the cavities (second term of (Eq. A.**5**).

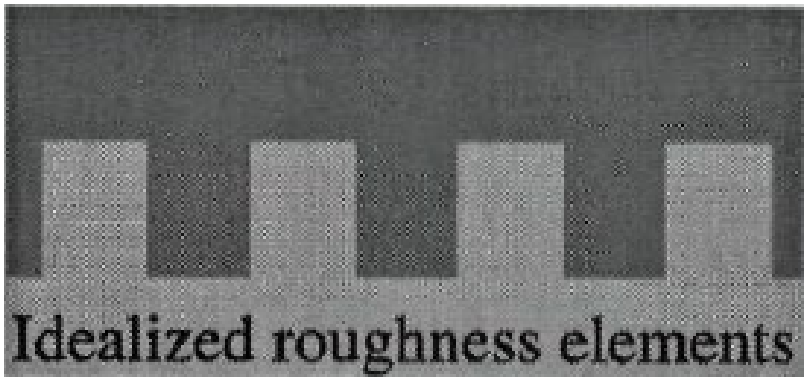

Figure A.18. Idealized surface roughness. (Fortin and Perron, 2012)

Consider an ice contaminated FPS bearing as the one shown in Figure A.19, if the slider displaces from point A to point B adhesive and cohesive strength of ice on the concave surface can be described using (Eq. A.**5**. However, in order for the slider to move, cohesive strength of ice along L1 and L2 (Figure A.19) must be overcome, hence the second term of the sum in (Eq. A.**5** needs to be modified to account for the extra cohesive strength along these lines.

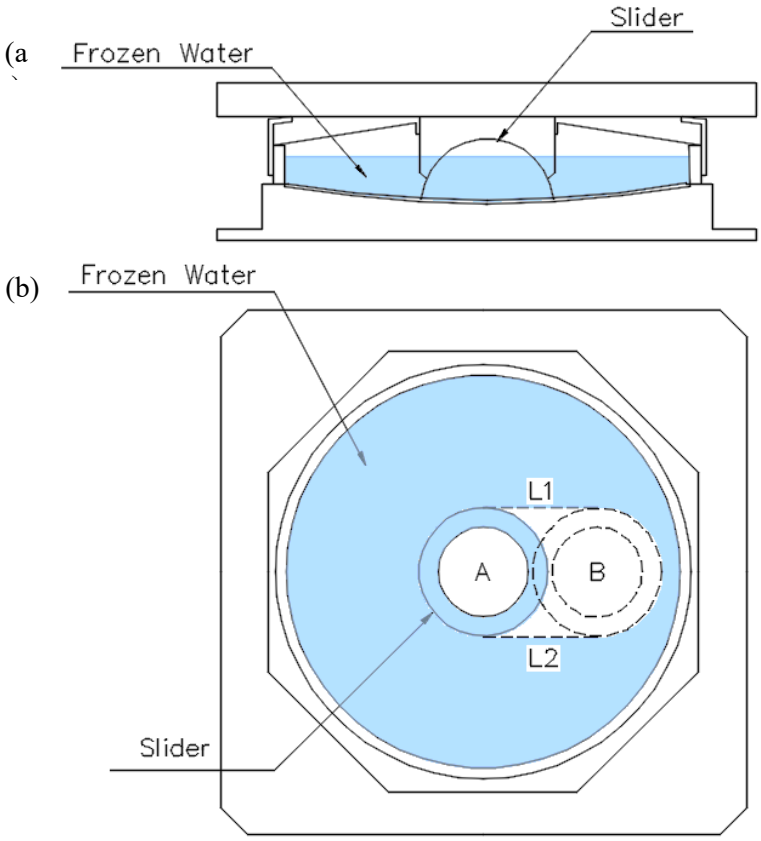

Figure A.19. Ice contaminated FPS bearing drawing (a) Elevation (b) Plan view

Fortin and Perron (2011) also conducted a centrifugal test to validate the model, where the results showed an adhesive strength of 0.50 MPa for ice density of 773 kg/m^3 at -10 ºC on an aluminum substrate with surface roughness of 0.7 µm. Due to the low roughness of the material, the fraction of mechanical locking was assumed to be 0 (pure adhesion).

A-3.3. Ice Crushing

Another failure mechanism is possible in a friction pendulum bearing with ice trapped in a confined space. Ice spalling caused by the load of an object moving into the ice (e.g. an indenter or the bearing slider) is known as ice crushing. Joordan and Timco (1988) conducted experiments on ice crushing by pushing a 63.5 mm wide indenter into a 7000 mm x 16000 mm x 9 mm ice sheet with walls on all perimeter faces except the loaded face, as shown in Figure A.20, which is a non-scaled schematic representation of the experiment. From the data, a model was developed for ice stiffness and crushing force. The model assumed that a crushed or pulverized layer formed at the contact zone and the rest of the ice was undamaged.

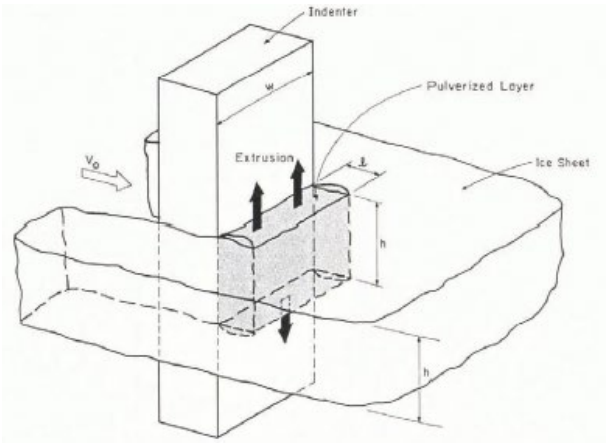

Figure A.20. Schematic illustration of pulverized ice layer in continuous indentation experiment (Joordan and Timco, 1988)

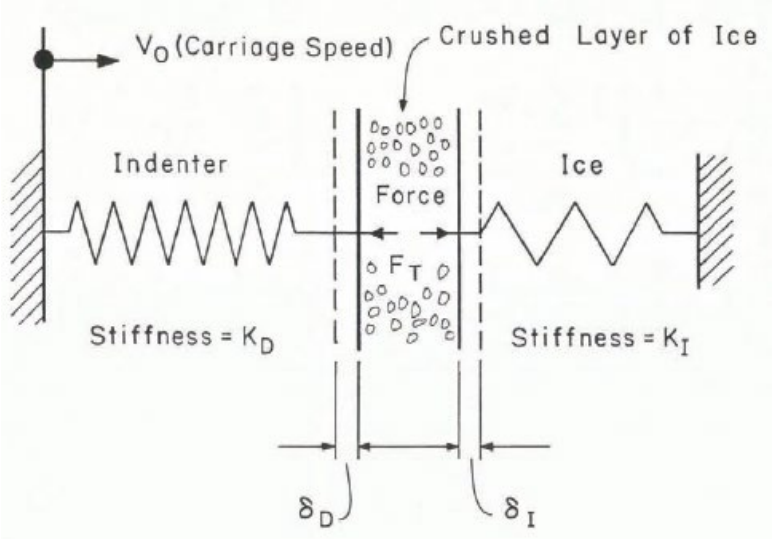

Figure A.21. Mechanical model for pulverized ice layer, indenter and ice (Joordan and Timco, 1988)

Based on the idealized system shown in Figure A.21, from elasticity theory, the ice stiffness K_I is:

$$K_I = 0.085\pi Eh \qquad \textbf{(Eq. A. 7)}$$

The reaction force F per unit width produced by the crushed layer into the indenter is computed as:

$$F = \vartheta v_0 \left(\frac{h}{l}\right)^3 \qquad \textbf{(Eq. A. 8)}$$

where:

E = Ice elastic modulus (assumed as 10000 MPa)
h = Thickness of ice layer
ϑ = Viscosity of crushed layer
l = Length of crushed layer

The mechanical models for adhesion and ice crushing are starting points, and may need to be modified and combined to represent the effects of ice in FPS bearings.

A-3.4. Ice Friction

If the adhesive strength of ice exceeds its cohesive strength, the ice will fail first, and an ice layer will remain on the surface. In this case, the concave sliding surface in FPS bearings will be covered by a thin ice layer, and the slider is expected to slide over the ice layer. Hence, the frictional properties between ice and different substrates (e.g. SS or PTFE) are relevant.

The friction coefficient of ice in contact with different substrates is still under study by the tribology community due to the complexity of the system and the variables that affect it. Four regimes on friction within ice are recognized: dry friction, boundary friction, mixed friction and hydrodynamic friction (Kietzig et al., 2010). Dry friction refers to the state where ice behaves as any other solid, with no lubrication between ice and the other substrate. Boundary friction is the state where a liquid-like layer has formed on the surface of ice and the temperature is just slightly lower than the melting point. In addition, the liquid-like layer thickness is much smaller than the characteristic roughness of the ice. Mixed friction is almost the same as boundary friction, except that the temperature at some locations is higher than the melting point. Finally, the hydrodynamic regime is achieved when the liquid-like layer thickness is greater than the characteristic roughness of the ice surface, and significant melting has initiated. Figure A.22 illustrates the variation of the friction coefficient as ice transitions through the different friction regimes. Experimental data by Dosch et al. (1995) and Furukawa et al. (1987) suggests that the liquid like layer on ice disappears at temperatures around -15°C and colder.

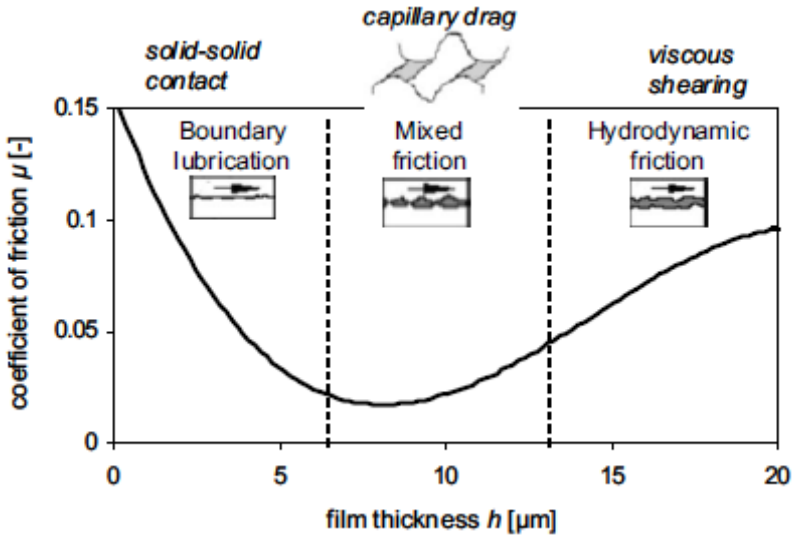

Figure A.22. Friction regimes relevant to ice friction (Kietzig et al., 2010)

Velkavrh et al. (2019) tested a steel slider over an ice surface at -8°C and ambient temperature of -4°C. The samples were stored in a freezer for about 24 hours prior to testing and the velocities of testing ranged from 0.02 to 0.38 m/s. For SS samples with different surface roughness, the coefficient of friction was observed to increase with decreasing surface roughness. This trend was attributed to higher viscous friction, which is a characteristic of the hydrodynamic regime. The results are shown in Figure A.23; gray lines correspond to SS with surface roughness below 0.1 μm, which corresponds to the surface roughness of commercially polished to mirror finished SS sheets. The friction coefficient for this surface roughness ranges

from 0.14 to 0.08 as velocity increases. Colored lines in Figure A.23 correspond to SS with surface roughness ranging from 0.8 to 3 μm.

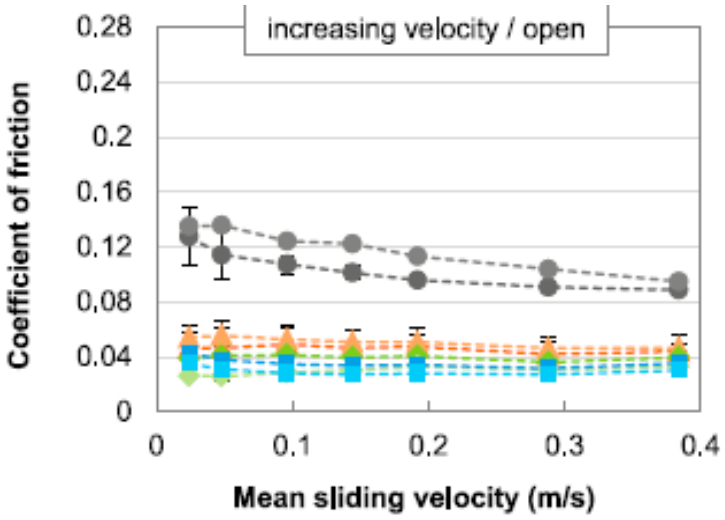

Figure A.23. Coefficient of friction of SS with different surface roughness for different velocities (Velkavrh et al., 2019)

Marmo et al. (2005) took measurements of friction coefficient for ice on steel over a temperature range from -27°C to 0.5°C and a velocity range 0.008 to 0.37 m/s at a normal force of 2.10 to 4.20 N. The coefficient of friction ranged from 0.042 to 0.17. A strong dependence of friction coefficient on temperature was observed for temperatures below -15°C. At temperatures higher than -15°C the coefficient of friction was less than 0.05, and for temperature and velocity above -18.5°C and 0.006 m/s, respectively, the coefficient of friction decreased rapidly. The observations were presented in an ice friction map (Figure A.24).

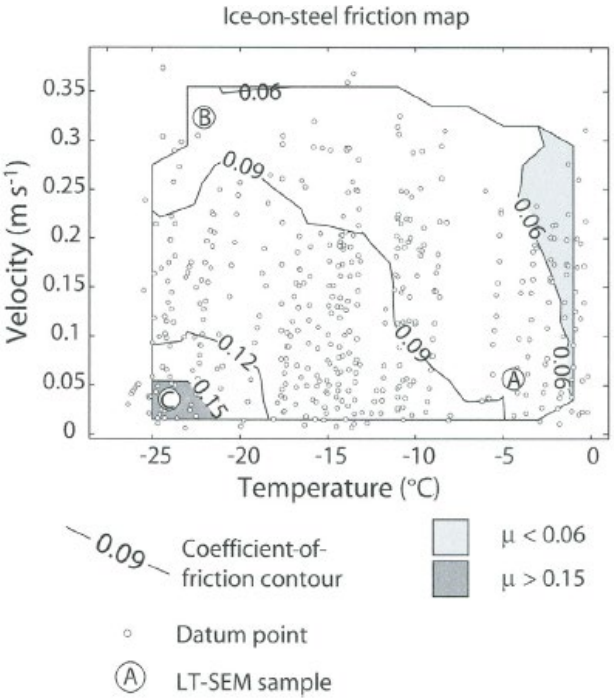

Figure A.24. μ–V-T map for ice on steel (Marmo et al., 2005)

Makkonen and Tikanmaki (2014) developed a model to predict the coefficient of friction of ice in contact with different substrates. To validate the model, the analytical results were compared with the experimental results obtained by Marmo et al. (2005) (Figure A.24) and they showed good agreement. An important consideration is that when the slider is much warmer than the ice surface, the friction between slider and ice should be modeled through conventional lubrication theory, which was not considered in Makkonen and Tikanmaki (2014) model. Figure A.25 plots the modeled friction coefficient vs velocity for ice on different sliding interfaces.

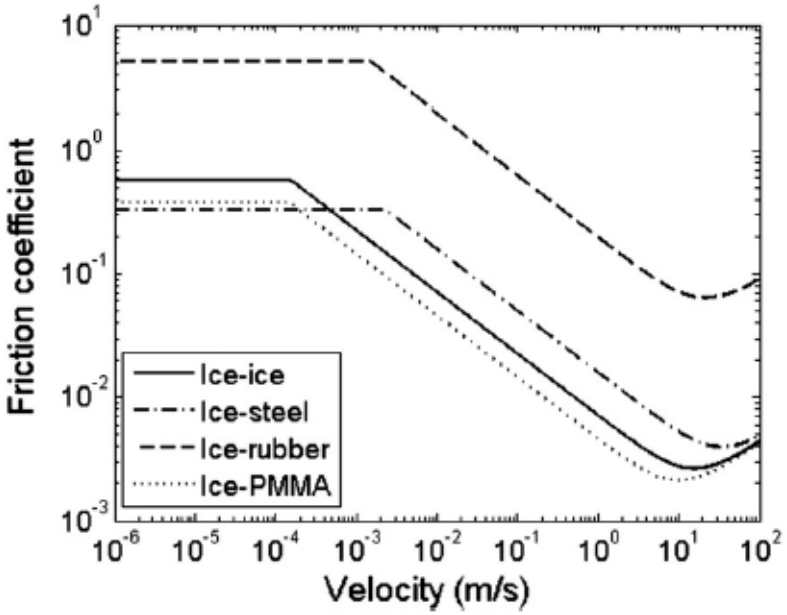

Figure A.25. Modeled ice friction. (Makkonen and Tikanmaki, 2014)

Overall, all authors agree that coefficient of friction decreases with increasing velocity and increases with decreasing temperature for steel sliding on ice. There is not much information about frictional properties of PTFE sliding on ice. However, Makkonen and Tikanmaki (2014) simulated PMMA sliding on ice, which might be considered similar to PTFE. The coefficient of friction was generally lower than for steel sliding over ice, but the trend was very similar, as shown in Figure A.25.

APPENDIX B: TESTS CONDUCTED

Phase 1 Test

Table B. 1. Tests conducted day 1 - 09/20/2021 – Aged Susitna 1

Run	Type	Axial Load (kips)	Peak Disp (in)	Rate (Hz)	Peak vel (in/s)	No. of Cycles	Direction	Condition	Water/ice level (in)	Comment	File_name	Plot Appendix C
1	sinusoidal	100	0.93	0.96	0.89	6	1	Dry	-	As received	20210920_104735.csv	-
2	sinusoidal	100	1.86	0.73	1.35	6	1	Dry	-	As received	20210920_110414.csv	-
3	sinusoidal	100	3.72	0.57	2.14	6	1	Dry	-	As received	20210920_111729.csv	Figure C20
4	sinusoidal	100	3.72	0.57	2.14	6	2	Dry	-	As received	20210920_115832.csv	Figure C21
5	GM1	100	-	-	-	0	12	Dry	-	Max disp X = 3.72 in. Max disp Y = 3.34 in.	20210920_121112.csv	-
6	sinusoidal	100	3.72	0.57	2.14	6	1	Dry	-	Clean bearing	20210920_144314.csv	Figure C26
7	sinusoidal	100	3.72	0.57	2.14	6	2	Dry	-	Clean bearing	20210920_144602.csv	Figure C29
8	sinusoidal	100	0.93	0.96	0.89	6	1	Dry	-	Clean bearing	20210920_144814.csv	-
9	sinusoidal	100	1.86	0.73	1.35	6	1	Dry	-	Clean bearing	20210920_145530.csv	-
10	sinusoidal	100	2.79	0.63	1.75	6	1	Dry	-	Clean bearing	20210920_145807.csv	-
11	sinusoidal	100	3.72	0.57	2.14	6	1	Dry	-	Control run	20210920_150036.csv	-
12	sinusoidal	100	4.65	0.54	2.51	6	1	Dry	-	Clean bearing	20210920_152835.csv	-
13	sinusoidal	100	3.72	0.29	1.07	6	1	Dry	-	Rate variation. Clean bearing	20210920_153700.csv	-
14	sinusoidal	100	3.72	1.15	4.27	6	1	Dry	-	Rate variation. Clean bearing	20210920_153915.csv	-
15	sinusoidal	100	7.45	0.48	3.58	6	1	Dry	-	Clean bearing	20210920_154059.csv	-
16	sinusoidal	100	3.72	0.57	2.14	12	1	Dry	-	To compare with wet test. Clean bearing	20210920_154310.csv	-
17	sinusoidal	100	3.72	0.57	2.14	6	1	Dry	-	Frictional Check	20210920_154500.csv	-

Table B.2. Tests conducted day 2 - 09/21/2021 – Aged Susitna 1

Run	Type	Axial Load (kips)	Peak Disp (in)	Rate (Hz)	Peak vel (in/s)	No. of Cycles	Direction	Condition	Water/ice level (in)	Comment	File_name	Plot Appendix C
1	sinusoidal	100	3.72	0.57	2.14	6	1	Frozen	2.65	Initial temperature -15 C.	20210921_101220.csv	Figure C28
2	sinusoidal	100	3.72	0.57	2.14	6	2	Frozen	2.65	Initial temperature -15 C.	20210921_101420.csv	Figure C31
3	GM1	100	-	-	-	-	12	Frozen	2.65	Initial temperature -15 C. Max disp X = 3.72 in. Max disp Y = 3.34 in	20210921_102028.csv	-
4	sinusoidal	100	3.72	1.15	4.27	6	1	Frozen	2.65	Initial temperature -15 C.	20210921_102731.csv	-
5	sinusoidal	100	3.72	0.57	2.14	6	1	Wet	0.1	Thin lubrication layer.	20210921_144046.csv	-
6	sinusoidal	100	3.72	0.57	2.14	6	2	Wet	0.1	Thin lubrication layer.	20210921_144714.csv	-
7	GM1	100	3.72				1	Wet	0.1	Thin lubrication layer. Max disp = 3.72 in	20210921_145009.csv	-
8	GM1	100					12	Wet	0.1	Thin lubrication layer. Max disp X = 3.72 in. Max disp Y = 3.34 in	20210921_145145.csv	-

Table B.3. Tests conducted day 3 - 09/22/2021 – Aged Susitna 1

Run	Type	Axial Load (kips)	Peak Disp (in)	Rate (Hz)	Peak vel (in/s)	No. of Cycles	Direction	Condition	Water/ice level (in)	Comment	File_name	Plot Appendix C
1	sinusoidal	55	8.00	0.48	3.84	9	1	Frozen	2.65	Ramping sine	20210922_101814.csv	Figure C33
2	sinusoidal	55	8.00	0.48	3.84	9	2	Frozen	2.65	Ramping sine	20210922_103046.csv	Figure C34
3	sinusoidal	55	3.72	0.57	2.14	6	1	Wet	1.325		20210922_135909.csv	Figure C23
4	sinusoidal	55	3.72	0.57	2.14	6	2	Wet	1.325		20210922_140749.csv	Figure C25
5	GM1	55	-	-	-	-	1	Wet	1.325		20210922_142011.csv	-
6	GM1	55	-	-	-	-	12	Wet	1.325		20210922_142348.csv	-
7	sinusoidal	55	8.00	0.48	3.84	9	1	Wet	1.325	Ramping sine	20210922_145247.csv	Figure C32
8	sinusoidal	100	3.72	0.57	2.14	6	1	Wet	2.65		20210922_151325.csv	-
9	sinusoidal	100	3.72	0.57	2.14	6	2	Wet	2.65		20210922_153133.csv	-

Table B.4. Tests conducted day 4 - 09/23/2021 – Aged Susitna 1

Run	Type	Axial Load (kips)	Peak Disp (in)	Rate (Hz)	Peak vel (in/s)	No. of Cycles	Direction	Condition	Water/ice level (in)	Comment	File_name	Plot Appendix C
1	sinusoidal	100	8.00	0.48	3.84	9	1	Frozen	2.65	Initial Temperature -16 C. Ramping Sine	20210923_094204.csv	Figure C36
2	sinusoidal	100	8.00	0.48	3.84	9	2	Frozen	2.65	Initial Temperature -16 C. Ramping Sine.	20210923_094436.csv	Figure C38
3	sinusoidal	100	3.72	0.57	2.14	6	1	Wet	1.325	-	20210923_112934.csv	Figure C27
4	sinusoidal	100	3.72	0.57	2.14	6	2	Wet	1.325	-	20210923_113437.csv	Figure C30
5	sinusoidal	50	3.72	0.57	2.14	6	1	Dry	-	-	20210923_144753.csv	Figure C22
6	sinusoidal	50	3.72	0.57	2.14	6	2	Dry	-		20210923_145114.csv	Figure C24
7	GM1	50	3.72	-	-	0	1	Dry	-	-	20210923_145315.csv	-
8	GM1	50	3.34	-	-	0	2	Dry		-	20210923_145459.csv	-
9	GM1	50	-	-	-	0	12	Dry	-	Max disp X = 3.72 in. Max disp Y = 3.34 in	20210923_145659.csv	-

10	sinusoidal	50	3.72	0.57	2.14	6	1	Dry		Friction check.	20210923_145852.csv	-
11	GM1	100	3.72	-	-	0	1	Dry	-	Max disp = 3.72in	20210923_151021.csv	-
12	GM1	100	3.34	-	-	0	2	Dry	-	Max disp = 3.34in	20210923_151157.csv	-
13	GM2	100	8.60	-	-	0	1	Dry	-	El Centro sc=2.02	20210923_151431.csv	-
14	GM2	100	6.20	-	-	0	2	Dry	-	El Centro sc=2.02	20210923_151559.csv	-
15	GM2	100	-	-	-	0	12	Dry	-	Max disp X = 8.00 in. Max disp Y = 6.20 in	20210923_151754.csv	Figure C45
16	sinusoidal	100	8.00	0.48	3.84	9	1	Dry	-	Ramping Sine	20210923_152130.csv	Figure C35
17	sinusoidal	100	8.00	0.48	3.84	9	2	Dry	-	Ramping	20210923_152339.csv	Figure C37
18	sinusoidal	100	3.72	0.57	2.14	6	1	Dry	-	Friction check	20210923_152524.csv	-

Table B.5. Tests conducted day 5 - 09/24/2021 – Aged Susitna 1

Run	Type	Axial Load (kips)	Peak Disp (in)	Rate (Hz)	Peak vel (in/s)	No. of Cycles	Direction	Condition	Water/ice level (in)	Comment	File_name	Plot Appendix C
1	GM2	100	-	-	-	-	12	Frozen	2.65	Max disp X = 8.00 in. Max disp Y = 6.20 in	20210924_094525.csv	Figure C46

Table B.6. Tests conducted day 6 - 09/27/2021 - Robertson

Run	Type	Axial Load (kips)	Peak Disp (in)	Rate (Hz)	Peak vel (in/s)	No. of Cycles	Direction	Condition	Water/ice level (in)	Comment	File_name	Plot Appendix C
1	sinusoidal	25	4.05	0.63	2.57	6	1	Dry	-	-	20210927_100820.csv	-
2	sinusoidal	25	4.05	0.63	2.57	6	2	Dry	-	-	20210927_101100.csv	-
3	sinusoidal	25	1.01	1.06	1.07	6	1	Dry	-	-	20210927_101302.csv	-
4	sinusoidal	25	2.03	0.8	1.62	6	1	Dry	-	-	20210927_101425.csv	-
5	sinusoidal	25	3.04	0.69	2.11	6	1	Dry	-	-	20210927_101538.csv	-
6	sinusoidal	25	4.05	0.63	2.57	6	1	Dry	-	Friction Control.	20210927_101701.csv	-
7	sinusoidal	25	5.06	0.59	3.01	6	1	Dry	-	-	20210927_102333.csv	-
8	sinusoidal	25	4.05	0.32	1.28	6	1	Dry	-	Rate variation	20210927_102455.csv	-
9	sinusoidal	25	4.05	1.27	5.14	6	1	Dry	-	Rate variation	20210927_102647.csv	-
10	sinusoidal	25	4.05	0.63	2.57	6	1	Dry	-	-	20210927_102818.csv	-
11	sinusoidal	25	4.05	0.63	2.57	6	1	Dry	-	Friction Control.	20210927_103301.csv	-
12	GM3	25	3.98	-	-	-	1	Dry	-	Imperial Valley - El centor array #9 sc=1.56	20210927_104029.csv	-
13	GM3	25	4.02	-	-	-	2	Dry	-	Imperial Valley - El centor array #9 sc=1.56	20210927_104206.csv	-
14	GM3	25	-	-	-	-	12	Dry	-	Imperial Valley - El centor array #9 sc=1.56	20210927_104350.csv	Figure C17
15	sinusoidal	25	4.05	0.63	2.57	6	1	Dry	-	Friction Control.	20210927_104540.csv	-
16	GM4	25	2.83	-	-	-	1	Dry	-	Northridge - Saticoy sc=1.475	20210927_112521.csv	-
17	GM4	25	4.05	-	-	-	2	Dry	-	Northridge - Saticoy sc=1.475	20210927_112640.csv	-
18	GM4	25	-	-	-	-	12	Dry	-	Northridge - Saticoy sc=1.475	20210927_112749.csv	-
19	sinusoidal	25	4.05	0.63	2.57	6	1	Dry	-	Friction Control.	20210927_112911.csv	-
20	sinusoidal	15	4.05	0.63	2.57	6	1	Dry	-	-	20210927_114140.csv	-
21	sinusoidal	15	4.05	0.63	2.57	6	2	Dry	-	-	20210927_114249.csv	-
22	sinusoidal	15	4.05	0.63	2.57	6	1	Dry	-	-	20210927_114415.csv	-

23	GM3	15	3.98	-	-	-	1	Dry	-	Imperial Valley - El centor array #9 sc=1.56	20210927_114557.csv	-
24	GM3	15	4.02	-	-	-	2	Dry	-	Imperial Valley - El centor array #9 sc=1.56	20210927_114724.csv	-
25	GM3	15	-	-	-	-	12	Dry	-	Imperial Valley - El centor array #9 sc=1.56	20210927_114851.csv	-
26	sinusoidal	15	4.05	0.63	2.57	6	1	Dry	-	Friction Control.	20210927_133600.csv	-
27	sinusoidal	15	4.05	0.63	2.57	6	1	Wet	0.1	-	20210927_135119.csv	-
28	sinusoidal	15	4.05	0.63	2.57	6	1	Wet	1.25	-	20210927_135852.csv	-
29	sinusoidal	15	4.05	0.63	2.57	6	1	Wet	2.5	-	20210927_141740.csv	-
30	sinusoidal	25	4.05	0.63	2.57	6	2	Wet	1.25	-	20210927_142631.csv	-
31	GM3	25	3.98	-	-	0	1	Wet	1.25	Imperial Valley - El centor array #9 sc=1.56. Water halfway.	20210927_144945.csv	-
32	GM3	25	4.02	-	-	-	2	Wet	1.25	Imperial Valley - El centor array #9 sc=1.56.	20210927_145511.csv	-
33	GM3	25	-	-	-	-	12	Wet	1.25	Imperial Valley - El centor array #9 sc=1.56.	20210927_150125.csv	Figure C18
34	sinusoidal	25	4.05	0.63	2.57	6	1	Wet	0.1	-	20210927_152300.csv	-
35	sinusoidal	25	4.05	0.63	2.57	6	2	Wet	0.1	-	20210927_152751.csv	-
36	GM3	25	3.98	-	-	-	1	Wet	0.1	Imperial Valley - El centor array #9 sc=1.56.	20210927_152926.csv	-
37	GM3	25	4.02	-	-	-	2	Wet	0.1	Imperial Valley - El centor array #9 sc=1.56.	20210927_153046.csv	-
38	GM3	25	4.02	-	-	-	12	Wet	0.1	Imperial Valley - El centor array #9 sc=1.56.	20210927_153219.csv	-

Table B.7. Tests conducted day 7 - 09/28/2021 - Robertson

Run	Type	Axial Load (kips)	Peak Disp (in)	Rate (Hz)	Peak vel (in/s)	No. of Cycles	Direction	Condition	Water/ice level (in)	Comment	File_name	Plot Appendix C
1	sinusoidal	25	4.05	0.63	2.57	6	1	Frozen	2.5	Full of ice. Initial Temp -20C.	20210928_101522.csv	Figure C13
2	sinusoidal	25	4.05	0.63	2.57	6	2	Frozen	2.5	Initial Temp -20C.	20210928_101646.csv	Figure C14
3	sinusoidal	25	4.05	0.63	2.57	6	1	Wet	2.5	-	20210928_135946.csv	-
4	sinusoidal	25	4.05	0.63	2.57	6	2	Wet	2.5	-	20210928_140115.csv	-
5	GM3	25	3.98	-	-	-	1	Wet	2.5	Imperial Valley - El centor array #9 sc=1.56.	20210928_140831.csv	-
6	GM3	25	4.02	-	-	-	2	Wet	2.5	Imperial Valley - El centor array #9 sc=1.56.	20210928_141001.csv	-
7	GM3	25	4.02	-	-	-	12	Wet	2.5	Imperial Valley - El centor array #9 sc=1.56	20210928_141904.csv	-

Table B.8. Tests conducted day 8 - 09/29/2021 - Robertson

Run	Type	Axial Load (kips)	Peak Disp (in)	Rate (Hz)	Peak vel (in/s)	No. of Cycles	Direction	Condition	Water/ice level (in)	Comment	File_name	Plot Appendix C
1	sinusoidal	25	4.05	0.63	2.57	6	1	Frozen	2.5	Initial Temp -28C	20210929_135930.csv	Figure C15
2	sinusoidal	25	4.05	0.63	2.57	6	2	Frozen	2.5	Initial Temp -28C	20210929_140056.csv	Figure C16

Table B.9. Tests conducted day 9 - 09/30/2021 - Robertson

Run	Type	Axial Load (kips)	Peak Disp (in)	Rate (Hz)	Peak vel (in/s)	No. of Cycles	Direction	Condition	Water/ice level (in)	Comment	File_name	Plot Appendix C
1	GM1	25	-	-	-	-	12	Frozen	2.5	Initial Temp -28C.	20210930_113430.csv	Figure C19

Table B.10. Tests conducted day 10 - 10/01/2021 - Robertson & New Susitna

Run	Type	Axial Load (kips)	Peak Disp (in)	Rate (Hz)	Peak vel (in/s)	No. of Cycles	Direction	Condition	Water/ice level (in)	Comment	File_name	Plot Appendix C
1	sinusoidal	25	4.05	0.63	2.57	6	1	Frozen	1.25	Robertson. Initial Temp -25C.	20211001_101133.csv	Figure C9
2	sinusoidal	25	4.05	0.63	2.57	6	2	Frozen	1.25	Robertson. Initial Temp -25C.	20211001_101247.csv	Figure C12
3	sinusoidal	100	3.724	0.574	2.136	6	1	Dry	-	New Susitna	20211001_140847.csv	-
4	sinusoidal	100	0.931	0.959	0.893	6	1	Dry	-	New Susitna	20211001_140951.csv	-
5	sinusoidal	100	1.862	0.725	1.35	6	1	Dry	-	New Susitna	20211001_141057.csv	-
6	sinusoidal	100	2.793	0.628	1.755	6	1	Dry	-	New Susitna	20211001_141207.csv	-
7	sinusoidal	100	4.655	0.538	2.505	6	1	Dry	-	New Susitna	20211001_141312.csv	Figure C77
8	sinusoidal	100	3.724	0.574	2.136	6	1	Dry	-	New Susitna	20211001_141409.csv	-
9	sinusoidal	100	3.724	0.574	2.136	6	2	Dry	-	New Susitna	20211001_142600.csv	-
10	sinusoidal	100	3.724	0.287	1.068	6	1	Dry	-	New Susitna	20211001_142659.csv	-
11	sinusoidal	100	3.724	1.147	4.272	6	1	Dry	-	New Susitna	20211001_142813.csv	-
12	sinusoidal	100	8	0.48	3.84	6	1	Dry	-	New Susitna. Ramping Sine	20211001_142942.csv	Figure C82
13	sinusoidal	100	8	0.48	3.84	6	2	Dry	-	New Susitna. Ramping Sine	20211001_143049.csv	Figure C84
14	sinusoidal	100	3.724	0.574	2.136	6	1	Dry	-	New Susitna	20211001_143154.csv	-
15	GM2	100	8.6	-	-	-	1	Dry	-	New Susitna. El centro sc=2.02	20211001_144456.csv	-

16	GM2	100	6.2	-	-	-	2	Dry	-	New Susitna. El centro sc=2.02	20211001_144615.csv	-
17	GM2	100	8.6	-	-	-	12	Dry	-	New Susitna. El centro sc=2.02	20211001_144729.csv	-
18	GM1	100	3.72	-	-	-	1	Dry	-	New Susitna	20211001_144853.csv	-
19	GM1	100	3.34	-	-	-	2	Dry	-	New Susitna	20211001_145004.csv	-
20	GM1	100	3.72	-	-	-	12	Dry	-	New Susitna	20211001_145154.csv	-
21	sinusoidal	100	3.724	0.574	2.136	6	1	Dry	-	New Susitna	20211001_145347.csv	-
22	sinusoidal	50	3.724	0.574	2.136	6	1	Dry	-	New Susitna	20211001_150938.csv	Figure C73
23	sinusoidal	50	3.724	0.574	2.136	6	2	Dry	-	New Susitna	20211001_151051.csv	Figure C75
24	GM2	50	8.6	-	-	-	1	Dry	-	New Susitna. El centro sc=2.02	20211001_151205.csv	-
25	GM2	50	6.2	-	-	-	2	Dry		New Susitna. El centro sc=2.02	20211001_151352.csv	-
26	GM2	50	8.6	-	-	-	12	Dry	-	New Susitna. El centro sc=2.02	20211001_151507.csv	-
27	sinusoidal	50	3.724	0.574	2.136	6	1	Dry		Friction Check. 5 mins pause after the friciton check	20211001_151636.csv	-
28	GM1	50	3.72	-	-	-	1	Dry	-	New Susitna	20211001_153111.csv	-
29	GM1	50	3.34	-	-	-	2	Dry		New Susitna	20211001_153215.csv	-
30	GM1	50	3.72	-	-	-	12	Dry	-	New Susitna	20211001_153326.csv	-
31	sinusoidal	50	3.724	0.574	2.136	6	1	Dry		New Susitna	20211001_153442.csv	-

Table B.11. Tests conducted day 11 - 10/04/2021 - New Susitna

Run	Type	Axial Load (kips)	Peak Disp (in)	Rate (Hz)	Peak vel (in/s)	No. of Cycles	Direction	Condition	Water/ice level (in)	Comment	File_name	Plot Appendix C
1	sinusoidal	100	8	0.48	3.84	9	1	Frozen	2.65	Initial Temp -15C. Fereezing over the weekend.	20211004_141450.csv	Figure C86
2	sinusoidal	100	8	0.48	3.84	9	2	Frozen	2.65	Initial Temp -15C. Fereezing over the weekend	20211004_141622.csv	Figure C87

Table B.12. Tests conducted day 12 - 10/05/2021 - New Susitna

Run	Type	Axial Load (kips)	Peak Disp (in)	Rate (Hz)	Peak vel (in/s)	No. of Cycles	Direction	Condition	Water/ice level (in)	Comment	File_name	Plot Appendix C
1	sinusoidal	100	8	0.48	3.84	9	1	Frozen	2.65	Ramping sine. Initial temp -22 C	20211005_115112.csv	Figure C83
2	sinusoidal	100	8	0.48	3.84	9	2	Frozen	2.65	Ramping sine. Initial temp -22 C	20211005_115309.csv	Figure C85
3	sinusoidal	100	3.724	0.574	2.136	6	1	Wet	2.65	Full of water	20211005_142613.csv	-
4	sinusoidal	100	3.724	0.574	2.136	6	2	Wet	2.65	Full of water	20211005_144700.csv	-
5	GM1	100	8.6	-	-	-	1	Wet	2.65	El centro sc=2.02.	20211005_144837.csv	-
6	GM1	100	6.2	-	-	-	2	Wet	2.65	El centro sc=2.02.	20211005_144959.csv	-
7	GM1	100	8.6	-	-	-	12	Wet	2.65	El centro sc=2.02	20211005_145120.csv	-
8	sinusoidal	100	3.724	0.574	2.136	6	1	Wet	1.325	-	20211005_150919.csv	Figure C79
9	sinusoidal	100	3.724	0.574	2.136	6	2	Wet	1.325	-	20211005_151809.csv	Figure C78
10	GM1	100	8.6	-	-	-	1	Wet	1.325	-	20211005_152548.csv	-
11	GM1	100	6.2	-	-	-	2	Wet	1.325	-	20211005_152726.csv	-
12	GM1	100	8.6	-	-	-	12	Wet	1.325	-	20211005_152907.csv	-

Table B.13. Tests conducted day 13 - 10/06/2021 - New Susitna

Run	Type	Axial Load (kips)	Peak Disp (in)	Rate (Hz)	Peak vel (in/s)	No. of Cycles	Direction	Condition	Water/ice level (in)	Comment	File_name	Plot Appendix C
1	sinusoidal	55	8	0.48	3.84	6	1	Frozen	2.65		Filtered_20211006_094720.csv	Figure C80
2	sinusoidal	55	8	0.48	3.84	6	2	Frozen	2.65		Filtered_20211006_094848.csv	Figure C81
1	sinusoidal	55	8	0.48	3.84	6	1	Frozen	0.1		20211006_133739.csv	-
2	sinusoidal	55	8	0.48	3.84	6	2	Frozen	0.1		20211006_155234.csv	-

Table B.14. Tests conducted day 14 - 10/07/2021 - New Susitna

Run	Type	Axial Load (kips)	Peak Disp (in)	Rate (Hz)	Peak vel (in/s)	No. of Cycles	Direction	Condition	Water/ice level (in)	Comment	File_name	Plot Appendix C
1	sinusoidal	55	8	0.48	3.84	6	1	Frozen	2.65	Initial Temp -24C.	Filtered_20211007_100707.csv	Figure C88
2	sinusoidal	55	8	0.48	3.84	6	2	Frozen	2.65	Initial Temp -24C.	Filtered_20211007_100950.csv	Figure C89
3	sinusoidal	55	8	0.48	3.84	9	1	Dry		-	20211007_102800.csv	-
4	sinusoidal	55	8	0.48	3.84	9	2	Dry		-	20211007_102937.csv	-
5	sinusoidal	100	8	0.48	3.84	9	1	Dry		-	20211007_104343.csv	-
6	sinusoidal	100	8	0.48	3.84	9	2	Dry		-	20211007_104507.csv	-
7	sinusoidal	100	3.724	0.574	2.136	6	1	Wet	0.1	-	20211007_133331.csv	-
8	sinusoidal	100	3.724	0.574	2.136	6	2	Wet	0.1	-	20211007_133438.csv	-
9	GM1	100	-	-	-	0	1	Wet	0.1	-	20211007_133558.csv	-
10	GM1	100	-	-	-	0	2	Wet	0.1	-	20211007_133722.csv	-
11	GM1	100	-	-	-	0	12	Wet	0.1	-	20211007_133907.csv	-
12	sinusoidal	55	3.724	0.574	2.136	6	1	Wet	0.1	-	20211007_134655.csv	-
13	sinusoidal	55	3.724	0.574	2.136	6	2	Wet	0.1	-	20211007_134747.csv	-
14	sinusoidal	55	3.724	0.574	2.136	6	1	Wet	1.325	-	20211007_135807.csv	Figure C74
15	sinusoidal	55	3.724	0.574	2.136	6	2	Wet	1.325	-	20211007_135926.csv	Figure C76
16	sinusoidal	55	3.724	0.574	2.136	6	1	Wet	2.65	-	20211007_140714.csv	-
17	sinusoidal	55	3.724	0.574	2.136	6	2	Wet	2.65	-	20211007_142152.csv	-

Start of Phase 2 Tests

Table B.15. Tests conducted day 15 - 12/07/2021 - New Susitna

Run	Type	Axial Load (kips)	Peak Disp (in)	Rate (Hz)	Peak vel (in/s)	No. of Cycles	Direction	Condition	Water/ice level (in)	Comment	File_name	Plot Appendix C
1	sinusoidal	55	10	0.45	2.222	6	2	Frozen	2.65	Initial Temp -24C	20211207_133401.csv	-
2	sinusoidal	55	10	0.45	2.222	6	1	Frozen	2.65	Initial Temp -24C	20211207_133542.csv	-

Table B.16. Tests conducted day 16 - 12/09/2021 - Aged Susitna 1

Run	Type	Axial Load (kips)	Peak Disp (in)	Rate (Hz)	Peak vel (in/s)	No. of Cycles	Direction	Condition	Water/ice level (in)	Comment	File_name	Plot Appendix C
1	sinusoidal	55	10	0.45	2.222	6	2	Frozen	2.65	Initial Temp -24C	20211209_104537.csv	Figure C44
2	sinusoidal	55	10	0.45	2.222	6	1	Frozen	2.65	Initial Temp -24C	20211209_104704.csv	Figure C41
3	sinusoidal	55	3.724	0.574	2.136	6	1	Dry	-		20211209_142956.csv	-
4	sinusoidal	55	3.724	0.574	2.136	6	2	Dry	-		20211209_143253.csv	-
5	sinusoidal	55	10	0.45	2.136	6	1	Dry	-		20211209_143456.csv	Figure C39
6	sinusoidal	55	10	0.45	2.136	6	2	Dry	-		20211209_143616.csv	Figure C42
7	sinusoidal	55	3.724	0.574	2.136	6	1	Dry	-		20211209_143738.csv	-
8	sinusoidal	55	3.724	0.574	2.136	6	2	Dry	-		20211209_143857.csv	-
9	sinusoidal	55	3.724	0.574	2.136	6	1	Wet	1.30		20211209_145318.csv	-
10	sinusoidal	55	3.724	0.574	2.136	6	2	Wet	1.30		20211209_145449.csv	-
11	sinusoidal	55	10	0.45	2.136	6	1	Wet	1.30		20211209_145641.csv	Figure C40
12	sinusoidal	55	10	0.45	2.136	6	2	Wet	1.30		20211209_150115.csv	Figure C43

Table B.17. Tests conducted day 17 - 12/16/2021 - Aged Susitna 2

Run	Type	Axial Load (kips)	Peak Disp (in)	Rate (Hz)	Peak vel (in/s)	No. of Cycles	Direction	Condition	Water/ice level (in)	Comment	File_name	Plot Appendix C
1	sinusoidal	55	10	0.45	4.5	6	2	Frozen	as received	As received frozen -22C	20211216_131541.csv	Figure C47
2	sinusoidal	55	10	0.45	4.5	6	1	Frozen	as received	As received frozen -22C	20211216_131710.csv	Figure C48
3	sinusoidal	55	3.724	0.574	2.136	6	1	Wet			20211216_145848.csv	-
4	sinusoidal	55	3.724	0.574	2.136	6	2	Wet			20211216_150029.csv	-
5	sinusoidal	55	10	0.45	4.5	6	1	Wet			20211216_150152.csv	-
6	sinusoidal	55	10	0.45	4.5	6	2	Wet			20211216_150313.csv	-

Table B.18. Tests conducted day 18 - 12/17/2021 - Aged Susitna 2

Run	Type	Axial Load (kips)	Peak Disp (in)	Rate (Hz)	Peak vel (in/s)	No. of Cycles	Direction	Condition	Water/ice level (in)	Comment	File_name	Plot Appendix C
1	sinusoidal	55	10	0.45	4.5	6	2	Frozen	2.65	Temp -29C	20211217_120816.csv	Figure C66
2	sinusoidal	55	10	0.45	4.5	6	1	Frozen	2.65	Temp -29C	20211217_120933.csv	Figure C62
3	sinusoidal	55	3.724	0.574	2.136	6	1	Dry		Cleaned bearing	20211217_145653.csv	-
4	sinusoidal	55	3.724	0.574	2.136	6	2	Dry		Cleaned bearing	20211217_145801.csv	-
5	sinusoidal	55	10	0.45	4.5	6	1	Dry		Cleaned bearing	20211217_145913.csv	Figure C59
6	sinusoidal	55	10	0.45	4.5	6	2	Dry		Cleaned bearing	20211217_150028.csv	Figure C63

Table B.19. Tests conducted day 19 - 12/22/2021 - Aged Susitna 2

Run	Type	Axial Load (kips)	Peak Disp (in)	Rate (Hz)	Peak vel (in/s)	No. of Cycles	Direction	Condition	Water/ice level (in)	Comment	File_name	Plot Appendix C
1	sinusoidal	100	10	0.45	4.5	6	2	Frozen	2.65	Temp -30C	20211222_095537.csv	Figure C72
2	sinusoidal	100	10	0.45	4.5	6	1	Frozen	2.65	Temp -30C	20211222_095713.csv	Figure C69
3	sinusoidal	55	3.724	0.574	2.136	12	1	Wet			20211222_120558.csv	Figure C50
4	sinusoidal	55	10	0.45	4.5	12	2	Wet			20211222_120716.csv	Figure C64
5	sinusoidal	55	3.724	0.574	2.136	12	2	Wet			20211222_121223.csv	Figure C52
6	sinusoidal	55	10	0.45	4.5	12	1	Wet			20211222_121401.csv	Figure C60
7	sinusoidal	100	3.724	0.574	2.136	6	1	Dry			20211222_141543.csv	Figure C55
8	sinusoidal	100	3.724	0.574	2.136	6	2	Dry			20211222_141656.csv	Figure C57
9	sinusoidal	100	10	0.45	4.5	6	1	Dry			20211222_141848.csv	Figure C67
10	sinusoidal	100	10	0.45	4.5	6	2	Dry			20211222_142010.csv	Figure C70
11	sinusoidal	100	3.724	0.574	2.136	12	1	Wet			20211222_142919.csv	Figure C56
12	sinusoidal	100	3.724	0.574	2.136	12	2	Wet			20211222_143036.csv	Figure C58
13	sinusoidal	100	10	0.45	4.5	12	1	Wet			20211222_143200.csv	Figure C68
14	sinusoidal	100	10	0.45	4.5	12	2	Wet			20211222_143707.csv	Figure C71

Table B.20. Tests conducted day 20 - 12/29/2021 - Robertson

Run	Type	Axial Load (kips)	Peak Disp (in)	Rate (Hz)	Peak vel (in/s)	No. of Cycles	Direction	Condition	Water/ice level (in)	Comment	File_name	Plot Appendix C
1	sinusoidal	15	4.05	0.63	2.57	6	2	Frozen	2.55	temp -24C	20211229_105139.csv	Figure C3
2	sinusoidal	15	4.05	0.63	2.57	6	1	Frozen	2.55	temp -24C	20211229_105251.csv	Figure C6
3	sinusoidal	15	4.05	0.63	2.57	6	1	Wet	1.31		20211229_131956.csv	Figure C2
4	sinusoidal	15	4.05	0.63	2.57	6	2	Wet	1.31		20211229_132817.csv	Figure C5
5	sinusoidal	25	4.05	0.63	2.57	6	1	Wet	1.31		20211229_134839.csv	Figure C8
6	sinusoidal	25	4.05	0.63	2.57	6	2	Wet	1.31		20211229_135001.csv	Figure C11
7	sinusoidal	25	4.05	0.63	2.57	6	1	Dry			20211229_151402.csv	Figure C7
8	sinusoidal	25	4.05	0.63	2.57	6	2	Dry			20211229_151531.csv	Figure C10
9	sinusoidal	15	4.05	0.63	2.57	6	1	Dry			20211229_152235.csv	Figure C1
10	sinusoidal	15	4.05	0.63	2.57	6	2	Dry			20211229_152337.csv	Figure C4

Table B.21. Tests conducted day 21 - 01/05/2022 - Aged Susitna 1 and 2

Run	Type	Axial Load (kips)	Peak Disp (in)	Rate (Hz)	Peak vel (in/s)	No. of Cycles	Direction	Condition	Water/ice level (in)	Comment	File_name	Plot Appendix C
1	sinusoidal	55	3.724	0.574	2.136	6	1	Baked soil		Aged Susitna 2	20220105_101646.csv	Figure C49
2	sinusoidal	55	3.724	0.574	2.136	6	2	Baked soil		Aged Susitna 2	20220105_101809.csv	Figure C51
3	sinusoidal	55	10	0.45	4.5	6	1	Baked soil		Aged Susitna 2	20220105_101922.csv	Figure C61
4	sinusoidal	55	10	0.45	4.5	6	2	Baked soil		Aged Susitna 2	20220105_102038.csv	Figure C65
5	sinusoidal	55	3.724	0.574	2.136	6	1	Dry		Aged Susitna 2	20220105_102153.csv	Figure C53
6	sinusoidal	55	3.724	0.574	2.136	6	2	Dry		Aged Susitna 2	20220105_102257.csv	Figure C54
7	sinusoidal	55	3.724	0.574	2.136	6	1	Dry		Aged Susitna 1	20220105_134433.csv	-
8	sinusoidal	55	3.724	0.574	2.136	6	2	Dry		Aged Susitna 1	20220105_134538.csv	-
9	sinusoidal	55	10	0.45	2.136	6	1	Dry		Aged Susitna 1	20220105_134642.csv	-
10	sinusoidal	55	10	0.45	2.136	6	2	Dry		Aged Susitna 1	20220105_134742.csv	-

APPENDIX C: SELECTED TEST RESULTS

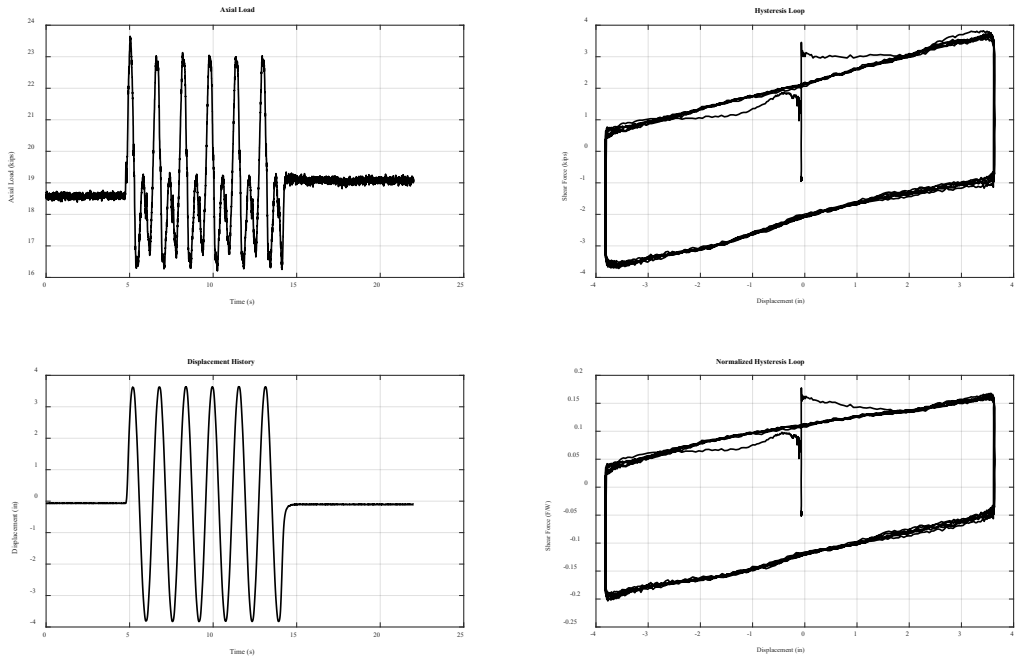

Figure C1. 12/29/2021 Robertson- Dry: 15 kips, sinusoidal X @ 0.63Hz. Max disp = 4.05in

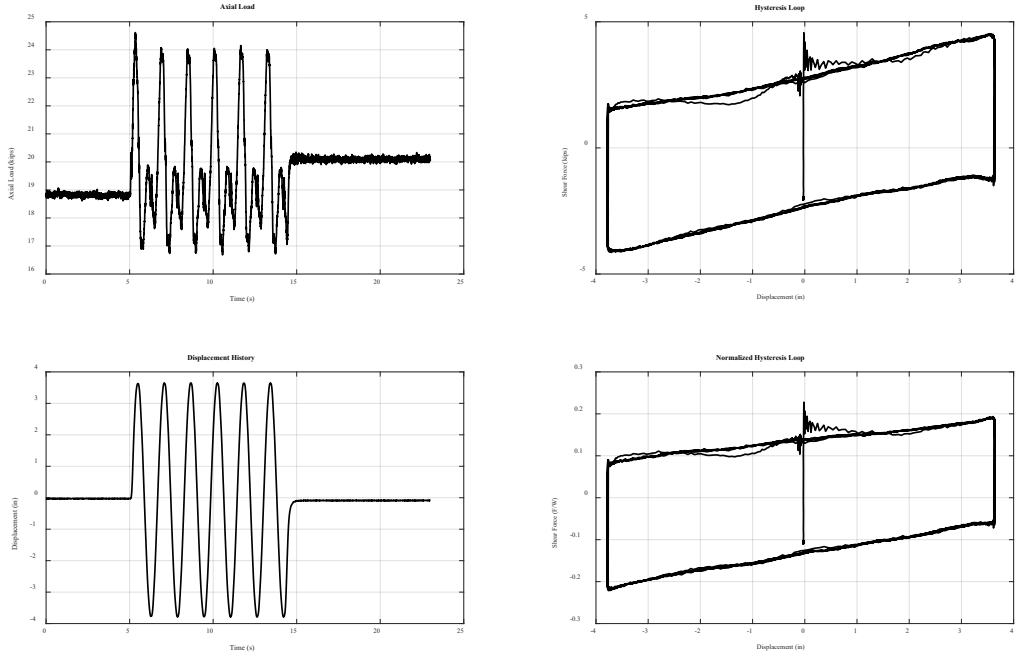

Figure C2. 12/29/2021 Robertson- Wet: 15 kips, sinusoidal X @ 0.63Hz. Max disp = 4.05in

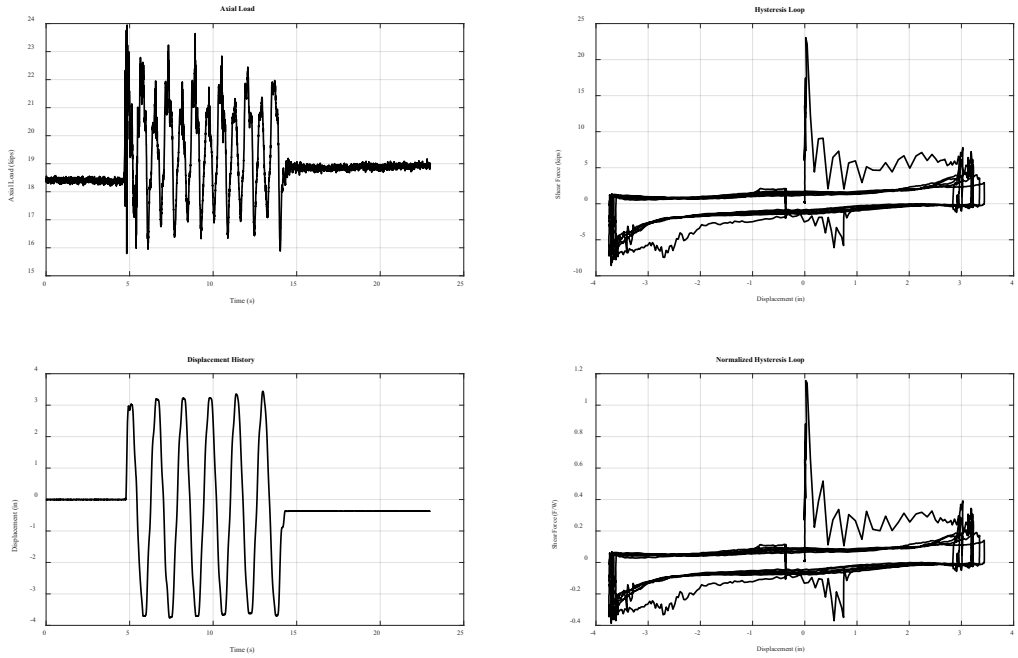

Figure C3. 12/29/2021 Robertson- Frozen @ -24°C: 15 kips, sinusoidal Y @ 0.63Hz. Max disp = 4.05 in

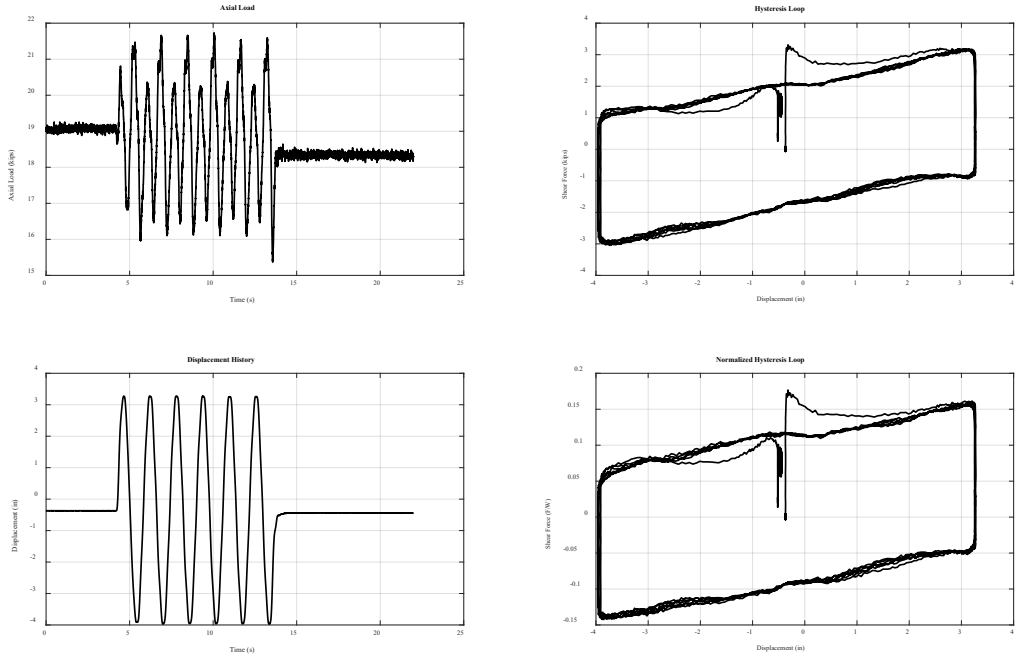

Figure C4. 12/29/2021 Robertson- Dry: 15 kips, sinusoidal Y @ 0.63Hz. Max disp = 4.05in

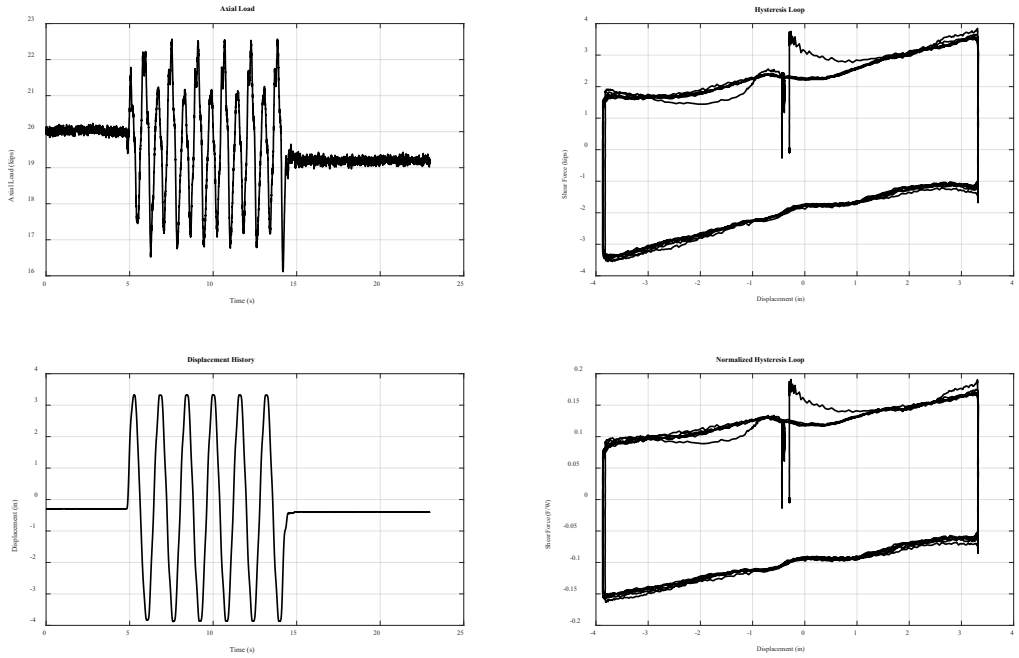

Figure C5. 12/29/2021 Robertson- Wet: 15 kips, sinusoidal Y @ 0.63Hz. Max disp = 4.05in

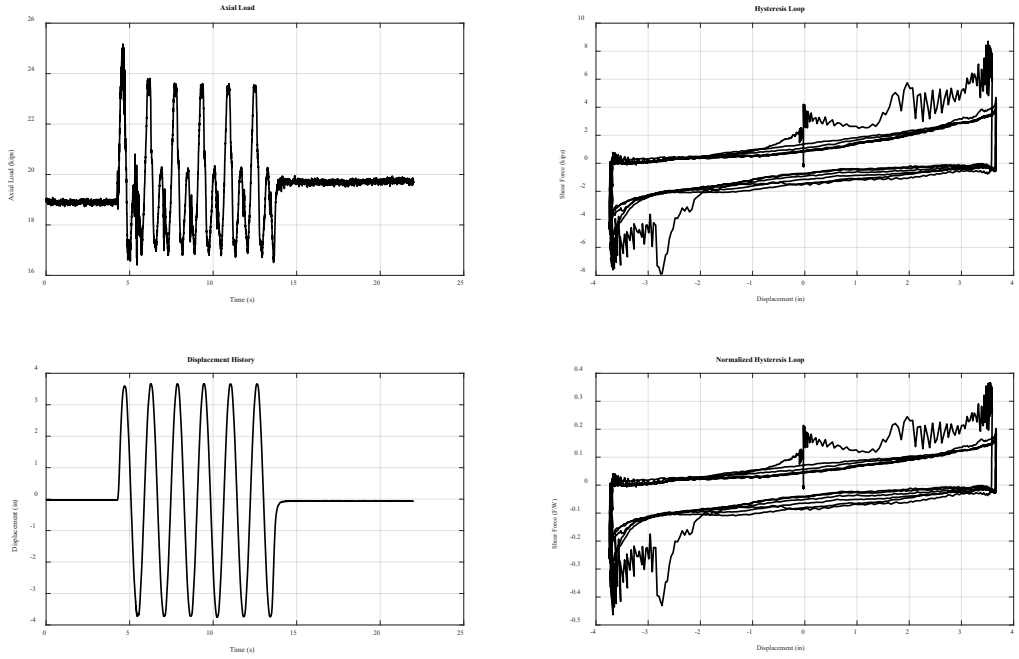

Figure C6. 12/29/2021 Robertson- Frozen @ -24°C: 15 kips, sinusoidal X @ 0.63 Hz. Max disp = 4.05 in

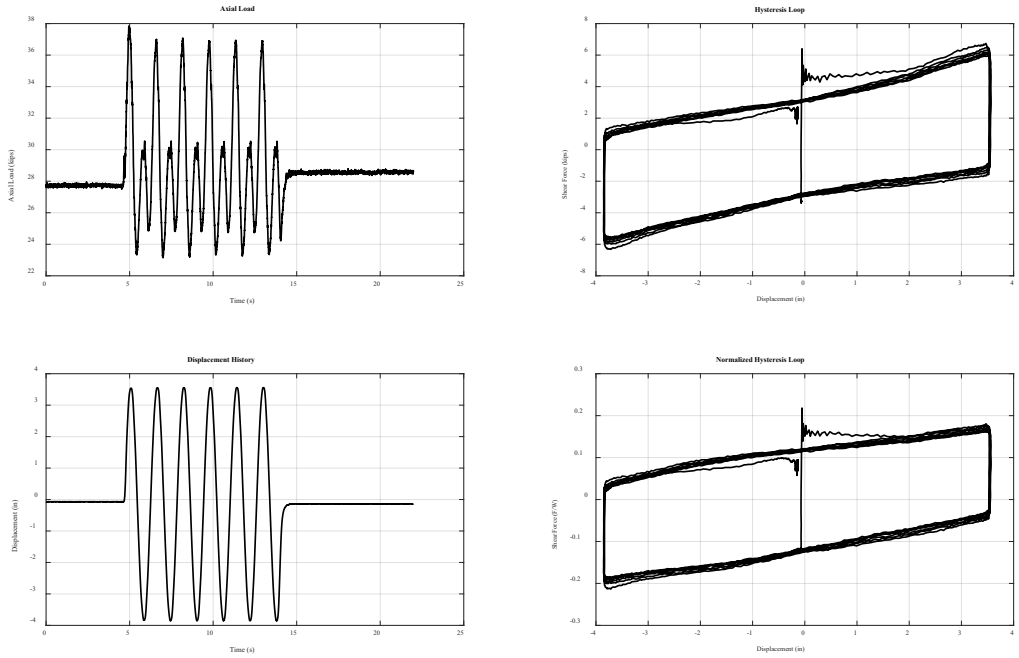

Figure C7. 12/29/2021 Robertson- Dry: 25 kips, sinusoidal X @ 0.63Hz. Max disp = 4.05in

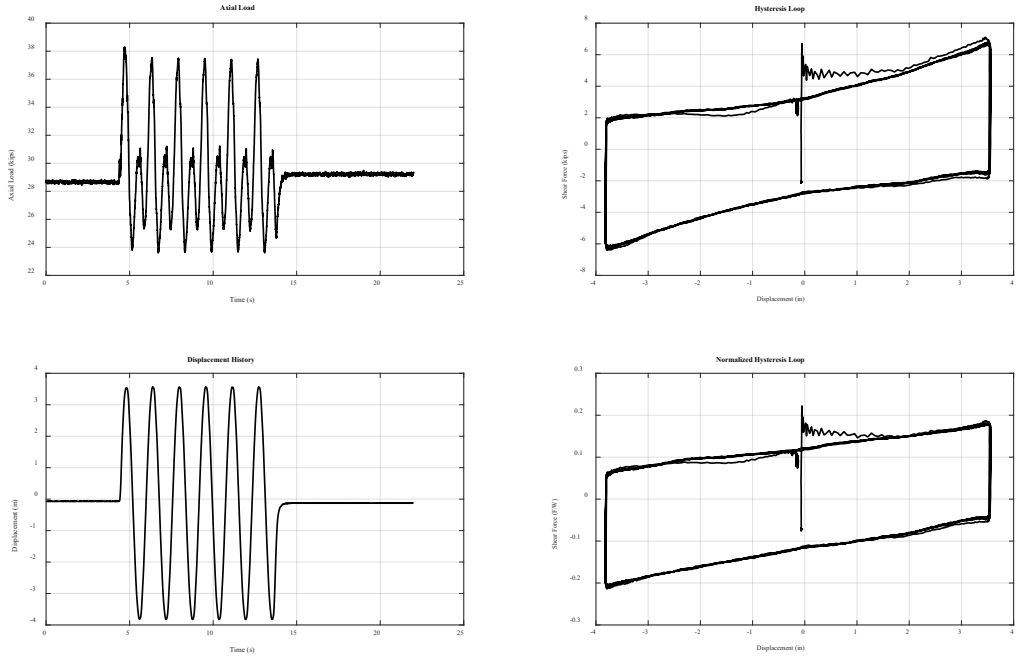

Figure C8. 12/29/2021 Robertson- Wet: 25 kips, sinusoidal X @ 0.63Hz. Max disp = 4.05in

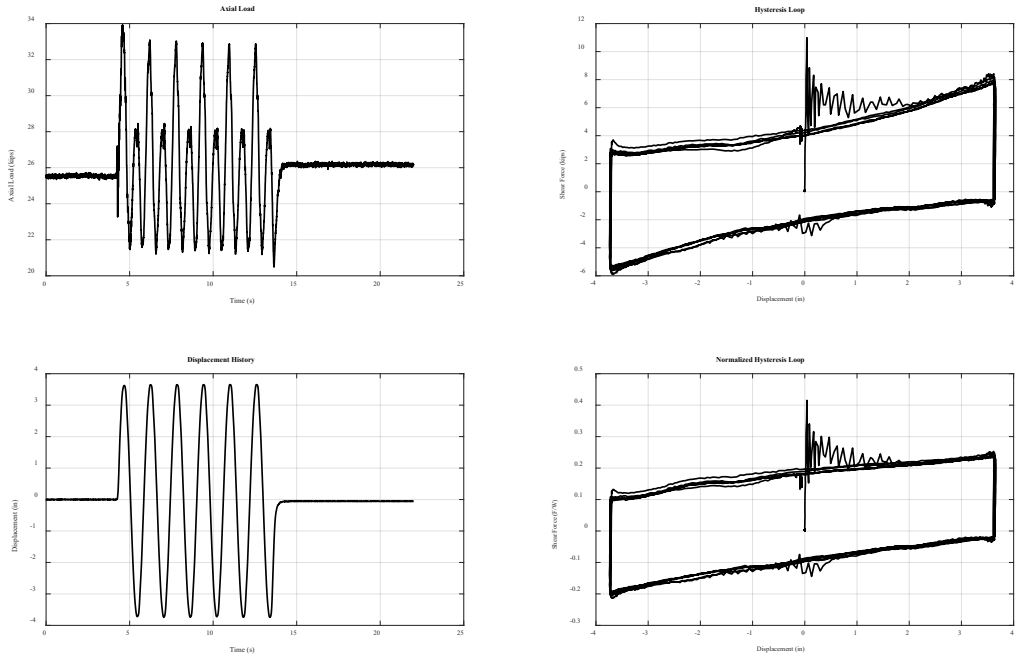

Figure C9. 10/1/2021 Robertson- Frozen half layer ice @ -25°C: 25 kips, sinusoidal X @ 0.63Hz. Max disp = 4.05in

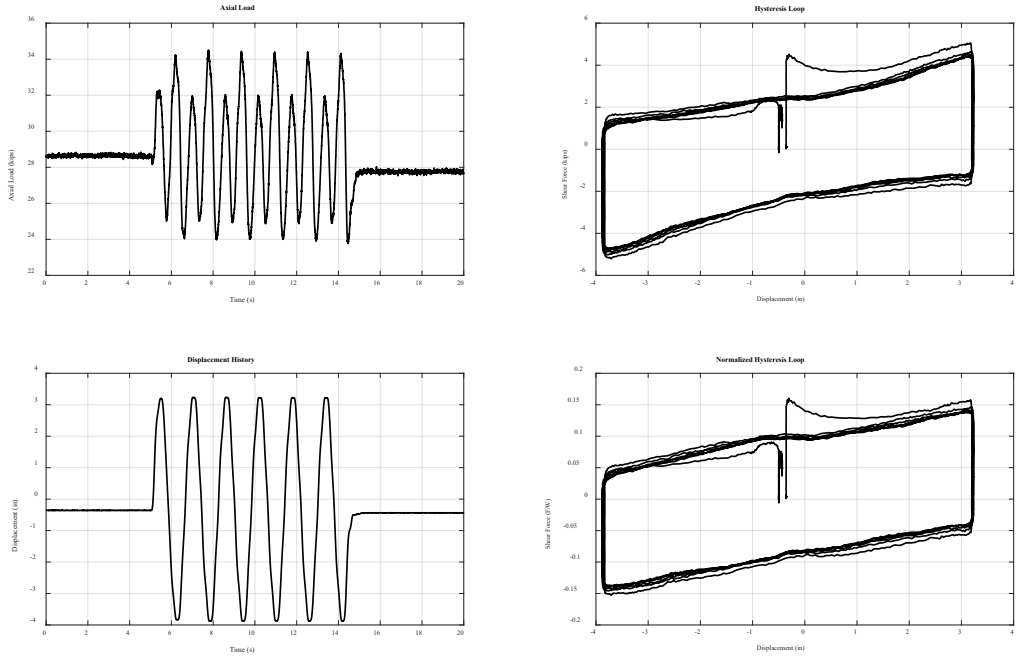

Figure C10. 12/29/2021 Robertson- Dry: 25 kips, sinusoidal Y @ 0.63Hz. Max disp = 4.05in

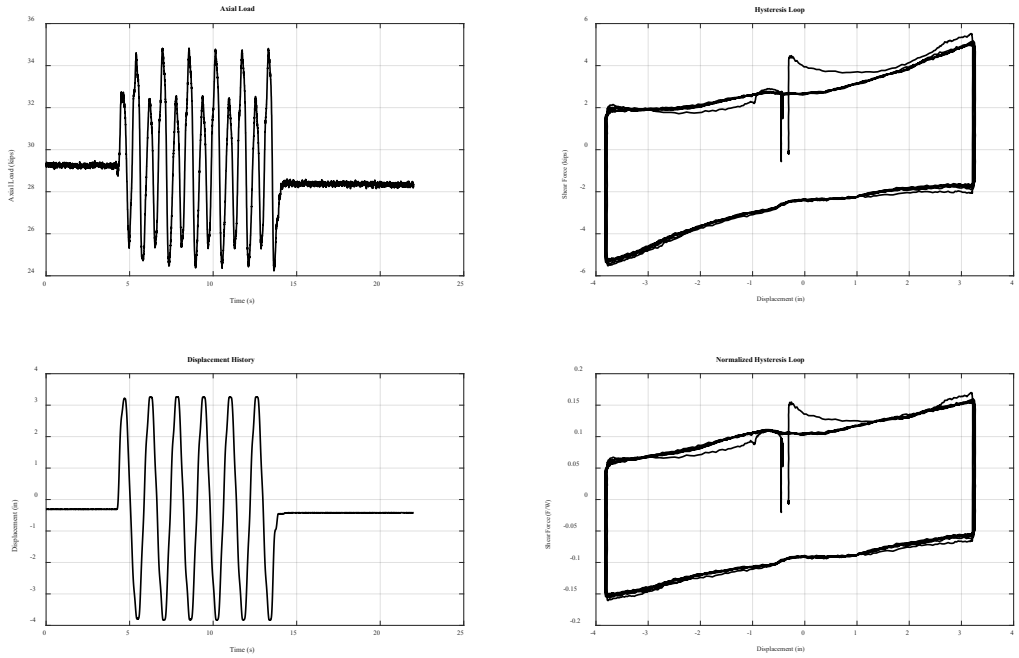

Figure C11. 12/29/2021 Robertson- Wet: 25 kips, sinusoidal Y @ 0.63Hz. Max disp = 4.05in

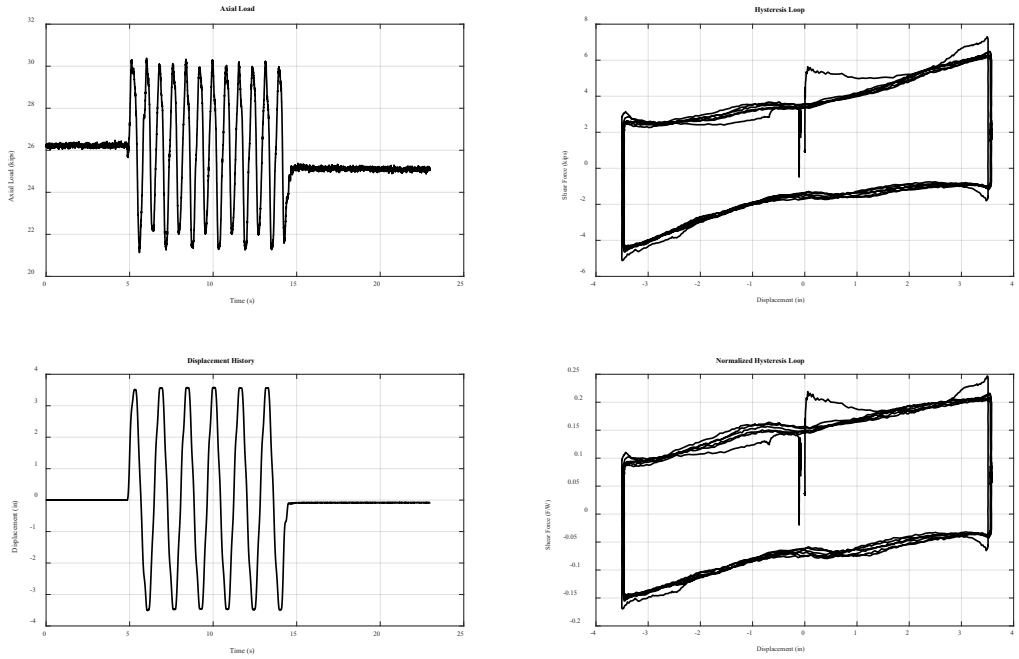

Figure C12. 10/1/2021 Robertson- Frozen half layer ice @ -25°C: 25 kips, sinusoidal Y @ 0.63Hz. Max disp = 4.05in

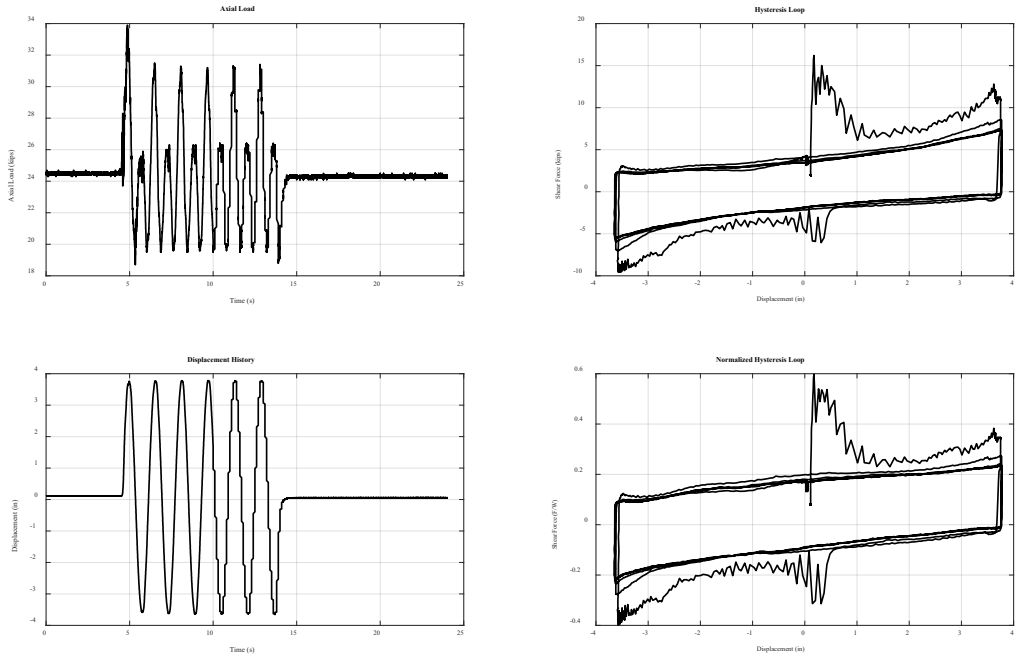

Figure C13. 9/28/2021 Robertson- Frozen @ -20°C: 25 kips, sinusoidal X @ 0.63Hz. Max disp = 4.05in

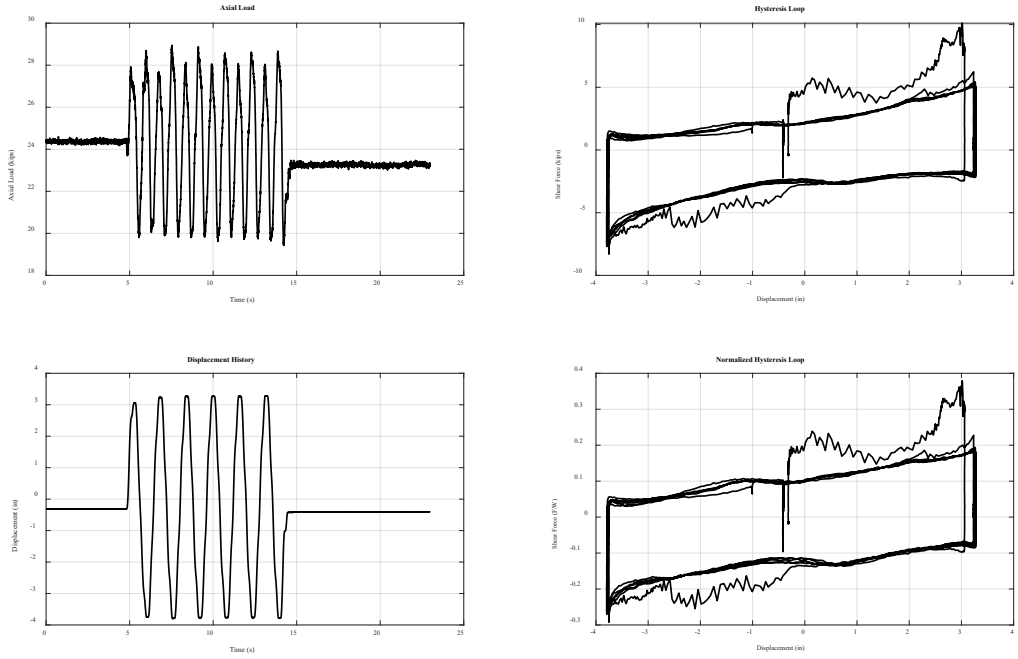

Figure C14. 9/28/2021 Robertson- Frozen @ -20°C: 25 kips, sinusoidal Y @ 0.63Hz. Max disp = 4.05in

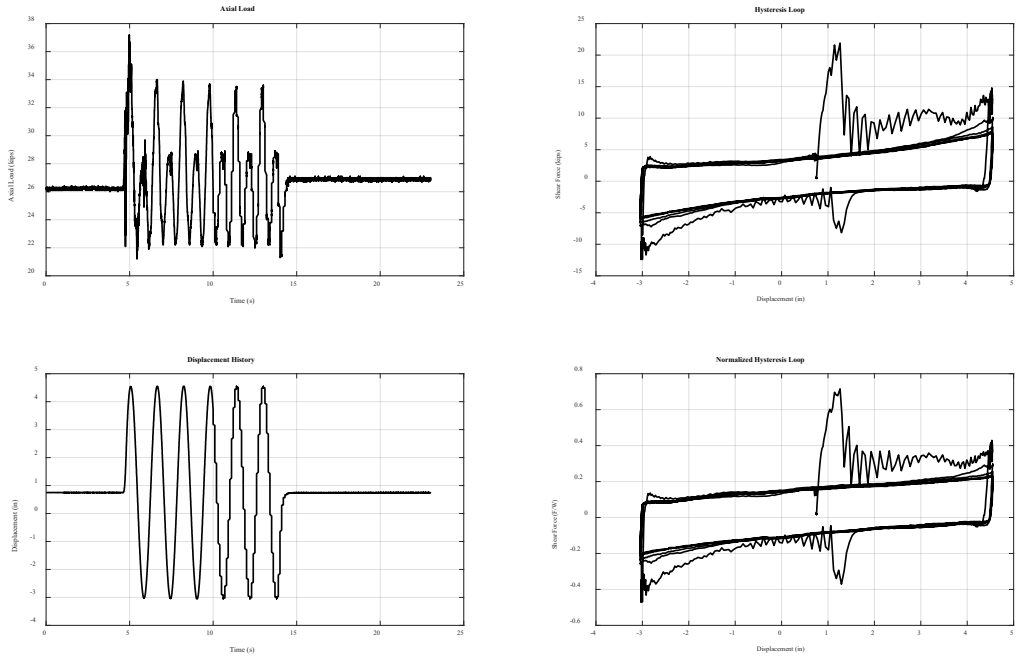

Figure C15. 9/29/2021 Robertson- Frozen @ -28°C: 25 kips, sinusoidal X @ 0.63Hz. Max disp = 4.05in

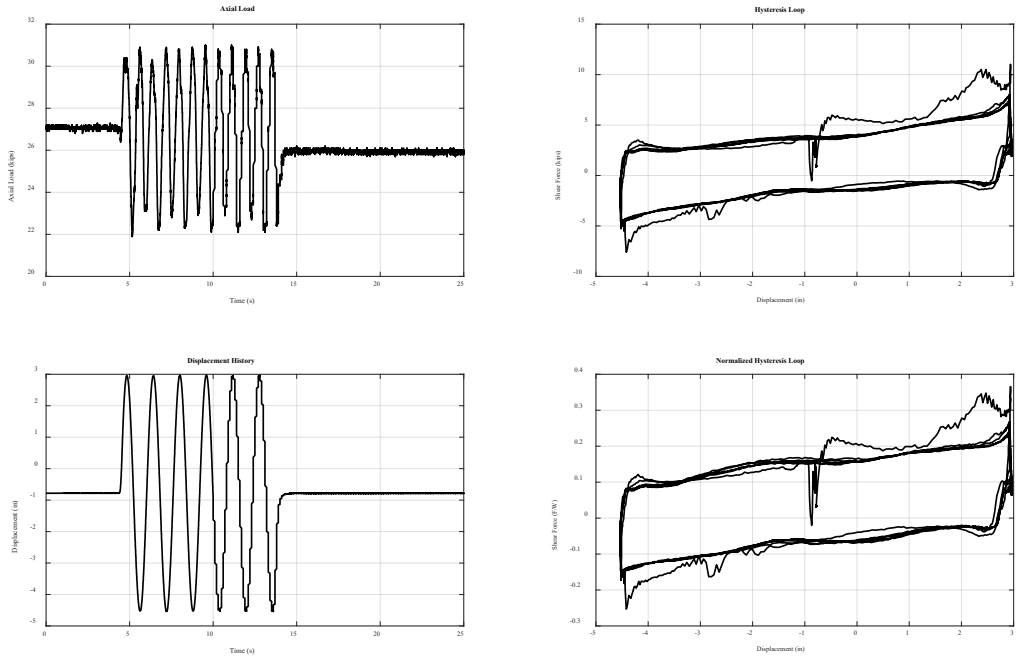

Figure C16. 9/29/2021 Robertson- Frozen @ -28°C: 25 kips, sinusoidal Y @ 0.63Hz. Max disp = 4.05in

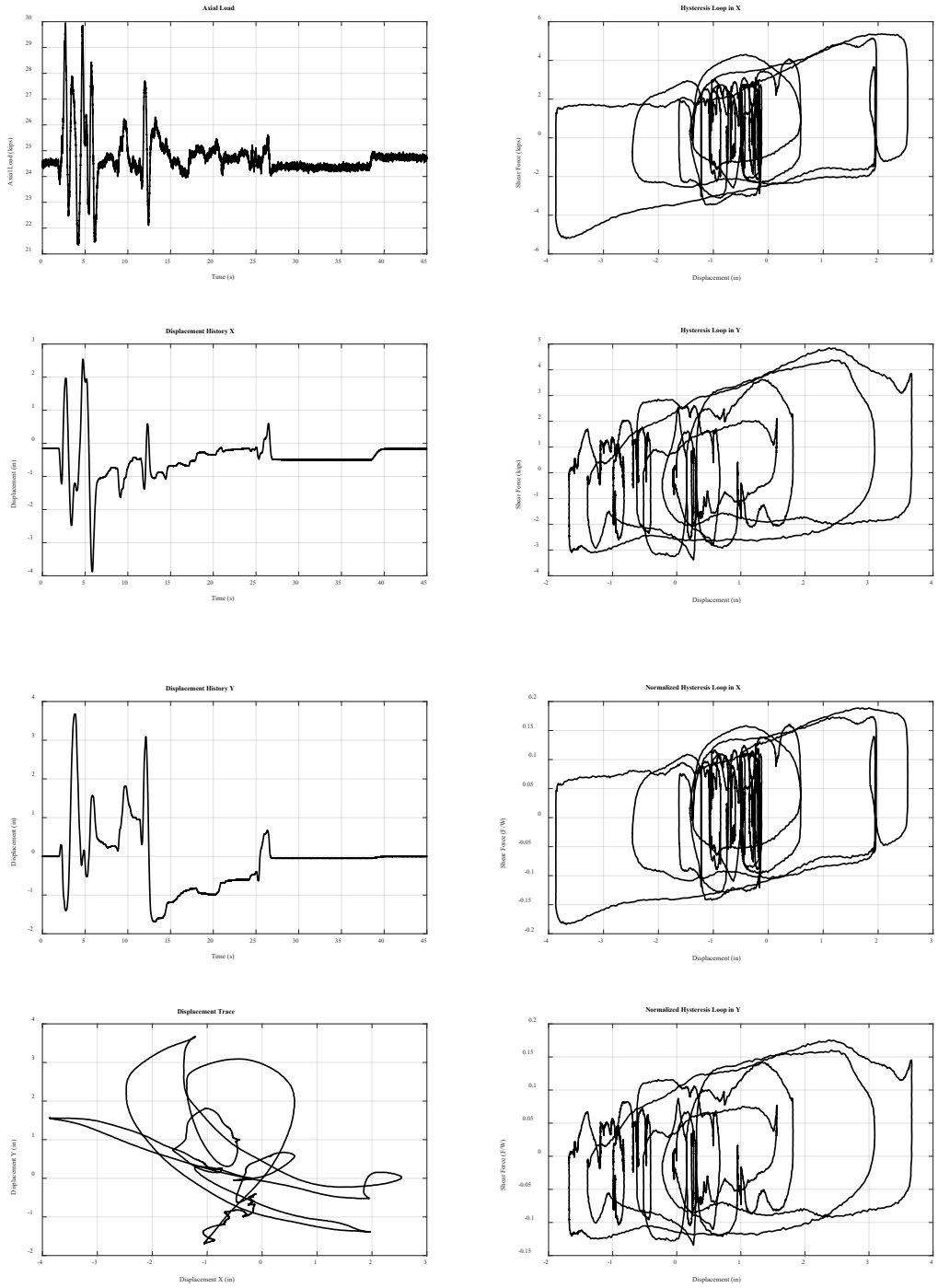

Figure C17. 9/27/2021 Robertson- Dry: 25 kips, GM3 X/Y. Imperial Valley. Max disp = 4.02in w/ scale factor = 1.56

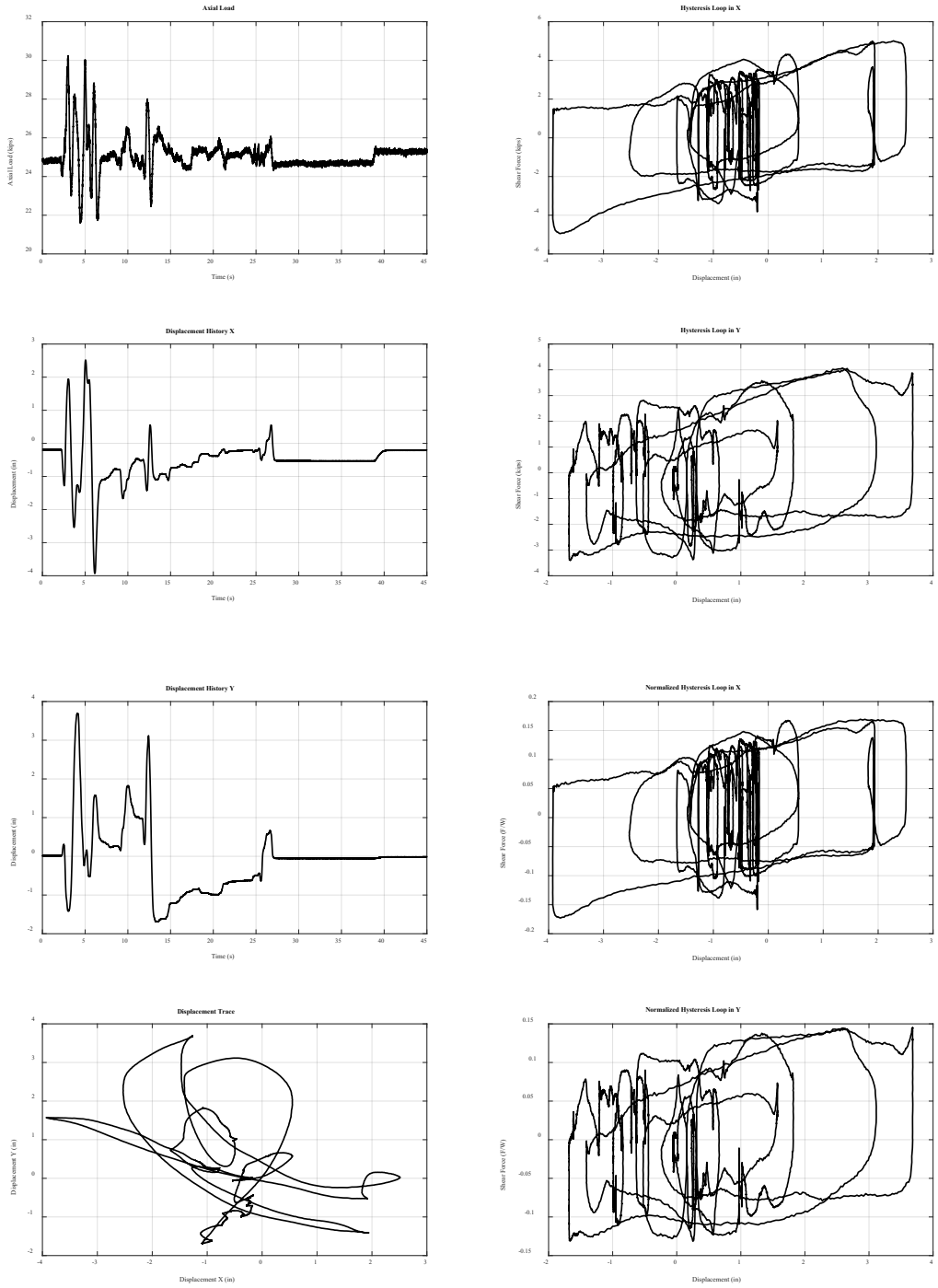

Figure C18. 9/27/2021 Robertson- Wet: 25 kips, GM3 X/Y. Imperial Valley. Max disp = 4.02in w/ scale factor = 1.56

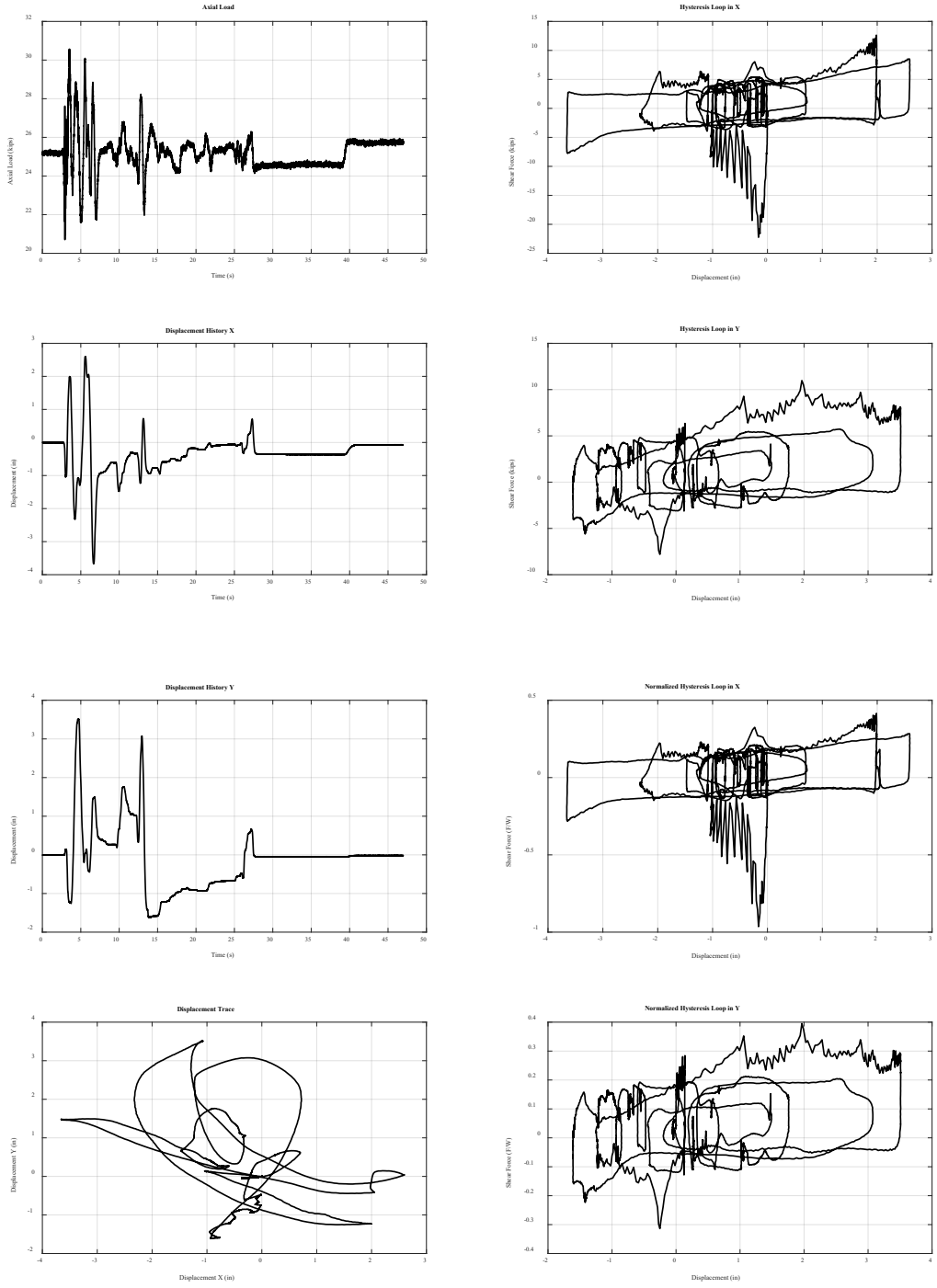

Figure C19. 9/30/2021 Robertson- Frozen @ -28°C: 25 kips, GM1 X/Y. Imperial Valley. Max disp = 4.02in w/ scale factor = 1.56

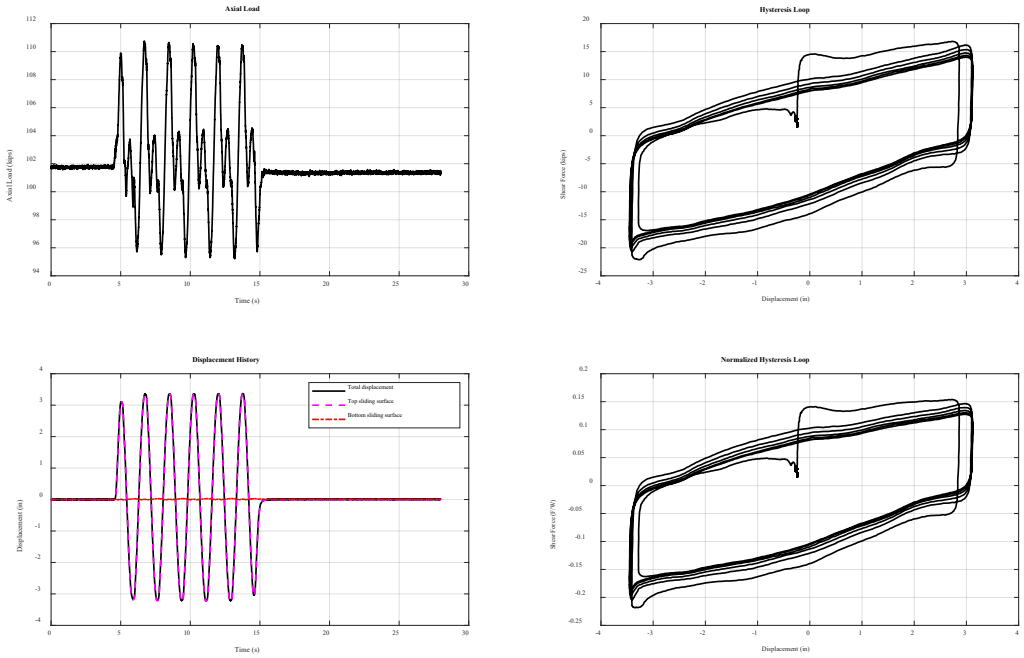

Figure C20. 9/20/2021 Aged Susitna 1- Dry as received full of dirt: 100 kips, sinusoidal X @ 0.57Hz. Max disp = 3.72in

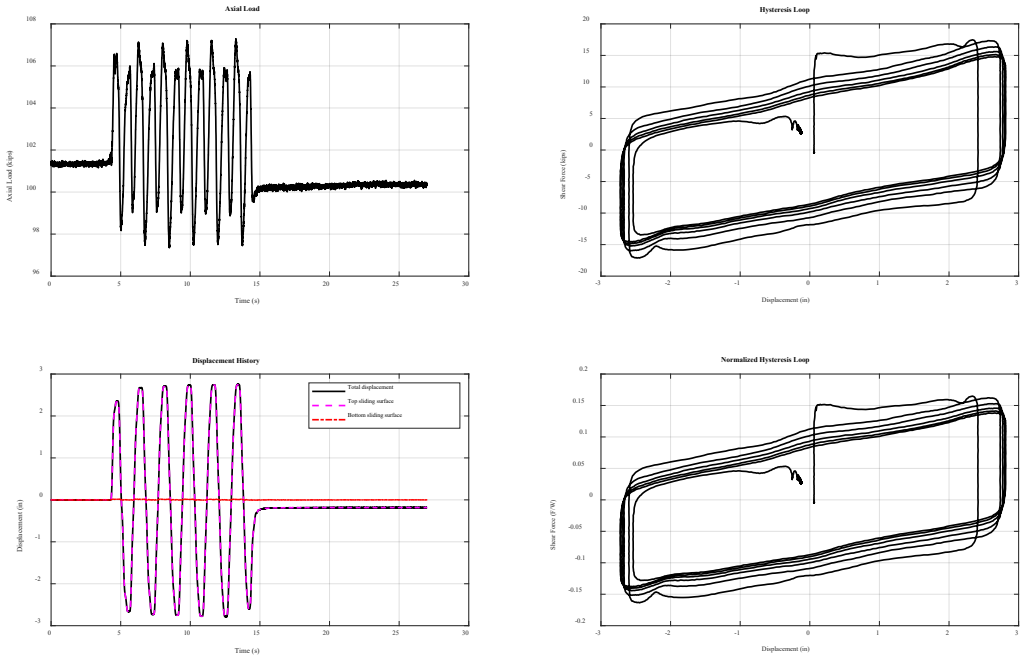

Figure C21. 9/20/2021 Aged Susitna 1- Dry as received full of dirt: 100 kips, sinusoidal Y @ 0.57Hz. Max disp = 3.72in

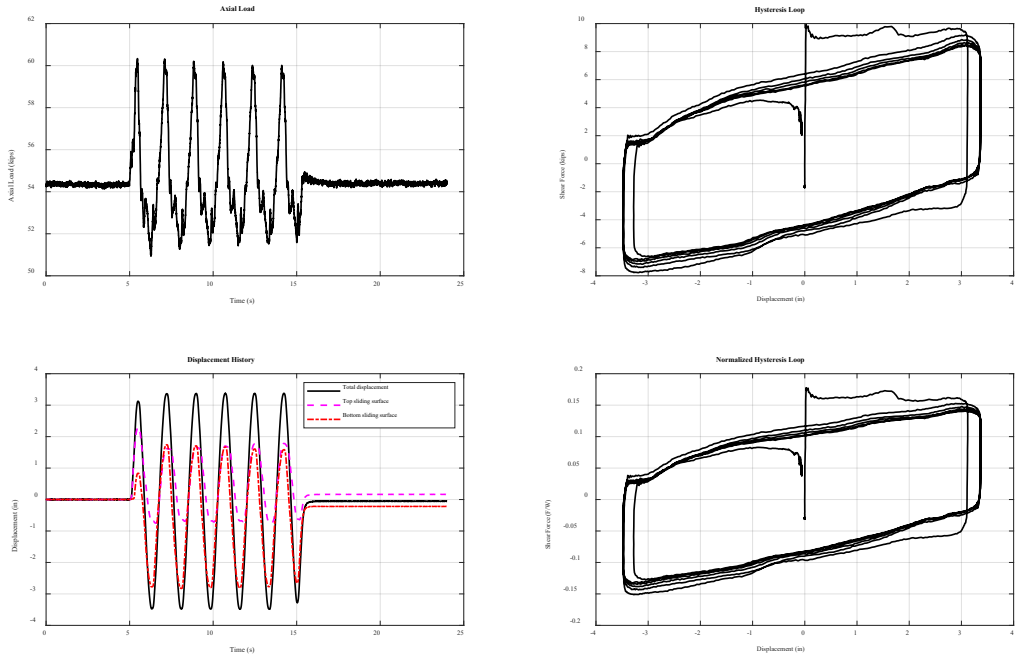

Figure C22. 9/23/2021 Aged Susitna 1- Dry: 55 kips, sinusoidal X @ 0.57Hz. Max disp = 3.72in

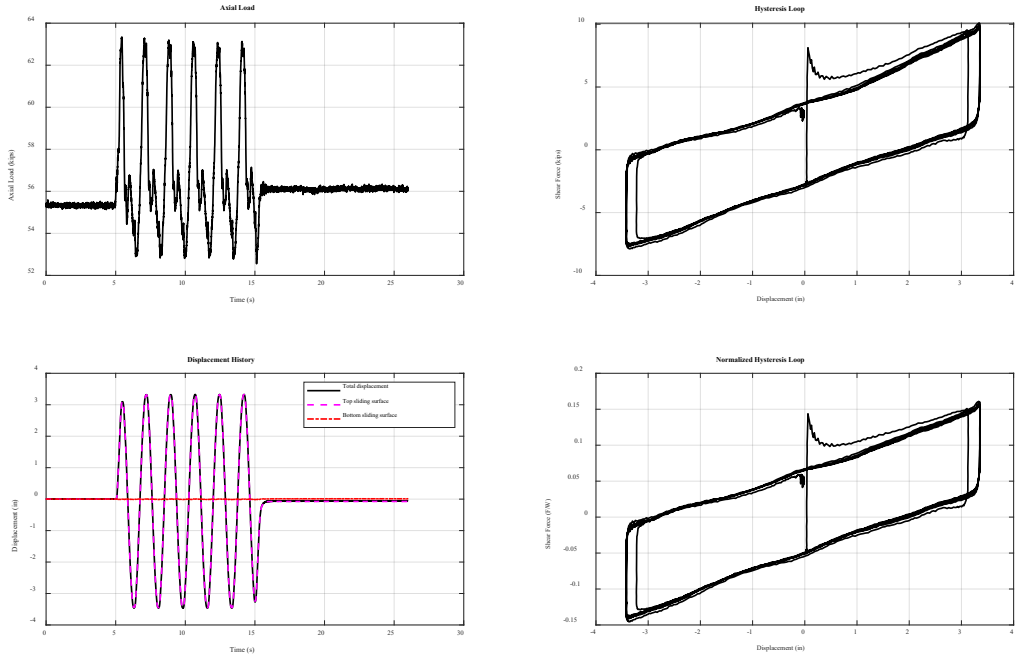

Figure C23. 9/22/2021 Aged Susitna 1- Wet: 55 kips, sinusoidal X @ 0.57Hz. Max disp = 3.72in

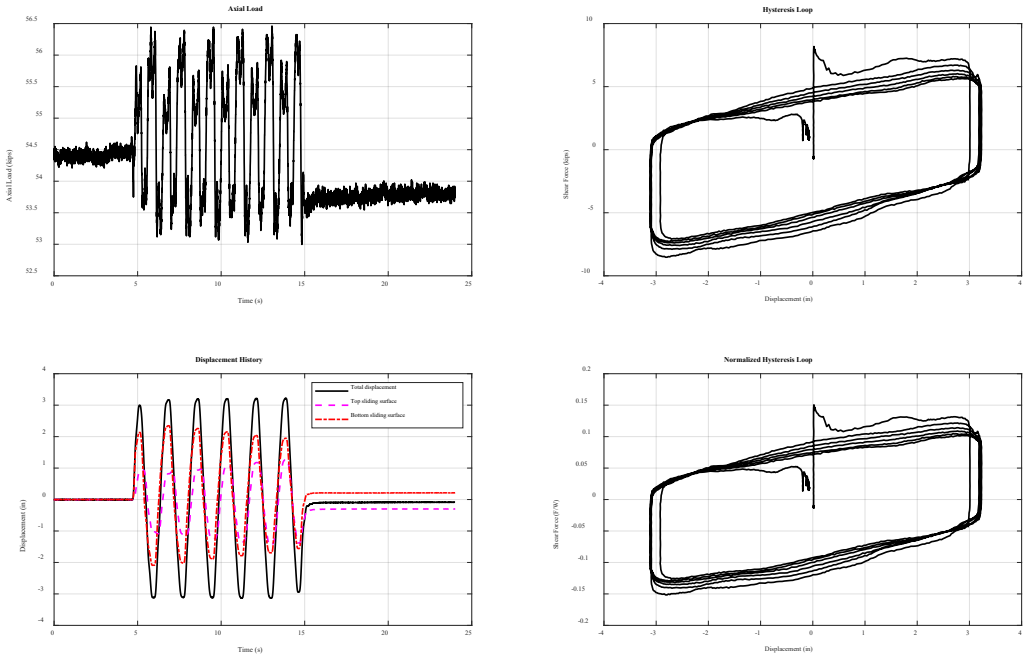

Figure C24. 9/23/2021 Aged Susitna 1- Dry: 55 kips, sinusoidal Y @ 0.57Hz. Max disp = 3.72in

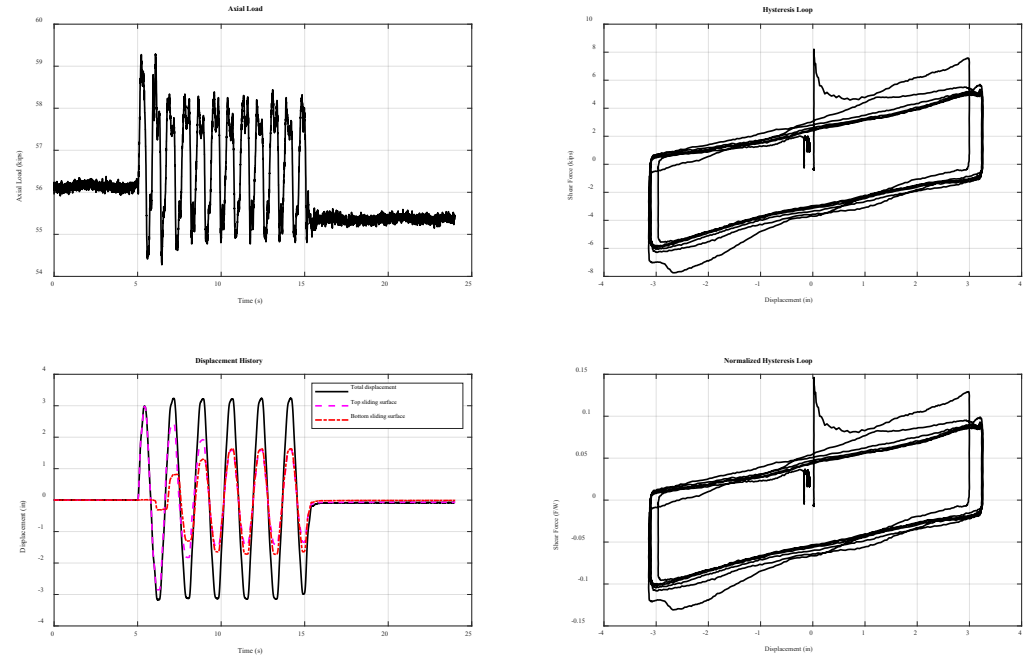

Figure C25. 9/22/2021 Aged Susitna 1- Wet: 55 kips, sinusoidal Y @ 0.57Hz. Max disp = 3.72in

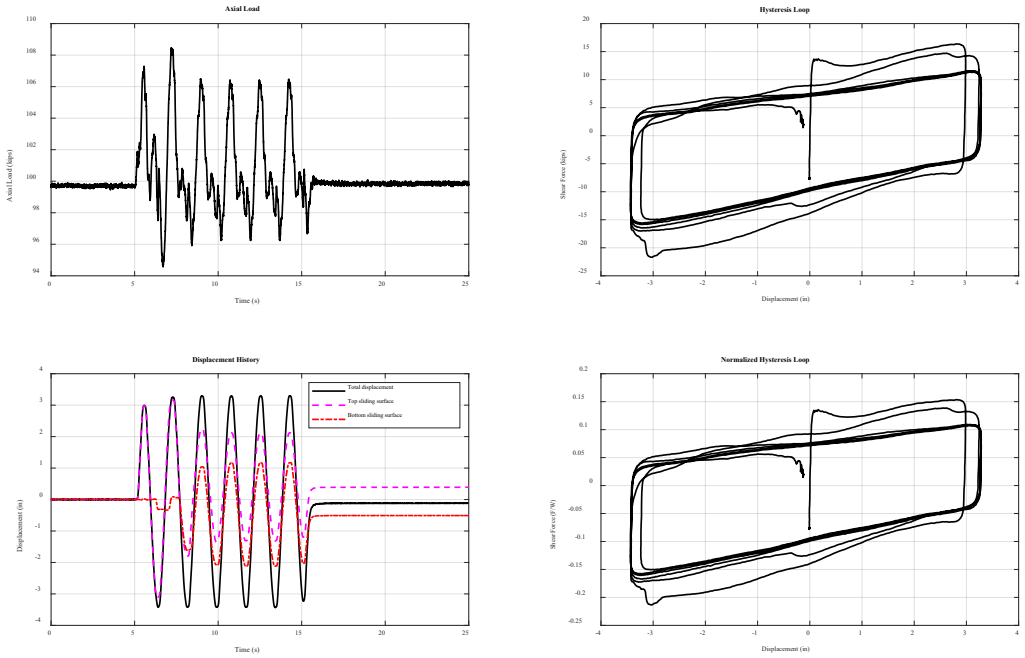

Figure C26. 9/20/2021 Aged Susitna 1- Dry: 100 kips, sinusoidal X @ 0.57Hz. Max disp = 3.72in

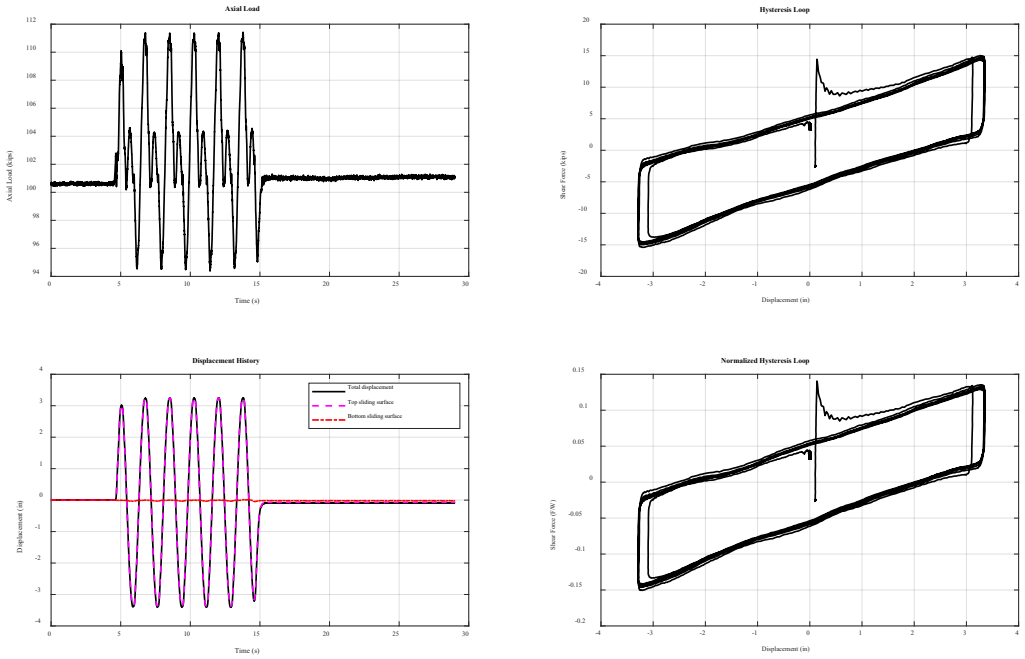

Figure C27. 9/23/2021 Aged Susitna 1- Wet: 100 kips, sinusoidal X @ 0.57Hz. Max disp = 3.72in

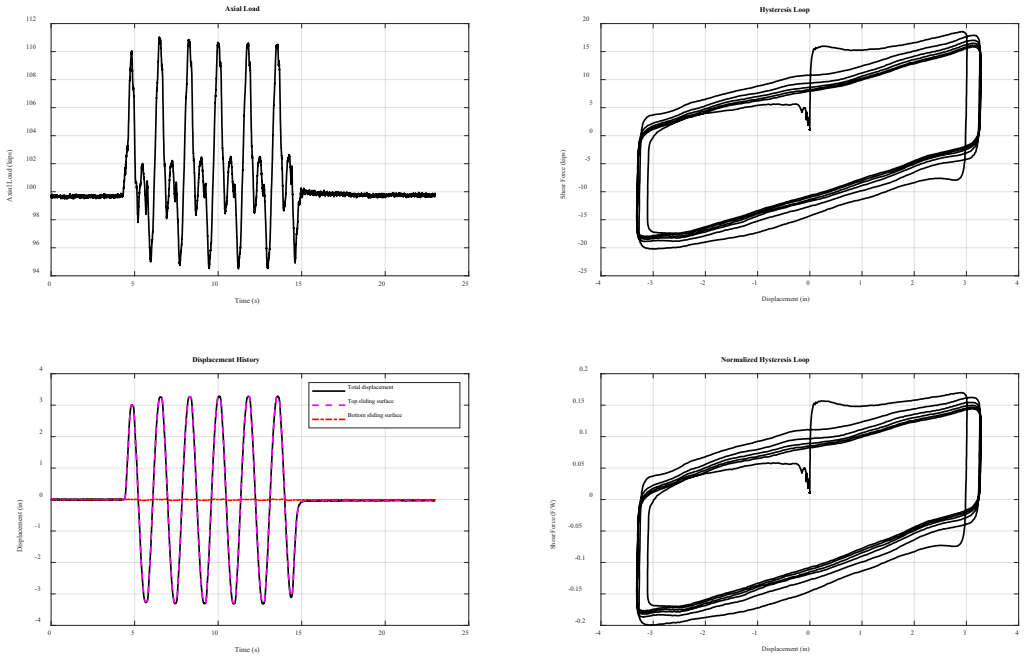

Figure C28. 9/21/2021 Aged Susitna 1- Frozen @ -15°C: 100 kips, sinusoidal X @ 0.57Hz. Max disp = 3.72in

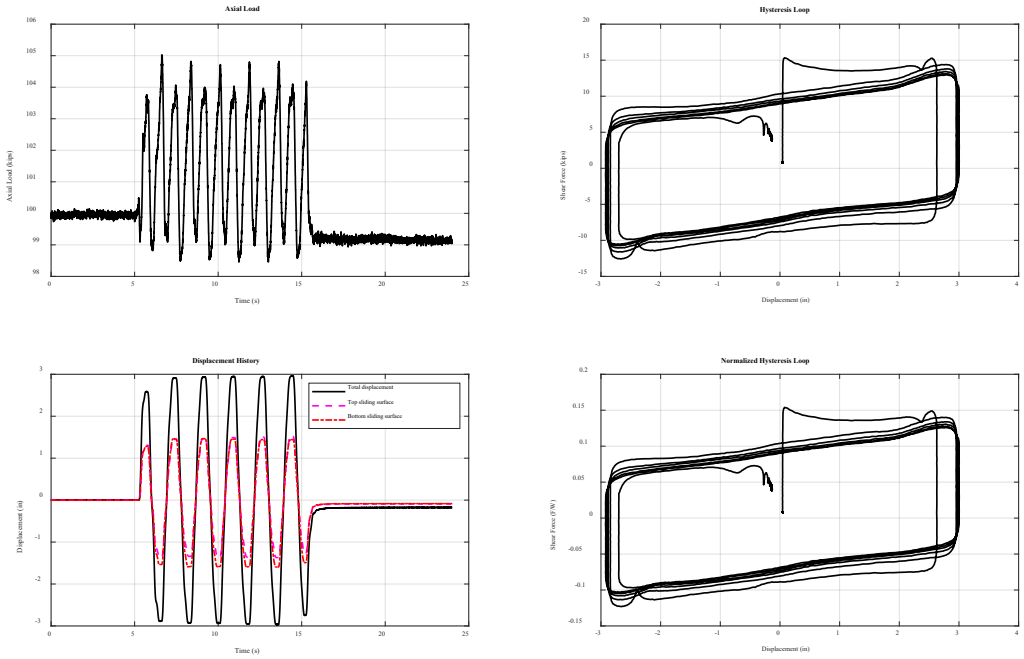

Figure C29. 9/20/2021 Aged Susitna 1- Dry: 100 kips, sinusoidal Y @ 0.57Hz. Max disp = 3.72in

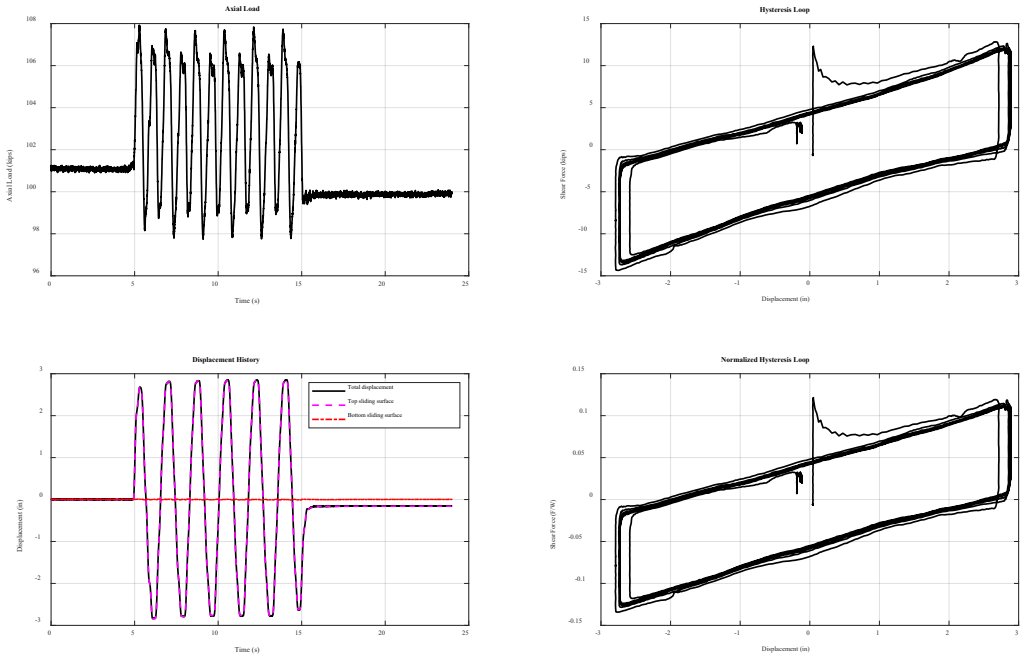

Figure C30. 9/23/2021 Aged Susitna 1- Wet: 100 kips, sinusoidal Y @ 0.57Hz. Max disp = 3.72in

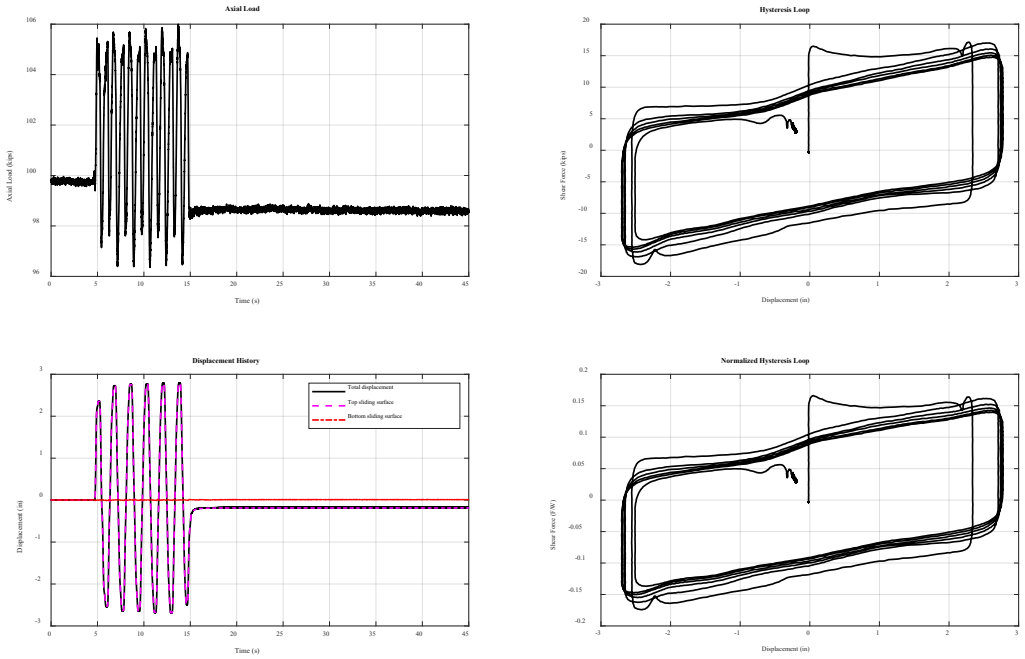

Figure C31. 9/21/2021 Aged Susitna 1- Frozen @ -15°C: 100 kips, sinusoidal Y @ 0.57Hz. Max disp = 3.72in

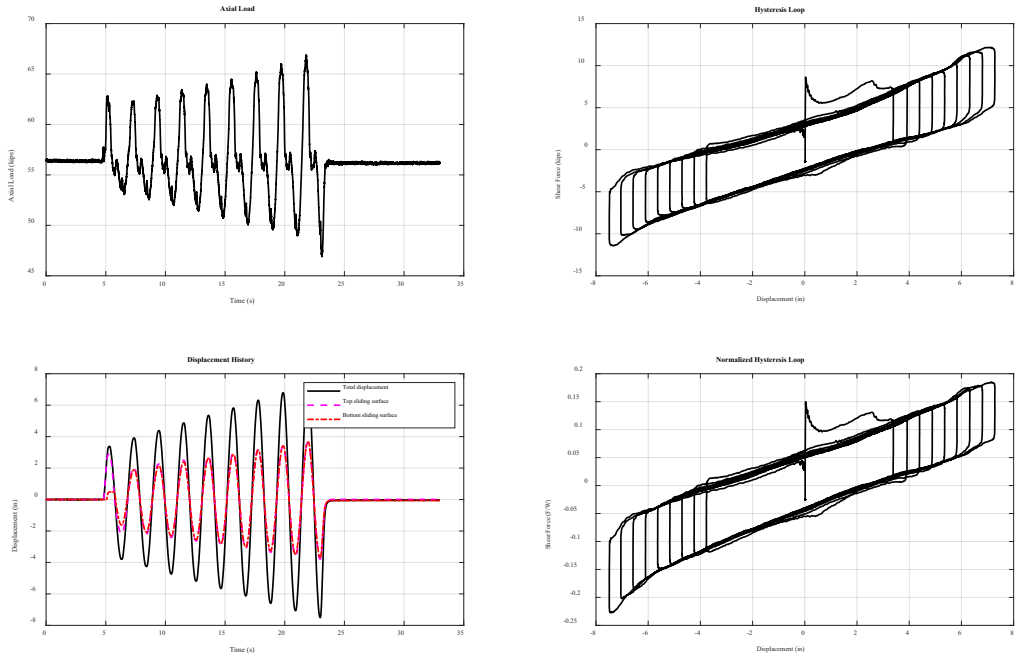

Figure C32. 9/22/2021 Aged Susitna 1- Wet: 55 kips, ramping sinusoidal X @ 0.48Hz. Max disp = 8in

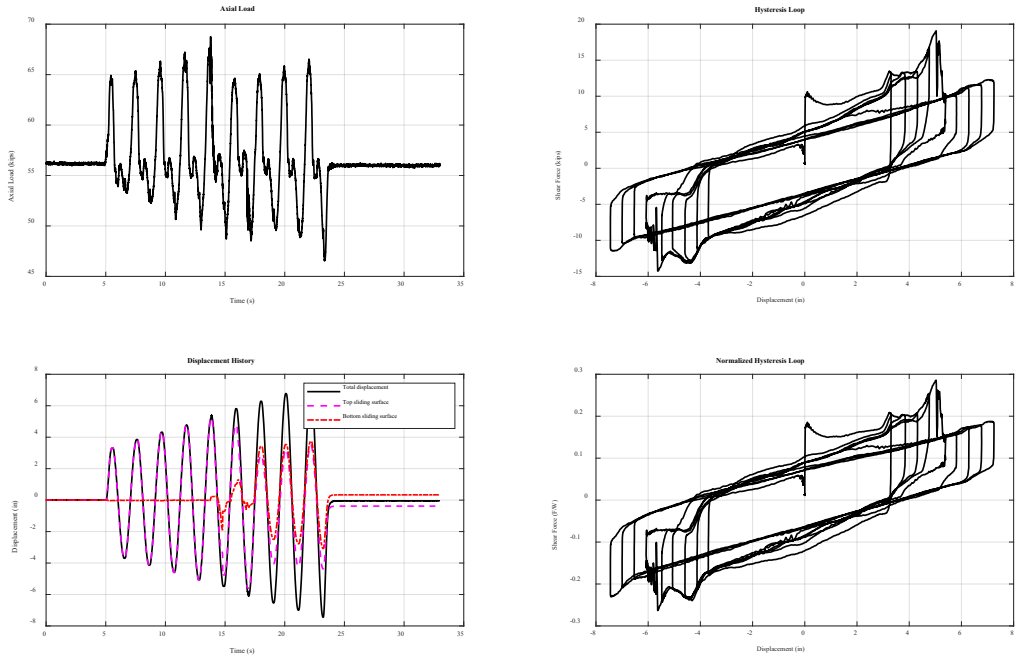

Figure C33. 9/22/2021 Aged Susitna 1- Frozen @ -18°C: 55 kips, ramping sinusoidal X @ 0.48Hz. Max disp = 8in

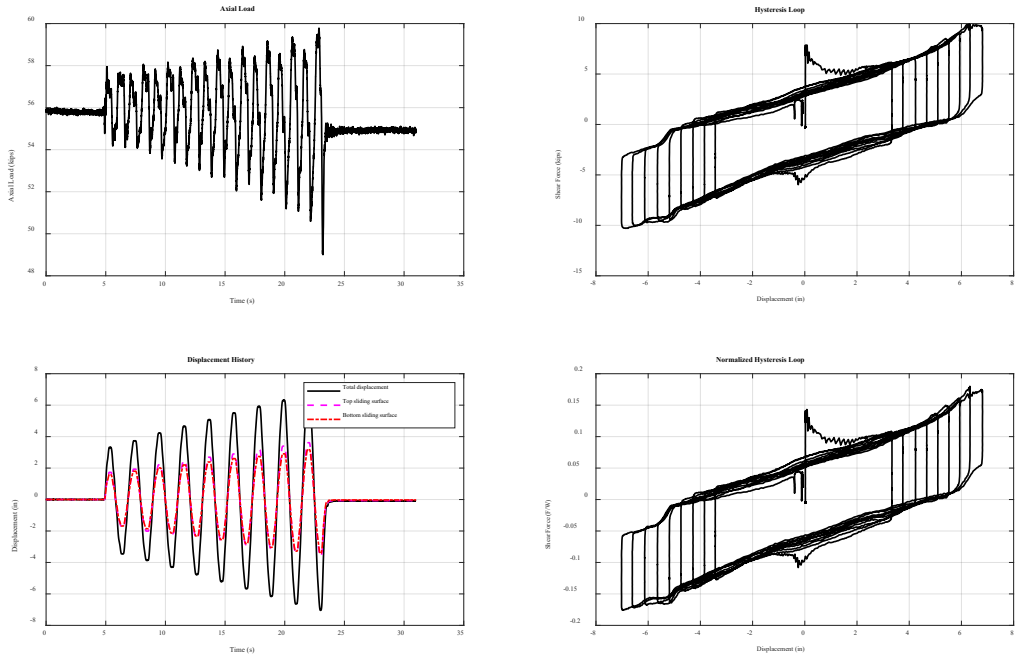

Figure C34. 9/22/2021 Aged Susitna 1- Frozen @ -18°C: 55 kips, ramping sinusoidal Y @ 0.48Hz. Max disp = 8in

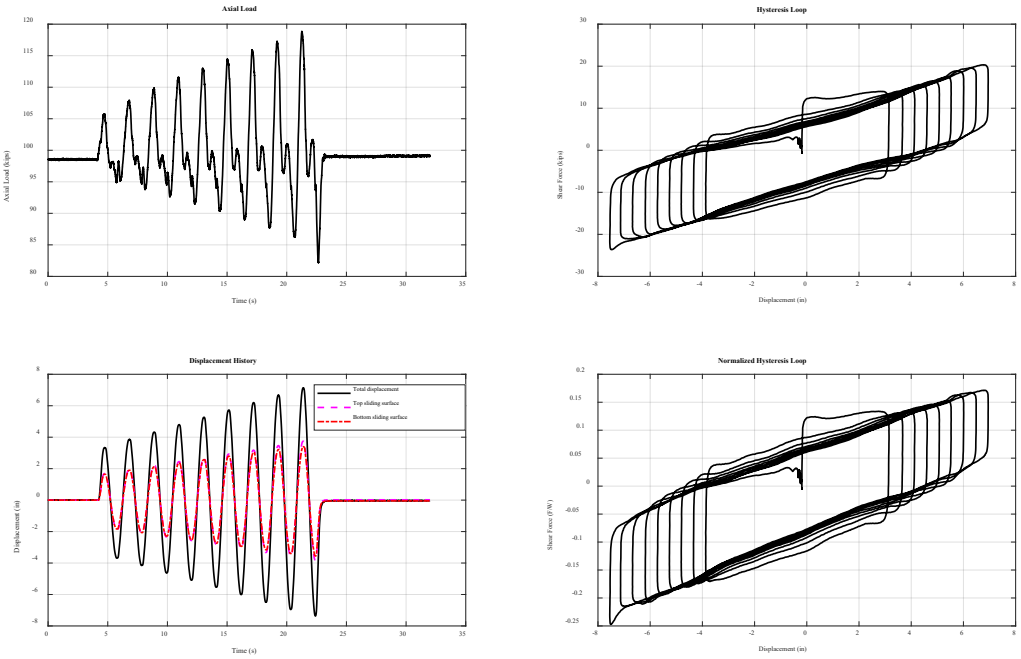

Figure C35. 9/23/2021 Aged Susitna 1- Dry: 100 kips, ramping sinusoidal X @ 0.48Hz. Max disp = 8in

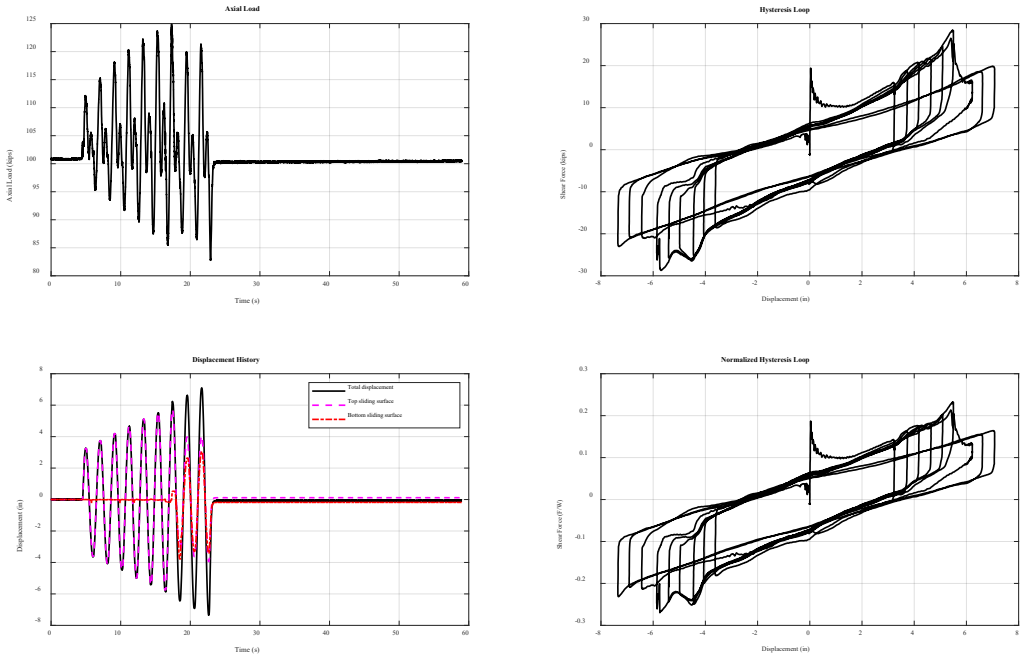

Figure C36. 9/23/2021 Aged Susitna 1- Frozen @ -16°C: 100 kips, ramping sinusoidal X @ 0.48Hz. Max disp = 8in

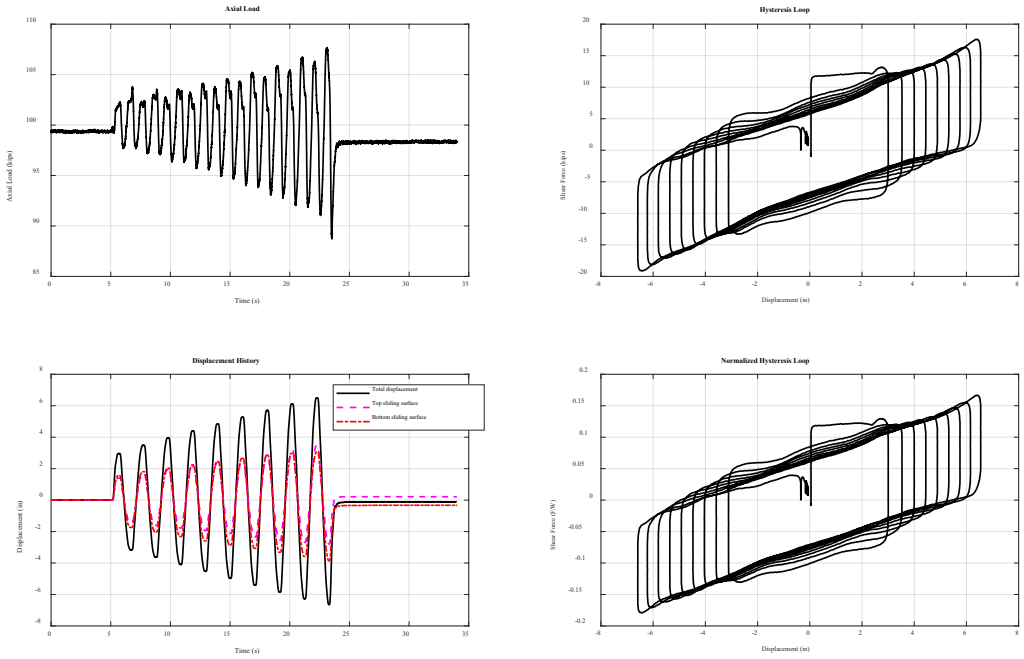

Figure C37. 9/23/2021 Aged Susitna 1- Dry: 100 kips, ramping sinusoidal Y @ 0.48Hz. Max disp = 8in

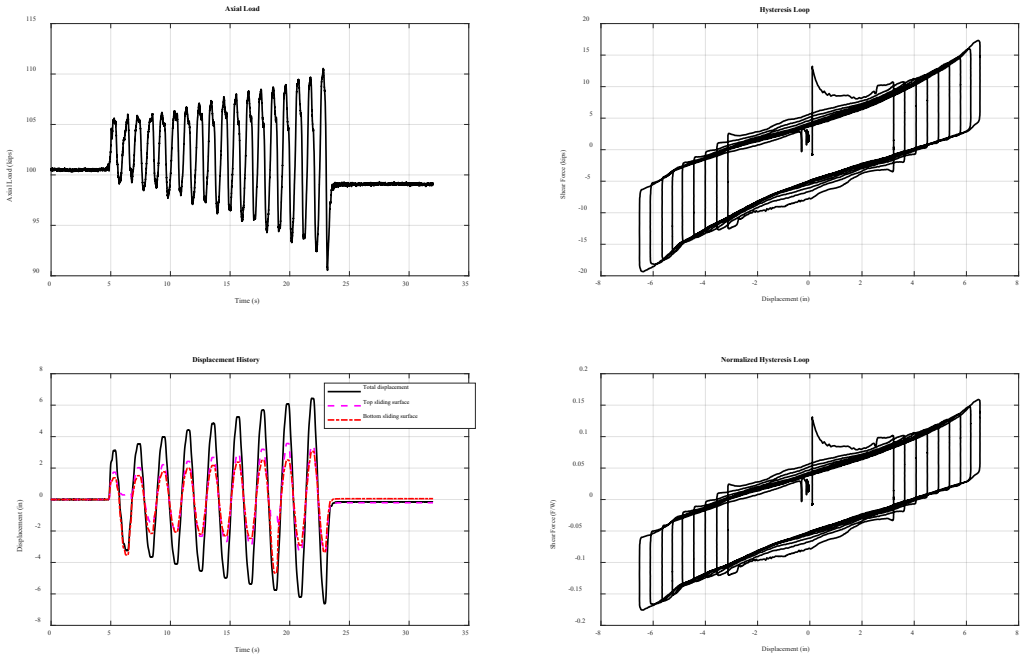

Figure C38. 9/23/2021 Aged Susitna 1- Frozen @ -16°C: 100 kips, ramping sinusoidal Y @ 0.48Hz. Max disp = 8in

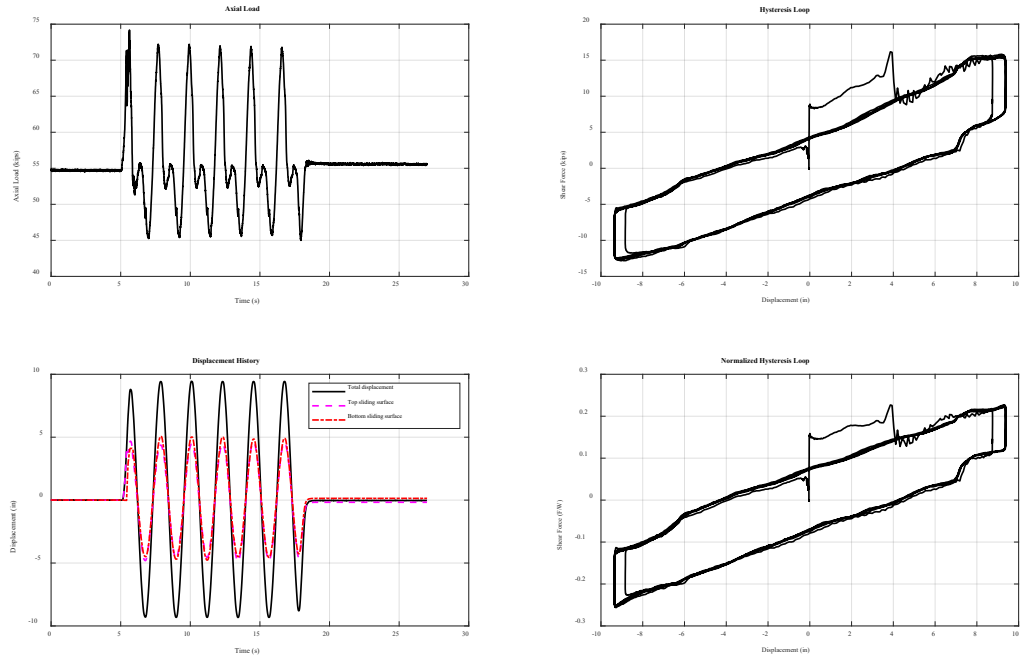

Figure C39. 12/9/2021 Aged Susitna 1- Dry: 55 kips, sinusoidal Y @ 0.45Hz. Max disp = 10in

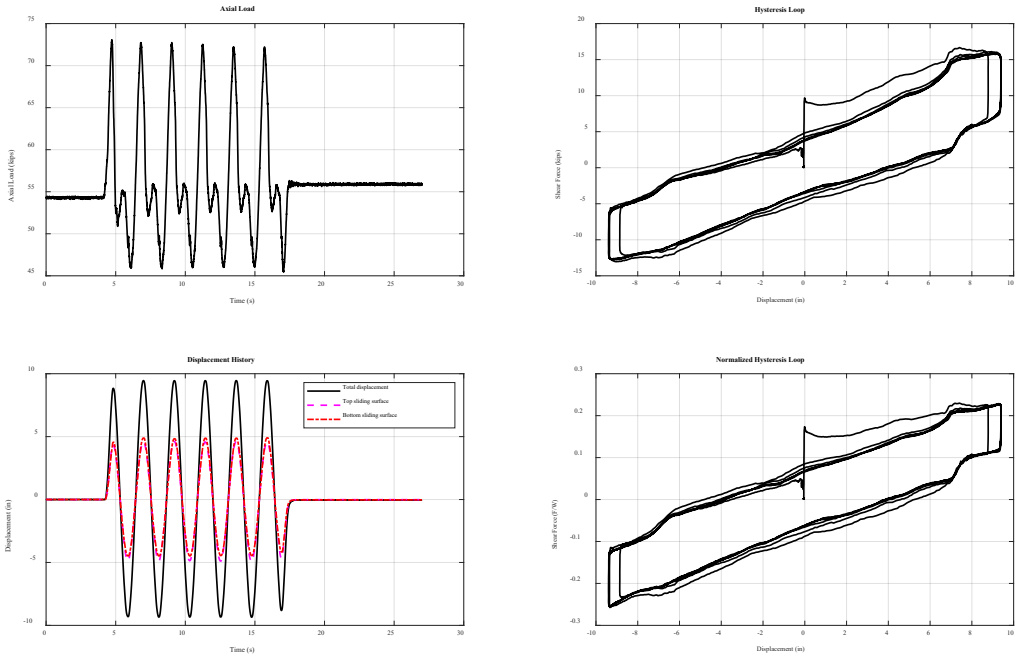

Figure C40. 12/9/2021 Aged Susitna 1- Wet: 55 kips, sinusoidal X @ 0.45Hz. Max disp = 10in

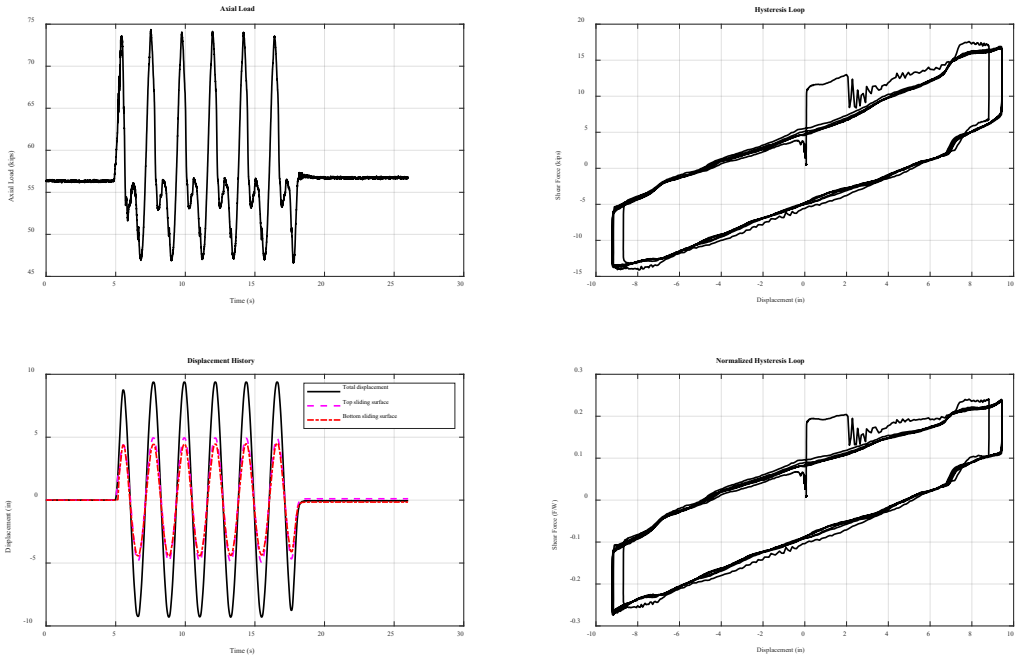

Figure C41. 12/9/2021 Aged Susitna 1- Frozen @ -24°C: 55 kips, sinusoidal X @ 0.45Hz. Max disp = 10in

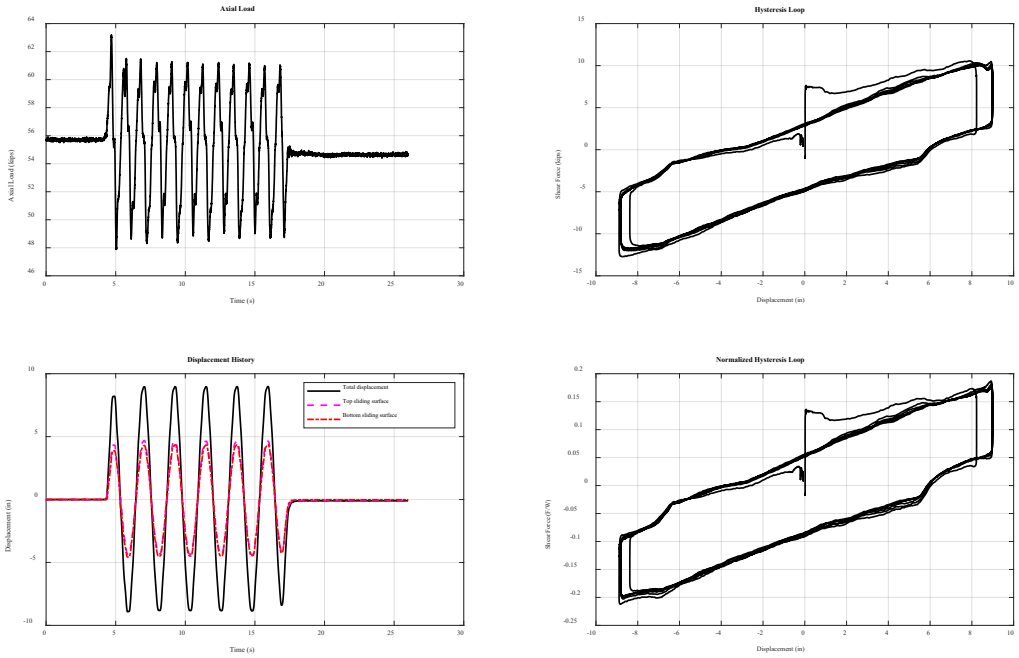

Figure C42. 12/9/2021 Aged Susitna 1- Dry: 55 kips, sinusoidal Y @ 0.45Hz. Max disp = 10in

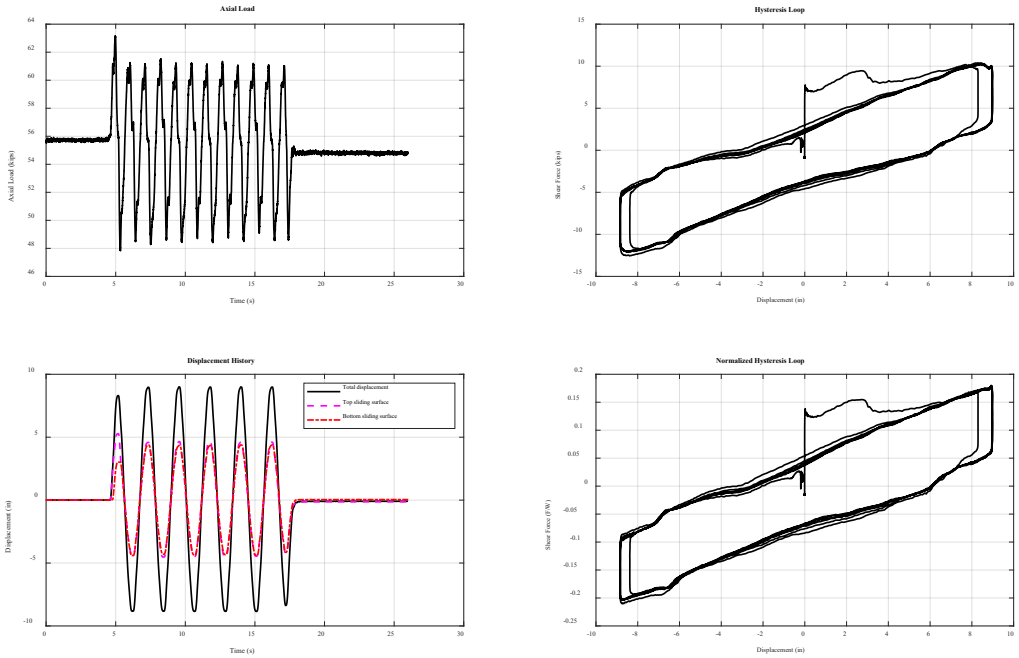

Figure C43. 12/9/2021 Aged Susitna 1- Wet: 55 kips, sinusoidal Y @ 0.45Hz. Max disp = 10in

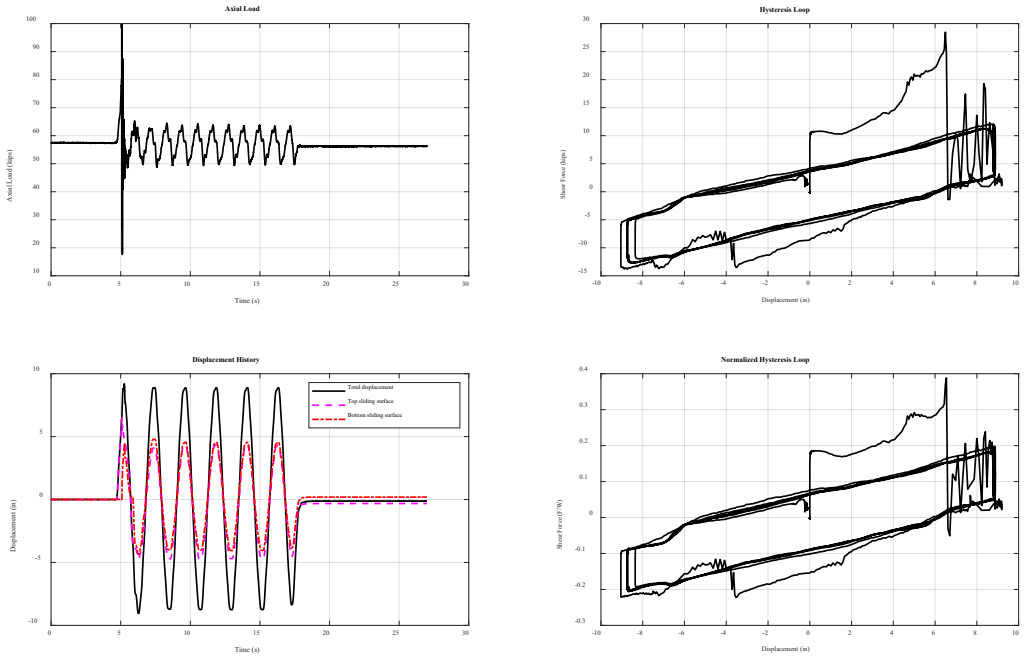

Figure C44. 12/9/2021 Aged Susitna 1- Frozen @ -24°C: 55 kips, sinusoidal Y @ 0.45Hz. Max disp = 10in

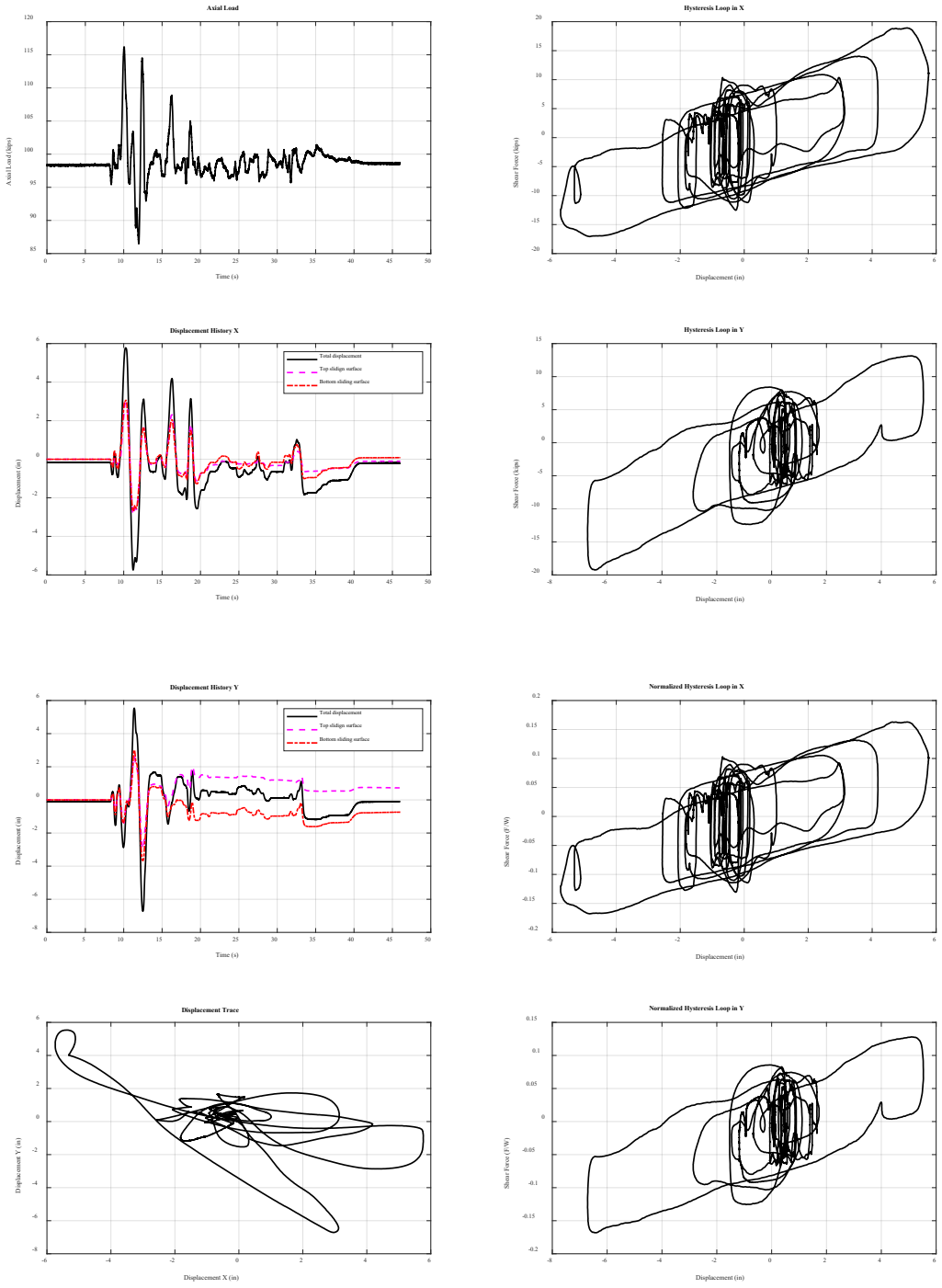

Figure C45. 9/23/2021 Aged Susitna 1- Dry: 100 kips, GM2 X/Y. El Centro. Max disp = 8.6in w/ scale factor = 2.02

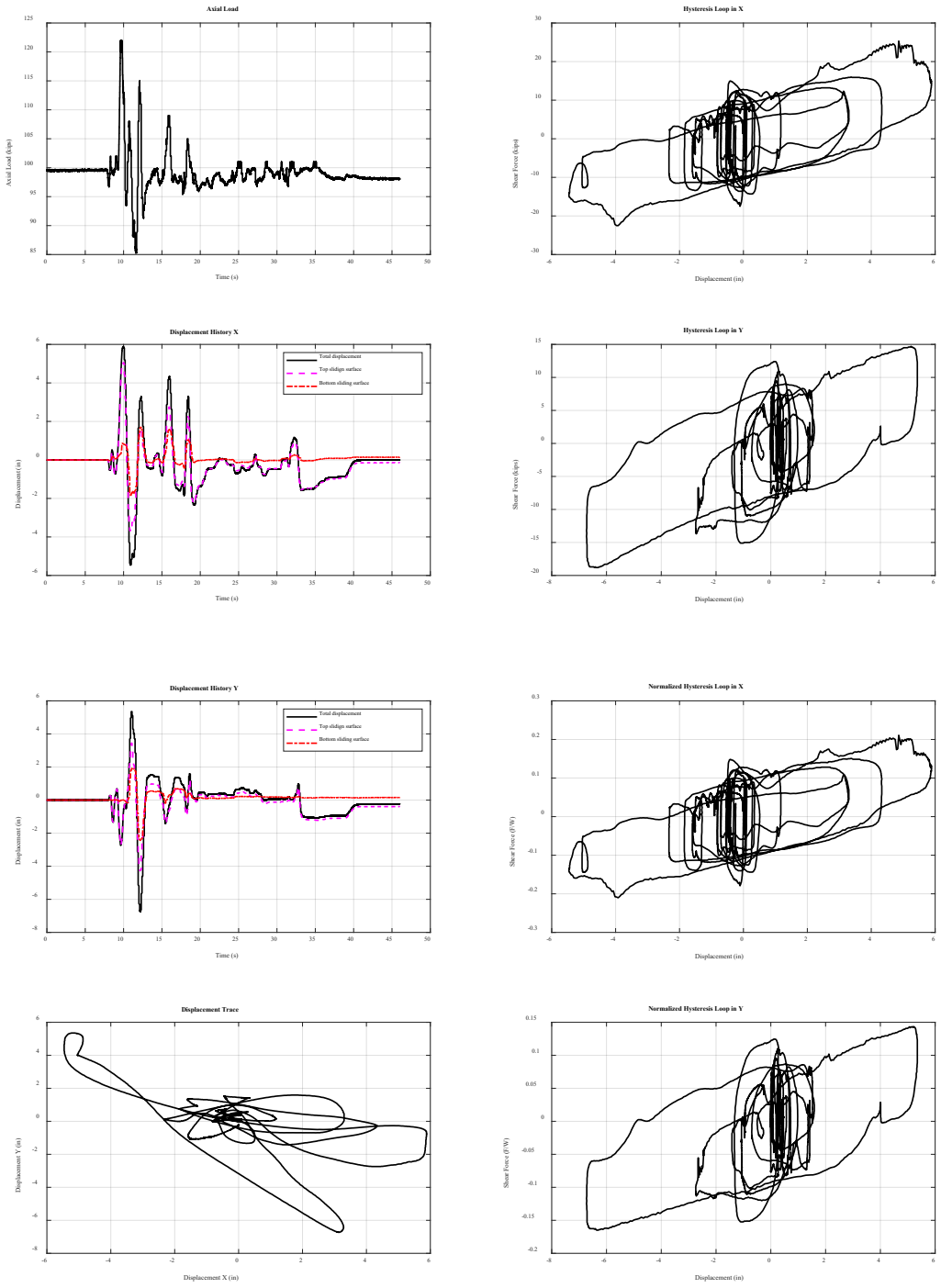

Figure C46. 9/24/2021 Aged Susitna 1- Frozen: 100 kips, GM2 X/Y. El Centro. Max disp = 8.6in w/ scale factor = 2.02

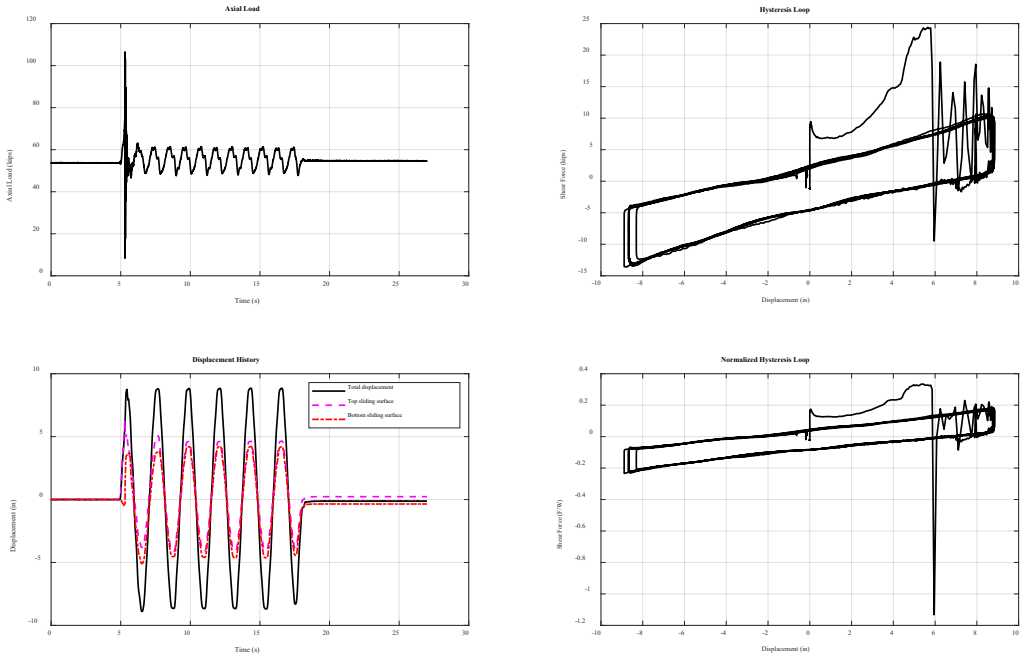

Figure C47. 12/16/2021 Aged Susitna 2- Frozen as received thin layer of dirt & ice @ -22°C: 55 kips, sinusoidal Y @ 0.45Hz. Max disp = 10in

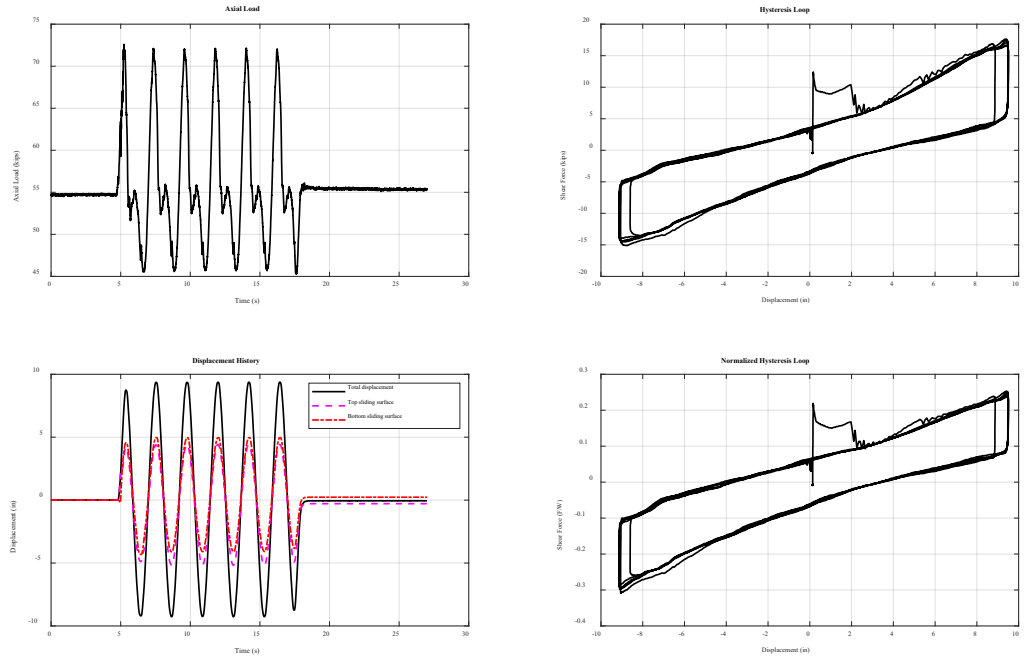

Figure C48. 12/16/2021 Aged Susitna 2- Frozen as received thin layer of dirt & ice @ -22°C: 55 kips, sinusoidal X @ 0.45Hz. Max disp = 10in

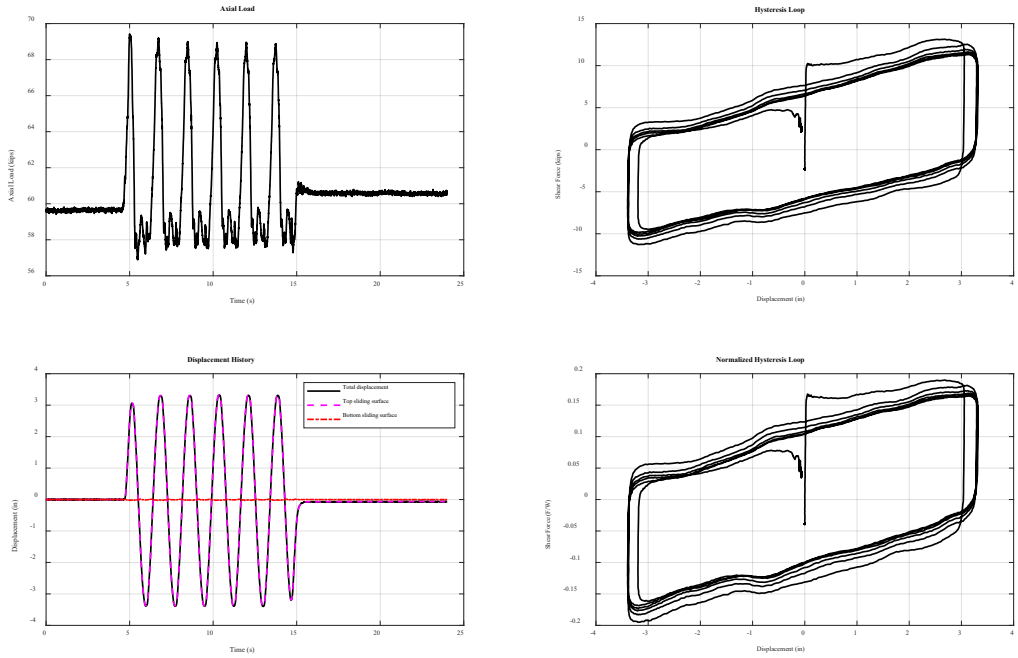

Figure C49. 1/5/2022 Aged Susitna 2- Baked Soil: 55 kips, sinusoidal X @ 0.57Hz. Max disp = 3.72in

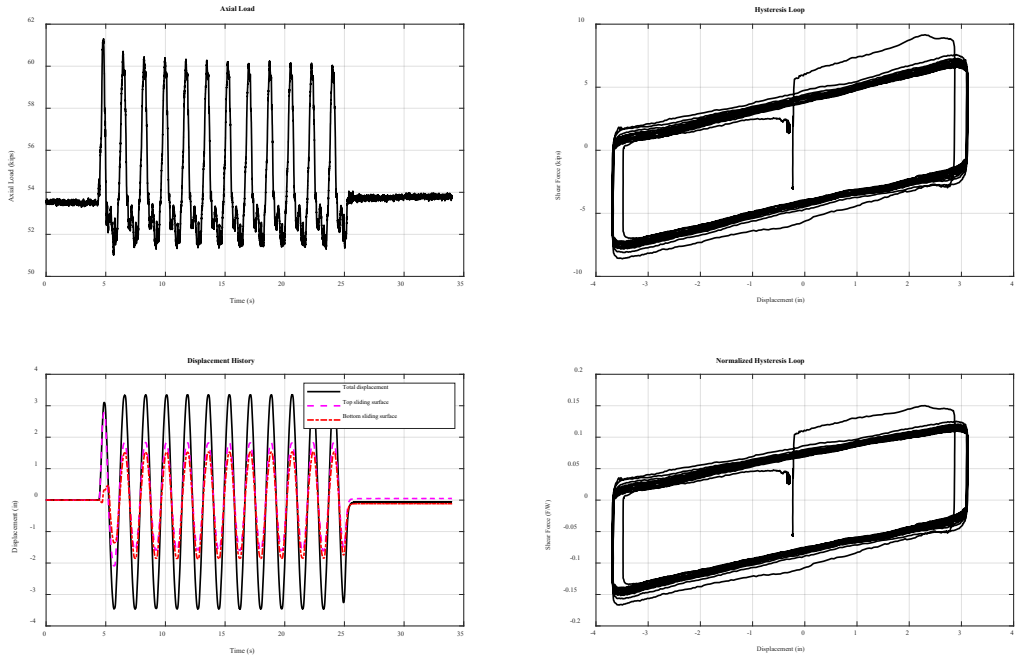

Figure C50. 12/22/2021 Aged Susitna 2- Wet: 55 kips, sinusoidal X @ 0.57Hz. Max disp = 3.72in

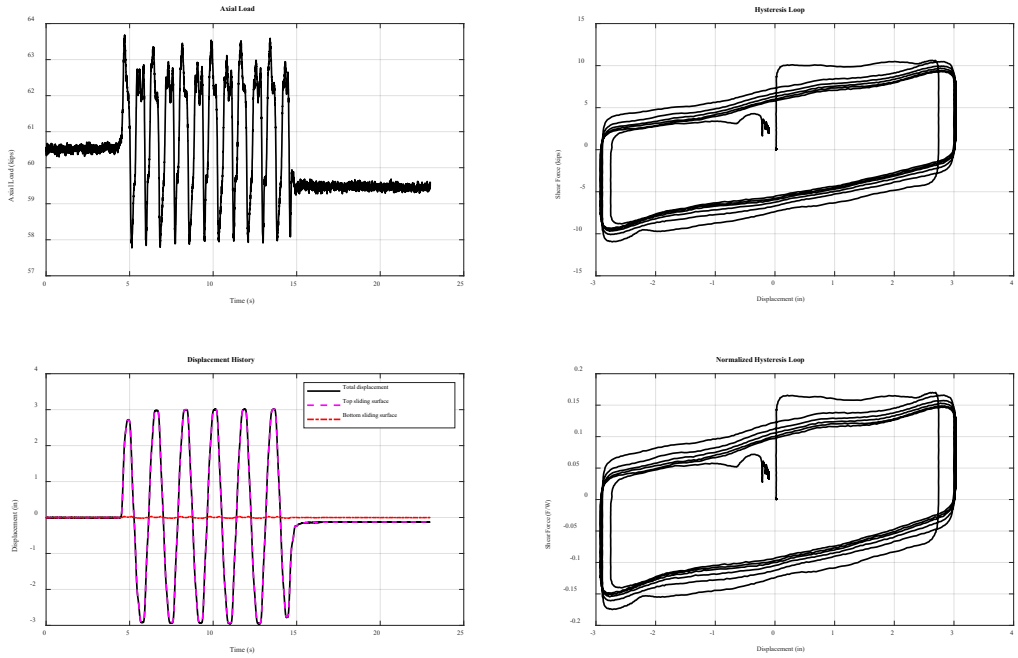

Figure C51. 1/5/2022 Aged Susitna 2- Baked Soil: 55 kips, sinusoidal Y @ 0.57Hz. Max disp = 3.72in

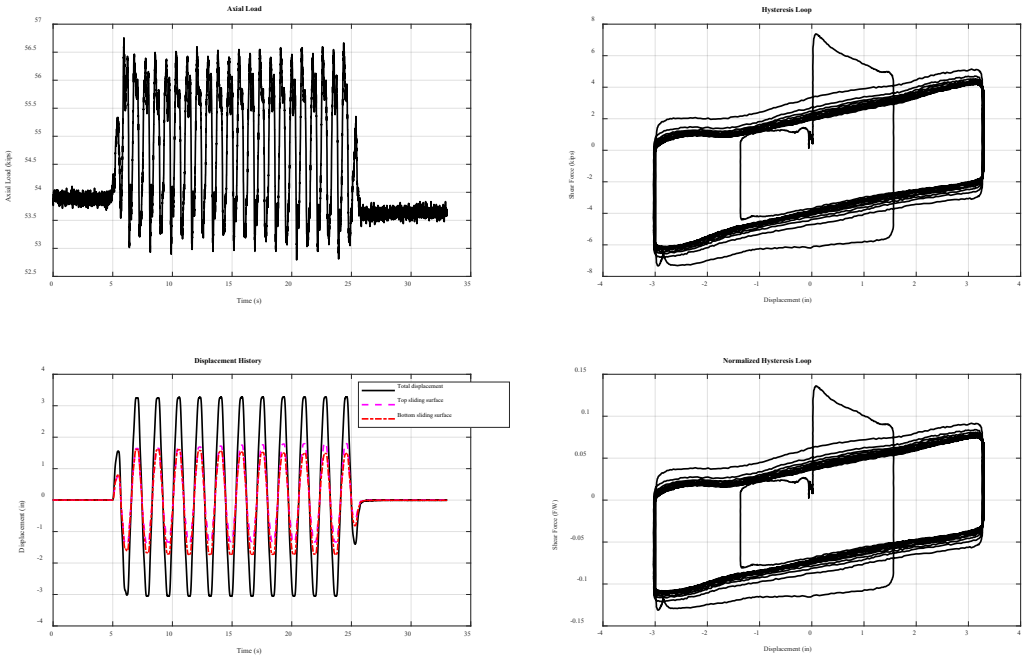

Figure C52. 12/22/2021 Aged Susitna 2- Wet: 55 kips, sinusoidal Y @ 0.57Hz. Max disp = 3.72in

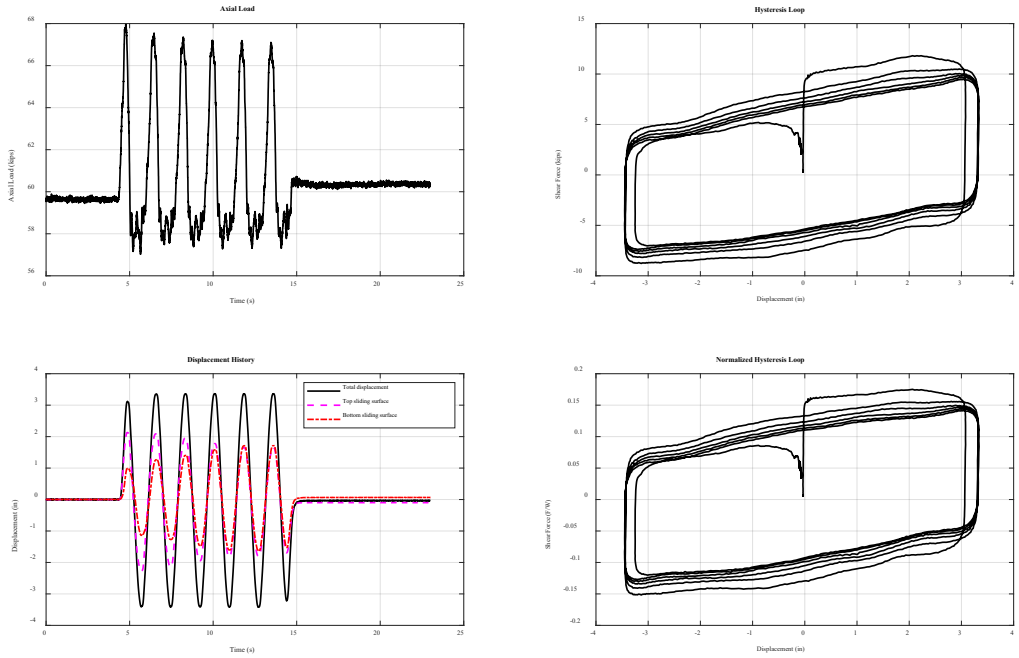

Figure C53. 1/5/2022 Aged Susitna 2- Dry following baked soil tests: 55 kips, sinusoidal X @ 0.57Hz. Max disp = 3.72in

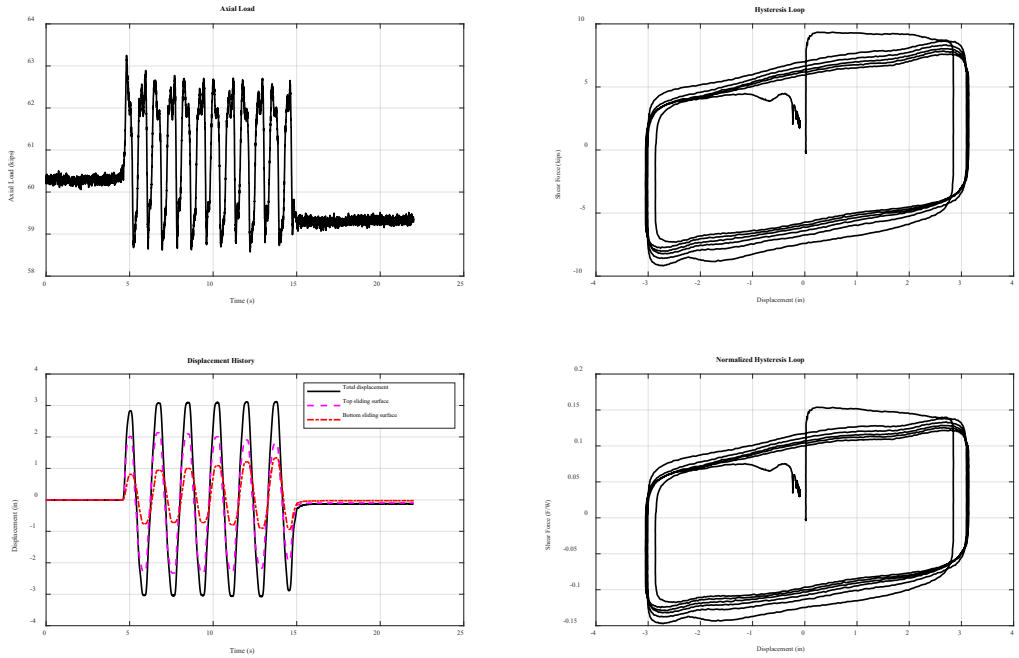

Figure C54. 1/5/2022 Aged Susitna 2- Dry following baked soil tests: 55 kips, sinusoidal Y @ 0.57Hz. Max disp = 3.72in

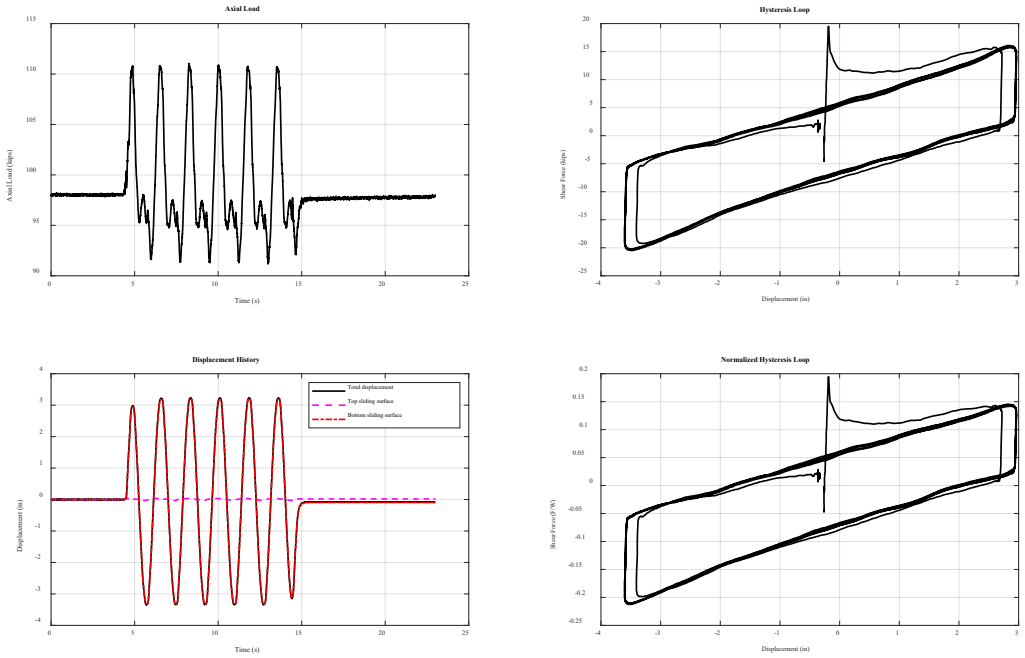

Figure C55. 12/22/2021 Aged Susitna 2- Dry: 100 kips, sinusoidal X @ 0.57Hz. Max disp = 3.72in

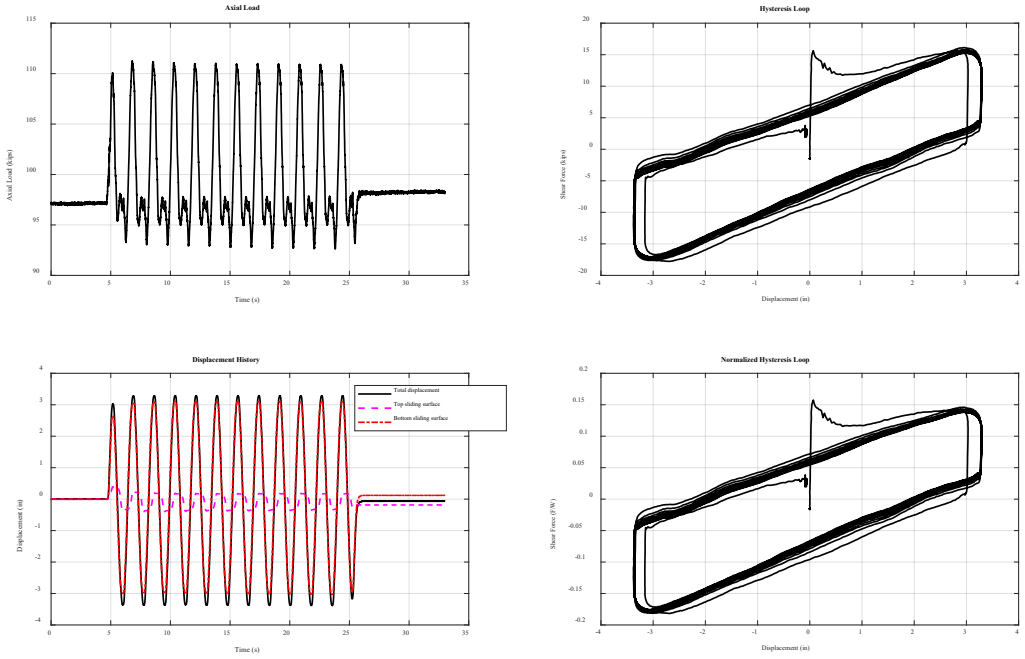

Figure C56. 12/22/2021 Aged Susitna 2- Wet: 100 kips, sinusoidal X @ 0.57Hz. Max disp = 3.72in

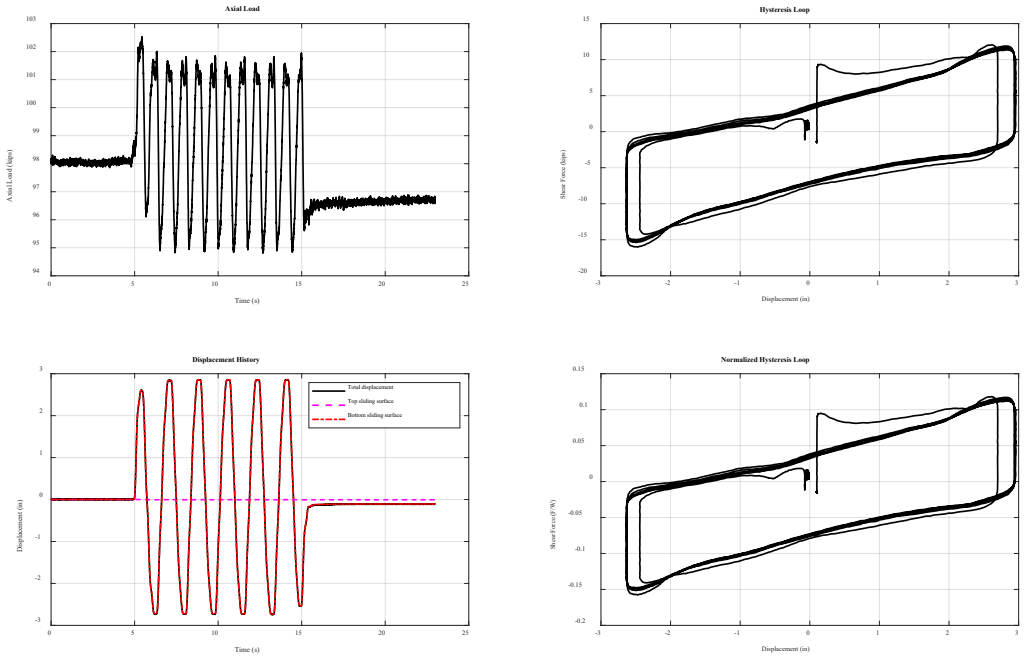

Figure C57. 12/22/2021 Aged Susitna 2- Dry: 100 kips, sinusoidal Y @ 0.57Hz. Max disp = 3.72in

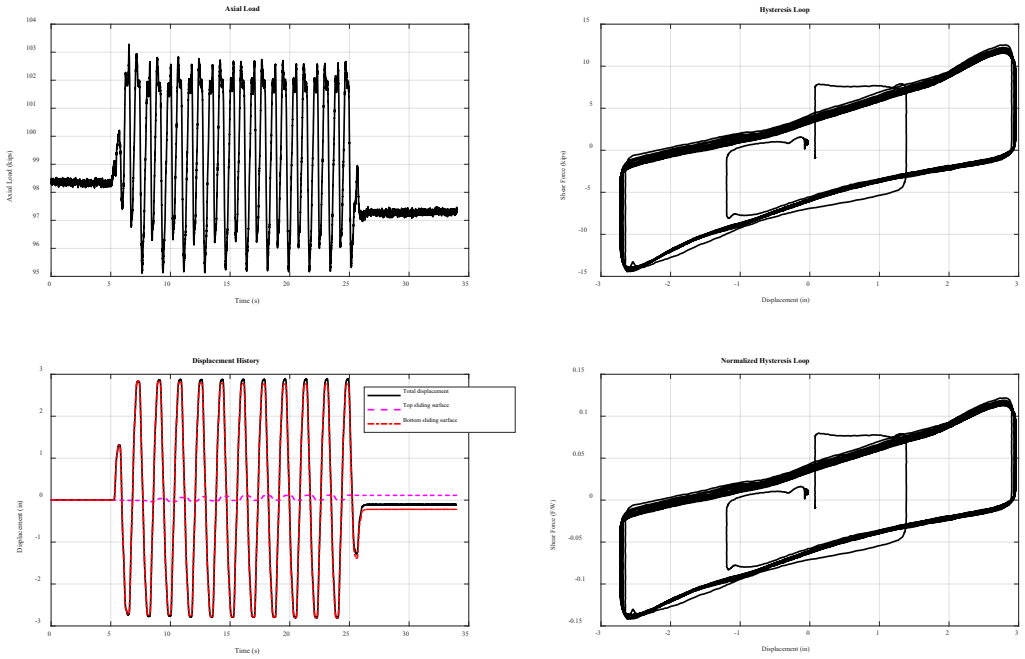

Figure C58. 12/22/2021 Aged Susitna 2- Wet: 100 kips, sinusoidal Y @ 0.57Hz. Max disp = 3.72in

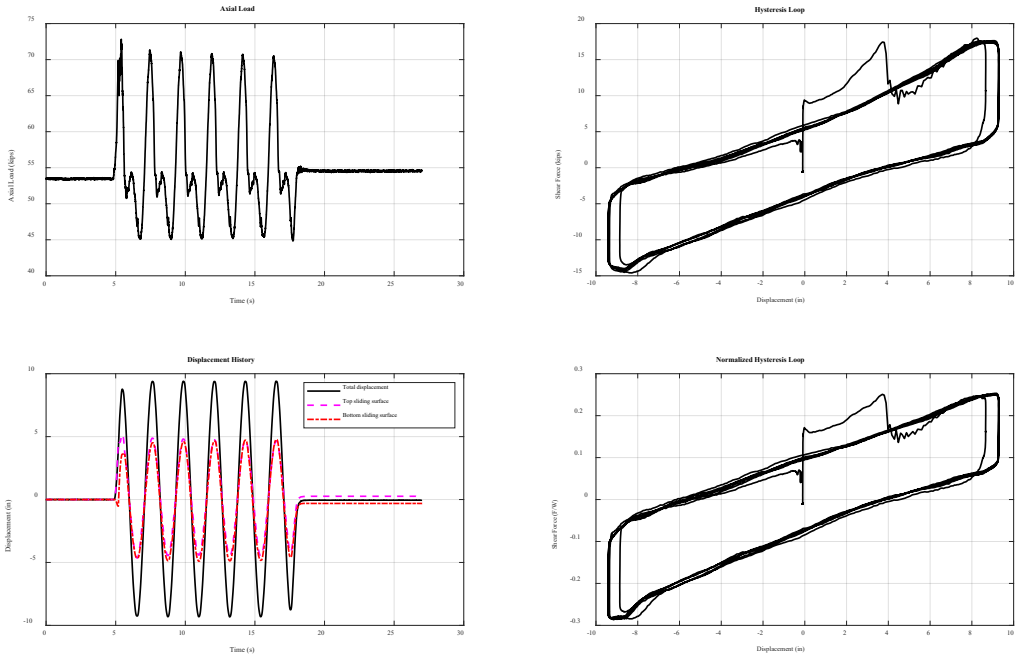

Figure C59. 12/17/2021 Aged Susitna 2- Dry: 55 kips, sinusoidal X @ 0.45Hz. Max disp = 10in

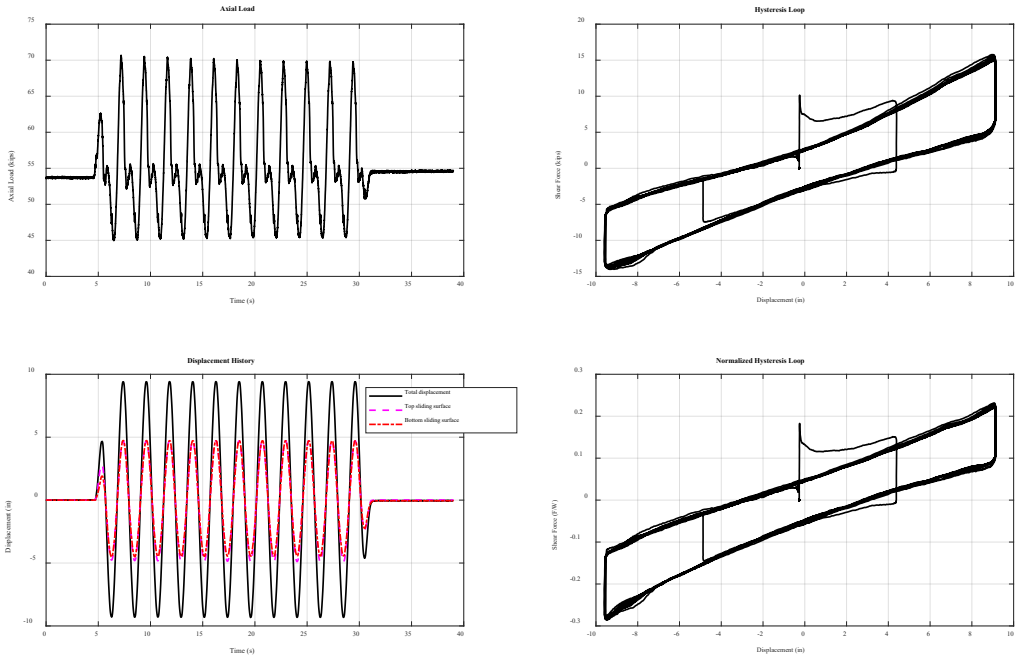

Figure C60. 12/22/2021 Aged Susitna 2- Wet: 55 kips, sinusoidal X @ 0.45Hz. Max disp = 10in

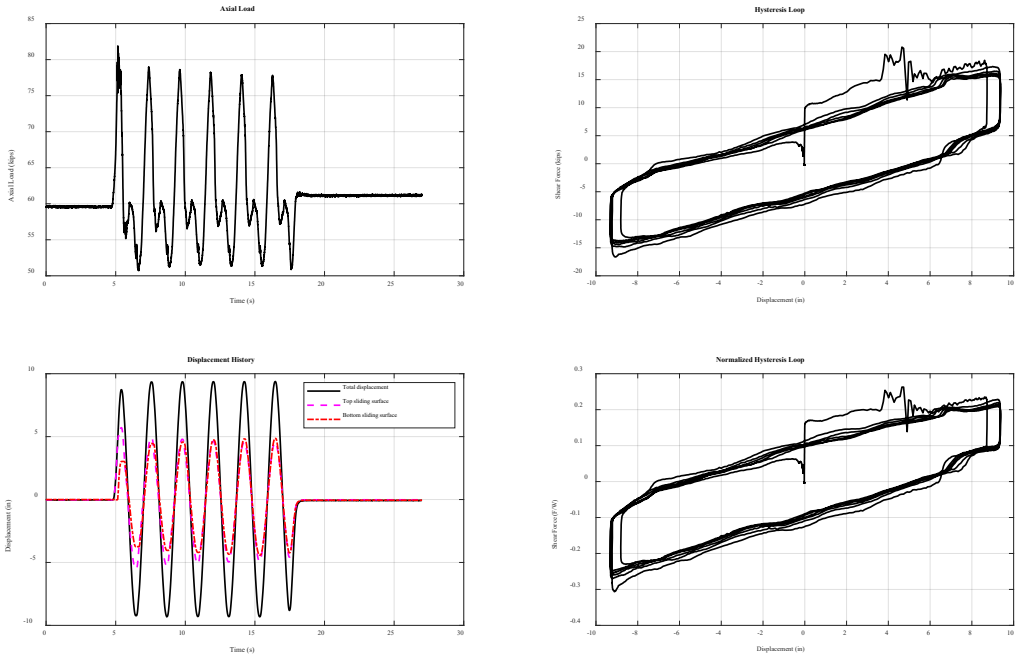

Figure C61. 1/5/2022 Aged Susitna 2- Baked Soil: 55 kips, sinusoidal X @ 0.45Hz. Max disp = 10in

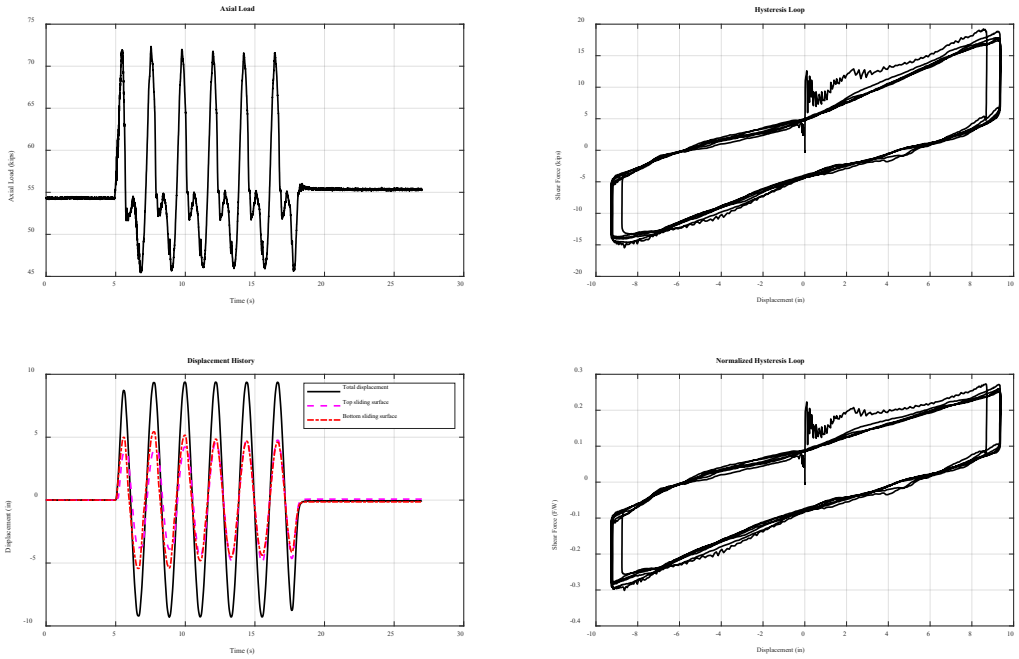

Figure C62. 12/17/2021 Aged Susitna 2- Frozen @ -29°C: 55 kips, sinusoidal X @ 0.45Hz. Max disp = 10in

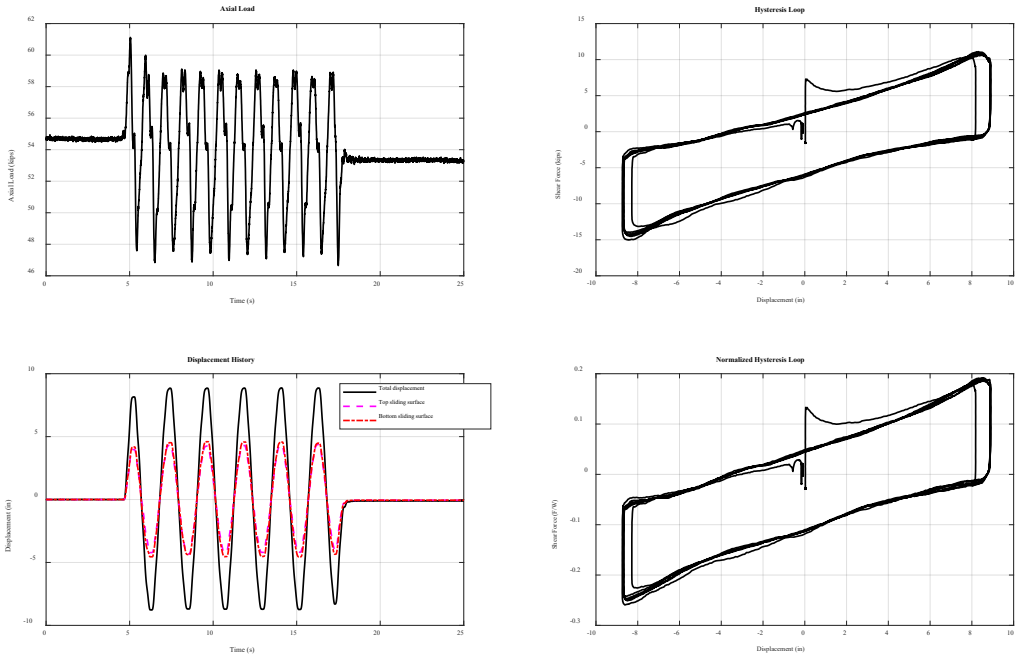

Figure C63. 12/17/2021 Aged Susitna 2- Dry: 55 kips, sinusoidal Y @ 0.45Hz. Max disp = 10in

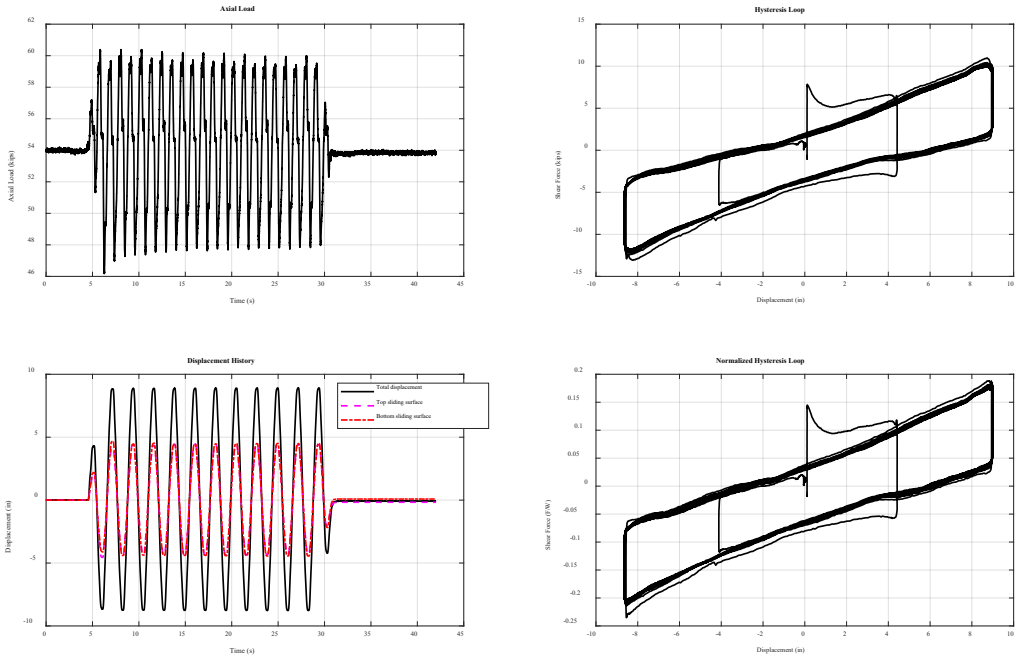

Figure C64. 12/22/2021 Aged Susitna 2- Wet: 55 kips, sinusoidal Y @ 0.45Hz. Max disp = 10in

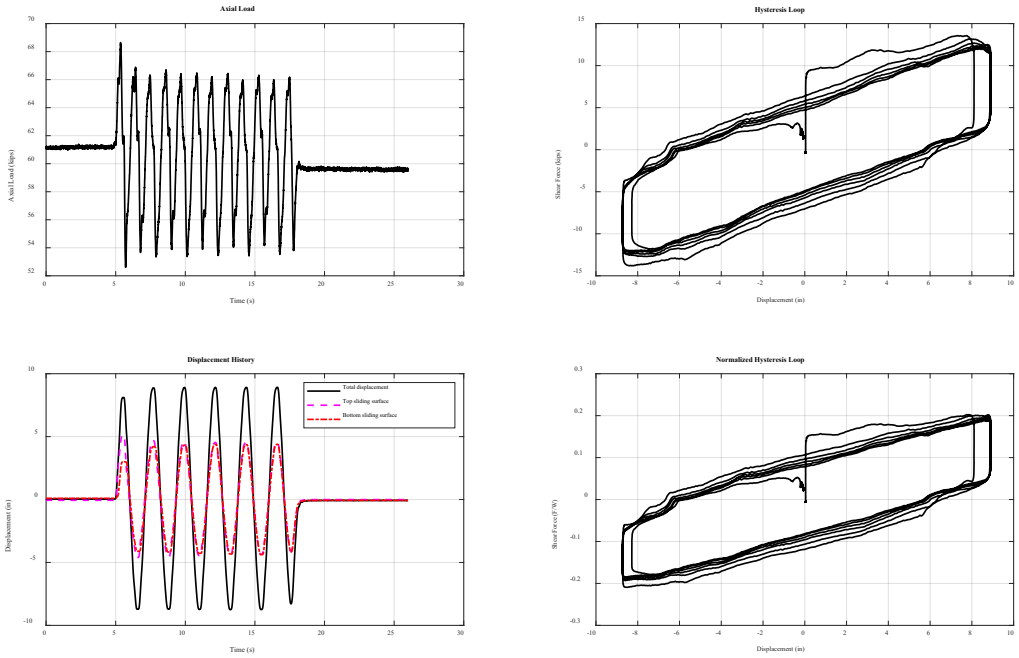

Figure C65. 1/5/2022 Aged Susitna 2- Baked Soil: 55 kips, sinusoidal Y @ 0.45Hz. Max disp = 10in

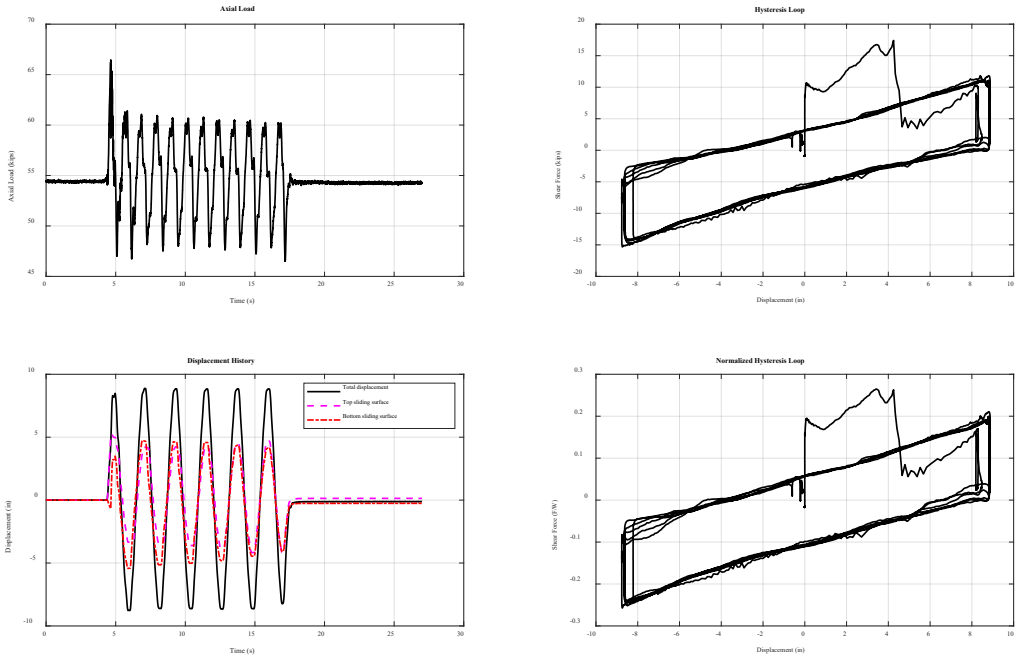

Figure C66. 12/17/2021 Aged Susitna 2- Frozen @ -29°C: 55 kips, sinusoidal Y @ 0.45Hz. Max disp = 10in

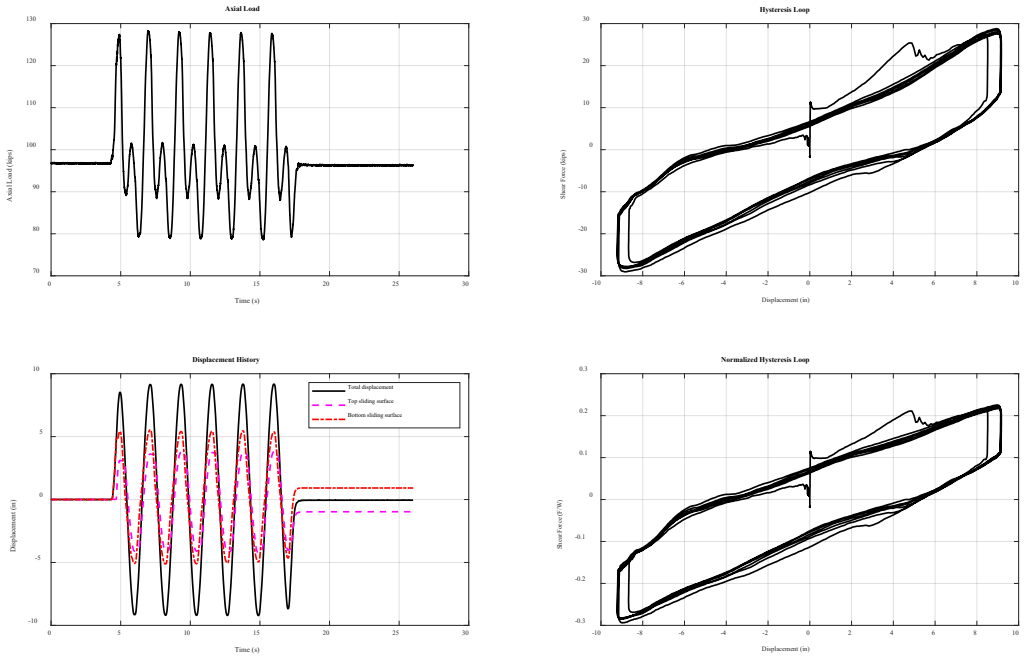

Figure C67. 12/22/2021 Aged Susitna 2- Dry: 100 kips, sinusoidal X @ 0.45Hz. Max disp = 10in

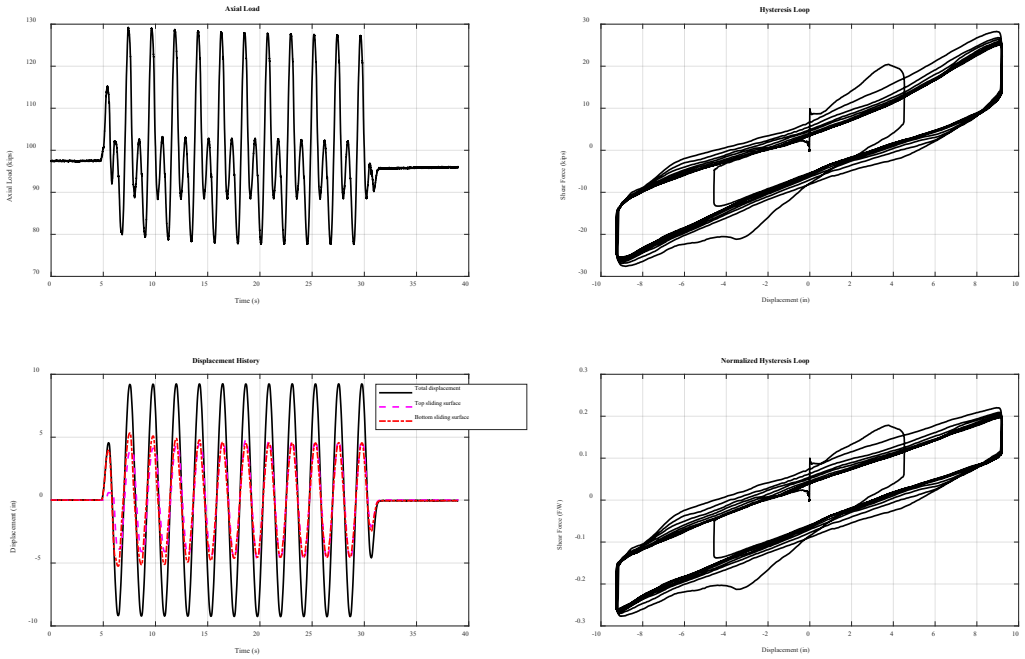

Figure C68. 12/22/2021 Aged Susitna 2- Wet: 100 kips, sinusoidal X @ 0.45Hz. Max disp = 10in

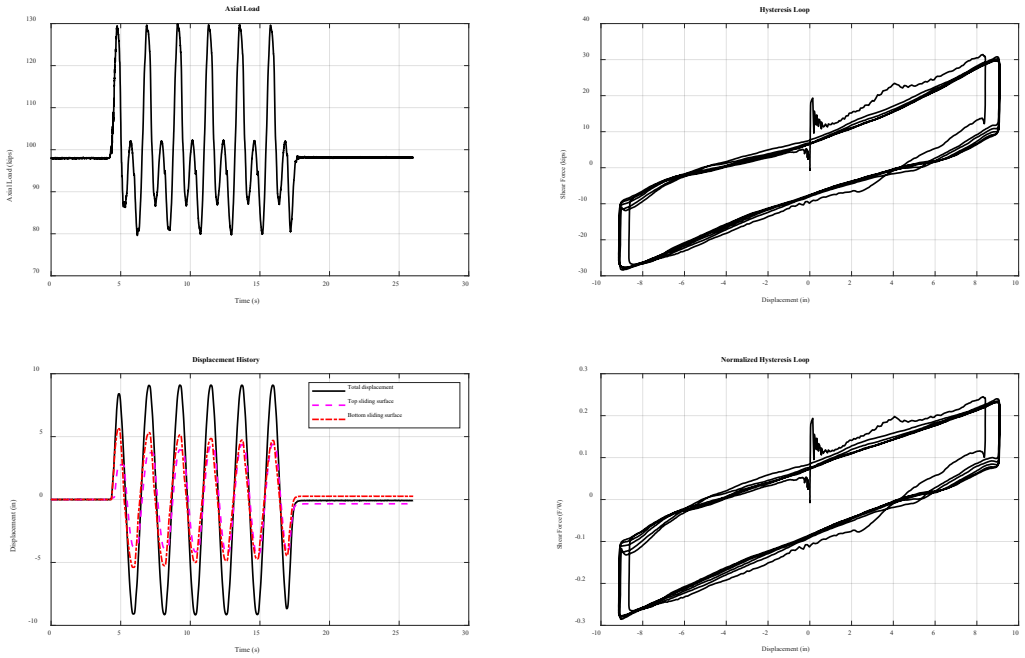

Figure C69. 12/22/2021 Aged Susitna 2- Frozen @ -30°C: 100 kips, sinusoidal X @ 0.45Hz. Max disp = 10in

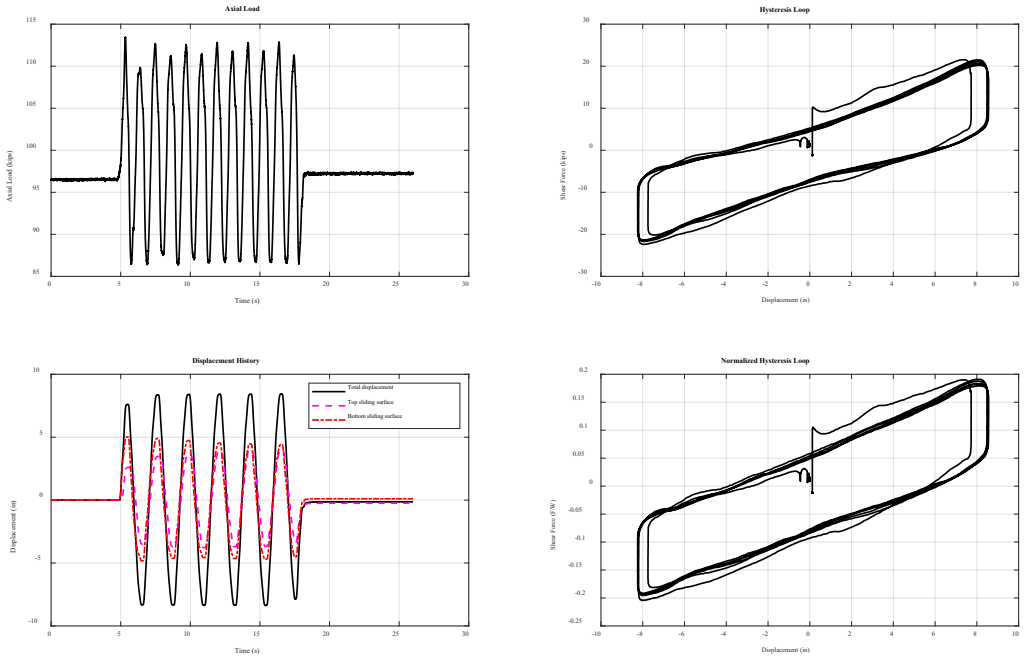

Figure C70. 12/22/2021 Aged Susitna 2- Dry: 100 kips, sinusoidal Y @ 0.45Hz. Max disp = 10in

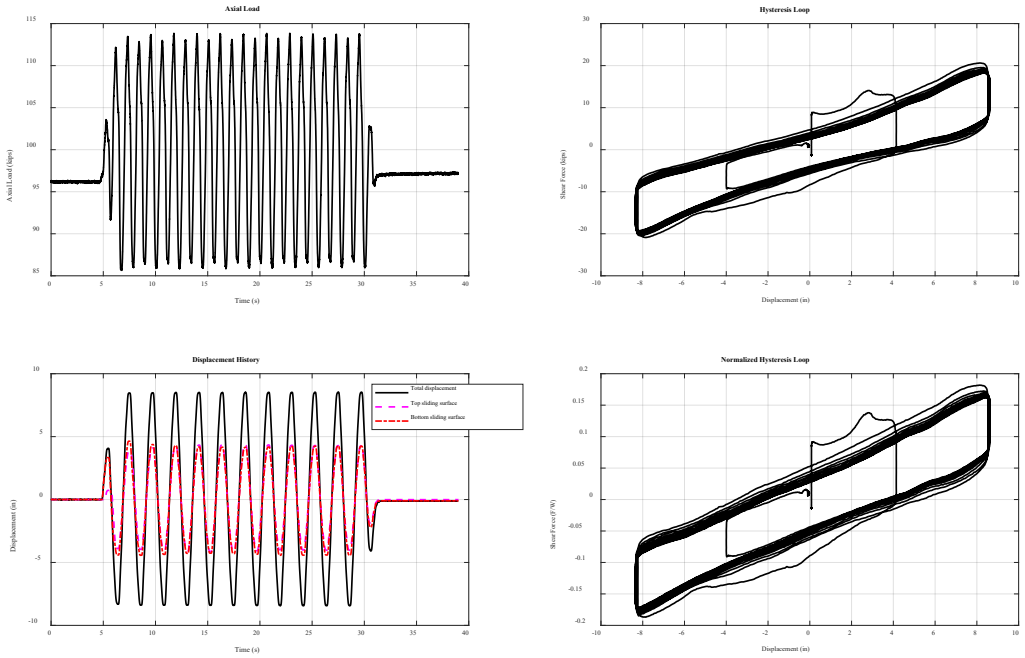

Figure C71. 12/22/2021 Aged Susitna 2- Wet: 100 kips, sinusoidal Y @ 0.45Hz. Max disp = 10in

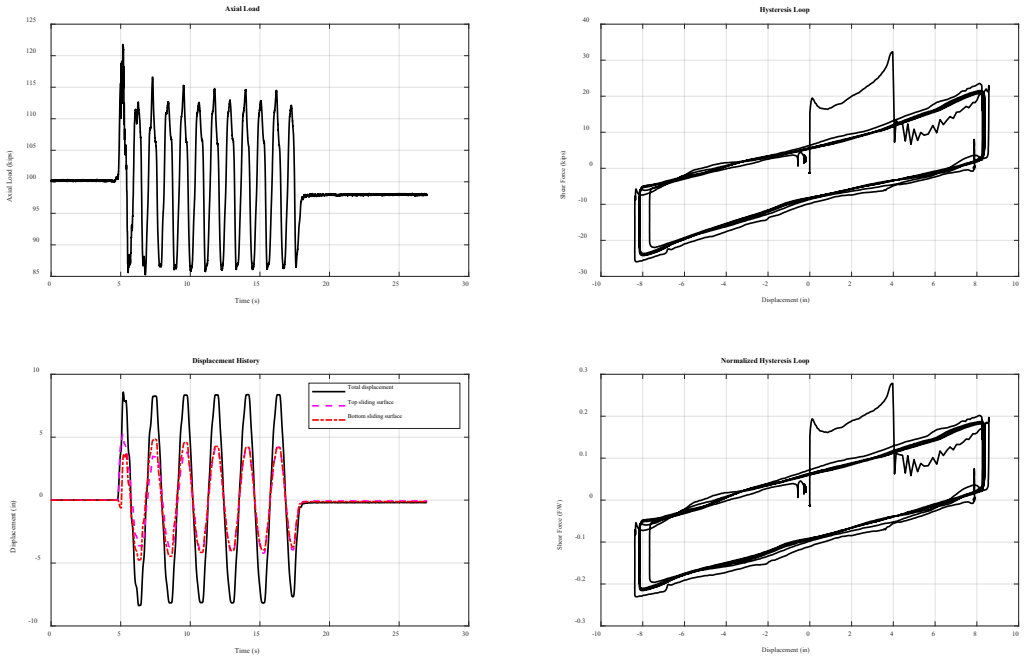

Figure C72. 12/22/2021 Aged Susitna 2- Frozen @ -30°C: 100 kips, sinusoidal Y @ 0.45Hz. Max disp = 10in

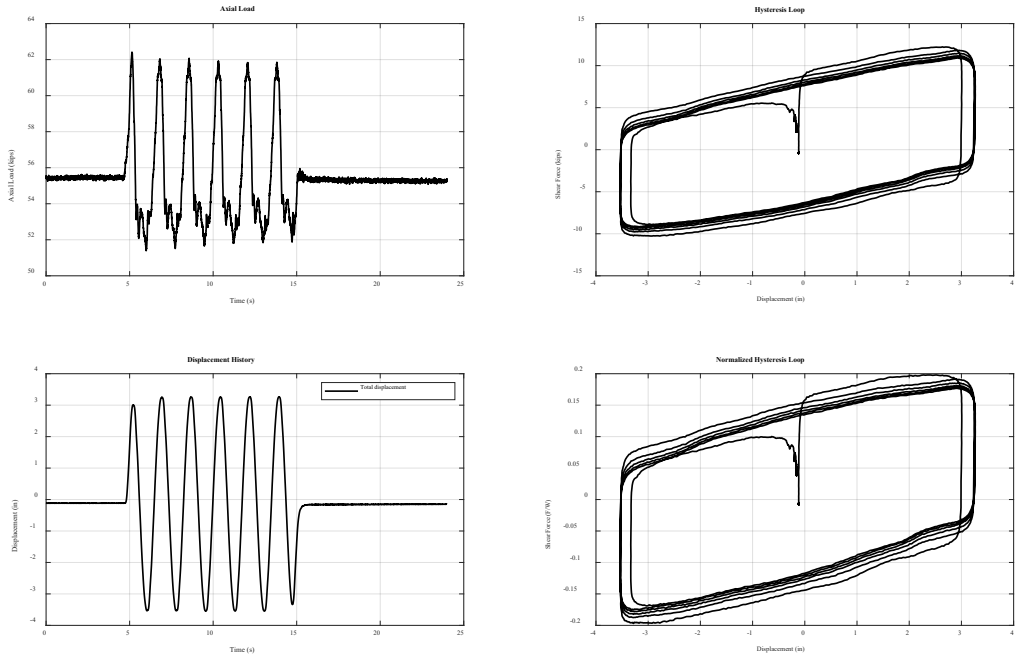

Figure C73. 10/1/2021 New Susitna- Dry: 55 kips, sinusoidal X @ 0.57Hz. Max disp = 3.72in

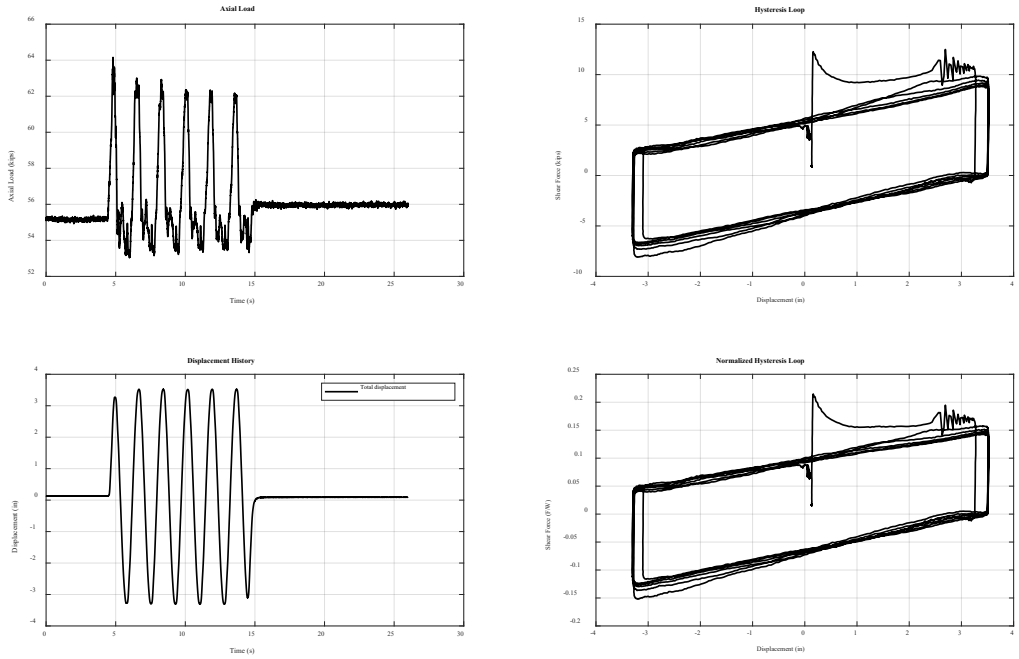

Figure C74. 10/7/2021 New Susitna- Wet: 55 kips, sinusoidal X @ 0.57Hz. Max disp = 3.72in

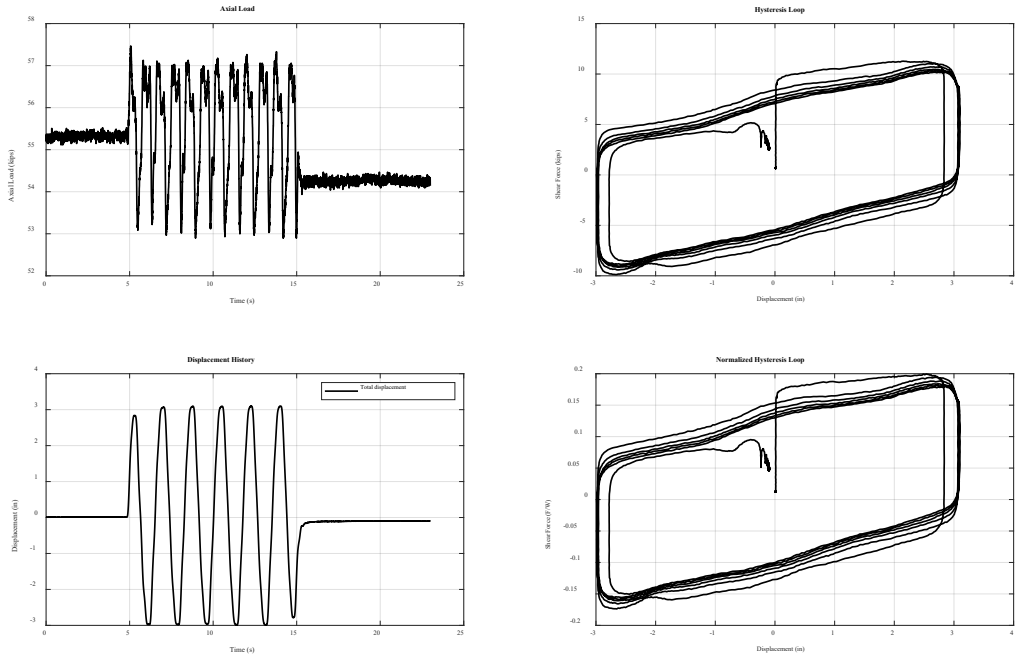

Figure C75. 10/1/2021 New Susitna- Dry: 55 kips, sinusoidal Y @ 0.57Hz. Max disp = 3.72in

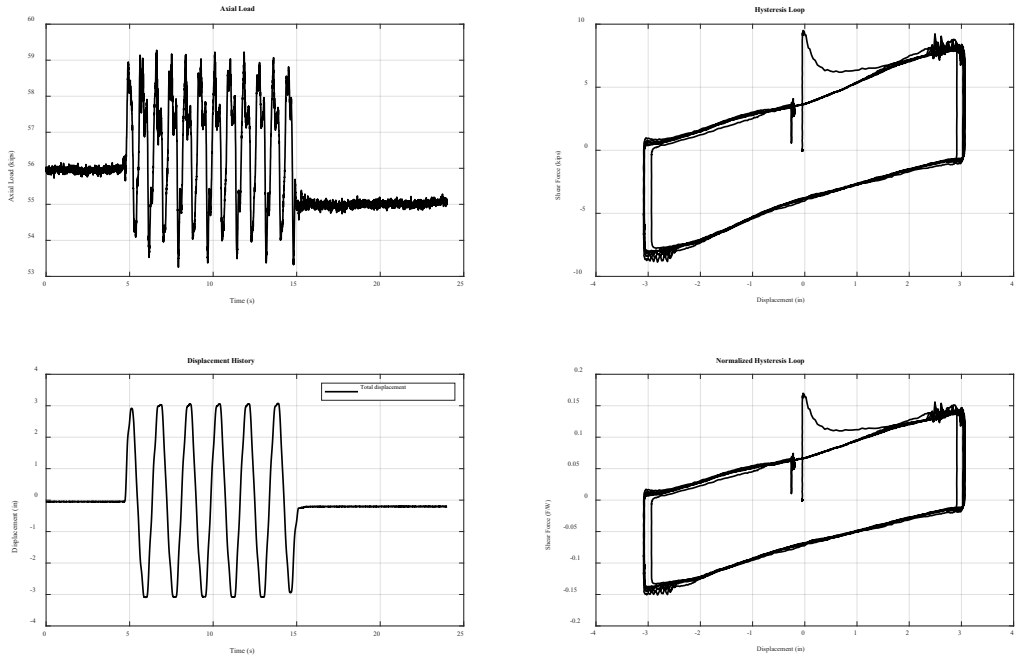

Figure C76. 10/7/2021 New Susitna- Wet: 55 kips, sinusoidal Y @ 0.57Hz. Max disp = 3.72in

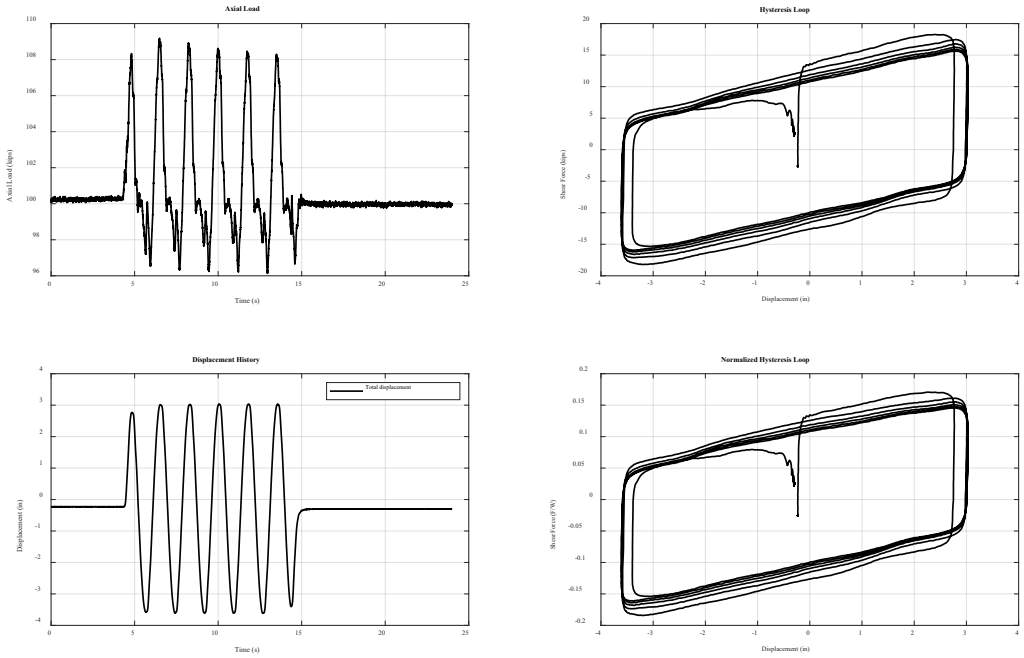

Figure C77. 10/1/2021 New Susitna- Dry: 100 kips, sinusoidal X @ 0.57Hz. Max disp = 3.72in

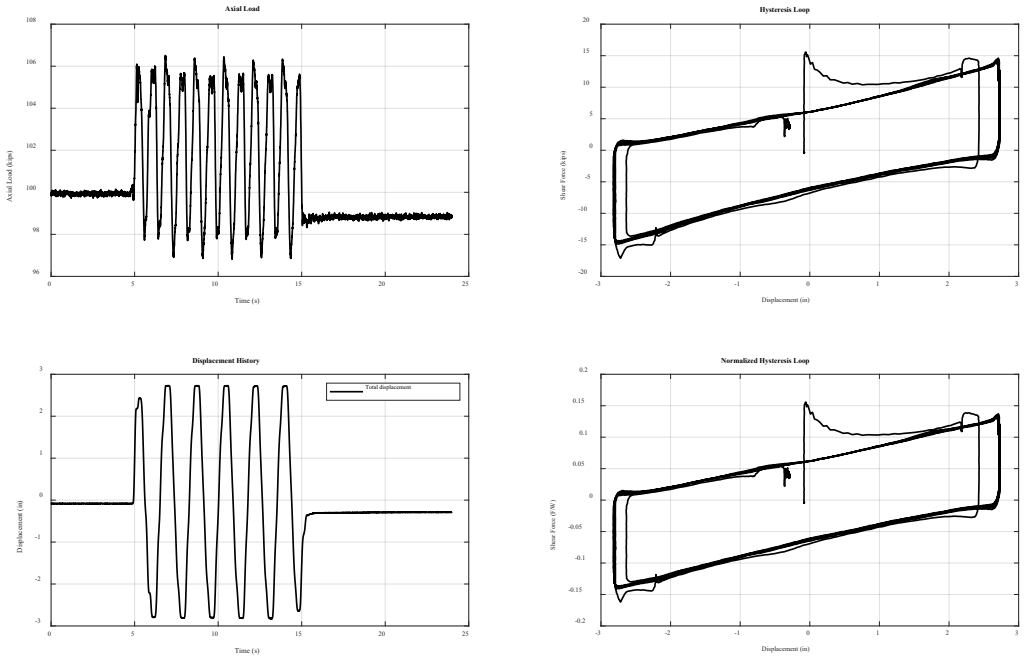

Figure C78. 10/5/2021 New Susitna- Wet: 100 kips, sinusoidal Y @ 0.57Hz. Max disp = 3.72in

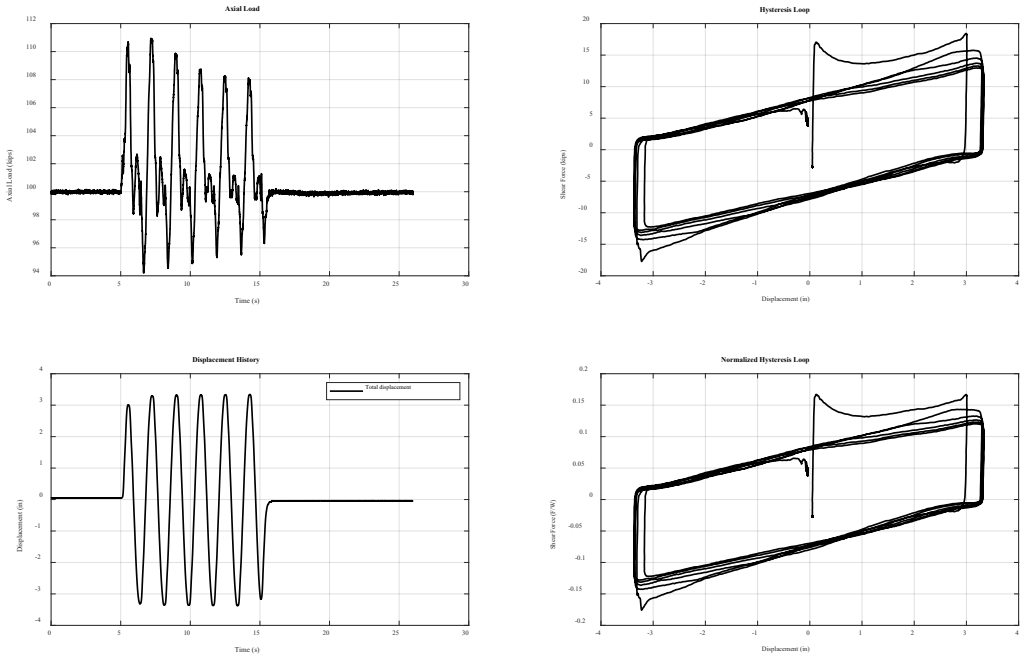

Figure C79. 10/5/2021 New Susitna- Wet: 100 kips, sinusoidal X @ 0.57Hz. Max disp = 3.72in

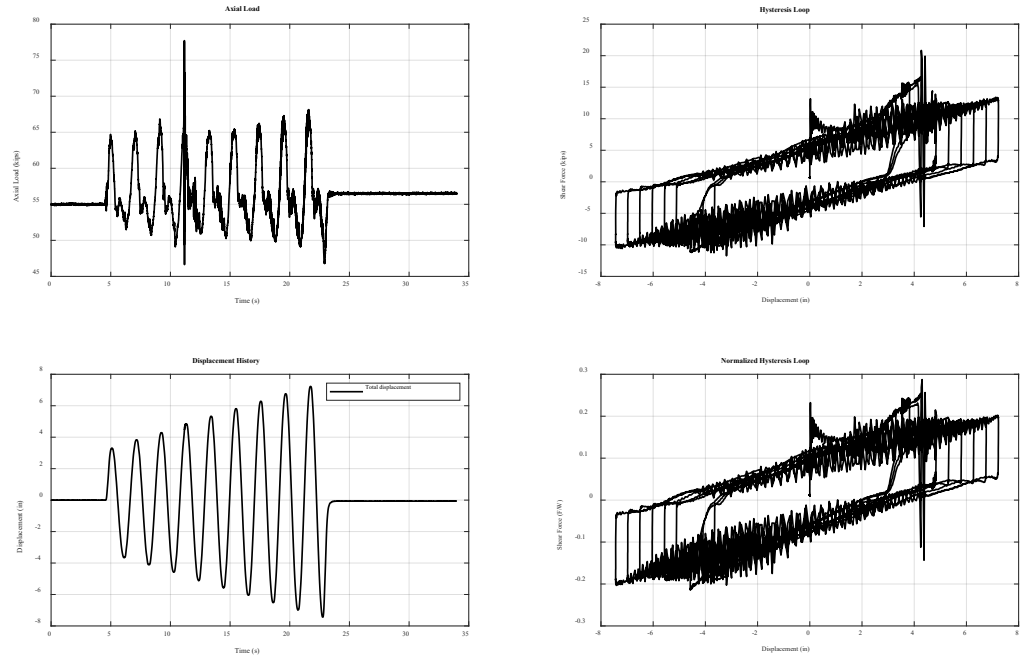

Figure C80. 10/6/2021 New Susitna- Frozen @ -24°C: 55 kips, ramping sinusoidal X @ 0.48Hz. Max disp = 8in

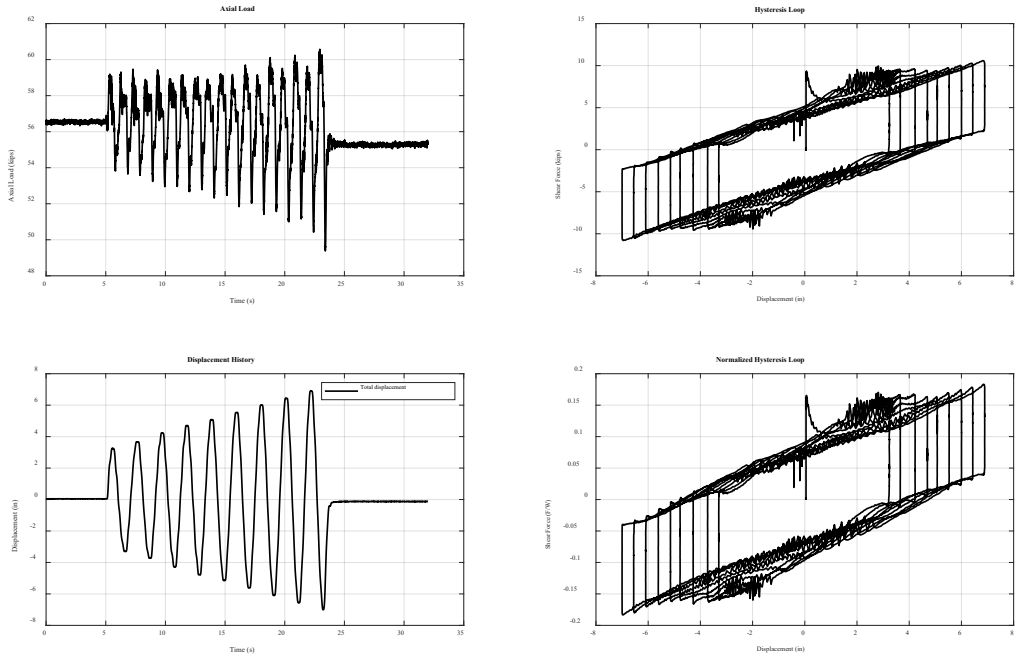

Figure C81. 10/6/2021 New Susitna- Frozen @ -24°C: 55 kips, ramping sinusoidal Y @ 0.48Hz. Max disp = 8in

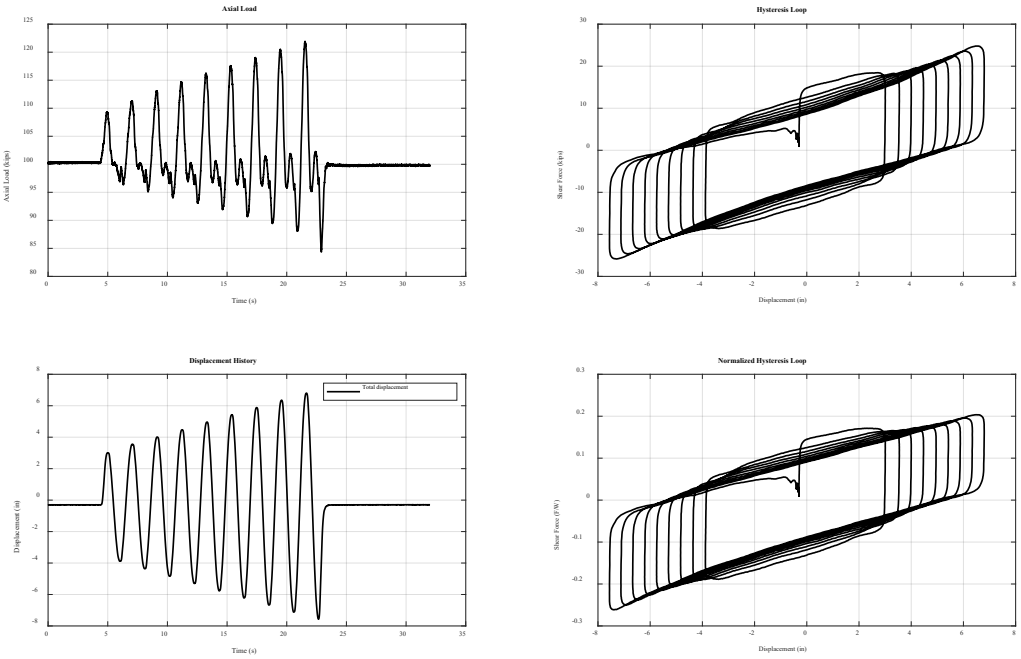

Figure C82. 10/1/2021 New Susitna- Dry: 100 kips, ramping sinusoidal X @ 0.48Hz. Max disp = 8in

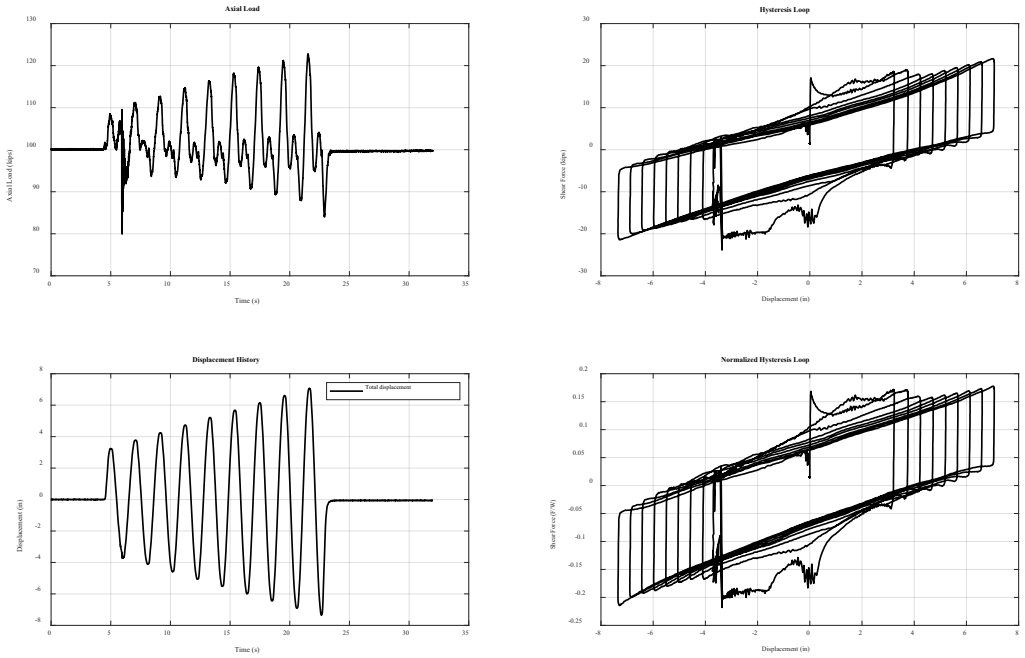

Figure C83. 10/5/2021 New Susitna- Frozen seals on @ -22°C: 100 kips, ramping sinusoidal X @ 0.48Hz. Max disp = 8in

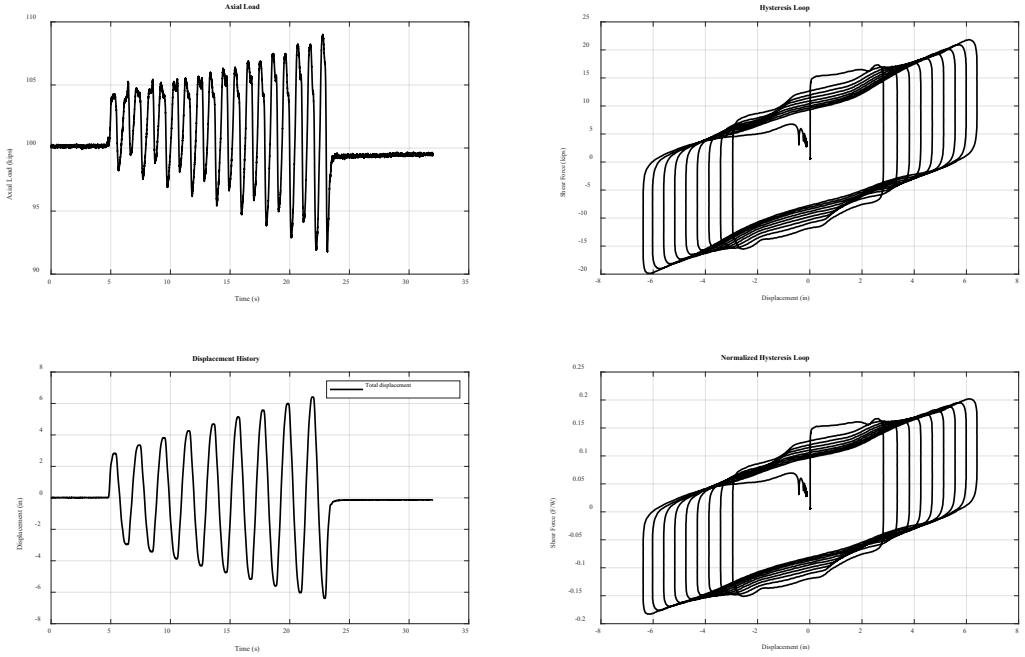

Figure C84. 10/1/2021 New Susitna- Dry: 100 kips, ramping sinusoidal Y @ 0.48Hz. Max disp = 8in

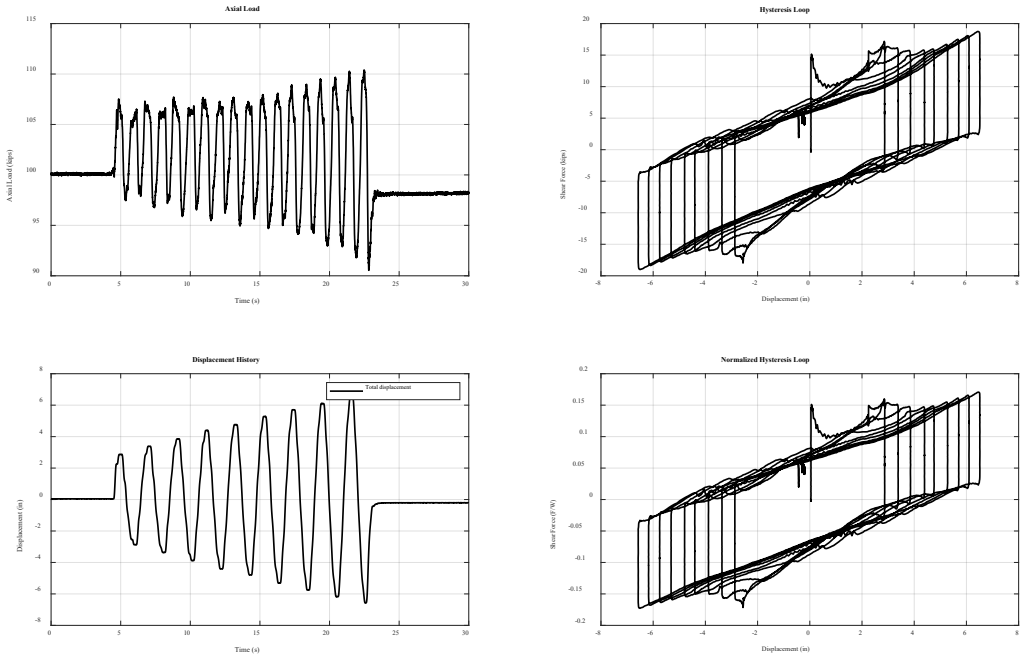

Figure C85. 10/5/2021 New Susitna- Frozen seals on @ -22°C: 100 kips, ramping sinusoidal Y @ 0.48Hz. Max disp = 8in

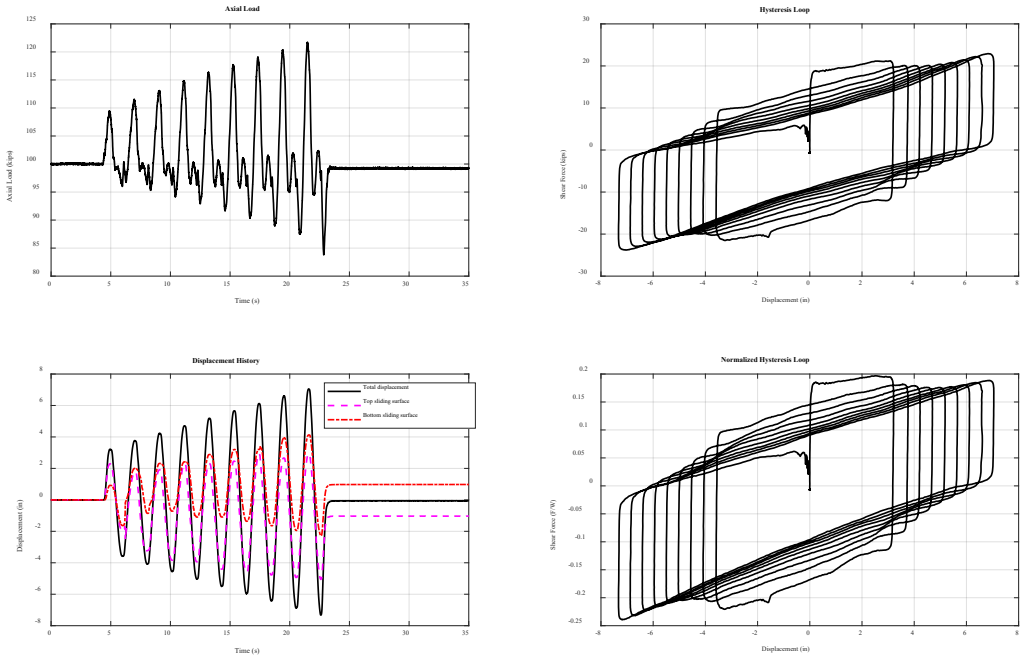

Figure C86. 10/4/2021 New Susitna- Frozen long freezing @ -15°C: 100 kips, ramping sinusoidal X @ 0.48Hz. Max disp = 8in

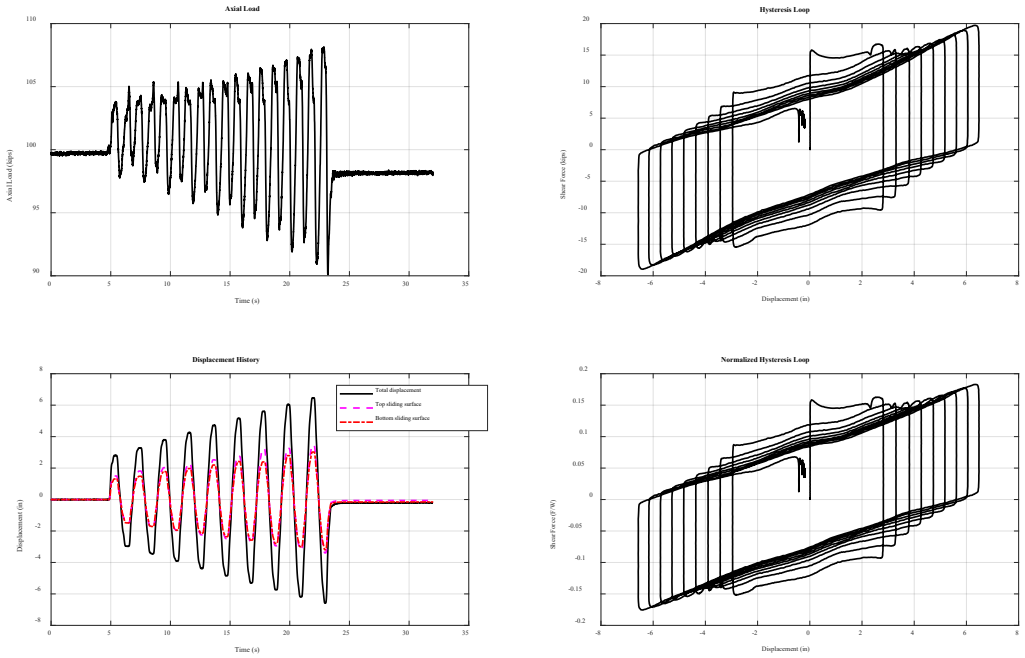

Figure C87. 10/4/2021 New Susitna- Frozen long freezing @ -15°C: 100 kips, ramping sinusoidal Y @ 0.48Hz. Max disp = 8in

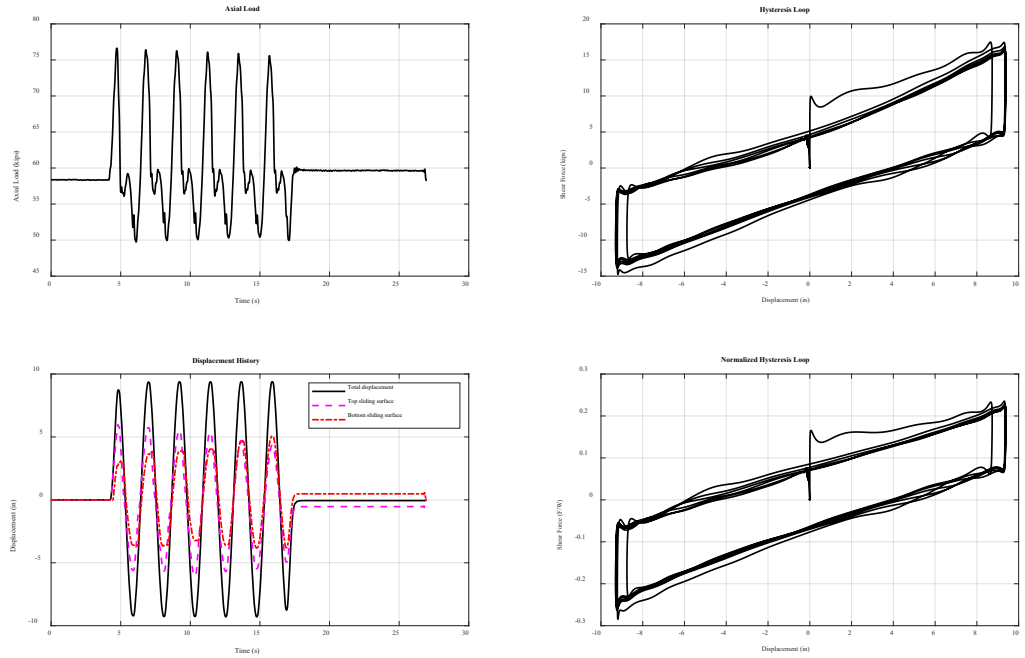

Figure C88. 10/7/2021 New Susitna- Frozen @ -24°C: 55 kips, sinusoidal X @ 0.45Hz. Max disp = 10in

APPENDIX D: SUPPLEMENTARY ANALYSIS RESULTS

The following tables provide ratios of the peak simulated responses in DPB contamination scenarios relative to nominal DPB (NDPB) simulation. The response codes can be interpreted as follows:

- u_b,trans, u_b,long, u_b are peak displacements in any bearing, in the transverse, longitudinal, and combined (vector sum) direction
- u_b11 to u_b62 are peak displacements in specific bearings. The first index (1 to 6) refers to pier or abutment number. The second index is the bearing number (two at each pier). Thus, u_b32 is displacement in Pier 3, bearing 2.
- f_b,trans/W_s and f_b,long/W_s are the peak bearing forces summed over all bearings normalized by superstructure weight, in the transverse and longitudinal directions, respectively. The forces are summed at each time instant, and the peak is computed over time.
- f_b1,trans to f_b6,trans and f_b1,long to f_b6,long are peak bearing forces, summed for the two bearings at each pier or abutment, in the transverse or longitudinal direction, respectively. The index 1 to 6 refers to the pier or abutment number.
- F_p2,trans to F_p5,trans and F_p2,long to F_p5,long are the peak forces in the pier column in the transverse or longitudinal direction, respectively. The index 2 to 5 refers to the pier or abutment number.

Significant changes in the peak response in contaminated condition relative to NDPB are indicated by color-coded highlighting of the ratios according to intensity according to the table below.

	Ratio Value	Interpretation
R1	0.90 - 0.95	5 to 10% reduction
R2	<0.90	>10% reduction
R3	1.05 - 1.10	5 to 10% increase
R4	>1.1	>10% increase

Table D1. Ratio of responses for WC S1 to NDPB

	GM 1	GM 2	GM 3	GM 4	GM 5	GM 6	GM 7	GM 8	GM 9	GM 10	GM 11	Average
u_b,trans	1.095	1.009	1.064	1.065	1.068	1.105	1.072	1.118	1.066	1.047	1.026	1.071
u_b,long	1.018	1.009	1.033	0.994	1.004	1.022	1.020	1.020	1.018	1.014	1.041	1.017
u_b	1.053	1.009	1.064	1.016	1.059	1.112	1.072	1.019	1.029	1.014	1.039	1.048
u_b11	1.048	1.010	1.064	1.016	1.063	1.111	1.072	1.020	1.026	1.009	1.049	1.048
u_b12	1.054	1.007	1.064	1.013	1.060	1.104	1.071	1.019	1.029	1.014	1.047	1.048
u_b21	1.026	1.013	1.035	1.005	1.025	1.042	1.040	1.019	1.016	1.017	1.044	1.027
u_b22	1.031	1.011	1.035	1.001	1.023	1.037	1.039	1.019	1.018	1.016	1.043	1.027
u_b31	1.005	1.009	0.999	0.987	0.994	0.963	1.000	1.021	1.010	1.014	1.039	1.003
u_b32	1.006	1.007	0.999	0.984	0.993	0.961	1.000	1.021	1.010	1.014	1.041	1.003
u_b41	1.007	1.008	0.999	0.990	0.994	0.963	0.997	1.021	1.010	1.013	1.042	1.003
u_b42	1.006	1.009	0.999	0.992	0.995	0.965	0.998	1.021	1.010	1.013	1.040	1.003
u_b51	1.031	1.006	1.034	1.006	1.026	1.038	1.036	1.021	1.018	1.013	1.041	1.027
u_b52	1.026	1.008	1.034	1.009	1.029	1.044	1.038	1.021	1.016	1.013	1.041	1.027
u_b61	1.053	1.008	1.062	1.018	1.057	1.106	1.072	1.020	1.029	1.025	1.045	1.049
u_b62	1.048	1.010	1.062	1.021	1.059	1.113	1.073	1.020	1.026	1.025	1.046	1.049
f_b1,trans	0.878	0.851	0.970	0.820	0.929	0.912	0.933	0.850	0.874	0.841	0.820	0.892
f_b2,trans	0.920	1.023	1.027	1.000	1.016	1.004	1.020	1.017	1.005	1.032	1.000	1.007
f_b3,trans	1.009	0.996	0.998	1.000	0.992	0.982	0.995	0.983	0.999	0.999	1.004	0.996
f_b4,tran	0.996	0.997	1.007	0.999	0.992	0.981	0.996	0.994	1.000	0.998	1.004	0.997
f_b5,trans	1.014	1.001	1.022	1.001	1.011	1.017	1.014	1.002	1.007	0.993	1.002	1.010
f_b6,trans	0.920	0.847	0.959	0.829	0.890	0.917	0.923	0.851	0.874	0.835	0.832	0.891
f_b1,long	0.882	0.866	0.830	0.846	0.850	0.855	0.844	0.898	0.873	0.864	0.837	0.861
f_b2,long	0.983	1.004	0.998	0.997	0.998	1.006	1.010	1.009	1.006	1.007	1.011	1.003
f_b3,long	1.005	1.003	1.001	1.000	1.004	1.004	1.008	1.009	1.007	1.006	1.015	1.006
f_b4,long	1.004	1.002	1.005	1.003	1.003	1.004	1.010	1.009	1.012	1.004	1.013	1.006
f_b5,long	1.004	1.002	1.006	0.999	1.003	1.005	1.007	1.007	1.005	1.004	1.008	1.005
f_b6,long	0.881	0.860	0.834	0.861	0.846	0.845	0.855	0.887	0.863	0.863	0.847	0.860
f_b,trans/W_s	0.981	0.990	1.009	0.989	0.993	0.986	0.999	0.990	0.991	0.988	0.989	0.993
f_b,long/W_s	0.993	0.992	0.971	0.985	0.989	0.991	0.984	0.998	0.994	0.996	1.002	0.991
F_p2,trans	0.995	0.995	1.002	1.001	1.000	0.996	0.995	0.993	1.000	0.993	0.997	0.997
F_p3,trans	1.005	1.003	0.998	0.998	0.998	1.006	0.998	0.999	1.007	0.998	1.001	1.001
F_p4,trans	1.000	1.001	0.998	1.003	0.999	1.003	1.000	1.003	0.995	0.999	1.000	1.000
F_p5,trans	1.009	0.997	1.013	0.997	0.994	1.003	0.999	1.003	1.000	0.983	0.997	1.000
F_p2,long	0.999	0.999	1.014	0.991	0.998	1.004	0.999	1.004	1.001	1.003	0.985	0.999
F_p3,long	1.008	0.997	1.010	0.998	1.001	1.010	0.996	1.005	1.002	1.000	0.978	1.000
F_p4,long	0.993	0.998	0.999	0.996	1.003	1.005	0.999	1.007	1.003	0.997	0.981	0.998
F_p5,long	1.001	0.995	0.999	0.998	1.001	0.983	0.989	1.007	0.995	0.998	0.984	0.996

Table D2. Ratio of responses for WC S2 to NDPB

	GM 1	GM 2	GM 3	GM 4	GM 5	GM 6	GM 7	GM 8	GM 9	GM 10	GM 11	Average
u_b,trans	1.139	1.017	1.201	1.078	0.997	1.057	1.230	1.313	1.006	0.959	0.975	1.127
u_b,long	1.062	1.049	1.179	0.932	0.982	1.029	1.136	1.090	1.061	1.113	1.051	1.059
u_b	1.036	1.049	1.202	1.003	0.965	1.052	1.235	1.091	1.034	1.110	1.041	1.099
u_b11	1.123	1.017	1.202	1.003	1.099	0.989	1.235	1.089	1.091	1.119	1.033	1.116
u_b12	1.125	1.017	1.202	0.999	1.101	0.995	1.234	1.091	1.090	1.134	1.032	1.118
u_b21	1.142	1.067	1.182	0.989	1.113	1.053	1.221	1.091	1.095	1.124	1.050	1.121
u_b22	1.143	1.066	1.182	0.989	1.114	1.057	1.220	1.093	1.094	1.124	1.051	1.121
u_b31	1.105	1.049	1.139	0.994	1.098	1.080	1.169	1.099	1.088	1.095	1.040	1.101
u_b32	1.111	1.047	1.138	0.997	1.097	1.080	1.167	1.099	1.090	1.096	1.043	1.101
u_b41	1.048	1.014	1.077	0.976	1.040	1.038	1.089	1.094	1.068	1.083	1.031	1.060
u_b42	1.054	1.010	1.077	0.973	1.036	1.036	1.087	1.094	1.072	1.086	1.035	1.060
u_b51	1.013	1.013	1.001	1.014	0.985	1.005	1.024	1.083	1.047	1.082	1.033	1.026
u_b52	1.016	1.011	1.001	1.008	0.983	1.003	1.022	1.086	1.050	1.086	1.034	1.026
u_b61	1.003	1.018	0.951	0.917	0.966	0.998	0.988	1.076	1.034	1.136	1.033	1.004
u_b62	1.006	1.016	0.951	0.907	0.965	0.997	0.985	1.080	1.038	1.140	1.033	1.005
f_b1,trans	1.171	0.999	1.144	0.970	1.105	1.085	1.112	0.998	1.039	0.921	1.020	1.064
f_b2,trans	0.871	0.834	1.081	0.835	0.950	0.909	1.009	0.925	0.896	0.871	0.819	0.928
f_b3,trans	1.034	0.809	1.012	0.851	0.936	0.900	0.983	0.896	0.891	0.830	0.820	0.919
f_b4,tran	1.038	0.994	1.070	1.001	1.029	1.028	1.023	0.997	1.019	0.975	1.010	1.022
f_b5,trans	1.011	0.998	1.001	1.006	0.987	1.010	0.990	0.996	1.010	0.998	1.001	1.001
f_b6,trans	0.930	0.994	0.971	1.017	0.979	0.983	0.957	1.020	0.997	0.930	0.987	0.977
f_b1,long	1.003	1.008	1.017	0.991	1.028	1.002	1.037	1.043	1.029	1.038	1.007	1.019
f_b2,long	0.856	0.884	0.818	0.849	0.840	0.867	0.896	0.932	0.872	0.918	0.876	0.876
f_b3,long	0.880	0.879	0.833	0.860	0.835	0.857	0.896	0.926	0.865	0.903	0.874	0.876
f_b4,long	1.015	1.000	1.010	0.985	1.024	1.004	1.041	1.034	1.028	1.026	1.013	1.017
f_b5,long	1.009	1.002	1.008	0.968	1.024	1.018	1.049	1.030	1.017	1.026	1.002	1.014
f_b6,long	1.015	1.000	1.009	0.969	0.993	1.016	1.047	1.027	1.016	1.030	1.001	1.012
f_b,trans/W_s	0.985	0.927	1.041	0.928	0.977	0.960	0.990	0.927	0.960	0.928	0.923	0.968
f_b,long/W_s	0.955	0.945	0.951	0.915	0.920	0.938	0.979	0.984	0.990	0.974	0.947	0.955
F_p2,trans	0.895	0.886	0.959	0.929	0.904	0.852	0.916	0.946	0.934	0.848	0.995	0.919
F_p3,trans	0.800	0.866	0.971	0.913	0.885	0.849	0.952	0.884	0.916	0.815	1.003	0.901
F_p4,trans	1.018	0.998	1.027	0.977	1.007	0.992	1.008	1.042	0.990	0.991	1.000	1.006
F_p5,trans	0.969	0.976	1.001	1.007	1.000	1.004	0.999	0.973	0.995	0.929	0.995	0.987
F_p2,long	0.958	1.108	1.023	0.907	0.922	0.935	0.967	0.961	0.898	0.982	0.981	0.975
F_p3,long	0.922	1.052	1.000	0.933	0.904	0.901	0.974	0.972	0.849	0.909	0.967	0.946
F_p4,long	0.973	0.989	0.982	0.980	0.977	0.990	0.986	1.022	0.971	0.978	0.970	0.984
F_p5,long	0.971	0.979	0.976	0.969	0.999	0.950	0.941	1.025	1.020	0.994	0.970	0.983

Table D3. Ratio of responses for WC S3 to NDPB

	GM 1	GM 2	GM 3	GM 4	GM 5	GM 6	GM 7	GM 8	GM 9	GM 10	GM 11	Average
u_b,trans	1.259	1.036	1.216	1.130	1.100	1.075	1.238	1.442	1.080	1.005	1.047	1.175
u_b,long	1.166	1.080	1.365	1.041	0.942	1.110	1.354	1.230	1.111	1.203	1.136	1.153
u_b	1.191	1.082	1.218	1.000	1.079	1.097	1.263	1.225	1.120	1.201	1.121	1.166
u_b11	1.214	1.051	1.218	0.913	1.130	1.086	1.263	1.227	1.139	1.259	1.131	1.170
u_b12	1.218	1.052	1.218	0.915	1.130	1.087	1.263	1.225	1.138	1.270	1.129	1.171
u_b21	1.221	1.117	1.219	0.912	1.127	1.106	1.267	1.217	1.137	1.220	1.148	1.173
u_b22	1.223	1.117	1.219	0.913	1.127	1.106	1.267	1.215	1.137	1.216	1.145	1.172
u_b31	1.197	1.082	1.218	1.096	1.125	1.095	1.268	1.253	1.140	1.179	1.121	1.180
u_b32	1.199	1.083	1.217	1.095	1.126	1.095	1.268	1.255	1.139	1.178	1.121	1.180
u_b41	1.193	1.059	1.216	1.048	1.133	1.092	1.268	1.245	1.141	1.170	1.124	1.174
u_b42	1.193	1.058	1.216	1.047	1.132	1.092	1.268	1.245	1.142	1.173	1.125	1.175
u_b51	1.194	1.048	1.217	1.137	1.103	1.097	1.280	1.234	1.129	1.209	1.125	1.179
u_b52	1.194	1.046	1.217	1.137	1.101	1.098	1.281	1.235	1.131	1.214	1.129	1.179
u_b61	1.191	1.055	1.216	0.985	1.081	1.097	1.291	1.221	1.120	1.278	1.122	1.170
u_b62	1.191	1.054	1.216	0.987	1.079	1.098	1.292	1.226	1.122	1.285	1.128	1.172
f_b1,trans	1.010	0.863	1.075	0.831	0.957	0.976	1.008	0.861	0.918	0.736	0.828	0.936
f_b2,trans	0.889	0.841	1.111	0.837	0.964	0.934	1.009	0.863	0.906	0.872	0.828	0.935
f_b3,trans	1.068	0.821	1.090	0.854	0.957	0.944	1.008	0.889	0.906	0.820	0.826	0.945
f_b4,trans	0.992	0.814	1.084	0.854	0.956	0.962	0.978	0.848	0.906	0.749	0.843	0.928
f_b5,trans	0.957	0.835	1.054	0.841	0.911	0.981	0.997	0.834	0.914	0.821	0.839	0.927
f_b6,trans	0.946	0.838	1.037	0.827	0.911	0.982	0.970	0.862	0.898	0.774	0.836	0.917
f_b1,long	0.903	0.882	0.852	0.827	0.878	0.864	0.956	0.989	0.918	0.940	0.856	0.901
f_b2,long	0.906	0.901	0.843	0.824	0.829	0.881	0.958	0.998	0.978	0.951	0.907	0.910
f_b3,long	0.896	0.892	0.869	0.839	0.822	0.884	0.959	0.987	0.938	0.932	0.912	0.905
f_b4,long	0.899	0.874	0.860	0.821	0.904	0.864	0.945	0.976	0.921	0.918	0.905	0.901
f_b5,long	0.951	0.877	0.867	0.797	0.872	0.870	0.951	1.001	0.913	0.928	0.879	0.904
f_b6,long	0.919	0.868	0.852	0.824	0.835	0.886	0.953	0.977	0.909	0.913	0.858	0.893
f_b,trans/W_s	1.000	0.845	1.081	0.845	0.943	0.958	1.006	0.863	0.907	0.815	0.838	0.940
f_b,long/W_s	0.898	0.886	0.887	0.812	0.825	0.870	0.964	0.985	1.010	0.936	0.919	0.910
F_p2,trans	0.888	0.893	0.961	0.929	0.910	0.850	0.917	0.916	0.926	0.826	0.993	0.915
F_p3,trans	0.814	0.872	1.007	0.907	0.881	0.827	0.970	0.933	0.911	0.821	1.001	0.911
F_p4,trans	0.804	0.913	1.016	0.892	0.881	0.893	0.980	0.878	0.923	0.825	0.993	0.916
F_p5,trans	0.877	0.898	1.018	0.902	0.852	0.898	0.926	0.914	0.944	0.827	0.950	0.915
F_p2,long	0.953	1.081	1.070	0.869	0.892	0.919	0.965	1.022	0.889	0.995	0.948	0.969
F_p3,long	0.925	1.027	1.054	0.904	0.885	0.915	0.970	1.038	0.830	0.909	0.917	0.942
F_p4,long	0.963	0.994	0.941	0.969	0.861	0.867	0.904	1.028	0.855	0.823	0.883	0.919
F_p5,long	1.096	0.955	0.824	0.992	0.889	0.789	0.807	1.061	0.904	1.017	0.871	0.936

Table D4. Ratio of responses for SSSB S1 to NDPB

	GM 1	GM 2	GM 3	GM 4	GM 5	GM 6	GM 7	GM 8	GM 9	GM 10	GM 11	Average
u_b,trans	1.006	1.012	1.003	1.008	0.926	1.014	0.978	0.929	1.047	0.946	0.965	0.990
u_b,long	0.965	1.006	1.000	1.022	0.989	0.987	0.989	0.957	0.981	1.034	0.992	0.989
u_b	0.949	1.006	1.003	1.005	0.930	0.999	0.977	0.955	0.966	1.033	0.992	0.982
u_b11	0.955	1.012	0.827	0.982	0.947	1.000	0.845	0.956	1.003	0.988	0.993	0.931
u_b12	0.950	1.013	0.828	0.990	0.949	1.002	0.848	0.954	1.000	1.002	0.992	0.932
u_b21	0.972	1.004	0.921	1.003	0.982	1.013	0.933	0.965	0.984	1.033	0.992	0.970
u_b22	0.969	1.005	0.921	1.008	0.984	1.014	0.935	0.962	0.982	1.032	0.992	0.970
u_b31	0.986	1.006	1.035	1.015	0.997	1.012	1.024	0.954	0.990	1.033	0.992	1.007
u_b32	0.986	1.007	1.035	1.016	0.998	1.011	1.025	0.951	0.990	1.033	0.992	1.006
u_b41	0.985	1.009	1.036	1.021	0.994	1.010	1.027	0.954	0.989	1.039	0.992	1.007
u_b42	0.985	1.008	1.036	1.019	0.994	1.011	1.026	0.956	0.989	1.040	0.992	1.007
u_b51	0.967	1.012	0.927	1.004	0.967	1.012	0.945	0.954	0.981	1.039	0.994	0.971
u_b52	0.970	1.010	0.927	0.997	0.964	1.011	0.942	0.957	0.984	1.042	0.995	0.971
u_b61	0.943	1.010	0.827	0.985	0.933	0.999	0.868	0.950	0.966	1.003	0.991	0.931
u_b62	0.949	1.009	0.827	0.978	0.930	0.998	0.864	0.954	0.970	1.005	0.993	0.931
f_b1,trans	1.209	1.111	1.471	1.136	1.260	1.388	1.372	1.178	1.269	1.166	1.040	1.268
f_b2,trans	0.920	0.981	0.963	1.005	0.983	1.017	0.960	0.995	0.995	0.978	0.996	0.979
f_b3,trans	1.066	1.006	1.020	0.998	0.999	1.000	1.034	1.009	1.010	1.006	1.000	1.015
f_b4,trans	1.044	1.003	1.046	0.998	1.001	1.003	1.014	0.999	0.999	1.005	1.000	1.014
f_b5,trans	0.979	0.988	0.955	1.002	0.983	1.019	0.966	0.998	0.990	0.985	0.999	0.984
f_b6,trans	1.303	1.137	1.337	1.102	1.273	1.372	1.318	1.215	1.288	1.151	1.156	1.258
f_b1,long	1.337	1.284	1.114	1.280	1.350	1.274	1.247	1.466	1.380	1.304	1.220	1.306
f_b2,long	1.010	1.002	0.991	0.996	0.997	0.997	0.994	0.977	1.033	1.012	0.996	1.000
f_b3,long	0.982	1.003	1.003	0.997	0.996	0.999	0.992	0.985	1.005	1.012	0.996	0.997
f_b4,long	0.983	1.003	0.998	1.002	1.009	0.999	0.990	0.986	0.974	1.013	1.002	0.996
f_b5,long	0.983	1.003	0.998	0.994	1.000	0.992	0.985	0.987	1.022	1.012	0.998	0.998
f_b6,long	1.391	1.309	1.144	1.278	1.312	1.234	1.204	1.400	1.363	1.343	1.218	1.298
f_b,trans/W_s	1.010	1.011	1.018	1.018	1.017	1.041	1.028	1.019	1.021	1.007	1.011	1.019
f_b,long/W_s	1.015	1.028	1.005	1.029	1.024	1.023	1.008	1.024	1.031	1.036	1.020	1.023
F_p2,trans	1.004	0.999	1.008	0.999	0.993	0.983	1.001	0.989	1.002	1.020	0.998	1.000
F_p3,trans	0.998	0.992	1.000	1.001	0.996	1.010	0.998	1.013	0.998	1.002	1.000	1.000
F_p4,trans	1.006	1.001	1.010	0.999	1.007	1.011	0.999	1.012	1.005	1.000	1.000	1.005
F_p5,trans	1.003	1.004	0.986	0.996	0.999	1.004	1.010	1.013	1.000	0.981	0.998	0.999
F_p2,long	0.996	1.005	1.011	1.008	0.999	1.000	1.008	0.995	1.002	1.005	1.005	1.003
F_p3,long	0.974	1.010	1.004	1.006	1.000	1.000	1.008	0.987	1.002	1.005	1.007	1.001
F_p4,long	0.990	1.010	1.008	1.006	1.001	0.999	1.008	0.990	1.001	1.002	1.009	1.002
F_p5,long	0.974	1.018	0.999	1.001	0.995	0.988	1.005	0.994	0.988	1.007	1.005	0.999

Table D5. Ratio of responses for SSSB S2 to NDPB

	GM 1	GM 2	GM 3	GM 4	GM 5	GM 6	GM 7	GM 8	GM 9	GM 10	GM 11	Average
u_b,trans	0.988	0.896	1.091	1.092	1.002	1.282	0.985	1.002	1.288	0.954	1.000	1.070
u_b,long	0.877	1.019	1.023	1.085	0.973	0.966	0.967	0.860	0.976	1.100	0.974	0.970
u_b	0.915	1.019	1.090	1.044	0.966	1.215	0.985	0.868	1.177	1.101	0.956	1.033
u_b11	0.923	1.059	0.836	1.044	0.933	1.257	0.881	0.865	1.250	1.109	0.988	0.980
u_b12	0.932	1.063	0.837	1.036	0.930	1.247	0.879	0.868	1.262	1.123	0.989	0.981
u_b21	0.857	0.967	0.760	0.971	0.885	1.110	0.817	0.824	1.113	1.075	0.932	0.906
u_b22	0.862	0.972	0.760	0.963	0.883	1.103	0.816	0.826	1.124	1.075	0.933	0.907
u_b31	0.859	0.973	0.756	0.954	0.880	1.005	0.812	0.817	1.025	1.079	0.937	0.888
u_b32	0.855	0.974	0.755	0.959	0.887	1.006	0.813	0.816	1.026	1.078	0.937	0.889
u_b41	0.936	1.041	0.892	1.056	0.955	1.074	0.924	0.858	1.125	1.166	0.990	0.977
u_b42	0.933	1.040	0.891	1.066	0.958	1.075	0.926	0.853	1.127	1.169	0.989	0.978
u_b51	0.934	1.051	1.025	1.075	0.977	1.007	1.021	0.871	1.015	1.178	0.992	1.005
u_b52	0.937	1.051	1.025	1.075	0.975	1.000	1.023	0.869	1.029	1.180	0.992	1.006
u_b61	0.911	1.054	1.118	1.071	0.968	0.915	1.077	0.886	0.964	1.131	0.993	1.012
u_b62	0.915	1.054	1.118	1.067	0.966	0.905	1.079	0.886	0.979	1.135	0.993	1.013
f_b1,trans	0.936	0.946	0.926	1.008	0.965	1.152	0.884	1.028	1.035	0.994	1.004	0.980
f_b2,trans	1.090	1.108	1.429	1.217	1.205	1.511	1.321	1.082	1.294	1.189	1.089	1.256
f_b3,trans	1.150	1.148	1.402	1.206	1.198	1.437	1.344	1.178	1.327	1.197	1.118	1.267
f_b4,tran	1.045	0.992	0.948	1.008	0.963	1.054	0.958	1.013	0.998	0.994	1.005	0.994
f_b5,trans	1.107	0.969	1.012	0.992	0.988	1.008	0.984	0.998	0.985	0.980	1.001	1.003
f_b6,trans	1.050	1.009	1.039	1.008	0.977	0.999	1.003	1.025	0.987	1.043	1.008	1.015
f_b1,long	0.934	1.013	1.013	1.002	1.036	0.998	0.960	0.920	1.100	1.016	1.020	0.998
f_b2,long	1.282	1.280	1.119	1.278	1.238	1.214	1.135	1.293	1.544	1.396	1.228	1.279
f_b3,long	1.217	1.293	1.037	1.220	1.252	1.193	1.107	1.292	1.362	1.409	1.242	1.246
f_b4,long	0.926	1.009	1.002	0.994	1.034	0.997	0.966	0.951	0.992	1.056	1.011	0.993
f_b5,long	0.927	1.017	0.996	1.031	1.029	0.991	0.970	0.963	0.915	1.060	0.995	0.990
f_b6,long	0.885	1.020	0.999	1.051	1.008	0.982	0.971	0.971	0.921	1.069	0.990	0.986
f_b,trans/W_s	1.103	1.055	1.160	1.100	1.076	1.239	1.138	1.102	1.124	1.096	1.055	1.122
f_b,long/W_s	1.029	1.130	0.992	1.128	1.102	1.090	1.040	1.103	1.186	1.204	1.084	1.102
F_p2,trans	0.950	0.962	1.129	0.993	0.970	0.945	1.113	1.011	1.089	1.088	0.924	1.017
F_p3,trans	0.956	0.945	1.148	0.991	0.945	1.044	1.268	0.990	1.089	1.017	0.907	1.029
F_p4,trans	1.025	1.001	0.987	0.999	0.994	1.011	1.018	0.914	1.011	0.947	0.993	0.991
F_p5,trans	1.022	1.009	1.009	0.972	1.000	1.006	0.996	0.994	1.009	0.967	0.988	0.997
F_p2,long	1.008	0.918	1.158	0.949	0.992	1.005	0.965	1.084	1.016	1.032	0.907	0.991
F_p3,long	1.027	0.926	1.032	0.918	0.999	0.993	0.975	1.095	1.027	1.034	0.893	0.989
F_p4,long	0.947	1.040	1.089	1.018	0.993	1.000	1.025	0.978	1.004	1.004	1.020	1.009
F_p5,long	0.934	1.070	1.017	1.008	0.997	0.962	1.005	1.001	0.945	1.030	1.018	1.002

Table D6. Ratio of responses for SSSB S3 to NDPB

	GM 1	GM 2	GM 3	GM 4	GM 5	GM 6	GM 7	GM 8	GM 9	GM 10	GM 11	Average
u_b,trans	0.873	0.864	0.741	1.030	0.861	1.116	0.786	0.896	1.236	0.966	0.946	0.895
u_b,long	0.752	1.010	1.028	1.213	0.942	0.927	0.879	0.728	1.120	1.130	0.940	0.950
u_b	0.798	1.017	0.741	1.133	0.835	1.056	0.779	0.747	1.219	1.128	0.944	0.904
u_b11	0.805	1.091	0.741	1.132	0.931	1.092	0.777	0.746	1.308	1.200	0.964	0.925
u_b12	0.804	1.095	0.741	1.133	0.930	1.091	0.778	0.747	1.305	1.215	0.964	0.926
u_b21	0.779	1.056	0.733	1.064	0.871	1.087	0.800	0.696	1.236	1.096	0.983	0.901
u_b22	0.778	1.050	0.733	1.065	0.868	1.086	0.801	0.697	1.235	1.096	0.981	0.901
u_b31	0.790	0.975	0.737	1.067	0.860	1.064	0.817	0.697	1.188	1.114	0.909	0.892
u_b32	0.790	0.978	0.737	1.067	0.864	1.063	0.816	0.698	1.190	1.114	0.910	0.893
u_b41	0.794	1.010	0.741	1.100	0.826	1.061	0.809	0.705	1.230	1.171	0.922	0.901
u_b42	0.794	1.009	0.741	1.101	0.829	1.061	0.809	0.705	1.234	1.176	0.924	0.901
u_b51	0.792	1.047	0.740	1.109	0.849	1.051	0.797	0.703	1.180	1.206	0.941	0.902
u_b52	0.793	1.043	0.740	1.109	0.847	1.051	0.797	0.703	1.186	1.213	0.941	0.902
u_b61	0.796	1.078	0.741	1.135	0.840	1.050	0.795	0.736	1.202	1.201	0.965	0.911
u_b62	0.798	1.074	0.741	1.133	0.835	1.050	0.795	0.740	1.206	1.209	0.966	0.911
f_b1,trans	1.367	1.071	1.374	1.129	1.193	1.550	1.287	1.244	1.554	1.155	1.035	1.288
f_b2,trans	1.104	1.099	1.382	1.207	1.172	1.521	1.315	1.088	1.447	1.263	1.094	1.265
f_b3,trans	1.173	1.136	1.376	1.211	1.157	1.520	1.345	1.147	1.612	1.231	1.122	1.295
f_b4,tran	1.293	1.061	1.360	1.200	1.165	1.527	1.318	1.262	1.514	1.136	1.164	1.290
f_b5,trans	1.308	1.041	1.307	1.189	1.176	1.530	1.300	1.238	1.536	1.286	1.155	1.289
f_b6,trans	1.377	1.099	1.254	1.110	1.165	1.499	1.269	1.217	1.394	1.137	1.139	1.253
f_b1,long	1.128	1.321	1.190	1.402	1.453	1.260	1.163	1.208	1.561	1.378	1.246	1.300
f_b2,long	1.180	1.384	1.115	1.360	1.218	1.205	1.142	1.141	1.513	1.405	1.203	1.263
f_b3,long	1.072	1.297	1.085	1.298	1.228	1.186	1.122	1.158	1.431	1.434	1.213	1.233
f_b4,long	1.065	1.302	1.145	1.327	1.292	1.195	1.116	1.202	1.366	1.451	1.207	1.245
f_b5,long	1.062	1.341	1.102	1.344	1.275	1.191	1.096	1.226	1.347	1.480	1.206	1.247
f_b6,long	0.975	1.364	1.126	1.344	1.282	1.207	1.119	1.266	1.623	1.508	1.211	1.274
f_b,trans/W_s	1.275	1.116	1.364	1.213	1.167	1.524	1.308	1.238	1.519	1.267	1.141	1.302
f_b,long/W_s	1.063	1.299	1.056	1.335	1.232	1.199	1.170	1.191	1.512	1.420	1.202	1.246
F_p2,trans	0.955	0.941	1.135	0.987	0.970	0.954	1.107	0.956	1.095	1.068	0.922	1.010
F_p3,trans	0.958	0.913	1.159	0.990	0.932	1.103	1.215	0.914	1.100	0.906	0.901	1.009
F_p4,trans	0.993	0.988	1.216	0.990	0.941	1.212	1.271	0.960	1.126	0.914	0.993	1.060
F_p5,trans	1.058	1.011	1.248	0.925	0.993	1.183	1.157	1.062	1.137	0.939	0.980	1.067
F_p2,long	0.950	0.977	1.137	0.992	1.003	1.011	0.998	0.963	1.033	1.048	0.934	0.996
F_p3,long	0.943	0.998	1.161	0.959	1.003	0.997	1.028	1.001	1.040	1.057	0.930	1.005
F_p4,long	1.005	1.050	1.121	0.926	0.990	1.018	1.001	1.020	1.034	1.094	0.950	1.017
F_p5,long	0.953	1.125	0.979	0.963	0.984	1.100	0.980	1.058	1.060	1.133	0.950	1.030